Elucidating structure over atomic length scales through advanced synchrotron-based methodologies

Jonathan Keating

University College London

A thesis presented in partial fulfilment of the requirements for the degree of Doctor of Engineering

2014

Declaration

I, Jonathan Keating, confirm that the work presented in this thesis is my own. Where information has been derived from other sources, I confirm that this has been indicated in the thesis.

Signed _____

Abstract

The work undertaken in this project has focused on developing methodologies to determine the atomic architecture of catalytic materials over short-, medium- and long-range structures. The main objective of the work has been to employ *in situ* techniques at synchrotron sources to enable development of new analytical methods which will provide a unique opportunity to characterise multi-phase systems.

The reduction behaviour of a model cobalt Fisher-Tropsch catalyst was investigated using *in situ* combined XANES/EXAFS/XRD techniques where the sensitivity and selectivity of X-ray absorption spectroscopy (XAS) was exploited to obtain detailed structural information on the dynamic local structure. From these studies a new model on the structure of Co/Al_2O_3 catalyst in the reduced form has been proposed.

Model metallic cobalt systems consisting of both HCP and FCC structures were characterised in detail using both pair distribution function (PDF) and XAS techniques. In-depth structural knowledge over the short-short and medium-range order has been garnered through multi-cluster modelling of EXAFS and PDF data providing new insights into the cobalt phase composition and phase transformation.

In situ PDF studies were carried out on a Pd/Al_2O_3 model catalyst to determine, quantitatively, the phase composition at various temperatures during which PdO ↔ Pd transformations occur. Differential PDF analysis was successful in characterising the metal particles of interest despite the significant contribution from the disordered support phase. Supporting *in situ* XAS studies were undertaken and the findings were in good agreement with those from PDF.

Finally, using low energy chlorine K-edge XAS, real Vehicle Emission Control (VEC) catalysts were studied in order to determine the speciation of chloroplatinate

compounds within fresh and road aged catalysts. With a high sensitivity and selectivity, an investigation of this type demonstrated the advantages of performing XAS speciation studies at the chlorine K-edge.

Table of Contents

List of Figures

List of Tables

Acknowledgements

During the course of my EngD I have met, collaborated with and obtained guidance and support from a number of people at UCL, Johnson Matthey and the synchrotrons I have worked at; some of whom I would like to pay thanks to.

Firstly, I would like to pay big thanks to my supervisor, Professor Sankar, for his inspiration, motivation and continued support during my EngD. His ideas and encouragement were pivotal to any accomplishments I have made.

I would like to thank Tim Hyde, Johnson Matthey, for his supervising role whilst at JM and helping me to adjust from academia to industry. I feel I have obtained very useful insight into the industrial aspect of research and development through working with Tim.

Recognition should be paid to the beamline scientists I have worked with. In particular I would like to thank Shinji Kohara at SPring-8, Japan, whom I enjoyed working with and who provided great scientific help during beamtime. I would also like to show appreciation to Carmello Pristipino at the ESRF for his help and staying long hours with our experiments. Thanks to Martin Shaffer at the SRC, USA for the opportunity to carry out work in Madison. I also appreciate the valuable discussions had with Toru Wakihara, introducing me to PDF and his help orientating a disorientated tourist in Japan.

I would like express my gratitude to Pete Ash, Hoi Jobson and Pete Ellis at Johnson Matthey for their useful discussions, experience and help with the transferral of my project to Johnson Matthey. In particular, I would like to thank Hoi for her patience and help. Recognition should also be paid to John Pignon and John Godfrey for their valuable technical assistance on the project at Johnson Matthey. This period involved some very early starts and long journeys and I would really like to thank John Kilmartin and Kerry Simmance who took me safely to and from Johnson

Matthey every day for two and a half years. Without their driving, conversation and humour the days would have been very long.

I would like to show appreciation to the other members of the Sankar group and UCL members, past and present, who assisted me on beamtime, keeping me company during the long hours, late nights and early mornings. Thanks Martin, Vlad, Andy, John and Kerry.

I am very grateful for funding provided by EPSRC and Johnson Matthey, enabling me to carry out research at both UCL and Johnson Matthey.

Without the support of my close friends this would have not been possible or enjoyable so I would like to thank in particular: Chlöe, Ed, John, Sinead and Rosie for all their encouragement and much needed distraction these past years.

Finally, a special thank you goes to my parents, Terry and Lou, for their constant belief and continuous support over many years especially during my writing up period. This work is dedicated to them.

Chapter 1 Introduction

1.1 Heterogeneous catalysis

The chemical disciplines over which heterogeneous catalysis extends is vast, ranging from physical to organic, bio to environmental, electro to inorganic [1]. What may appear even wider ranging are the industrial processes, modern technologies and chemical reactions that rely upon a catalytic reaction, or at least involve catalysis in one of the steps. Heterogeneous catalysts are, to name but a few, used in making polymers and plastics, controlling pollution and in the energy, medical and food industries [2], the list is almost boundless. It is no surprise, therefore, that over 90 % of industrial chemicals produced have gone through some catalytic process [3]. Heterogeneous catalysis is, undoubtedly, extremely important in manufacturing, technology and chemistry and its global impact is quite remarkable; heterogeneous catalysis is estimated to contribute up to 35 % of the world's Gross Domestic Product (GDP) [4]. Enormous amounts of money are invested in the catalyst industry globally - worldwide catalyst sales exceed one trillion dollars [5] and the economic worth of them is considerably more. The major contribution to the global economy involving catalysis is from fuels for energy release, which rely upon small amounts of catalysts in petroleum refineries.

Much of the discovery of new catalytic processes and materials has traditionally originated within industry [6]. These processes include ammonia synthesis (BASF), catalytic cracking (UOP), zeolite cracking (Mobil), Methanol synthesis (ICI), and the Fischer-Tropsch synthesis (Ruhrchemie) and products such as Nylon (DuPont), Styrene (Dow) and Kevlar (DuPont). Johnson Matthey is a world leader in vehicle emission control catalysts [7-9]. Commonly, industrial catalysts are divided into petrochemical, chemical, polymerisation and environmental industries [6] although these are quite broad fields which encompass many subdivisions of heterogeneous catalysis. Catalysis is indeed a multidisciplinary field in research and industry and many new technologies are emerging through advances in catalyst research. The development and discovery of new exotic materials, as catalysts, are actually driving

new technological methods and industries such as electrocatalysis, fuel cells and photocatalysis [3].

In heterogeneous catalysis, the catalyst is in a different phase to those of the reactants in contrast to homogeneous catalysis where both reactants and catalyst are in the same phase. Frequently, in heterogeneous catalysis, the catalyst is a solid and the reactants are in a gaseous or liquid phase. The advantage here is that the catalyst is easily separated from the reaction mixture at the end of the reaction so it can be recycled [10-12]. The overall function of the catalyst is to accelerate the chemical transformation of reactants to products without affecting the position of the equilibrium. In doing so, transition states are created where the catalyst is bound in one form to the reactants and in another form releases the products. The energy diagram showing various transition states and energy barriers during a catalytic reaction is depicted in Figure 1-1. Overall the catalyst remains unchanged at the end of the reaction [13].

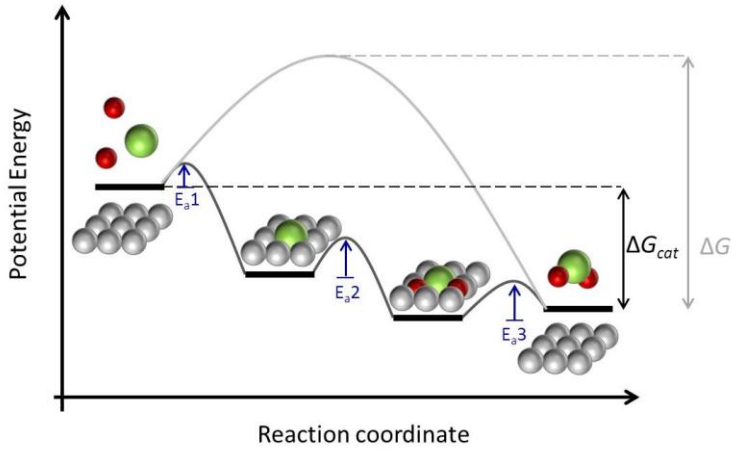

Figure 1-1. *Energy diagram showing a hypothetical catalytic reaction. The catalyst lowers the overall activation barrier to the reaction (grey line) as the reaction proceeds via a series of transition states (black line).*

The dynamic process of catalysis is controlled by kinetic processes such as molecular mobility, translation, diffusion and mass transport [1]. Understanding the kinetics is of major importance since knowledge of the reaction mechanisms and

reaction rate are pre-requisites for designing reactors and optimising reactions [13]. Catalytic reactions rarely occur under ambient or static conditions and involve changes in temperature and energy within the system and therefore thermodynamic phenomena are also involved.

A huge variety of catalysts exist with an ever increasing range of applications. Usually, these catalysts contain a metal, either deposited on a support or present in an oxidic form. The catalytic reactions occur at active sites in the catalyst structure and the performance of an overall catalyst is determined by the average of the different active surface sites on the catalyst [2]. Both catalyst selectivity and activity are crucial requirements in heterogeneous catalysis. Selectivity, for example, may be of paramount concern above all else, and is especially important in the production of specialty chemicals such as those in the fine chemical and pharmaceutical industry [14, 15]. Another important consideration is the catalyst lifetime. Heterogeneous catalysis using precious metals, such as gold, platinum, palladium and rhodium exhibits some of the most active and selective catalysts[12]. Monometallic and bimetallic Pd, Pt and Au catalysts are frequently used in catalysis, especially in emission control technologies and with relatively high costs of using platinum group metals (PGMs) a long catalyst life is desirable. Overall, the superior catalytic efficiency of noble metals as catalysts in fuel production and emissions control and the added value they bring far outweighs the high cost of the catalyst itself [16]. In addition to noble metal catalyst, less expensive transition metal catalysts known as base metal catalysts are used widely in heterogeneous catalysis. Nickel and copper are examples of these and are used extensively in speciality chemical applications [17]. As with noble metal catalysts, base metal catalysts are frequently dispersed on metal oxide supports. One large scale industrial process that requires this type of base metal catalyst is the Fischer-Tropsch synthesis in which supported iron or cobalt catalysts are used [18].

1.2 Classification of heterogeneous catalysts

The unique properties of materials are exploited for use in heterogeneous catalysis where new materials and their novel properties for novel catalytic processes are in high demand. Many new exotic materials are driving new technological methods and industries such as electrocatalysis, fuel cells and photocatalysis [3]. The largest family of catalysts represent oxides, whether they are microporous, clays, supports or multi-component oxides [19]. Some of the common types of heterogeneous catalysts used for industrial applications are discussed here.

1.2.1 Zeolites

Zeolites are "shape-selective catalysts" where their cavities, that are the dimensions of small molecules, make them superior materials for a range of catalytic applications including gasoline production [20], environmental waste removal [21] and gas separation [22] and as photocatalysts [23]. Consequently, they are extremely important catalysts in the field of environmental chemistry. In the methanol to gasoline (MTG) process, for example, the zeolite H-ZSM-5 allows the diffusion of the reactant molecules (methanol or styrene as in Figure 1-2) into the pores of the structure to reach the active site [24]. It so happens that these pores are 0.55 nm in diameter and are thus termed nanoporous materials. The catalysis takes place such that products of no longer than C_{11} (gasoline) are formed which is a direct result of the channel length of the zeolite [25]. Their unique framework structure of varying channel lengths, pore sizes and dimensionalities has been exploited in the last 50 years where new and interesting structures are being developed to suit different applications [26]. Zeolites are now widely used in catalysis for catalytic cracking and hydrocracking of petroleum feedstocks and also the production of gasoline from methanol [3]. This has extended to synthesising novel microporous materials for use in catalysis such as AlPOs [27] and MOFs [28]. These porous materials have replaced environmentally hazardous and toxic homogeneous catalysts [19].

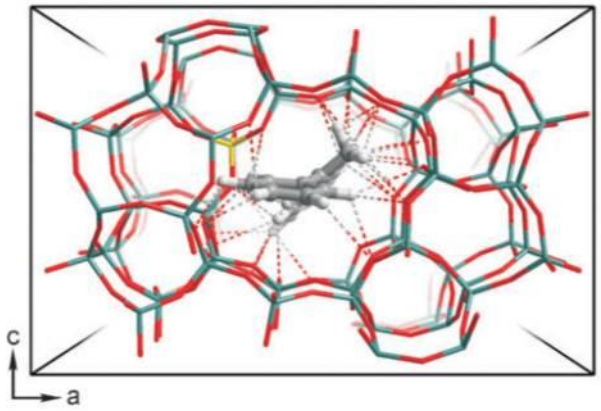

Figure 1-2. *The oligomerization reaction of styrene within the pores of Zeolite H-ZSM-5 (viewed along b axis)*[29].

1.2.2 Mixed oxide catalysts

In addition to open framework structures, such as Zeolites, another type of catalyst includes dense oxide framework structures. An example of this type of catalyst includes bismuth molybdates. These materials act as catalysts in the selective partial oxidation and ammoxidation of olefins, in particular propylene. This is an important industrial catalytic process for the production of intermediates and organic molecules such as Acrolein and propylene oxide for various applications and manufacturing of products [30]. The use of catalysts for this synthesis is critical in reducing unwanted side-products such as CO and CO_2 that are more thermodynamically favourable than Acrolein [31]. Not only are they some of the most efficient catalysts for the oxidation/ammoxidation of olefins[31] but also display interesting electronic and ionic conductivity properties making them ideal for gas sensor applications [32]. This ionic conduction is attributed to oxygen vacancies which become highly mobile leading to changes in bulk conductance [33]. Three phases have been identified to possess these catalytic properties: α-$Bi_2Mo_3O_{12}$, β-$Bi_2Mo_2O_9$ and γ-Bi_2MoO_6 [34]. These structures contain layers of $[Bi_2O_2]^{2+}$, O^{2-} and $[MoO_2]^{2+}$ [35]. These multimetallic catalysts have multifunctionalities in the oxidation of hydrocarbons. Furthermore, these Bi_2O_3/MoO_3 Bi—Mo—O solid oxide catalysts can be modified by addition of other metals. Most of these catalysts go through a Mars van Krevelin reaction mechanism, a redox mechanism where oxygen in the catalyst is involved in the reaction and leaves the system within the product. Having multi-sites, the bismuth molybdate is simultaneously oxidised and reduced at two different sites [36] as illustrated in Figure

1-3. These multicomponent catalysts have demonstrated improved catalytic performance when more than one phase is present in the catalyst, a cooperative synergistic effect that enhances catalytic activity [34].

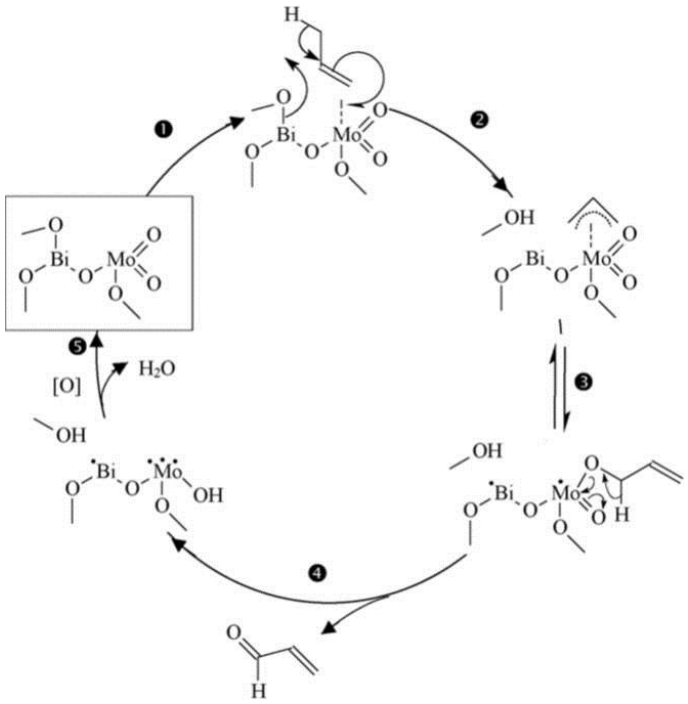
H
O
Bi
Mo
O
O
O

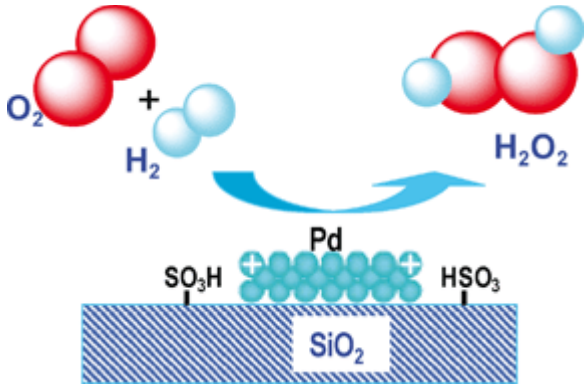

Figure 1-4. *Functionalised silica supported palladium catalysed synthesis of H_2O_2 [39].*

1.2.3.1 Fischer-Tropsch (FT) synthesis

One viable process of producing "synthetic" petroleum is the Fischer – Tropsch (FT) synthesis. Developed in the 1920s by scientists Hans Fischer and Franz Tropsch, FT synthesis was industrialised by Ruhrchimie into a process technology where syngas, a mixture of carbon monoxide and hydrogen, is converted into a synthetic crude oil [18, 40, 41]. It was, in fact, during world war one that Fischer and Tropsch had attempted to address Germany's lack of oil by attempting to convert coal to petroleum. They had little success before the end of the war although continued their research. Their efforts came to fruition; so much so that during the second world war FT processes were producing an estimated 9 % of Germany's fuels and 25 % of its automotive fuel [40]. When peacetime resumed, the production of synthetic diesel fuel was not seen initially seen as a viable fuel alternative since it was more costly than producing fuel from crude oil. The development of the FT process did, however, continue in South Africa where coal was abundant. Sasol set up plants in the 1950s and in the late 1970s South Africa was hit by economic sanctions and apartheid forcing the nation to survive on its own feedstocks and making FT technology more valuable than ever [42]. In recent years due to a crude oil demand outweighing supply and with environmental and economic concerns there is a greater demand for this type of fuel alternative and renewed interest in FT synthesis has been generated [41, 43]. Currently, FT process technology is a full scale global

industry with plants in South Africa (Sasol), Malaysia (Shell), Qatar (Exxon and Sasol) and Nigeria (Sasol/Chevron) [44]. FT synthesis is a desirable method for producing synthetic fuel since not only is it a "clean" technology that produces zero CO_2 (producing syngas however is energy intensive), a green technology using less environmentally unfriendly chemicals such as H_2SO_4, HF and chloroalkanes [45], but also the sulphur and nitrogen free products can be directly used as gasoline and high quality diesel without further hydro-processing [18]. This type of gas-to-liquid (GTL) process is important in today's energy industry. The water produced in FT synthesis can react to oxidise CO to CO_2 and thus the water-gas shift reaction can take place, in parallel to FT synthesis. The reaction mechanisms are outlined below. Depending on the catalyst, temperature and H_2/CO ratio these reactions can be optimised and equilibrium reached [18].

FT synthesis: $H_2 + nCO \rightarrow C_nH_{(2n+2)} + nH_2O$ (1)

Water-gas shift reaction: $H_2O + CO \rightarrow CO_2 + H_2$ (2)

Cobalt and iron based catalysts, for syngas conversion, are the most common FT catalysts used today [41]. The choice of Co or Fe as a catalyst is a consideration of various criteria, some of which are summarised in Table 1-1. Although Co catalysts are more expensive than their Fe analogues, their higher productivity, resistivity to deactivation, lower WGS activity and lower operating temperatures make them a preferred choice in many FT reactors. The low temperature FT process, driven by Co catalysts, has seen a significant development in the last few decades fuelled by advanced understanding and design of these Co based catalysts. After initial use of pure cobalt oxides and binary metal oxides as catalysts the use of high surface area carriers to deposit the metal onto was realised. Silica and alumina and are the most commonly used catalyst supports [46].

Table 1-1. Summary of Co and Fe based catalysts for FT synthesis[41]

Parameter	Cobalt catalyst	Iron catalyst
Cost	More expensive	Less expensive
Lifetime	Longer	Shorter
Activity	Comparable	
Productivity at high conversion	Higher	Lower
Maximum sulphur content	<0.1 ppm	<0.2 ppm
Water-gas shift reaction	Less significant	More significant
Attrition resistance	Good	Poor

1.2.3.2 Auto-exhaust

In spite of depleting crude oil supplies and emerging technologies that aim to use alternative sources of fuel, including hydrogen cars and battery driven vehicles, there is still heavy demand for fossil fuels as a fuel source. The automotive industry continues to grow as new and old industrialised nations develop. With this comes an emphasis and increased responsibility in reducing the amount of harmful vehicle exhaust emissions that are produced. This has primarily been driven by new legislation, in particular since the 1990s, that has been enforced to combat the potentially harmful and irreversible effects of pollutants such as unburnt hydrocarbons, CO and NOx that are emitted from automotive engine exhausts. The term "three-way" catalyst (TWC) is derived from these three pollutants which it simultaneously treats [47]. Nowadays, virtually all road vehicles contain engine exhaust catalysts catalyst, termed "auto-catalysts" [48]. Principally, noble metal-based catalysts including platinum, palladium and rhodium are used as auto-exhaust catalysts since they exhibit significantly higher activity and resistance to poisoning than base metal catalysts in the conversion of hydrocarbons, CO and NOx to H_2O, CO_2 and N_2 within automotive engine emissions [6, 49]. Pt alone is effective, however Rh has superior NOx reducing activity and so is a feature in all TWC in modern vehicles thus it is added to produce a bimetallic catalyst of exceptional efficiency [47].

The use of these noble metals have also directly lead to the discontinued use of lead in petrol which acts by poisoning the catalyst [47]. Typically, 2 – 5.5 g l^{-1} of noble metal per catalyst volume are used [49] and these noble metals are frequently supported on alumina, ceria and mixed ceria-zirconia oxides [50]. Ceria in particular has attracted a lot of attention recently owing to its multifunctional properties, as an additive to TWCs, whereby it is reported to increase metal dispersion, stabilise Al_2O_3 supports and store and release oxygen under lean and rich conditions, respectively, to name but a few [51]. The catalyst exists either as a cordierite monolith in the auto-catalyst or as a wash coat layer and the noble metal is preferentially applied in a non-uniform distribution to enhance activity due to kinetics. The noble metals are present as highly dispersed particles in the catalyst, often up to 50 %, leaving just single atomic layers exposed in the catalyst [49]. Optimal catalytic performance is achieved in complex systems that contain numerous metals, supports and additives such as promoters and stabilisers [48].

1.2.3.3 Methane oxidation

Methane, CH_4, is an abundant gas found predominantly in large reserves of natural gas throughout the world. Additionally, it is an undesirable by-product from many industrial processes in which it possesses a much higher "greenhouse" activity than CO_2 [52]. Meeting alternative energy demands and addressing environmental concerns has generated much interest into new ways of converting methane, to harness its energy, and abating it as an unwanted by-product of gas turbines and gas fuelled vehicles [52]. Methane's natural abundance and precursor in a variety of reactions, such as partial oxidation to syngas [53, 54], steam reforming [55, 56] and reforming for H_2 production for fuel cells [57, 58], make it an attractive prospect for future fuel demands. At present, energy is produced from methane in gas turbines; however these processes emit harmful NOx. Noble-metal catalysed partial oxidation of methane operates at lower temperatures than conventional combustion and thus generates fewer NOx emissions [52]. It is, therefore, a valuable process in environmental catalysis. It has been for some time that Pd/Al_2O_3 catalysts exhibit some of the highest turnover rates and lowest temperature operation for the catalytic total oxidation of methane [59] and supported Pd catalysts continue to be used for

commercial catalytic combustors. In these catalysts there is still debate surrounding the active state of the catalyst, although many authors point to oxidised Pd (PdO) as being responsible for the methane conversion [60, 61]. Discrepancies still arise however in relating the precise atomic architecture of these catalysts to their activity towards methane combustion based on the support used [62, 63], particle size [64, 65] and support and metal phase [64, 66] that are responsible.

In summary, materials science, particularly over the last decade, has innovated new designs for catalytic materials and its knowledge of catalytic processes. With such a large and diverse range of industrial processes relying on a catalyst, a more fundamental approach to understanding the chemistry is taking place in the field of catalysis.

1.3 Structure – function relationships

As chemical and technological processes that rely on catalysts become more prevalent and the catalysis therein more complex, there is a strong desire to attribute catalyst performance to its physicochemical properties. The development and design of new catalytic materials cannot proceed without asking fundamental questions about the structure of catalysts. Indeed, understanding the characteristic properties of the material and attributing them to catalytic behaviour is one of the primary concerns in catalyst research. The ultimate goal is to derive a structure–function or structure–activity relationship. In general this involves attempting to identify a specific species, structure or site in the active catalyst and attributing it to the activity, selectivity and function. Similarly, it is desirable to understand how any loss of activity can be ascribed to changes within the structure of the catalyst. To complicate matters, the selectivity and activity need not be related to the same property of the material and so unique relationships between structure and activity and selectivity are sought [67]. If this type of dependence can be determined then the time in which new catalytic materials can be brought to market, and the cost in doing so, can be significantly reduced. Moreover, our fundamental understanding of catalytic processes can be refined and advanced. Elucidating these relationships may

be challenging, however with advanced characterisation techniques and analytical methods greater insight into these correlations has been obtained than ever before.

Chen and Goodman [68] identified the structure-activity relationship for supported Au nanoparticles which catalytically oxidise CO. Here, the particle morphology was found to be critical to catalytic activity. Au oxidation state and support effects also played a role in deriving this relationship highlighting the intricate interplay of various structural features, at various length scales. A study by Ruth *et al* [69] highlighted special activity of Mo-V-Nb oxide catalysts to the oxidation of ethane to acetic acid. They showed that this was accredited to microscopic morphology that exhibited mixtures and interactions of crystalline phases within the material and an amorphous phase which showed highest catalytic selectivity. The addition of gold to palladium, a Pd-Au alloy catalyst, has been shown to enhance the acetoxylation of ethylene to vinyl acetate. It was deduced in their study that Au greatly enhances the activity, stability and selectivity of Pd and the role of Au is to isolate single Pd sites that facilitate the coupling of the reactant species at Au surfaces [70].

1.4 Structural characterisation of catalysts

Catalytic efficiency including activity, selectivity, lifetime, and cost are not only vital considerations in the selection of a catalyst but also in designing new catalysts. This task requires knowledge of the way in which active sites, usually surface sites, can be manipulated or modified [6] in a thoughtful way rather than by trial and error through performance which has traditionally been carried out [71]. Various parameters influence the catalytic activity, including surface area, pore volume and distribution, acidity or basicity and number of active sites [72]. Controlling these is critical to developing new more efficient catalysts. A fundamental understanding of the kinetics, thermodynamics and structure of catalytic systems enables new catalyst design and development to be carried out in a methodical and intellectual manner.

1.4.1 Laboratory techniques

A plethora of physical techniques exist today through which the structure and properties of a catalyst can be determined. Much has advanced since early days of catalyst characterisation, mostly limited to X-ray diffraction for crystalline structure, chemical analysis for composition and measurements of texture by pore size distribution and surface area [73]. Whilst these are useful, the overall picture of the workings of a catalyst remains incomplete. New techniques have quickly been adapted to the problems in catalysis and the physicochemical properties of catalysts with a vast range of approaches that are applicable to tackling catalyst characterisation. Frequently these can be undertaken within the laboratory ensuring that they are easily accessible to industries. The list of these techniques is indeed expansive and cannot be listed exhaustively here. We can group these techniques, more definitively, into some of the physical attributes they encompass: molecular spectroscopy, resonances, surfaces and X-rays. Clearly, there is some overlap not to mention that certain techniques have sensitivities to surface and bulk, for instance. If we want to probe the functional groups in catalysis, for example, then IR [A, C] and NMR [B] are principally used, although Raman and UV-Vis spectroscopy are also useful[C, D, E]. For structure of a particular site then diffraction is preferentially used (XRD, electron, neutron). UV-Vis, XPS[F] and Mossbauer spectroscopies can extract information on electronic structure [73]. The surface structure of a catalyst can be characterised through XPS and for internal surfaces of a porous material both absorption measurements and bulk techniques are applicable [73]. Cyclic voltammetry is used as a characterisation tool in electrocatalysts for fuel cell applications [74]. The breadth of information derived using a multitude of techniques can certainly develop our understanding of catalyst structure however there is a limit to the knowledge we can obtain and what is fundamentally required. Often is the case that the structural measurements made using these techniques are obtained under conditions that are not comparable to those in which catalytic measurements are made or indeed the conditions under which catalytic reactions occur. Under such "unrealistic" conditions we cannot derive any information on the active state of the catalyst. For surface studies in particular, the high vacuum required is a major drawback. More generally, sample environments and resolution of the techniques

are restricting factors when undertaking advanced characterisation within the laboratory where techniques are routinely performed *ex situ* due to these limitations.

1.4.2 High resolution techniques

The future of heterogeneous catalysis will, undoubtedly, be influenced by environmental, economic and energy related factors. Major scientific challenges are also encountered involving catalyst design, preparation, optimisation and characterisation [19]. Many mechanisms of a catalyst, its activity and selectivity are still unknown or cannot be distinguished [72]. Therefore, characterising the structure of these catalysts is vital to addressing these issues. In a wider sense, structural characterisation in materials science is paramount to understanding the fundamental physiochemical principles that underlie solid state chemistry and in developing advanced functional materials. As we have seen there is a great deal of effort placed upon determining structure–activity relationships in working catalysts. Structural knowledge of the reactive site within a catalyst is required, usually at an atomic-level although it is also important to understand the structure over various length scales *via* selected techniques [75].

Catalyst characterisation has advanced considerably over the last 40 years with high resolution techniques now routinely employed. Of utmost importance in deriving structure-function relationships is the characterisation of the catalyst structure during its reaction or under operating conditions. Just as catalytic measurements are performed *in situ*, it is necessary to characterise the working catalyst *in situ*. This so called *operando* characterisation garners new information about the dynamic structure of the catalyst that is otherwise lost during a post mortem characterisation. Reactive gases, temperature and pressure changes can affect the properties of the material and its structure. Moreover, transition states and intermediate structures can only be elucidated by performing this type of characterisation using *in situ* techniques [76]. It is indispensable that measurements on the catalyst structure can be made at comparable temperatures and conditions at which catalytic phenomena occur. This has seldom been achieved in the laboratory. The terms *operando* and *in*

situ are loosely similar and often used interchangeably. Their distinction is slightly unclear; *in situ* characterisation refers to determining the structure under dynamic conditions, usually as a function of some experimental parameter such as temperature, gas, pressure or concentration, *operando* is frequently associated with the entire experimental setup mimicking that of a working catalyst [77, 78]. In essence and irrespective of terminology, data are measured when the catalyst is in its active state [79] hence the characterisation is performed in an environment similar to that of the real working catalyst. *In situ* techniques employed are temporally and spatially resolved often with atomic-scale resolution and in the timeframe of the reaction which is crucial for studying the short lived activated complexes formed in catalysis.

The majority of catalysts do not exhibit perfectly crystalline structures that can easily be characterised by, for example, X-ray diffraction (XRD). Indeed many catalysts are poorly crystalline and contain constituent components that have varying degrees of crystallinity. Often is the case in such materials, and many other materials of technological importance, that the long-range structure deviates from the local structure, which may be that of the active site in catalysis. Local deviations from the well-ordered long range structure or nanocrystalline structures require a different approach to characterising their structures, one in which the intrinsic localised disorder can be elucidated and not discarded [80]. XRD is a widely used technique for characterisation of the long-range structure and crystallinity within materials. It is not, however, amenable to probing the short-range order and is insensitive to very low concentrations of metal ions, such as those of the active site, or dopant ions displaced from crystallographic positions. In spite of these limitations, XRD is a useful tool in catalyst characterisation where it can be performed either *ex situ* or *in situ* (as a function of temperature, gas, pressure) within the laboratory with relatively simple setups. Useful information on how the catalyst's overall structure is maintained, or otherwise, during catalysis can be obtained where, depending on the desired information, analysis of XRD data can be executed at varying levels of complexity.

Various other laboratory techniques can be employed for structural characterisation of catalysts in particular nuclear magnetic resonance spectroscopy (NMR), infra-red spectroscopy (IR), UV-Visible spectroscopy (UV-Vis) and electron microscopy (SEM, TEM) [81]. These can be used as complementary techniques with each bringing new information surrounding a particular length scale or structural characteristic. Indeed, these techniques have consistently shown their usefulness in probing the structure of catalytic materials. The main drawbacks of these techniques are that they are routinely performed *ex situ*, although sometimes *in situ* studies are carried out within the laboratory. Nevertheless valuable information can be lost by not performing them under realistic conditions of a working catalyst. Although direct information surrounding the active state of the catalyst is not garnered in this manner these *ex situ* techniques performed within the laboratory have dedicated setups, are generally easy to perform and, after initial start-up, are low cost. *Ex situ* characterisation of catalysts is sometimes preferred if time resolved studies are not required thus circumventing the time and cost in going to central facilities. Samples may be pre-treated for example by heating, quenching or ball milling and the characterisation subsequently performed to see the effects of these treatments on the local or long-range structure. In all cases *ex situ* measurements will support those from *in situ* studies. In summary, there are limitations encountered using these techniques, both structurally and experimentally, as we are faced with more and more complex systems. This inherently becomes a materials chemistry problem, one that is not just faced by catalytic systems, where conventional techniques are inadequate and where we must look further afield for resolution.

The experimental setups of *operando* experiments are often not simple and, as previously mentioned, afford the need of highly sensitive techniques which have very high temporal resolution to resolve different structures occurring over the course of the reaction. Additionally, the active metal site of the catalyst may exist in very low concentration, ~0.1 %, therefore spatial resolution and detection is a concern. With these issues in mind high resolution techniques at central facilities must be employed to fully characterise the dynamic structure of a catalyst. Moreover, no single technique can provide all the information required and a suite of techniques are often needed to make sound conclusions on the structure-function

relationship. Each technique has its own advantages, limitations and requirements and by employing a range of techniques, sometimes in a single set-up, a more realistic picture of the working catalyst can be gained [82].

X-ray absorption spectroscopy (XAS) has been extensively used in the characterisation of catalytic materials. It is ideal for structural determination of the catalyst's active state due to its sensitivity to very low concentrations of metals within the materials, its element specificity and fast time resolution with which data can be acquired. Furthermore, the technique probes the local atomic structure without any requirements of periodicity or symmetry thus it is a much preferred technique for studying poorly crystalline and amorphous materials. XAS is rarely performed within the laboratory these days due to the availability of synchrotron light sources. These central facilities provide unparalleled spectral brilliance, such is that required for time resolved *in situ* studies [82] and versatility of sample environments. Precise XAS measurements made at synchrotron sources can derive in depth structural information surrounding the active state of a catalyst under operating conditions. The electronic state, local coordination geometry and bond lengths can be extracted with a high level of accuracy. Coordination numbers, particle sizes and information on the level of disorder within the system can also be obtained albeit with less accuracy. Although the active state, such as a metal site, of the catalyst may be localised, the catalyst's extended structure can play a cooperative role in the function of the catalyst. To characterise the system fully it is therefore desirable to have knowledge over various length scales. Modern setups at synchrotron sources facilitate the combination of XAS and XRD in a single set-up and this has been successfully applied to studying catalytic materials [83-85]. The combination and complementarity of these techniques, that can be performed *in situ*, enables both the long range average structure and local atomic structure to be followed simultaneously in a single experiment thus highlighting the advantages of using the multi-technique approach. In addition to XRD, XAS has also been combined with SAXS/WAXS [86], IR [87], UV-Vis [88] and UV-Vis/Raman [89, 90]. This amenability to combination with other techniques and reacting environments makes XAS one of the most powerful tools in *in situ* catalyst characterisation.

The requirement of long range periodic order in materials has, historically, retarded the characterisation of complex structures such as those exhibited by catalytic materials. Whilst XAS has been proven to be a powerful tool for determining the local atomic structure surrounding the absorbing atom, it provides very little information on the medium-range ordering. X-ray total scattering is a synchrotron based technique (although can be performed in some laboratories) applied to a vast range of materials that have varying degrees of structural coherence. In its infancy the technique was employed for characterisation of amorphous materials such as glasses and liquids. More recently, however, the technique has been transferred to crystalline structures with disorder. X-ray total scattering is essentially a diffraction performed at high energies, small wavelength, which yields the atomic pair distribution function (PDF) within the material. Because of this, it is commonly referred to as the PDF technique, which terminology we shall use for work in this thesis. The high energies of X-ray beams at synchrotron sources, combined with the high intensities of these X-rays, enables the PDF technique to be performed at sufficiently high resolution to determine the short-, medium- and long-range structure of the system. Crucially, the PDF is obtained from these experiments without crystallographic requirements where scattering from both diffuse and Bragg components within the material is measured and analysed. This has enabled the PDF technique to be applied to poorly crystalline, disordered, defect structured and nanocrystalline materials which make up the majority of technologically and catalytically important materials today. PDF provides complementary information to XAS where the total and partial PDFs are obtained, respectively. The technique has, up until recent years, not been exploited for use in catalysis which has principally been limited by current detector technology and method of analysis preventing time resolved studies from being performed. Currently however, fast measurements are being made on real catalytic systems where sample environments with variable temperature and pressure are being made. There is also a strong focus on developing new analytical methodologies to extract more detailed structural information from PDF data. Presently, the PDF technique, unlike XAS, is not combined with a range of other techniques in a single experimental set-up however the self-consistent manner in which structure can be determined over various length scales and new time resolved studies in this area makes it a very effective and unique technique in the field of catalysis, bringing great new interest. The combined use of XAS and

PDF techniques should glean new insights into systems that have hitherto been poorly characterised.

In this thesis, a range of advanced X-ray techniques were employed using both *ex situ* and *in situ* methods to determine structures of a variety of industrial supported catalysts. Highlights include implementation of multi-cluster models in the analysis of EXAFS and PDF data of supported catalysts.

1.5 References

[1] Weisz, P. B., *Annual Review of Physical Chemistry*, (1970) **21**, 175.

[2] Zaera, F., *Chemical Society Reviews*, (2013) **42**, 2746.

[3] Armor, J. N., *Catalysis Today*, (2011) **163**, 3.

[4] Ma, Z.; Zaera, F., Heterogeneous Catalysis by Metals, In *Encyclopedia of Inorganic Chemistry*, John Wiley & Sons, Ltd: (2006).

[5] Coons, R., Catalysts: Seeking the Next Big Thing, In (2007).

[6] Leach, B., Catalysis, Industrial, In University of Texas: Austin.

[7] Johnson, T., *Platinum Metals Review*, (2008) **52**, 23.

[8] Twigg, M. V., *Platinum Metals Review*, (2003) **47**, 157.

[9] Twigg, M. V., *Platinum Metals Review*, (2003) **47**, 15.

[10] McKetta, J., *Chemical Processing Handbook*, CRC Press: (1993).

[11] R. Santen, P. V. L., J. moulijn, *Catalysis: An Integrated Approach*, Elsevier: (2000).

[12] McKetta, J., *Chemical processing handbook*, CRC press: (1993).

[13] Hagen, J., *Industrial Catalysis: An integrated Approach*, Wiley-VCH: (2006).

[14] Mallat, T.; Orglmeister, E.; Baiker, A., *Chemical Reviews*, (2007) **107**, 4863.

[15] Blaser, H. U., *Catalysis Today*, (2000) **60**, 161.

[16] Rabo, J. A., *Catalysis Today*, (1994) **22**, 201.

[17] Kent, J., *Handbook of Industrial Chemistry and Biotechnology*, Springer: (2012).

[18] Dry, M. E., *Journal of Chemical Technology and Biotechnology*, (2002) **77**, 43.

[19] Fechete, I.; Wang, Y.; Vedrine, J. C., *Catalysis Today*, (2012) **189**, 2.

[20] Weitkamp, J., *Solid State Ionics*, (2000) **131**, 175.

[21] Vempati, R. K.; Biehl, E. R.; Gonzalez, J. M.; Yaksic, A.; Gharras, A.; Blum, J. D., *Abstracts of Papers of the American Chemical Society*, (2011) **242**,

[22] De Baerdemaeker, T.; De Vos, D., *Nature Chemistry*, (2013) **5**, 89.

[23] Corma, A.; Garcia, H., *Chemical Communications*, (2004), 1443.

[24] Bjørgen, M.; Svelle, S.; Joensen, F.; Nerlov, J.; Kolboe, S.; Bonino, F.; Palumbo, L.; Bordiga, S.; Olsbye, U., *Journal of Catalysis.*, (2007) **249**, 195.

[25] Meisel, S. L.; McCullough, J. P.; Lechthaler, C. H.; Weisz, P. B., *Chemtech*, (1976) **6**, 86.

[26] Corma, A., *Angewandte Chemie International Edition*, (2001) **40**, 1976.

[27] Simmance, K.; Sankar, G.; Bell, R. G.; Prestipino, C.; van Beek, W., *Physical Chemistry Chemical Physics*, (2010) **12**, 559.

[28] Dhakshinamoorthy, A.; Alvaro, M.; Corma, A.; Garcia, H., *Dalton Transactions*, (2011) **40**, 6344.

[29] Buurmans, I. L. C.; Pidko, E. A.; de Groot, J. M.; Stavitski, E.; van Santen, R. A.; Weckhuysen, B. M., *Physical Chemistry Chemical Physics*, (2010) **12**, 7032.

[30] Bettahar, M. M.; Costentin, G.; Savary, L.; Lavalley, J. C., *Applied Catalysis A-General*, (1996) **145**, 1.

[31] Grasselli, R. K.; Burrington, J. D., *Advances in Catalysis*, (1981) **30**, 133.

[32] Morrison, S. R., *Sensors and Actuators*, (1981) **2**, 329.

[33] Dadyburjor, D. B.; Ruckenstein, E., *Journal of Physical Chemistry*, (1978) **82**, 1563.

[34] Carson, D.; Coudurier, G.; Forissier, M.; Vedrine, J. C.; Laarif, A.; Theobald, F., *Journal of the Chemical Society, Faraday Transactions 1: Physical Chemistry in Condensed Phases*, (1983) **79**, 1921.

[35] Gellings, P. J.; Bouwmeester, H. J. M., *Catalysis Today*, (1992) **12**, 1.

[36] Vankrevelen, D. W., *Angewandte Chemie*, (1954) **66**, 455.

[37] Duprez, D., *Catalysis Today*, (2006) **112**, 17.

[38] Dry, M. E., *Catalysis Today*, (2002) **71**, 227.

[39] Blanco-Brieva, G.; de Frutos Escrig, M. P.; Campos-Martin, J. M.; Fierro, J. L. G., *Green Chemistry*, (2010) **12**, 1163.

[40] Leckel, D., *Energy & Fuels*, (2009) **23**, 2342.

[41] Khodakov, A. Y.; Chu, W.; Fongarland, P., *Chemical Reviews*, (2007) **107**, 1692.

[42] Extance, A., Liquid Assets, In *Chemistry World*, RSC: (2011).

[43] Kamara, B. I.; Coetzee, J., *Energy & Fuels*, (2009) **23**, 2242.

[44] Dry, M. E., *Applied Catalysis A-General*, (2004) **276**, 1.

[45] Steen, E. v.; Claeys, M., *Chemical Engineering & Technology*, (2008) **31**, 655.

[46] Oukaci, R.; Singleton, A. H.; Goodwin, J. G., *Applied Catalysis A-General*, (1999) **186**, 129.

[47] Thomas, J. M., *Principles and Practice of Heterogeneous Catalysis*, Wiley: (1996).

[48] Gandhi, H. S.; Graham, G. W.; McCabe, R. W., *Journal of Catalysis*, (2003) **216**, 433.

[49] Grassian, V., *Environmental Catalysis*, CRC Press: (2005).

[50] Kharas, K. C. C.; Robota, H. J.; Nunan, J. G.; Henk, M. G., Catalysts for exhaust gas treatment|also for removal of carbon monoxide and hydrocarbon comprises platinum alloyed with cobalt, nickel, copper, rhodium, palladium, silver and/or gold on an inert support, EP762926-A; WO9532790-A; WO9532790-A1; EP762926-A1; JP10501172-W; US5977012-A; EP762926-B1; DE69517687-E.

[51] Kaspar, J.; Fornasiero, P.; Graziani, M., *Catalysis Today*, (1999) **50**, 285.

[52] Choudhary, T. V.; Banerjee, S.; Choudhary, V. R., *Applied Catalysis A-General*, (2002) **234**, 1.

[53] Hickman, D. A.; Schmidt, L. D., *Science*, (1993) **259**, 343.

[54] Choudhary, V. R.; Mamman, A. S.; Sansare, S. D., *Angewandte Chemie-International Edition in English*, (1992) **31**, 1189.

[55] Choudhary, V. R.; Uphade, B. S.; Belhekar, A. A., *Journal of Catalysis*, (1996) **163**, 312.

[56] Ashcroft, A. T.; Cheetham, A. K.; Green, M. L. H.; Vernon, P. D. F., *Nature*, (1991) **352**, 225.

[57] Choudhary, V. R.; Banerjee, S.; Rajput, A. M., *Journal of Catalysis*, (2001) **198**, 136.

[58] Choudhary, T. V.; Goodman, D. W., *Journal of Catalysis.*, (2000) **192**, 316.

[59] Anderson, R. B.; Stein, K. C.; Feenan, J. J.; Hofer, L. J. E., *Industrial and Engineering Chemistry*, (1961) **53**, 809.

[60] Farrauto, R. J.; Lampert, J. K.; Hobson, M. C.; Waterman, E. M., *Applied Catalysis B-Environmental*, (1995) **6**, 263.

[61] Burch, R., *Catalysis Today*, (1997) **35**, 27.

[62] Hicks, R. F.; Qi, H. H.; Young, M. L.; Lee, R. G., *Journal of Catalysis.*, (1990) **122**, 280.

[63] Su, S. C.; Carstens, J. N.; Bell, A. T., *Journal of Catalysis.*, (1998) **176**, 125.

[64] Baldwin, T. R.; Burch, R., *Applied Catalysis*, (1990) **66**, 337.

[65] Haack, L. P.; Otto, K., *Catalysis Letters*, (1995) **34**, 31.

[66] Garbowski, E.; Feumijantou, C.; Mouaddib, N.; Primet, M., *Applied Catalysis A-General*, (1994) **109**, 277.

[67] Dias, E.; Davies, A. T.; Mantle, M. D.; Roy, D.; Gladden, L. F., *Chemical Engineering Science*, (2003) **58**, 621.

[68] Chen, M. S.; Goodman, D. W., *Catalysis Today*, (2006) **111**, 22.

[69] Ruth, K.; Burch, R.; Kieffer, R., *Journal of Catalysis.*, (1998) **175**, 27.

[70] Chen, M. S.; Kumar, D.; Yi, C. W.; Goodman, D. W., *Science*, (2005) **310**, 291.

[71] Casci, J. L.; Lok, C. M.; Shannon, M. D., *Catalysis Today*, (2009) **145**, 38.

[72] Leach, B. E., Catalysis, Industrial, In *Encyclopedia of Physical Science and Technology (Third Edition)*, Editor-in-Chief: Robert, A. M. Ed. Academic Press: New York, (2003); pp 491.

[73] Imelik, B., Vedrine, J., *Catalyst Characterization*, Springer: (1994).

[74] Gasteiger, H. A.; Kocha, S. S.; Sompalli, B.; Wagner, F. T., *Applied Catalysis B-Environmental*, (2005) **56**, 9.

[75] Weckhuysen, B. M., *Angewandte Chemie-International Edition*, (2009) **48**, 4910.

[76] Weckhuysen, B. M., *Chemical Communications*, (2002), 97.

[77] Weckhuysen, B. M., *Physical Chemistry Chemical Physics*, (2003) **5**, 4351.

[78] Tinnemans, S. J.; Mesu, J. G.; Kervinen, K.; Visser, T.; Nijhuis, T. A.; Beale, A. M.; Keller, D. E.; van der Eerden, A. M. J.; Weckhuysen, B. M., *Catalysis Today*, (2006) **113**, 3.

[79] Weckhuysen, B. M., *Physical Chemistry Chemical Physics*, (2003) **5**, 4351.

[80] Egami, T. B., S., *Underneath the Bragg Peaks: Structural Analysis of Complex Materials*, Elsevier: (2012); Vol. 2.

[81] Thomas, J. M.; Terasaki, O., *Topics in Catalysis*, (2002) **21**, 155.

[82] Bentrup, U., *Chemical Society Reviews*, (2010) **39**, 4718.

[83] Couves, J. W.; Thomas, J. M.; Waller, D.; Jones, R. H.; Dent, A. J.; Derbyshire, G. E.; Greaves, G. N., *Nature*, (1991) **354**, 465.

[84] Sankar, G.; Wright, P. A.; Natarajan, S.; Thomas, J. M.; Greaves, G. N.; Dent, A. J.; Dobson, B. R.; Ramsdale, C. A.; Jones, R. H., *Journal of Physical Chemistry*, (1993) **97**, 9550.

[85] Thomas, J. M.; Greaves, G. N., *Science*, (1994) **265**, 1675.

[86] Nikitenko, S.; Beale, A. M.; van der Eerden, A. M. J.; Jacques, S. D. M.; Leynaud, O.; O'Brien, M. G.; Detollenaere, D.; Kaptein, R.; Weckhuysen, B. M.; Bras, W., *Journal of Synchrotron Radiation*, (2008) **15**, 632.

[87] Newton, M. A.; Jyoti, B.; Dent, A. J.; Fiddy, S. G.; Evans, J., *Chemical Communications*, (2004), 2382.

[88] Tromp, M.; Sietsma, J. R. A.; van Bokhoven, J. A.; van Strijdonck, G. P. F.; van Haaren, R. J.; van der Eerden, A. M. J.; van Leeuwen, P.; Koningsberger, D. C., *Chemical Communications*, (2003), 128.

[89] Beale, A. M.; van der Eerden, A. M. J.; Kervinen, K.; Newton, M. A.; Weckhuysen, B. M., *Chemical Communications*, (2005), 3015.

[90] Gao, X. T.; Bare, S. R.; Weckhuysen, B. M.; Wachs, I. E., *Journal of Physical Chemistry B*, (1998) **102**, 10842.

Chapter 2 Experimental Methods

2.1 Chapter Overview

The majority of the work undertaken in this thesis has been performed at synchrotron radiation sources. The generation and uses of synchrotron radiation are discussed in this chapter. In addition to this, the techniques we have employed are described in detail along with some specifics of the beamlines that were used. The development of methodologies to model the *ex situ* and *in situ* X-ray data that were obtained is particularly relevant to this thesis and so shall be discussed in depth. This includes the more conventional methods of analysis we have used in addition to more advanced methodologies that were developed. In order to fully resolve the structures within the materials we have investigated, multi-cluster methodologies have been implemented using *ex situ* and *in situ* EXAFS and PDF data. The term "multi-cluster methodology" is applicable to the modelling of experimental data from both of these techniques. Through these methodologies we have obtained in-depth structural information on both the short-range and medium-range ordering in a self-consistent manner which is both insightful and challenging.

2.2 Synchrotron radiation

It took just over half a century after the discovery of X-rays by Rontgen, in 1895[1] , for synchrotron radiation (SR) to be observed by Elder *et al* [2]. It could not be envisaged then, how integral SR is to scientific research today spanning a wide range of scientific disciplines. It had been known for some time (as early as 1897 [3]) that accelerated charged particles emit electromagnetic radiation. Indeed, since it is a natural phenomenon in stars. It was, however, Langmuir in 1947 [2] who was accredited with first observing synchrotron white light through a 70 MeV synchrotron at the General Electric Laboratories as: "*a small spot of brilliant white light*". The electromagnetic radiation emitted by a synchrotron had, heretofore, been more of a nuisance than a useful tool as first generation synchrotrons were exclusively centres of high energy physics research [3]. The turning point came in 1956, in a paper by Tomboulian and Hartman, when the potential for SR to be harnessed for use in research other than accelerator physics was realised [4]. SR was put to use in far-ultraviolet/soft X-ray spectroscopy. Three major characteristics of the radiation produced by the synchrotron were unparalleled by any other source: (1) the intensity of the "white" electromagnetic radiation, (2) the spectral brightness and brilliance, and (3) the beam size of the emitted radiation. Additionally, the linear polarisation of the SR beam added to the important properties for use in spectroscopy and research. It took some time, however, before SR was used solely for condensed matter physics research.

In 1966 the inaugural SR source dedicated to SR research was installed at University of Wisconsin, Madison. This 240 MeV storage ring, Tantalus, was the advent of second generation SR sources [3]. Since then, advancements in optics and technology have facilitated the development of larger, more energetic, SR sources producing even more intense and brighter radiation. Nowadays, third generation SR sources, such as the ESRF (France) and Diamond Light Source (UK) are accessible and indispensable facilities for the scientific community throughout the world. There are currently more than 40 synchrotrons in 19 countries [5, 6] with even more being built and planned in particular in countries where SR sources do not currently exist. SR has, and continues to, advance a diverse range of fields that include, but are certainly not restricted to medicine [7, 8], catalytic chemistry [9-12], materials science [13-15],

surface physics [16, 17], structural biology [18-21] and geology [22-24]. The SESAME SR facility near Amman [25], currently in the latter stages of commissioning, is a highlight in the importance of SR to scientific research which has fostered collaboration between diverse societies in the middle-east.

2.2.1 Generation of synchrotron radiation

The acceleration of electrons in a circular trajectory passing through a magnetic field emits electromagnetic radiation tangentially to their orbit. SR is produced in this way when electrons are accelerated to ultrarelativistic velocities in a storage ring generating cones of polychromatic "white" light as the electrons change direction. The increase in the applied magnetic field strength, over time, with the increase in energy of the charged particles as they are accelerated through a circular path is synchronised and thus is the origin of the term "synchrotron" [26]. The synchrotron consists of several features including a linear accelerator (LINAC), a booster ring, a storage ring, insertion devices and experimental hutches. A schematic of a SR source is illustrated in Figure 2-1.

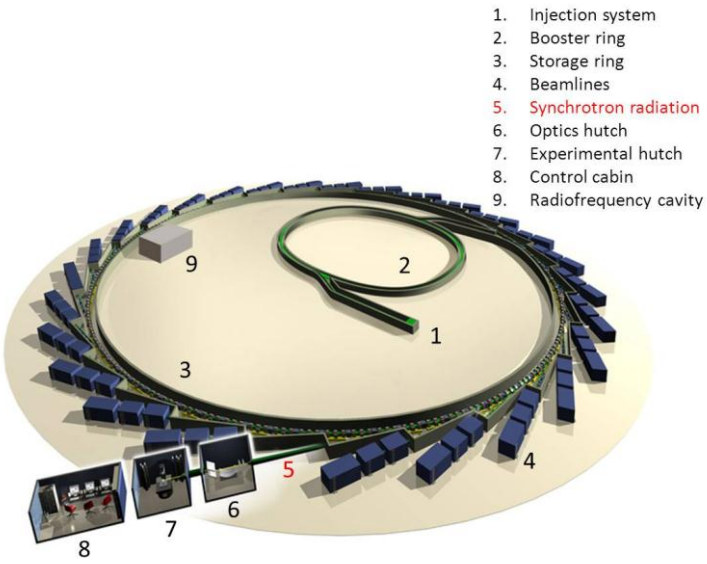

Figure 2-1 *Schematic diagram of a synchrotron radiation source. The key features are labelled* [5].

Electrons are produced from an electron gun and are accelerated to high energies using a linear accelerator (LINAC), typically in the range of a few hundred MeV to several GeV[27]. The electrons are then fed into a booster ring, located inside or outside the storage ring, where they are accelerated further to ultrarelativistic speeds. This process is known as injection. Once the electrons have reached sufficient energy, typically 3 or more GeV, they are injected into the main synchrotron ring, known as the storage ring. The storage ring is between *ca*. 120 [6] and 1400 m [28] in circumference; the larger ring the ring, the more the energy is transferred to the electrons and the higher the energy of X-ray photons that are produced. Electrons travelling through the storage ring are stored in bunches so that their loss in energy, as they accelerate round the ring, can be replaced by radiofrequency cavities [3]. After a certain time period (typically a few hours) the current reduces, however, and electrons are re-injected into the ring. Bending magnets located on the curved points in the storage ring focus the electrons round the storage ring and are the point at which a continuous spectrum of intense and coherent SR is emitted. SR radiation is also produced at points in the storage ring where insertion devices are located. These are periodic magnetic structures located on straight sections of the storage ring known as either wigglers or undulators [26]. Figure 2-2 depicts the creation of SR at a synchrotron source. Wigglers produce bright and spectrally continuous light with short wavelengths *via* the "wiggling" of the electron beam which yields a large angular divergence *via* a series of bending magnets of alternate polarities [26]. Undulators produce a gentler periodic orbit with a smaller angular divergence. As a result, interference of radiation causes an enhancement of flux and SR is observed over a narrower spectral range. The magnitude of the induced oscillations differentiates wigglers and undulators as insertion devices. The wavelength of the SR can be selectively chosen by moving the rows of magnets in the undulators closer together or further apart. The use of insertion devices in the storage ring enables a greater range of experiments to be performed at SR sources where the spectral requirements of each experiment can be met by locating the beamline at bending magnet, wiggler or undulator positions.

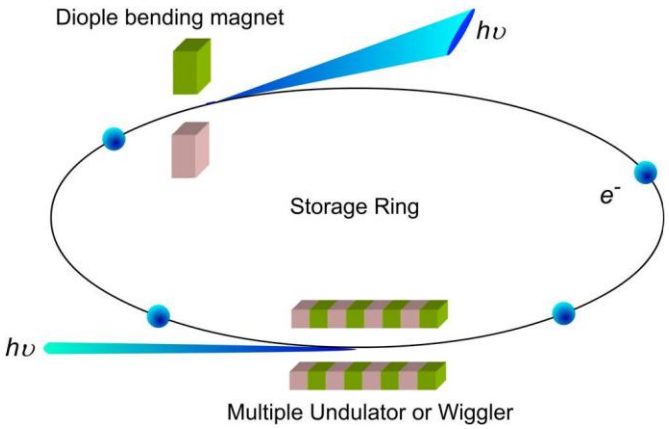

Figure 2-2. *The generation of synchrotron radiation [29]. Flux of synchrotron radiation emitted from an undulator insertion device can be several orders of magnitude higher than at a bending magnet and with a smaller angular divergence.*

A result of accelerating the electrons in bunches, rather than in a continuous manner, is that sub-nanosecond pulses of SR are produced at the bending magnets and insertion devices. For most experiments the time between the pulses is so short that it is inconsequential to the experiment's time resolution and thus is considered to be a continuous flux of SR [26]. Some very state-of-the-art experiments, however, are making use of femtosecond time pulses to probe atomic dynamics and excited states [30].

2.2.2 Unique properties of SR

The quite remarkable characteristics of SR produced at SR sources can be summarised as follows [31, 32]:

i. High intensity beams emitting from the storage ring from several kW to several MW, many orders of magnitude greater, for example, than X-rays produced from X-ray tubes.
ii. High degree of collimation; a small angular divergence of the beam, ranging between 1 mrad and 0.1 mrad.
iii. High linear polarisation in the plane of the ring or elliptical polarisation outside the plane.
iv. Large spectral range; a highly tuneable source providing a continuum of energies from microwaves to the hard X-ray region.

v. Pulsed beams as short as 50 ps.

vi. Very stable SR beams originating from the highly stable electron beam in the storage ring.

vii. High brightness (or brilliance) 10^4 to 10^{14} times more brilliant than lab X-ray sources and typically larger than 10^{18} photons/s/mm^2/mrad^2/0.1% bandwidth in third generation sources. Brightness is defined as the photon flux per unit area per unit solid angle at the source.

The above properties are incomparable to laboratory produced X-rays, for example. Features such as the high brightness of the X-ray beam (high flux with a low beam divergence) and the highly tuneable X-ray source are key to the success of highly spatially and temporally resolved experiments where specific wavelengths can be used for specific experiments. The rapid data collection at synchrotron light sources is also a major advantage over using laboratory sources, especially for *in situ* experiments that are performed. The specific properties of SR allows for numerous techniques to be employed and, moreover, for multi-technique experiments to be carried out on a diverse range samples and systems at SR sources. Well established techniques, such as X-ray absorption spectroscopy, and rapidly developing techniques, in particular the pair distribution function technique, have harnessed the power of SR with application to materials characterisation. A detailed description of these techniques shall now follow.

2.3 X-ray absorption spectroscopy (XAS)

Since the first measurement of an absorption edge by M. de Broglie in 1913 [33] and Fricke's first observation on fine structure in an absorption spectrum in 1920 [34], the theory that underpins X-ray absorption spectroscopy (XAS) has evolved substantially. A theory which aimed to understand the origins of the structure sensitive features in an X-ray absorption spectrum was first put forward to by Kronig in 1931 [35] however it wasn't until the late 1960s that a formulation was derived that could propel this technique into new fields of research and development. Kronig's theory used crystal structure to explain the existence of oscillations observed in the higher energy region of an X-ray absorption spectrum; his theory was inherently

based upon the assumption of long-range order (LRO) within a material. Short-range order (SRO) theories were also proposed in response to this [36]. In the following years encouraging work was being carried out but no major progress was made. Uncertainty as to whether the oscillations observed in the Extended X-ray Absorption Fine Structure (EXAFS) should lie with a LRO or SRO theoretical basis ensued up until 1971 when pioneering work by Sayers, Lyle and Stern demonstrated the SRO nature of EXAFS and used the Fourier transform as an analytical tool [37]. It had hitherto been unused! Their work between 1971 and 1975 laid the foundation for modern day EXAFS as a routine and powerful characterisation tool. This came at a fortuitous time where the advancements in theory were paralleled by developments in synchrotron X-ray sources [36]. Indeed, the relatively weak oscillations in the absorption spectrum and the subtle features in the X-ray Absorption Near-Edge Structure (XANES) require the high resolution X-rays produced at SR sources. The XANES and EXAFS regions of an X-ray absorption spectrum are highlighted in Figure 2-3.

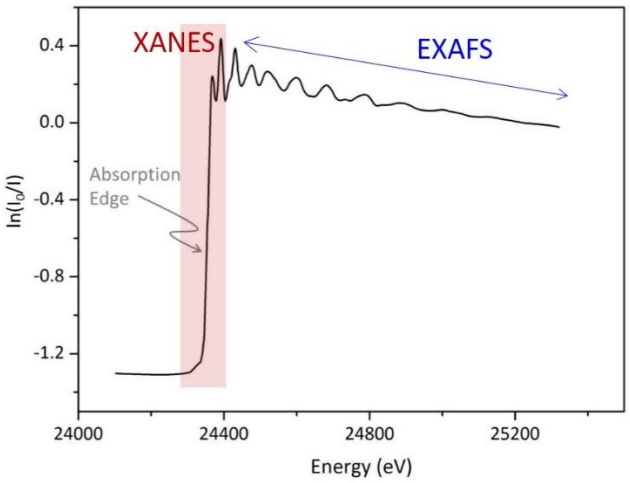

Figure 2-3. *The Pd K-edge absorption spectrum for palladium metal foil highlighting the XANES, edge and EXAFS regions.*

An XAS experiment seeks to determine the electronic state and local structure surrounding an absorbing atom. This is made possible by the chemical specificity of the experiment and the inherently local probe it is. Importantly, there are no

requirements of symmetry or periodicity which makes XAS a powerful tool in characterising industrially and technologically relevant materials that exhibit limit structural order. XAS can be applied to practically any type of material, irrespective of its crystallinity, to study the short-range order, extending from crystalline to highly disordered solids, glasses to liquids, even molecular gasses. The wide range of accessible X-ray energies at SR sources and the various edges that can be probed enables XAS to be a diverse structural tool for materials characterisation.

2.3.1 Theory

As X-rays pass through matter they are attenuated by the sample and the transmitted intensity, *I*, follows Beer's Law.

$$I = I_0\, e^{-\mu x}$$

The transmitted intensity, *I*, is a function of the intensity of the incident X-rays, I_0, the sample thickness, x, and the absorption coefficient, μ. This is represented in Figure 2-4.

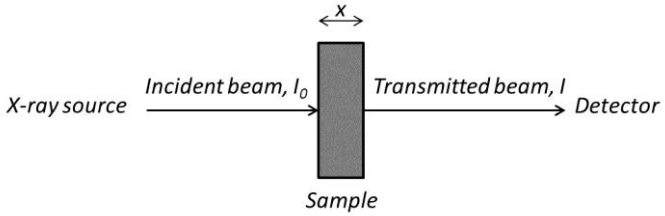

Figure 2-4. *The transmission of X-rays through a sample according to Beer's law. As X-rays pass through the sample they are absorbed and the transmitted intensity is attenuated as a function of the sample composition and the energy of the incident X-rays.*

In an XAS experiment the absorption coefficient, μ, is measured as a function of incident photon energy where $\mu(E)$ describes the attenuation of X-rays by the sample and is the key property in an XAS experiment. With increasing energy, the X-ray absorption spectrum exhibits a smooth decrease in absorption until the energy of the

incident X-rays are equal to the binding energy of a core-level electron. At this point there is a sharp rise in absorption which signifies the excitation of a core-level electron into the continuum and this corresponds to the absorption edge of the X-ray absorption spectrum. This process of X-ray absorption is graphically illustrated in Figure 2-5.

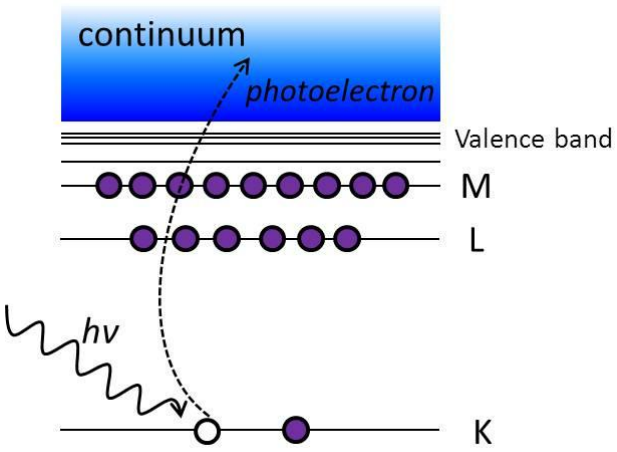

Figure 2-5. *Process of X-ray absorption (adapted from [38]). When an incident X-ray has sufficient energy (hυ) a core-level electron is ejected out of the atom. A photoelectron created from the ejection of a 1s electron is a K-edge absorption process. Subsequent filling of the core-hole by a higher level electron gives rise to X-ray (fluorescence) or electron (Auger) emission.*

Figure 2-3 displays the Pd K-edge X-ray absorption spectrum, $\mu(E)$, for palladium metal foil illustrating the increase in absorption probability at the absorption edge. This increase in absorption probability at the absorption edge is due to the promotion of a core-level *s* electron into an unoccupied *p* state, i.e. $1s \rightarrow 4p$ transition. The characteristic absorption edge is unique for each element and is exploited in XAS experiments where the X-ray energy can be finely tuned to the binding energies thus making XAS an element specific technique. Furthermore, probing different core-level electrons enables *K*-, *L*- and *M*-edges to be accessed that extend from light to heavy elements using hard to soft X-rays[49]. An alternative method of measuring the absorption coefficient is by using the X-ray fluorescence or Auger electron emission.

The yield of these processes indirectly measure $\mu(E)$ and will be described later in this chapter.

2.3.1.1 XANES

XANES extends to *ca*. 50 eV above the absorption edge and is highly sensitive to the chemical environment of the absorbing atom. The XANES of cobalt oxide, Co_3O_4, is displayed in Figure 2-6. The variety of shapes and features that are observed in XANES spectra arise due to its dependency on the electronic structure of the excited-state atom and its local geometry. The absorption edge is directly related to an allowed transition of a core-level electron to an unoccupied bound state which is governed by the dipole selection rule, $\Delta L = \pm 1$ [39]. At energies slightly above that of the absorption edge the photoelectron is ejected into the continuum, or excited into unbound states, and experiences scattering by neighbouring atoms [39]. The theory of XANES is not as well developed as EXAFS theory and consequently interpretation and analysis is restricted to a qualitative or semi-quantitative level. Principally, this is due to XANES being strongly influenced by multiple-scattering effects, as well as electronic effects, which originate from the scattering of the photoelectron from neighbouring atoms. These effects are significant and dominate in this energy region of the spectrum [40].

Detailed XANES calculations can be performed, for example using FEFF9 [41], however this level of analysis is seldom required or restricted to simple structures. Nevertheless, very useful information can still be extracted from the XANES region of the absorption spectrum. Furthermore, because the XANES signal is much stronger than that of the EXAFS and suffers from less noise it is, in most instances, easily obtained. One of the primary uses for interpretation of XANES spectra is for speciation [42-46]. A XANES spectrum of a sample will be unique to the electronic and geometric configuration of the absorbing atom. Several characteristic features are commonly observed in a XANES spectrum which may be present, prominent or completely absent. These are the pre-edge, edge, near-edge and white line marked in Figure 2-6.

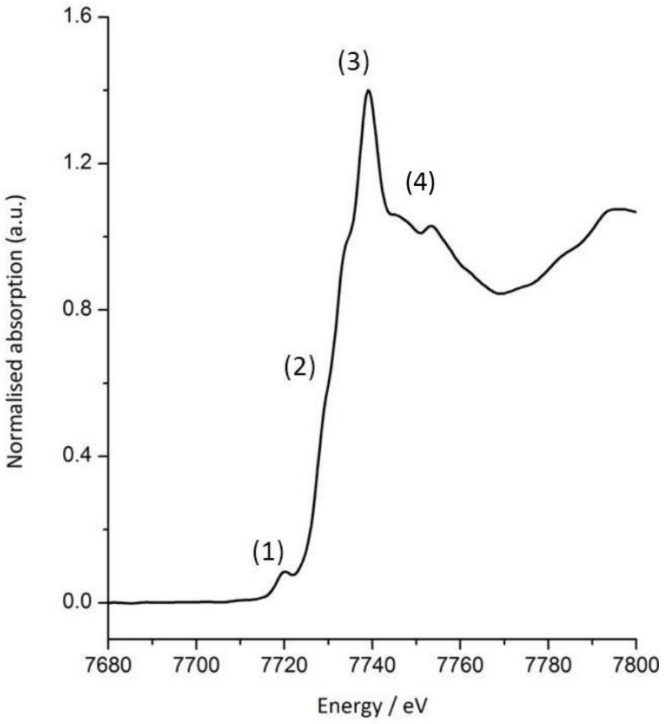

Figure 2-6. *Co K-edge XANES spectrum of Co_3O_4. Several distinguishing features are observed: 1) A weak pre-edge peak below the main edge arising from the 1s → 3d transition. This is a dipole forbidden transition but gains some intensity due to the overlap of d orbitals with p orbitals, termed 'dp mixing'. 2) The most intense absorption at the absorption edge which is due to the dipole allowed 1s → 4p transition. 3) The "white line" at the top of the rising edge. This intense peak originates from the presence of coordinating ligands such as oxygen in addition to the dependence on the density of unoccupied states. 4) Near-edge region which contains resonances that are strongly influenced by multiple-scattering.*

2.3.1.2 EXAFS

Whereas XANES is concerned with the promotion of a core-level electron within the absorbing atom and is thus an electronic spectroscopy, EXAFS originates from the scattering of the ejected photoelectron wave by neighbouring atoms in such a manner that the distance to neighbouring atoms determines the interference pattern caused by the outgoing and backscattered photoelectron waves. This interference gives rise to the fine oscillatory structure observed in $\mu(E)$ above the absorption edge which is a

fundamental property of the higher energy region of the X-ray absorption spectrum. In general, this feature begins at *ca*. 50 eV above the absorption edge and extends to *ca*. 1000 eV beyond it and is termed the extended X-ray absorption fine structure (EXAFS). Figure 2-7 displays the XANES and EXAFS regions of the K-edge X-ray absorption spectrum of palladium metal foil.

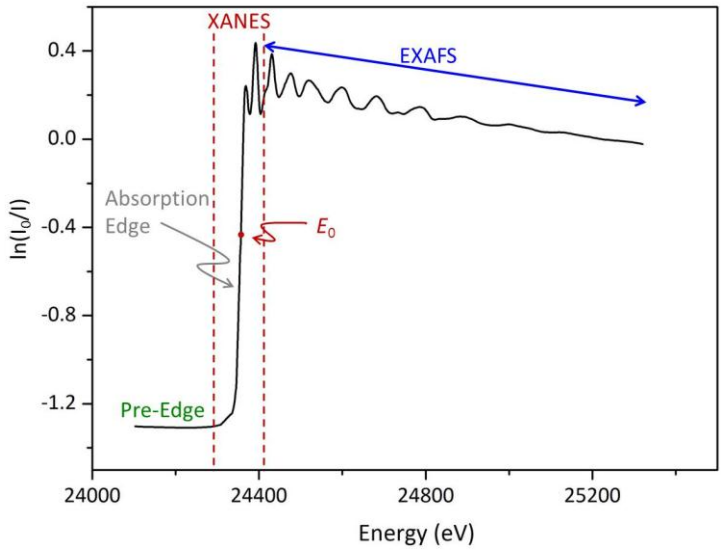

Figure 2-7. *The pre-edge, absorption edge, XANES and EXAFS regions in the μ(E) data of palladium metal foil. The energy value of the absorption edge is taken to be at E_0, the threshold energy, which defines the origin of the photoelectron wave vector, k.*

At energies above the binding energy, also referred to as the zero-point or threshold energy E_0, of the core-level electron the photoelectron has a kinetic energy, E_k, defined as

$$E_k = h\nu - E_{\text{binding}}$$

In this energy regime the photoelectron is considered to be a spherical wave, having left the atom, and thus has an associated wavelength, λ, given by

$$\lambda = \frac{2\pi}{k}$$

The EXAFS function, $\chi(E)$ given below, arises from the interference between the outgoing and backscattered photoelectron waves and therefore this region of the X-ray absorption spectrum contains detail surrounding the local structure around the absorbing atom

$$\chi(E) = \frac{\mu(E) - \mu_0(E)}{\Delta\mu_0(E)}$$

where $\mu_0(E)$ is the atomic background absorption of an isolated atom and $\Delta\mu_0(E)$ is the normalisation factor. This factor is normally represented by the jump in absorption at the edge, E_0. The outgoing photoelectron, behaving as a curved wave with an associated wavelength, is defined in terms of k, the photoelectron wave number. The conversion of energy to k, with reciprocal distance units ($Å^{-1}$) is given by,

$$k = \sqrt{\frac{2m(E - E_0)}{\hbar^2}}$$

where E_0 is the threshold energy and m is the mass of an electron. $\chi(k)$, referred to as the EXAFS function, contains precise information on the local atomic structure influenced by the type and distance of neighbouring atoms. The different frequencies in the oscillatory function, $\chi(k)$, correspond to different surrounding atoms, or coordination shells, where $\chi(k)$ is the summation of all interference patterns caused by scattering from all neighbouring atoms. Furthermore, interference can be in phase (constructive) or out of phase (destructive). The interference pattern changes as the energy of the photoelectron does. Consequently, the absorption

coefficient is modulated with energy where maxima and minima appear due to the constructive and destructive interference of the outgoing and backscattered photoelectron waves. This is depicted in Figure 2-8 which displays the $\chi(k)$ data for palladium metal foil. One important consequence of this phenomenon is that different atoms experience different phase shifts and hence the identity of the scatterer can be deduced.

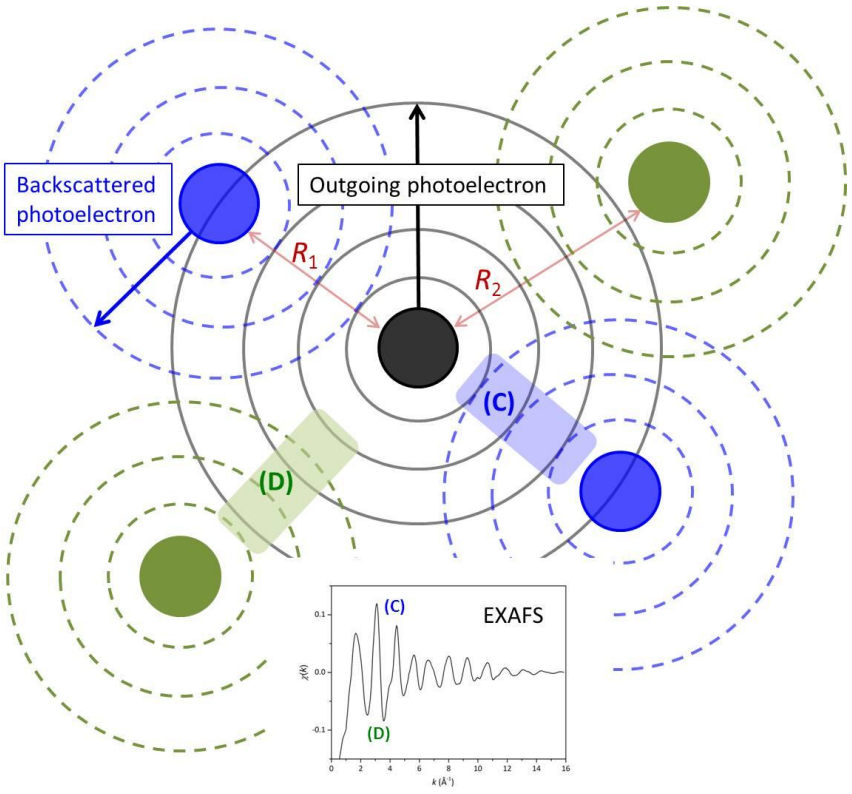

Figure 2-8. *Scattering of the outgoing photoelectron wave by the neighbouring atoms. Constructive (in phase) and destructuve (out of phase) interference gives rise to maxima (C) and minima (D) in the EXAFS, χ(k). The distance to neighbouring atoms in coordination shells (R_1, R_2) is determined by the associated phase shifts of the backscattered waves.*

Although the outgoing photoelectron is considered as a spherical wave, the construction of an equation that describes the EXAFS function has, for simplicity, used a single-scattering plane-wave approximation. The equation derived by Sayers et al in 1971, which remains useful for most analyses today, has been modified to include many-body interactions that give rise to multiple-scattering processes and

these that have been shown to be of importance in structural determination by EXAFS [47]. The general EXAFS equation is given below.

$$\chi(k) = S_0^2 \sum_j \frac{|f_j(k)|}{kR_j^2} N_j e^{(-2R_j/\lambda(k))} e^{(-2\sigma_j^2 k^2)} \sin(2kR_j + 2\delta + \phi_j)$$

This equation represents the summation of all interference patterns, or damped sine waves, from the scattering of all neighbouring atoms. From a phenomenological viewpoint the absorbing atom is surrounded by "shells" (*j*) of like atoms, at a distance from the absorber, R_j, of number N_j with a backscattering factor $f_j(k)$ that depends on the atomic number, *Z*, of the backscattering atom. As *Z* increases the scattering intensity increases. The $1/R^2$ dependence on amplitude means the oscillations diminish which has implications in the analysis of the EXAFS Fourier transform. Further dampening of the sine waves occurs due to the two exponential terms in the EXAFS equation. The first term which contains $\lambda(k)$ is due to the mean free path of the electron. This accounts for losses from inelastic scattering the photoelectron experiences. The consequence of this is that the EXAFS contains information up to ca. 10 Å. The second exponential dampening term contains σ^2 which represents the mean square displacement in R_j referred to as the Debye-Waller factor. This fluctuation in *R*j by σ^2 is due to both static disorder (σ_D) and thermal motion (σ_T) of the atoms, given as

$$\sigma^2 = \sigma_T^2 + \sigma_D^2$$

The sine term in the EXAFS equation represents the phase of the wave interference which arises from the atomic potentials of the absorbing and backscattering atoms. The 2*kR* phase shift denotes the fact that the photoelectron travels from the absorbing atom to the backscattering atoms and back again. From determination of phase shifts, the distance to the nearest neighbours (effectively half the scattering path length) can be determined. The S_0^2 term in Equation 2-6 is the amplitude

reduction factor due to many-body effects and is included to account for the shake-up and shake-off processes that occur in the central atom after photo-ionisation. Essentially this describes how not all the photoelectrons that are produced take place in the scattering phenomena by neighbouring atoms. A result of the additive nature of the scattering processes is that EXAFS is an element specific and an average technique that is sensitive to all surrounding atoms equally [9]. Additionally, the mean free path term in the EXAFS equation inherently makes EXAFS a local structural probe.

Since both the amplitude and phase parts of the EXAFS equation have dependence of *k*, analysis of the EXAFS data can yield structural information that is contained within. The *k* dependence of $f_j(k)$ identifies the backscattering element and similarly the phase shift determines the distance. Once these factors have been calculated, *N*, *R* and σ^2, as variable parameters, can extract the respective number, distance and disorder. The amplitude term of the EXAFS equation contains both *N* and σ^2 which are highly correlated thus the determination of *N* carries with it uncertainties of at least 10 % [48]. Estimates of σ^2 may be a little better known, through using standards, although the total σ^2 determined from the EXAFS equation contains both the thermal and static disorder contributions.

EXAFS data may be represented in *k*-space or, equally, in *R*-space *via* the Fourier transform of $\chi(k)$. The simulation and analysis of the EXAFS can be performed entirely using the EXAFS equation . It is, however, often preferable to reproduce EXAFS data as its Fourier transform whereby

$$FT(R) = \frac{1}{\sqrt{2\pi}} \int_{k_{min}}^{k_{max}} k^n \chi(k) e^{i2kr} dk$$

The FT is a weighted distribution of absorber-scatterer distances often referred to as a "pseudo" radial distribution function where groups of atoms, or "coordination shells" are separated by different distances corresponding to peaks in the FT. Data viewed in this way enables a more heuristic approach to interpreting the EXAFS. It is noteworthy that this visualisation represents the modulus of the FT whereas in fact

the FT is a complex function containing real and imaginary parts. For the EXAFS studies in this thesis work only the moduli are shown.

A consequence of the energy dependence of the phase shift, $\Phi_j(k)$, is that the position of the peaks in the FT do not directly correspond to inter-atomic distances. The position of these peaks are frequently between *ca*. 0.2 and 0.5 Å lower than the real distances and are generally similar for each element. The k^n term in the fourier transform corresponds to the weighting factor by which *k* is multiplied and which is commonly between 1 and 3. It is useful in EXAFS, and routinely applied in analysis, since multiplying by a higher *k*-weighting can compensate for the loss in amplitude in $\chi(k)$ at higher *k*. Moreover, this *k*-weighting is particularly useful for distinguishing between high and low *Z* scatterers; at low *k* values low *Z* scatterers dominate the EXAFS signal and at higher *k* values heavier elements scatter more significantly. Different regions of the EXAFS spectrum can therefore be emphasised to reveal contributions from different *Z* scatterers [9, 49]. Figure 2-9 highlights the different *k*-weighted EXAFS and FTs of palladium metal foil data.

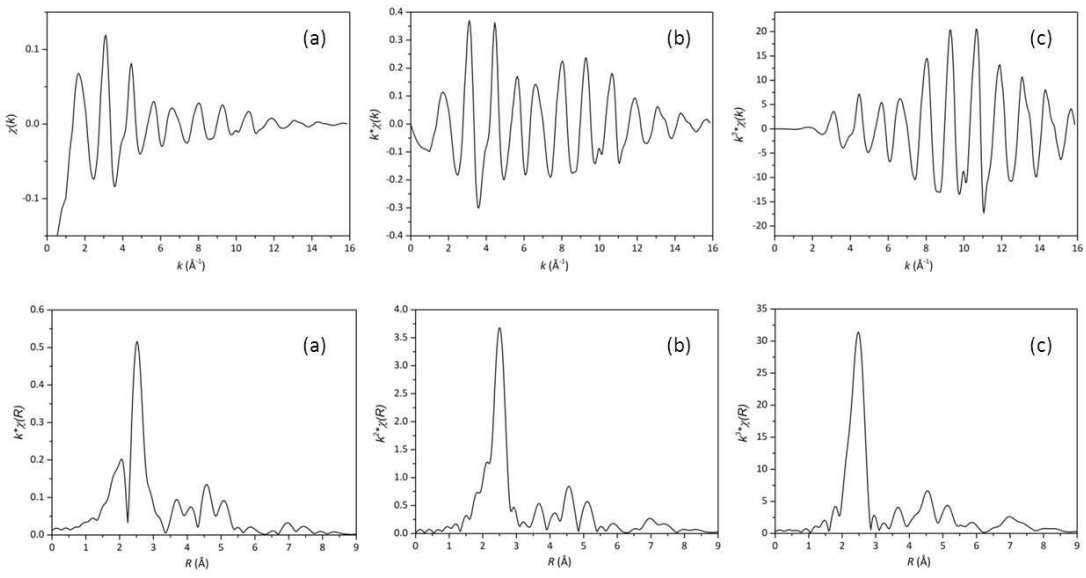

Figure 2-9. *k-weighted EXAFS and associated FTs for Pd foil. (a) k-weighted, (b) k^2-weighted and (c) k^3-weighted. With increasing k-weighting the higher values of k are emphasised. Fourier transform data can significantly vary, i.e. the first peak in the k- and k^3-weighted FTs. Note the y scale indicates the k-weighting.*

The EXAFS resolution can be approximated to $\pi/2\Delta k$ which arises from the FT of the EXAFS sine waves over a finite *k*-range. The k_{min} and k_{max} in Equation 2-8 are the integral limits of the FT and these values determine the width of the peaks in the FT so that a smaller *k*-window (*k*-range) gives broader peaks in the FT. This can be important in EXAFS analysis where coordination shells that are close together may be poorly resolved and appear a single peak in the FT. Another important result of the finite *k*-range is the available information content contained within an EXAFS spectrum. Essentially, this is determined by the number of independent points, N_{ind}, that a set number of parameters, N_{var}, can be used to model. This is estimated using the Nyquist theorem,

$$N_{ind} = \frac{2\Delta k \Delta r}{\pi} + 2$$

where Δk is the region in *k*-space over which the data is analysed and Δr is the region in *R*-space over which the fit is made. The upper limit of the data in k-space is restricted by the level of noise that dominates the signal more so than the attenuation by the exponential damping terms in Equation 2-6. This is of great consequence in modelling the data since N_{var} must be less than the N_{ind} to extract meaningful information [50].

2.3.2 XAS experimental modes

Figure 2-10 is a schematic diagram of an XAS setup at a beam-line. Depending on the sample matrix, the concentration of the absorbing element within the matrix and the desired surface sensitivity, XAS experiments can be performed in transmission, fluorescence or electron yield (TEY) modes. In all cases the measurement of $\mu(E)$ is needed for an X-ray absorption spectrum which should be obtained *via* an X-ray source with high photon flux and tuneability and recorded using high quality detectors [38]. Geometry and detectors characterise the differences between the experimental modes and it is the sample characteristics which include concentration, homogeneity and thickness, that determine the selection of the type of measurement.

The geometries of these setups and their requirements in an XAS experiment shall be briefly discussed.

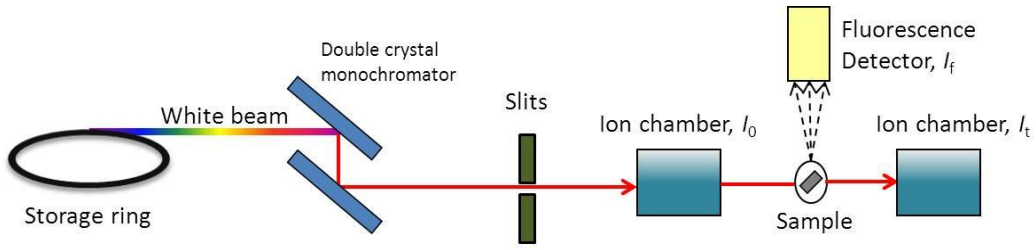

Figure 2-10. *Schematic diagram of the XAS experimental setup.*

2.3.2.1 Transmission

The measurement of $\mu(E)$ in a transmission experiment is given by

$$\mu(E) = \ln\frac{I_0}{I}$$

This represents the measurement of X-ray photons before and after the beam has passed through the sample. Transmission is the most frequently employed experimental geometry and is the preferred choice if the element of interest is concentrated in the sample, typically above ca. 500ppm [48]. It is a requirement of a transmission experiment that the sample is homogeneous where the grain size of the powder should be approximately equal to, or smaller then, the absorption length. Typically, the sample thickness is adjusted so that $\mu(E)x$ at the edge step is ≈ 1 (where the thickness of the sample is equal to one absorption length). This ranges from a few microns for metallic samples to millimetres for dilute samples [38] and can be calculated based on the elements and incident X-ray energy [51] . Ionisation chambers filled with gas are used as detectors which measure the intensity of the incident and transmitted X-ray beam. The gas composition is selectively adjusted so that the gas absorbs some of the incident and transmitted beams and the desired transmission intensity is reached. Inert gases such as He, Ne, Ar and N_2 are most commonly used and optimised based on the energy range of the experiment and the absorption coefficients of the gases [52].

2.3.2.2 Fluorescence

When lower concentrations of the target element are present within the sample (ppm level or less [38]) then Fluorescence measurements are favoured. Whilst fluorescence measurements do not directly measure the absorption coefficient, the fluorescence yield is proportional to the absorption cross-section as given by

$$\mu(E) \propto \frac{I_f}{I_0}$$

This is, however, is only upheld when (a) the sample is thin and concentrated, or (b) the sample is thick and dilute. A problem with using the fluorescence is that all elements at energies below that of the absorbing edge will produce fluorescence. In addition to this inelastic (Compton) scattering is produced thus a convoluted "noisy" spectrum of X-ray emission is generated. In order to obtain a reasonable $\mu(E)$, detectors need to have sufficient energy resolution to discriminate between the wanted and unwanted emitted X-rays thus improving the S/N ratio by filtering out background intensities. This is often achieved using modern solid state Si or Ge detectors of high energy resolution. The most efficient energy resolution is obtained when the detectors are perpendicular to the incident X-ray beam and the sample can be adjusted from 45 º to the beam. A pictorial view of the fluorescence geometry is displayed in Figure 2-11.

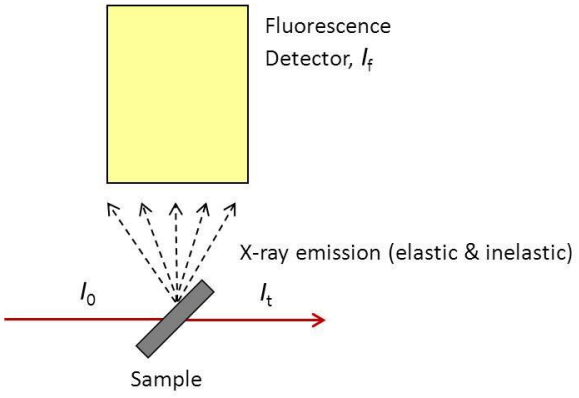

Figure 2-11. *The Fluorescence measurement in EXAFS (adapted from fundamentals of XAFS).*

Fluorescence measurements are usually made for dilute samples and thin films and are particularly important for catalysts and environmental samples where the absorbing element is contained in low concentrations within a matrix [48]. One problem that is encountered with making fluorescence measurements is that of self-absorption. In this process the fluorescence intensity is no longer proportional to the absorption coefficient and the result is that $\mu(E)$ is modulated in such a way that the absorption spectrum appears distorted where the amplitude of the oscillations in the EXAFS region are dampened. This is the process of the re-absorption of emitted fluorescence X-rays by the target element in the sample and occurs frequently in concentrated samples. Steps must accordingly be taken to correct for the self-absorption process in data analysis although, ideally, the sample should be thin and concentrated or thick and dilute to avoid this aberrancy altogether [49].

2.3.2.3 Total Electron Yield

Total electron yield (TEY) XAS involves the detection of electrons, rather than X-ray photons, that are emitted when the core-hole is refilled after excitation hence it is similar to fluorescence, in that secondary emission is detected[49] . TEY measurements overcome the problem of self-absorption in fluorescence however the surface sensitivities of the two techniques differ (TEY is more surface-sensitive than fluorescence) and thus a selection of which technique to use must be made based upon the information required and the sample characteristics [53]. The mean free path of the electron, which is dependent upon the incident X-ray energy, plays a key role in TEY measurements [54]. Chapter six exemplifies the use of the TEY technique in low energy XAS studies.

2.3.3 Limitations

XAS provides a detailed view of the surrounding coordination sphere of an absorbing atom where both the electronic structure, from XANES, and local coordination geometry, from EXAFS, can be gleaned. It is a powerful local probe of the short-range order where distances derived from EXAFS analysis are obtained reliably to within ± 0.01 Å. The amenability of the technique to most materials of industrial relevance has meant it has provided much of the information sought from understanding reaction mechanisms as they occur and on materials that do not

exhibit perfect structures. Unlike other local probes, such as EPR and NMR, the environment that the probe element exists in is always obtained, and without any requirements of crystallinity or symmetry, such as with XRD. As discussed in chapter one, with third generation synchrotron sources providing advanced setups, there is much opportunity to combine EXAFS with other techniques thus leading the way to structural determination without any ambiguity. Limitations of the technique do, however, arise and are generalised below.

1) EXAFS is a bulk averaging technique. When mixtures or multi-component systems are present the result of an EXAFS experiment is a spatially and temporally resolved average of all components in the material.

2) EXAFS data is unreliable below $k \approx 3$ Å^{-1} because the single scattering theory is not upheld. Multiple-scattering processes in the XANES region are significant and whilst EXAFS theory is well advanced, that of XANES is not as well understood. The absence of low-*k* information, which corresponds to high-*R* regions, can affect the determination of both interatomic distance and nearest neighbour coordination shells. This effect is more prominent in disordered systems. This can explain the origin of disagreements with EXAFS and other RDF techniques [55, 56].

3) The coordination number, *N*, cannot be determined with great accuracy due to the high correlation with the Debye-Waller factor, σ^2. The reliability of *N* drastically decreases after the first coordination shell and, in general, *N* is usually generated with 10 – 20 % accuracy [55]. For disordered systems, where Gaussian distribution is frequently not observed, the Debye-Waller approximation is inadequate and thus uncertainties propagate in the determination of *N*.

4) The inverse R^2 dependence on amplitude restricts the distance with which higher coordination shells can be analysed in the analysis.

5) Although the accuracy in the determination of bond lengths, R, is ≈ 0.01 Å, when there exists a relatively large distribution of R from various backscatterers the accuracy is much diminished from this value, and ΔR is more realistically ~ 0.1 – 0.2 Å. This is also strongly coupled to the k_{max} used in analysis where the resolution in R is given by $\Delta R \geq \pi/2\Delta k$ [56] and hence real, noisy, data impacts upon the extraction of R from analysis.

6) Backscattering atoms that are close in Z cannot be fully resolved as near-neighbours, e.g. C and N or Mn and Fe[87]. Conversely, however, elements that may appear at the same distance but have different backscattering and phase functions *can* be resolved [48].

In summary, intrinsic EXAFS limitations arise due to the theoretical basis upon which it is formulated and the real disordered systems that it capable of studying. These limitations do not apply in all samples all of the time and data quality has a considerable impact on the amount of extractable information. As theory advances, especially in XANES, and analysis procedures develop the uncertainties generated in analysis and the difficulties encountered in analysing systems are reduced.

2.4 X-ray total scattering

It was first postulated by Debye in 1915 that non-crystalline materials can produce diffraction patterns from the disordered array of atoms they contain [36]. The structural determination of amorphous materials has, however, traditionally not aroused the same level of interest as using crystallography to determine crystal structures. The periodic three-dimensional array of atoms in a lattice defines long-range order and the scattering of X-rays or electrons has undoubtedly provided the most information on crystalline materials. Of primary concern has been to solve the abundance of crystal structures which has synergistically advanced X-ray diffraction as an important technique for studying material structure. Materials such as glasses, liquids and gases do not contain long-range order and so characterising them has been limited to determining the short-range order which spans just a few atoms. Indeed, it has been little understood how the properties of many materials can be correlated to their local atomic structures. Focus has, therefore, remained on elucidating the long-range average structure extending over ten to hundreds of atoms [57].

In the absence of long-range order conventional X-ray diffraction is an inadequate structural probe and historically local structure techniques such as EXAFS, NMR and SAXS have routinely been employed [58, 59]. These techniques have their limitations too and often discrepancies from these techniques arise due to their inherent limitations and requirements and are useful only in probing the structure up to a few Ångstroms.

Many of the novel materials today that are of technological importance exhibit local structural deviations from that of the ideal, or long-range, structure. These deviations may play a key role in the functionality of the material. With a desire to understand the structure and properties of advanced functional materials, new techniques and methods that are capable of characterising these deviations are necessary, which may otherwise be "averaged out" using traditional crystallographic approaches [60].

For materials with nano-crystalline or disordered structures traditional X-ray diffraction analysis fails by taking into account only the Bragg reflections from the well-ordered component within the material. The lack of long-range order, or presence of atoms that deviate from the average structure, in these systems means that, in addition to Bragg scattering, diffuse scattering is produced. This diffuse scattering, hidden between the Bragg peaks, is disregarded in XRD analysis (usually it is removed as a background) however it contains all the structural information relating to the disordered regions and displacement of atoms from crystallographic sites. Moreover, the diffuse scattering extends widely over *Q*-space and contains a considerable portion of the total experimental scattering from the sample. If both the diffuse component and Bragg peaks can be analysed then a much clearer picture of the material's structure can be assembled. One technique that circumvents the loss of essential information, as in conventional diffraction, is X-ray total scattering. Although there are various factors that distinguish X-ray total scattering and X-ray diffraction as being different, they are essentially measuring the same data by the same experiment. X-ray total scattering is simply a diffraction measurement at low wavelength. The crucial difference that enables X-ray total scattering to be a structural probe of disordered systems is that, in addition to Bragg scattering, the diffuse scattering is both measured and analysed. The data are also represented in a different way to diffraction data in that the X-ray total scattering data are Fourier transformed into *r*-space to generate a pair distribution function (PDF). It is because of this unique way in which data are extracted that it is referred to commonly as the PDF technique or simply "PDF" [58].

2.4.1 Pair distribution function (PDF)

Unlike in EXAFS, for instance, that yields a partial pair correlation function of atoms, the Fourier transform of X-ray total scattering data generates the total atomic PDF; all atom-atom pairs within the material are sampled. This is a real-space method in which the weighted distribution of bond lengths contained in the PDF is directly interpretable. The PDF is a probability function of finding an atom at a distance, *r*, from another atom and distances far beyond that of a crystallographic unit cell can be obtained. The short- and long-range order aspects of the PDF have important implications for studying complex materials such as in nanomaterials

where crystallinity is restricted to the nanometer regime and conventional crystallography is not applicable. Alternatively, materials that exhibit long-range order with local distortions can be investigated using the PDF technique [61, 62]. Furthermore, the medium-range order, which has been seldom studied, has been investigated through atomic PDF analysis [57]. Crucially, the PDF being the Fourier transform of the total scattering structure factor, $S(Q)$, has no requirements of symmetry or periodicity for its generation. Materials ranging from bulk crystalline structures to completely amorphous show a PDF in this manner thus making the PDF technique versatile in its application to a wide range of materials. The short-range, medium-range and long-range order can be characterised simultaneously and even without sophisticated modelling limited information can be readily obtained. Thus the combination of high energy X-rays and atomic PDF analysis can yield structural information (a) on disordered and nanosized materials and (b) over various length scales, simultaneously, that no other technique has the capability of doing in such a self-consistent manner. Some of the theoretical treatment of how the PDF is obtained shall now be discussed.

2.4.2 Theory

In a PDF experiment the total scattering intensity, I_T, is given by

$$I_T = I_C + I_{IC} + I_{MS} + I_{BG}$$

where I_c is the coherent scattering intensity, I_{IC} is the incoherent scattering intensity, I_{MS} is the multiple scattering intensity and I_{BG} is the scattering intensity from the background. The incoherent scattering arises from Compton scattering by atoms in the sample and contains no structural information so is removed in data analysis procedures. Multiple-scattering is due to the re-scattering of scattered X-rays within the sample and also by the environment the sample is in. The background scattering is the scattering of X-rays by the environment, the container the sample is in and its surrounding parts. Critical to successful PDF measurements is the accurate measurement of background intensities since the diffuse scattering must be retained and analysed. Fourier transformation of diffuse scattering that does not originate from the sample, i.e. from the background, would give an erroneous PDF. The total

scattering intensity is a function of the X-ray wavelength, λ, where the diffraction vector, Q, is given by

$$Q = \frac{4\pi \sin\theta}{\lambda}$$

where θ is half the scattering angle between the incident and diffracted beams. For an isotropic sample Q is the scattering vector in all directions and is referred to as the momentum transfer. This equation has important meaning for PDF measurements where the wavelength, λ, determines the maximum value of Q accessible in the experiment. For laboratory sources that typically use Cu K_α radiation (λ = 1.54 Å) Q_{max} equates to *ca*. 8 Å^{-1}. For the high energy X-ray beams used at synchrotron sources, a λ of 0.1 Å can be employed and thus Q_{max} values above 40 Å^{-1} are readily achieved. High values of momentum transfer are necessary for PDF measurements since, (i) this provides the high real-space resolution of the PDF, given as $\Delta r = 2\pi/Q_{max}$, and, (ii) higher values of Q_{max} are needed to mitigate the effects of termination ripples in the PDF originating from truncation effects of the finite Fourier transform [58].

After corrections are applied to remove the incoherent, background and multiple scattering contributions, the coherent scattering intensity, $I_C(Q)$, is converted to the total scattering structure function, $S(Q)$, and is given by the relation

$$S(Q) = 1 + \frac{[I_C(Q) - \sum c_i |f_i(Q)^2|]}{|\sum c_i f_i(Q)^2|}$$

where c_i and f_i are the atomic concentration and X-ray scattering factor, respectively, for atomic species i. Figure 2-12 displays the $S(Q)$ data for a powder sample of copper metal.

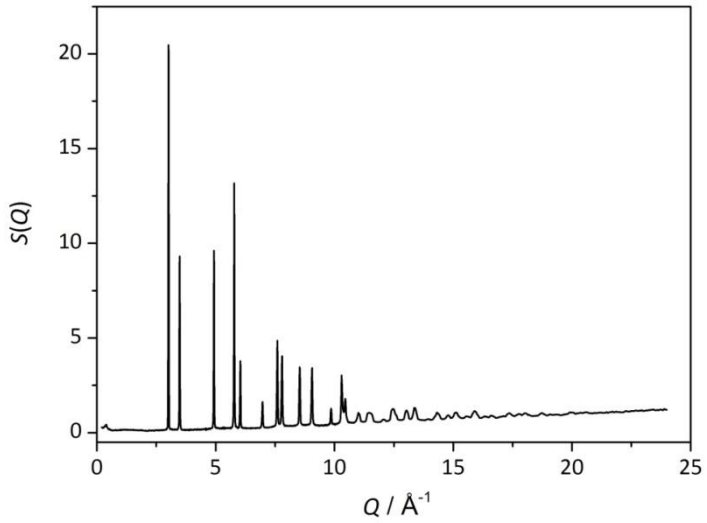

Figure 2-12. *S(Q) data of Copper metal powder.*

The $S(Q)$ contains scattering from both Bragg and diffuse components and is the sum of all the partial structure functions from all pairs of atoms that scatter within the sample. The Fourier transform of the experimentally observed structure function, $S(Q)$, yields the total PDF, $G(r)$ given by

$$G(r) = \frac{2}{\pi}\int_{Q_{min}}^{Q_{max}} Q[S(Q) - 1]\sin(Qr)\,dQ$$

The $Q(S(Q)\text{-}1)$ term denotes the reduced structure function as is frequently written as $F(Q)$. Q_{max} and Q_{min} are determined by the experiment and, as previously mentioned, as wide a Q-range as possible should be used. The real-space function $G(r)$ is a radial distribution function that describes the probability of finding a pair of atoms at a spherical distance, r, from a reference atom as given by

$$G(r) = 4\pi r[\rho(r) - \rho_0]$$

where ρ_0 is the average number density of the sample and $\rho(r)$ is the local atomic density. The Fourier transform of the $S(Q)$ data (in Figure 2-12) is represented in Figure 2-13 as the pair distribution function, $G(r)$.

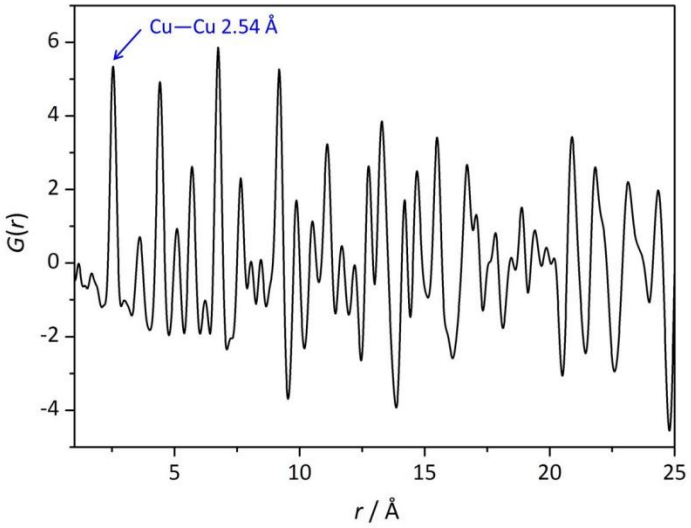

Figure 2-13. *The Fourier transform of S(Q) in Figure 2-12 yields G(r), the PDF of Cu metal foil (selected r-range of 25 Å). The first peak in the PDF corresponds to the first nearest neighbour and is the Cu—Cu bond length, 2.54 Å.*

The function, $G(r)$, is described as the reduced pair distribution function which is distinguished from $g(r)$, the atomic pair distribution function, in that it is the weighted sum of the partial PDFs, $g(r)$, thus is the total PDF representing all interatomic distances in the sample. Presentation of the PDF using $G(r)$ is often preferred for several reasons:

(1) $G(r)$ is the direct product of the Fourier transform of the experimental $S(Q)$.

(2) The amplitudes of the oscillations are constant in r, thus only instrument resolution factors and/or structural coherence influences any diminishment in amplitude in the PDF [58].

Alternative pair correlations functions can be used, in particular $T(r)$ and $D(r)$. These are simply weighted by different amounts using a multiplicative factor and emphasise the PDF at different distances. All contain the same information [63]. For work in this thesis we will use the notation, $G(r)$, for all PDF studies.

2.4.3 Limitations

Detailed structural information can be extracted via PDF analysis however as with all structural characterisation techniques, limitations arise. Some of these are described below.

1) The Fourier transformation of $S(Q)$ yields the total PDF and thus all the interatomic correlations within the sample are displayed. Deconvolution of the PDF may be challenging if there are many different scattering atoms present. One method to overcome this, by isolating certain correlations in the PDF, is to obtain the differential PDF [64]. Differential PDF analysis will be explained in more detail in chapter five.

2) As the radial distance increases the distances between successive coordination shells, and thus the peaks in the PDF, become closer together and overlap. It is vital therefore to have good resolution to resolve these distances. The resolution is determined by the Q-range of the experiment thus a PDF experiment can only be successful if the Q_{max} employed is sufficiently high to resolve the peaks.

3) Understanding the structure of nano-sized crystals or localised disorder by diffraction requires sophisticated method of analysis. Historically, these have been difficult to use or relatively sparse. Techniques such as RMC modelling are being successfully applied to PDF analysis to model complex structures [65-67]. Alternatively, PDF data analysis programs such as PDFgui have enabled structural information from crystalline and poorly crystalline systems to be obtained [68].

4) At present, there are significantly less PDF beamlines throughout the world's numerous synchrotron sources, especially in comparison with X-ray diffraction and X-ray absorption spectroscopy techniques. The relative inaccessibility of the PDF technique has been associated with less demand for its use. Now with more demand and with increasing availability of pulsed neutron sources and established X-ray sources the potential for PDF in materials characterisation has been fully realised. A dedicated X-ray PDF beamline at Diamond light source for example, is forthcoming [5]. This would complement the neutron PDF beamline at the ISIS facility neutron facility close by.

In summary, the major drawbacks of the PDF technique have, hitherto, been directly and indirectly attributed to the PDF community size. Now the advantages have been realised there is much development on-going in bringing PDF to the forefront of materials chemistry. Major developments are being made so that its application can become more routine and more powerful.

2.5 Data analysis methodologies

2.5.1 Commonalities of data analysis

Irrespective of the length scales involved, analysis of EXAFS, XRD and PDF data proceeds by much the same routine; the experimental data is fit to some sort of model wherein the analysis program computes a theoretical spectrum or pattern of a hypothetical structure using various experimental and structural parameters. Most commonly, this data modelling proceeds via a nonlinear least-squares curve fitting routine using mathematical algorithms (commonly the Levenberg-Marquardt method) [69, 70]. This is particularly true of EXAFS, XRD and PDF data analysis where standard curve fitting procedures are performed and values of structural and non-structural parameters are obtained during a refinement by minimising the mean square error between the data and the fit. This method requires that the global minimum in the least squares fitting is reached, not false minima, also known as local minima. This is usually achieved by widely varying the initial values in the refinement.

2.5.2 Statistical metrics

In order to evaluate how good the structural model is in describing the experimental data a series of statistical parameters are used. These parameters measure the goodness of fit, mathematically, which aids inspection of the fit, simply by eye, and evaluate the meaningfulness of the refined variables (parameters) obtained from the fit in terms of correlations, error bars and variation from initial values. The canonical method of obtaining these parameters and error bars by minimising the mean square error, $\epsilon^2(\{\alpha\})$, in nonlinear least-squares is given by the expression [71]

$$\epsilon^2(\{\alpha\}) = \frac{1}{N_{ind} - N_{var}} \sum_i \frac{Data_i - Fit_i(\{\alpha\}))^2}{s_i^2}$$

where $\{\alpha\}$ is the set of refined parameters, s^2_i represents the noise level and N_{ind} and N_{var} are the number of independent data points and the number of free parameters in

the fit, respectively. The function $\epsilon^2(\{\alpha\})$ is more commonly referred to as reduced-χ^2 in curve fitting analysis. This is particularly effective when comparing large numbers of fits which, depending on the statistical parameter, can be used to compare various structural models. The *R*-factor is frequently reported too which measures the overall residual of the fit, measured as the difference between the experimental and calculated data and, in EXAFS, is given by the expression

$$R = \sum_{i}^{N} \left(\frac{1}{\sigma}\right) \left(\left|\chi^{exp}(k_i) - \chi^{calc}(k_i)\right|\right) \times 100\ \%$$

$$\frac{1}{\sigma} = \frac{k_i^n}{\sum_j^N \left|\chi_i^{exp}(k_j)\right|}$$

where $\chi^{exp}(k_i)$ is the experimental EXAFS, $\chi^{calc}(k_i)$ is the theoretical (calculated) EXAFS, N is the number of data points and n is a weighting chosen so that experimental EXAFS has constant amplitude over the data range. The *R*-factor of a good fit is small. One disadvantage of using the *R*-factor alone is that it does not take into account the estimated uncertainties on the values nor does it take into account the number of data points, N_{ind}, and variables used in the fit, N_{var}, which is crucial when evaluating how meaningful the fit obtained really is.

The reduced-χ^2, on the other hand, takes into account the uncertainties on the refined values and correlations between them from the correlation matrix (which is where the errors are derived from). The reduced-χ^2 is very informative and a good metric when comparing different fits of a single data set to see, for example, how varying the parameterisation of one variable or how reducing the available data affects the fit. A combination of both is good practice in determining the best model for the data.

2.5.3 Analysis of X-ray absorption spectroscopy data

2.5.3.1 Obtaining the EXAFS, $\chi(k)$

Raw XAS data, whether obtained from transmission, fluorescence or electron yield measurements, are processed in order to extract the experimental $\chi(k)$ prior to any curve fitting analysis. Several programs are available for this, in particular Viper [72] and Athena [73, 74] (from the IFFEFIT suit of programs) are extensively used. XAS data reduction and processing in this thesis work was carried out using Athena and so shall be discussed from here on.

With programs such as Athena, time consuming data reduction of voluminous data sets can be mitigated by the in-built functionalities that allow one to process multiple data sets at once by transferring parameters across. A good understanding of the system is essential first, i.e. chemical transferability between data sets.

Within an XAS spectrum (Figure 2-3) the increase in absorption probability in $\mu(E)$ around the absorption edge is proportional to the concentration of the absorbing atom. It is often unknown what the exact concentration of the element is within the sample and other factors such as sample thickness and absorption by the matrix influence the measured signal. The normalisation procedure, wherein $\mu(E)$ data is divided by the edge step jump so that the edge step is set to one, accounts for the unknown concentration and also for sample thickness [71]. To determine the edge step the normalisation is carried out using pre- and post-edge polynomials above and below the absorption edge which fit to the lowest and highest energy limits of the data. These low order polynomials (linear or quadratic) can then be extrapolated to the point of the rising edge as displayed in Figure 2-14. The fitting ranges should exclude the EXAFS region close to the edge since this is highly dependent on local structure and thus would skew the normalisation.

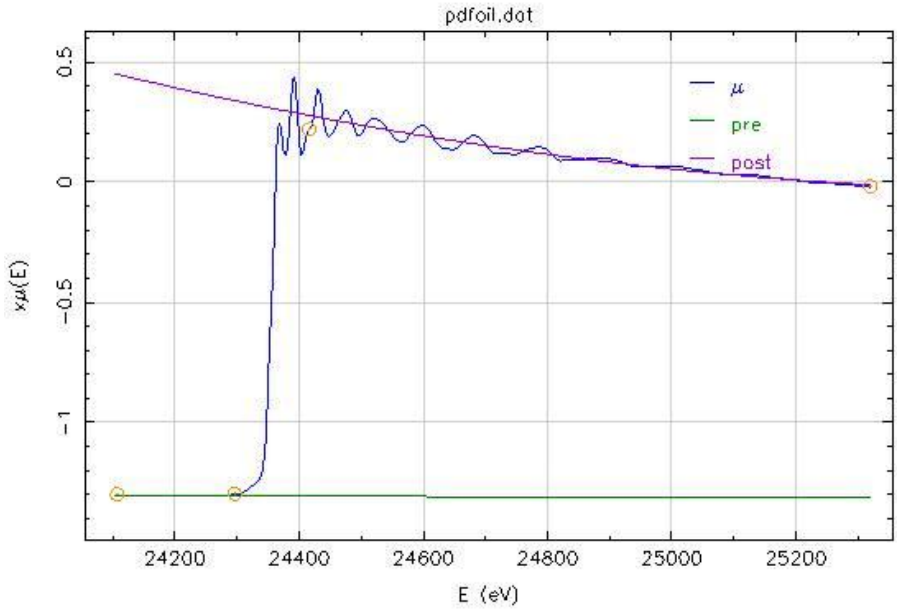

Figure 2-14. *The pre- and post-edge normalisation lines in raw μ(E).*

The raw $\mu(E)$ data in Figure 2-14 has a pre-edge line that is fit over the range −250 to −60 eV about E_0 and a post-edge line fit over the range +60 to +960 eV about E_0. Since the values of the fitted pre- and post-edge lines are defined in terms of $E - E_0$, the value of E_0 must first be chosen. Although a widely-off selection of E_0 can result in issues with modelling $\chi(k)$ further down the line, the choice of E_0 is somewhat arbitrary. Most importantly the choice of E_0 should be based at the same point on the rising absorption edge in the standard and in the unknown ensuring consistency in the data reduction and where only relative changes in E_0 between the unknown and standard are important [71]. The most commonly used points for E_0 selection are (1) the value at half of the edge step and (2) the inflection point (zero crossing in the second derivative). The inflection point is frequently chosen in a systematic fashion although electronic transitions or resonances at the edge may mask this actual position therefore the half height of the edge is preferably used [9]. Once the value for E_0 has been specified, the $\mu(E)$ data can be converted to a k-space grid ($Å^{-1}$).

The next step in data reduction is to remove the background ($\mu(E)$-$\mu_0(E)$), the slowly varying part of the absorption coefficient, after the absorption edge, i.e. the single atom behaviour in the near-edge and EXAFS regions. The atomic contribution is

usually determined using a cubic spline function [75] and removal carried out via a linear least squares fitting routine. It is crucial to fit the background function $\mu_0(E)$ to $\mu(E)$ without removing any of the real oscillatory structure. Fitting the $\mu(E)$ data using a cubic spline works fairly well where issues often encountered such as the background following the data too closely and low frequency oscillations not being removed are alleviated. The background function can be weighted by k^n (n = 1-3), so that it fits the lower and higher energy regions in $\mu(E)$ more adequately; for example k^3 is used for a better background at high k. The cubic spline must therefore have start and end energies to determine the number of points and the more data points the better the fit of the spline function. Figure 2-15 illustrates the cubic spline function for background removal.

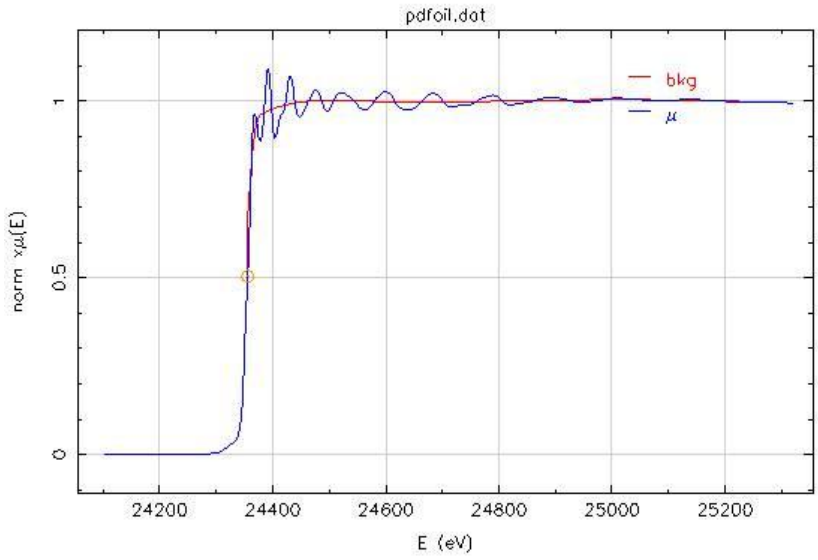

Figure 2-15. *The background removal of normalised μ(E). Note that the cubic spline extends from the position of E_0 (half the height of the edge jump) up to the end of the absorption spectrum.*

Smoothing functions such as *spline clamps* and the *Rbkg* parameter in Athena can be applied to improve the fit of the background. Once the total experimental absorption is normalised by the edge-step, generally around 50 eV after the absorption edge (performed automatically by the program), the $\chi(k)$ is obtained (Figure 2-9) and is calculated given by

$$\chi = \frac{\mu_{total} - \mu_{atomic}}{\mu_{atomic}}$$

The Fourier transform of $\chi(k)$, over a specified *k*-range and using various *k*-weightings, can now be calculated (Figure 2-9). The Athena project file now contains $\mu(E)$, $\chi(k)$ and $\chi(R)$ data available for analysis.

2.5.3.2 XANES analysis

For the work undertaken in this thesis XANES analyses were performed at a semi-quantitative level using sets of reference materials (empirical standards) and shall here forth be discussed in more detail.

2.5.3.3 Absorption edge and white line intensity analysis

As mentioned earlier, the binding energy of an atom within a sample is dependent on the oxidation state of the absorbing atom and can be modulated by neighbouring atoms since these affect the positions of the energy levels within the atom relative to the 1*s* energy level. Furthermore, the same sample measured at a different time or on a different beamline may encounter a shift in the binding energy. The absolute value of the binding energy within the sample cannot, therefore, be directly assigned to the oxidation state. The use of a set of reference materials or model compounds containing the absorbing atom with known oxidations state circumvents these issues and also negates full XANES calculations so that the oxidation state of the absorbing atom can be deduced in an unknown sample by comparison to the values in the reference materials. Often is the case that a sample contains mixtures and mixed oxidation states. In this instance the mixed valency is manifested through the shift in the absorption edge relative to the reference materials thus is informative when determining the existence of mixtures. This can include, for example, identifying if a sample has completely reduced or undergone a partial oxidation. As described earlier in this chapter, the existence and the intensity of the white line feature is influenced by the type of neighbouring atom and its coordination geometry. These

two features are, therefore, particularly useful in determining the extent of reduction and the species present.

2.5.3.4 Linear Combination Fitting (LCF)

Interpreting unknown data by comparing data to a reference material, provides characteristics of the atomic structure of the absorbing atom in the unknown sample. If more than one type of species exist then this comparison by fingerprinting the XANES spectra cannot be performed. It is desirable to deduce the exact nature of the species and their relative concentrations within the material. For time resolved data this is particularly useful where quantifying the component phases that enter and leave the system as a function of time gives a good idea of the kinetics and chemistry of the dynamic system [76-79]. If several species exist then the spectrum of the unknown sample is a fingerprint of the linear combination of the components that make it up and the superposition of these spectra, weighted by their relative concentration, makes up the unknown spectrum. This type of analysis is called linear combination fitting (LCF) and necessitates the use of a complete set of accurate standards to be used in the fitting, consisting of either as model compounds or reference materials. These standards reflect all the possible oxidation states and geometric arrangements of the absorbing atom that are contained within the constituent species.

LCF can be performed using EXAFS data by the same routine, using a set of complete standards, however with low *Z* scatterers, such as C, N and O, their respective contributions to the amplitude of the EXAFS is relatively weak and it is often difficult to distinguish atoms in EXAFS which are very close in atomic number. In contrast, when lighter atoms are present in the local coordination sphere around the absorbing atom, a sharp rise in the absorption probability at the top of the rising edge is observed. This is referred to as the white line intensity [80]. These features facilitate the use of XANES data for accurate LCF. For LCF analysis in this thesis work, XANES regions of *in situ* XAS data were used.

2.5.3.5 EXAFS analysis

The EXAFS equation derived by Stern, Sayers and Lytle is still used today as a very good approximation for interpreting and analysing EXAFS data. Extracting the values of the parameters in the EXAFS equation which determine the structural characteristics of the material is the primary goal in EXAFS analysis. So that the true global minimum is found in the least-squares fitting the values of the parameters in the refinement should be given good initial values that are, to varying extent, close enough to the true values. Different variables will have different sensitivities to the choice of starting values. The Debye-Waller factor (σ^2), coordination number (N), collectively the amplitude terms, are refined during a fit. Due to the multiplicative nature of these variables in the equation these parameters are highly correlated and can, consequently, carry enlarged uncertainties of up to *ca*. 20 %. In practice, one can reduce the impact of these correlations by fixing one of the parameters and letting the other refine in the fit however this is only permissible if chemically justifiable to do so. This is made more convoluted in that the total Debye-Waller factor, that is used in analysis, is the sum of the static and thermal components and disentangling these contributions is nontrivial.

In terms of the phase term, the parameters that are used in analysis are the Fermi energy, E_f, (also referred to as threshold energy, E_0) and the interatomic separation (R). E_f takes values from −10 eV to +10 eV and is dependent upon the selection of E_0 in the initial data reduction. This parameter is usually always refined. R, which is the half path length ($2R$ corresponds to the length of the scattering pathway from the central atom to the backscattering atom and back again) determines the interatomic separation and must be refined from an initial value that is not too distant from that of the true value. EXAFS gives a fairly accurate value of R, usually reported to two decimal places, from accurate calculations of the phase shifts for different backscattering atoms. Depending on the program, the method in which R is refined and is parameterised varies. This will be discussed in more detail later in the chapter.

EXAFS data analysis in this thesis work was performed using EXCURVE98 [81, 82] and Artemis [73, 74] programs. Whilst the overall aim is to extract structural

information using a model to fit the experimental data to, the data analysis methodology can differ substantially between the two programs. Both programs have their advantages and limitations; one is if often more suitable than the other depending on the material and the information required. A summary of the methodologies used and their benefits and shortcomings are discussed.

2.5.3.6 EXCURVE98

In EXCURVE98, atomic potentials and phase shifts are calculated for backscattering atoms relative to the absorbing atom. The muffin tin potential is the theoretical standard for calculating these. Once the EXAFS data have been read into the program (usually in a $\chi(k)$ format) a structural model is created by adding a number of coordination shells, the number of which depends on the required information, i.e. shells are usually added in increasing distance from the absorber. Often only the first, and sometimes second, peak in the FT is fit however these may contain a number of sub-shells, for example due to mixtures in the data. Each coordination shell contains a specified backscattering atom type, the coordination number, N, the interatomic distance, R, and the Debye-Waller factor, $2\sigma^2$. The AFAC parameter, which represents S_0^2 in the EXAFS equation, is set globally for the analysis and is obtained from fitting a metal foil or model compound of fixed coordination number. The analysis is performed in k-space with $\chi(k)$ data and the resultant fits are depicted for both the $\chi(k)$ and the Fourier transformed data. Statistical parameters are generated for the fit of which an R-factor is usually reported. Although the command driven platform may seem somewhat primitive, the flexibility with which hypothetical structures can be created makes EXCURVE98 a robust program for analysis of EXAFS data. There are no crystallographic requirements when creating a structural model and so it is suitable for all systems; well-ordered, amorphous, solids and liquids. Multiple scattering can be included in the model and there are several methods that this can be implemented. If the crystal structure (or space group) is known, i.e. FCC or HCP, multiple scattering can be applied to the entire structure. Alternatively, multiple scattering calculations can be performed on single moieties. Whole structure multiple scattering can generate a very large number of coordination shells where the contribution to the multiple scattering from each shell

is unknown. Furthermore, this is a computationally demanding method and adds significant time to the refinement.

2.5.3.7 Artemis

The EXAFS analysis program Artemis is part of the IFFEFIT suite of programs and uses the FEFF code for calculation of *ab initio* self-consistent real space multiple-scattering which yields the scattering amplitudes and phase shifts required for EXAFS analysis. The use of Artemis, for EXAFS analysis, in combination with Athena, for XAS data reduction, is advantageous in that the Athena project file containing the background subtracted and normalised $\mu(E)$ data can be directly read into Artemis, requiring no further data conversion. Artemis contains a data panel where the fit parameters are set. These include the Fourier transform *k*-space upper and lower limits, the fitting range in *R*-space and the *dk* and *dr* data processing parameters are also displayed. The *k*-weightings of the fit are also selected here and multiple *k*-weightings can be used in the fit. The analysis of EXAFS data can be performed in either *k*-space or *R*-space. Although not exclusively, frequently the structural model is based upon a crystallographic information file (CIF). Using crystallographic data (from the CIF) a FEFF calculation is performed up to a radial distance from the absorber, termed "cluster size" (NB: Artemis can handle calculations on non-crystallographic materials if they are in the form of a FEFF input file. This procedure was not utilised in our studies and thus is not described in any detail). This FEFF calculation generates all single scattering and multiple scattering paths at distances up to the specified cluster size. One of the main advantages of using Artemis (over EXCURVE98 for example) is the multiple scattering path expansions [83, 84]. Here, all single, double or triple scattering paths are evaluated wherein the estimated importance of each path is enumerated. Single scattering paths, for simple first shell fitting, can be constructed based on a FEFF calculation on an absorber-scatterer distance. Whilst this can only be used as a single shell it is useful when a CIF is not available. Several of these quick first shell theories can be performed if there exists a mixture of species in the first coordination shell (sub-shells).

The terms in the EXAFS equation; N, S_0^2, E_0, ΔR and σ^2 must be assigned values for each and every path in the fit. These are not themselves the parameters that FEFF calculates but are defined in terms of these parameters [85]. The choice is somewhat arbitrary however it is commonplace that the EXAFS parameters and associated FEFF parameters are used as listed in Table 2-1.

Table 2-2. *Structural terms in the EXAFS equation and their corresponding FEFF parameters.*

EXAFS parameter	**FEFF parameter**
N, degeneracy	Fixed in each path
S_0^2, amplitude reduction factor	*amp*
E_0, energy correction	*enot*
R, path length	*delR*
σ^2, Debye-Waller factor	*ss*

Some major differences between Artemis and EXCURV, in terms of parameters, are that Artemis (i) uses ΔR: The deviation from the theoretical distance in the FEFF calculation. The initial value of R should be not too far away from the true value, typically less than *ca*. 0.1 Å. This poses a limitation on using crystallographic data in the structural model where the distance would need to be recalculated using new phase shifts and scattering amplitudes. (ii) N is fixed in each path: The degeneracy of every single and multiple scattering path is not refined, rather the fraction of the reduction in coordination is refined. (iii) S_0^2 can be set for each path or take different values, for example, beyond the first coordination shell, using additional *amp* parameters. This can be particularly useful for more disordered systems where the assignment of a single S_0^2 to all shells may not be appropriate. The fit parameters are assigned in the *Guess, Def, Set* window of Artemis. Here each parameter is given a value which is either refined as a *Guess* or fixed to a numerical value as a *Set* or defined in terms of another parameter, *Def*. Mathematical expressions for

parameters can also be evaluated, if known. The parameterisation of fit parameters can greatly reduce the number of variables in the fit. After the fit Artemis produces a statistical analysis of each fit and the fitting parameters for each path are evaluated.

The crystallographic approach has its drawbacks, not least for the fact that disordered materials cannot be analysed in the way described. This, therefore, puts a strong limitation of the types of materials that can be analysed using Artemis. For instance, in metal oxides, often the second peak in the Fourier transform is much more intense than the first and a better quality fit is obtained when fitting the first two shells. If no crystallographic information is available then Artemis cannot be used since it is not possible to analyse beyond the first shell. EXCURVE98 in this instance would provide a much better solution. On the other hand, with multiple data set fitting, multiple scattering calculations for every shell and sub-shell and the ease of parameterising variables, Artemis is a sophisticated EXAFS analysis program for use on crystallographic systems.

2.5.4 Analysis of X-ray total scattering data

2.5.4.1 Obtaining the PDF

As described earlier in this chapter, the measured total scattering intensity consists of coherent scattering, incoherent scattering, background scattering and multi-scattering. Therefore in order to extract only the coherent scattering, the structure sensitive part, corrections to the raw X-ray total scattering data must be made. These corrections are performed on the raw data measured as the scattering intensity plot against two theta. Our PDF measurements were carried out at the BL04B2 High Energy Diffraction beamline [86] at SPring-8 synchrotron source, Japan and the data processing was performed using the Igor (WaveMetrics, Inc., Lake Oswego, OR, USA) program and using a macro developed by the beamline for the corrections to the raw scattering data. Often is the case, and for the work undertaken in this thesis, samples are presented to the X-ray beam in either a capillary (quartz or borosilicate) or as a pellet as a "containerless" sample. For capillary measurements, X-ray total scattering data on an empty capillary are obtained and used as a background in the data analysis where identical experimental parameters to those of the sample in the

capillary are used. For measurements which use containerless samples the background removal is adjusted using the macro. Data are introduced into the program along with a parameter file which details the type and relative amounts of each atom present, the incident X-ray energy, the density of the sample and the capillary thickness, if used. The data, which are contained within several data sets, are merged and interpolated onto the same two theta grid. Some of the corrections are performed automatically using the macro. The polarisation factor is adjusted in the gui so that the data, once converted to $S(Q)$, tends to unity at high-Q. The reduced $Q(S(Q)\text{-}1)$ data are converted to $G(r)$, using a specified value of Q_{max}, and then to $\underline{g}(r)$. At low-r, where a strong, usually negative, oscillation is usually present, the $G(r)$ data are set to zero. At this stage the $g(r)$ is converted to $G(r)$ and the data are subsequently backtransformed to $S(Q)$. An 85% smoothing is performed on the $S(Q)$ data which are then Fourier transformed to $G(r)$ using a Lorch window function. The total pair distribution function, $G(r)$, can be converted to the total correlation function, $T(r)$, at this point (not required in this thesis work).

2.5.4.2 Interpretation of the PDF

The reduced PDF contains structural information that can be obtained directly, without further corrections or curve fitting analyses. The peak positions in the PDF provide a direct measurement of the true interatomic separations within the material and – unlike in EXAFS analysis which requires the calculation of phase shifts or atomic potentials – this can be obtained without any *a priori* knowledge of the system. The PDF can also provide information regarding the particle size; a rapid decrease in intensity of peak amplitudes provides an estimate of the size of the particles. This is particularly instructive for nanoparticulate systems which contain well-ordered structures in the nano regime but lose the sharp oscillations in the $G(r)$ due to small particle sizes. The dampening of the peaks in the PDF is also due to the finite instrument resolution and this can be modelled in the PDF by using reference data.

2.5.4.3 PDF data analysis

The analysis of PDF data are performed in real-space using the $G(r)$ function *via* a standard nonlinear least squares curve fitting. One commonly used program for PDF analysis of crystalline materials is PDFgui [68]. All PDF analysis performed in our investigations was executed using PDFgui and the details of the fitting procedure are evaluated.

2.5.4.4 PDFgui

The fitting of PDF data, in real-space, is analogous to the Rietveld method used in analysis of X-ray diffraction data. Although diametrically opposed in refinement space, the two methods yield similar structural parameters. Whereas analysis of XRD data is based solely upon the long-range average structure, PDF analysis using PDFgui can be applied to systems which contain crystallographic symmetry but have intrinsic localised disorder or deviations from periodicity, i.e. ordered and disordered components. Therefore, the analysis of PDF data can yield structural information relating to the short-, medium- and long-range order. In PDFgui a structural model is created by using either a CIF or by using the program itself to create a structure based on symmetry and crystallographic parameters. The program imposes periodic boundary conditions to generate a theoretical PDF from the CIF.

The program has several functionalities. These include:

1. To plot the experimental PDF data as $G(r)$.
2. To calculate the PDF of a structure from a CIF or built in crystal structure.
3. To fit the experimental PDF data to a structural model.

In the phase configuration pane the crystal structure parameters must be specified. These include the lattice parameters (a, b, c), unit cell angles (α, β, γ), the fractional coordinates (x, y, z) and the occupancies (Occ) which are defined according to the symmetry constraints of the system. In the refinement the lattice parameters and the atomic displacement parameters, ADPs (U), are refined. The occupancies can also be refined. For crystallographic systems where the atoms are located on special positions, the fractional coordinates are fixed in the refinement. The *phase scale*

factor, which accounts for the difference in intensity between the experimental data and calculated PDF, is refined. The delta parameters (δ_1, δ_2), which are the linear and quadratic atomic correlations factors, account for correlated atomic motion at low-*r* and have the effect of sharpening the peaks in the PDF. Both δ_1 and δ_2 can be refined independently. Nanoparticle size can be modelled using the *spdiameter* parameter.

Calculation of a PDF from a crystal structure is performed using the calculation configuration pane. Here, the *r*-range over which the PDF is to be calculated is defined. The PDF can be calculated either as a neutron or X-ray PDF; the parameters used are the same for both. The Q_{max} of the experiment is defined along with the experimental parameters, Q_{damp} and Q_{broad}. These instrumental parameters account for the respective dampening and broadening of the peaks in the PDF at high distances. For a calculation Q_{damp} and Q_{broad} can be set to their default values of 0.001 and 0, respectively. The calculation is performed using the "cog" icon and the PDF displayed using the plot control window. As described in chapter one, the resolution of the PDF, i.e. the width of the peaks, is determined by the value of Q_{max}. A larger value of Q_{max} will resolve the peaks more clearly whereas a smaller value of Q_{max} will broaden the peaks in the PDF.

To fit the experimental PDF data to the calculated PDF, constraints are added to the fit parameters in the data pane. Both Q_{damp} and Q_{broad} are refineable parameters for fitting the PDF, although a small positive value must first be assigned. Depending on the *r*-range used in the fitting, the instrumental parameters may or may not have any effect on the fit. Below 10 Å it is unlikely that the PDF will have any appreciable peak broadening and damping and thus Q_{damp} and Q_{broad} will have little, or no, effect. The data can be sampled on a Nyquist grid in addition to the normal *r*-spacing of that contained within the data file. For complex structures, containing a large number of atoms and parametric terms, this provides a "rough and ready" fit of the data. Values obtained under Nyquist sampling may be close to, but differ from, the true values. Using Nyquist sampling aids the refinement in reaching a global minimum and so can be used initially before the real data sampling refinement is performed.

After a fit is performed, using the "cog" icon, a results page is displayed which provides the refined parameter values, the associated uncertainties and some statistical analysis which includes the reporting of the reduced-χ^2 and a goodness of fit, R_w, value. The experimental PDF, the fit and the residual spectrum can be visualised in the plotting window. A fitting model was considered to be successful when, in general, the residuum R_w is below ~ 0.15 and does not improve, the difference curve is reasonably close to zero in the plot, and the refined variables have physically meaningful values.

2.5.5 Multi-cluster methodologies

Often routine analysis is insufficient and more in depth modelling is required to determine the overall structure. This can, for example, include systems that contain mixtures or mixed phases. Modelling the short- or long-range structures may not provide a unique solution to the structure and understanding the medium-range ordering is required to resolve the structure. PDF and EXAFS, to some extent, are structural probes of the medium-range ordering and as we have seen can generate information *via* a crystallographic approach. Although EXAFS is routinely used as a local probe to determine the short-range ordering around the absorbing atom it can, in principal, be extended to higher distances than just the first few coordination spheres. This, of course, depends on the level of disorder and the quality of data. PDF is an ideal technique to garner information on the medium-range ordering since it is not limited by *R*-space data.

The terms "phase" and "cluster" are used interchangeably and are general terms describing a component of within a material's structure. This may imply a single crystalline constituent or one which lacks any structural coherence. These phases or clusters are characterised using X-ray techniques. We coin the term "multi-cluster" with reference to the analysis methodology. In this thesis we have developed this methodology using industrially relevant materials of which phase composition is of importance where information pertaining to the medium-range ordering on these systems has hitherto been lacking.

2.5.5.1 EXAFS

The multi-cluster methodology was implemented with EXAFS data of a cobalt system. This required both Co HCP and FCC phases to be included into the model. HCP and FCC have $P6_3/mmc$ and $Fm\bar{3}m$ space groups, respectively, and these structures were calculated using CIFs. The resulting FEFF calculations contain all single and multiple scattering paths up to a cluster size of 6 Å. Scattering paths from HCP and FCC FEFF calculations are added to the structural model, under each FEFF calculation pane to the right. Figure 2-16 illustrates Artemis used for multi-cluster modelling of the cobalt system illustrating multiple-scattering paths from the FEFF calculation. The fitting parameters used in the model are the same as those described previously with the addition of amplitude mixing parameters, *x* and *y*. These parameters were introduced in order to resolve the HCP and FCC phase contribution to the data and the overall phase composition. The magnitude of these parameters (0 to 1) attenuates the amplitude of the EXAFS signal and relates directly to the phase fraction. In the multi-cluster modelling of EXAFS data the coordination numbers, *N*, are set to their path degeneracies for each scattering path and the value for S_0^2 is set globally. Using the first single scattering path in the Co FCC FEFF calculation as an example, the path parameter expression for *N* is given by the syntax

N: **12** X S_0^2: *amp*y*,

And for the first single scattering path in the HCP phase, the syntax evaluating *N* is given by

N: **6** X S_0^2: *amp*x*,

It is noteworthy that the first coordination shell in the HCP structure is split into two shells of marginally different distance each with a coordination number of 6. In the *Guess, Def, Set* panel both *x* and *y* are *guess* parameters. Values of *x* and *y*, the respective FCC and HCP fractions, took initial values of 0.5 which would represent an equally mixed system. The refinement of these parameters yields values between 0 and 1 and in most cases the values summed to unity. When they did not, due to small particle sizes, the *x* and *y* phase fractions were renormalized to obtain the

phase composition. For the mixed HCP and FCC Co system it was found that by selecting all multiple scattering paths under both FEFF calculations the best fit was obtained. Significant time was spent developing and optimising the HCP/FCC model for different data sets with the omission of some multiple scattering paths, however the variation in the quality of fit and the reduced-χ^2 by varying path inclusion was negligible. Due to the differences in the degeneracies of the HCP and FCC clusters, in particular above *ca*. 4 Å, the total number of paths generated from the FEFF calculation for the HCP cluster, up to 6 Å, was 69 and for FCC the number was 34. According to the Nyquist sampling theorem (Equation 2-9) number of independent parameters, N_{var}, that are used to fit the data cannot exceed the number of independent data points. With an exponential increase in parameters with *R*, and only a linear increase in the number of independent data points, a large number of the path parameters must be parameterised to satisfy this constraint and avoid over fitting the data.

Similarly, only one *amp* parameter representing S_0^2 is used and, unlike in conventional EXAFS analysis - in which S_0^2 is obtained through refinement of Co foil data – it was determined by fitting the first shell of bulk cobalt metal powder data.To ensure the validity of this method and to verify the stability of the phase composition analysis, the S_0^2 was set to 0.8 (arbitrarily selected) in analysis of all *ex situ* EXAFS data (results not shown) to see the effect on the amplitude mixing terms. The effect on the fit quality was negligible for all multi-cluster analyses although the reduced χ^2 increased by setting the *amp* to 0.8. In all cases the refined values of *x* and *y* reduced slightly although the normalised phase fraction was consistent to within 5 % from both analysis routines. This demonstrates the robustness of the methodology and the stability of the phase composition.

The assignment of path length parameters, *delr*, and Debye-Waller factors, *ss*, for each path took numerical suffixes that increase with increasing path length, *ss1*, *ss2*, *ss3*,… and *delr1*, *delr2*, *delr3*, … and so on. The significant multiple-scattering effects originating at higher coordination shells meant the parameterisation of multi-scattering paths was particularly challenging where a vast number of double and triple scattering paths exist. The parameterisation of *delr* and *ss* in the models was crucial to obtaining a good and reliable fit of the experimental data. Within each

cluster *delr* parameters were grouped together by distance so that single and multiple scattering paths were assigned one *delr* parameter. For the Co system this seems to work adequately, especially at higher *R* where the amount of multiple scattering paths increased considerably. For different Co samples the parameterisation of *delr* had to be varied moderately to account for the different phase compositions including *in situ* data where the magnitude of *x* and *y* varied. All *delr* parameters for the FCC cluster were *def* parameters in terms of *delr* for the HCP cluster thus reducing the number of refined parameters and which allows for the *delr* parameter to be updated during the refinement in an iterative method.

The Debye-Waller factors, *ss*, were parameterised in a similar fashion to *delr* parameters; *ss* for the HCP cluster were free to vary and *ss* for the FCC cluster were parameterised in terms of *ss* for HCP. The parameterisation of *ss* is somewhat more straightforward than *delr* where a larger number of paths can be described using a single *ss* parameter than can be using a single *delr*. The number of *ss* parameters, usually between 4 and 6 for each cluster, was also restricted by correlations between the Debye-Waller terms which suffer from greater correlations that *R* terms, inherent in the EXAFS formalism.

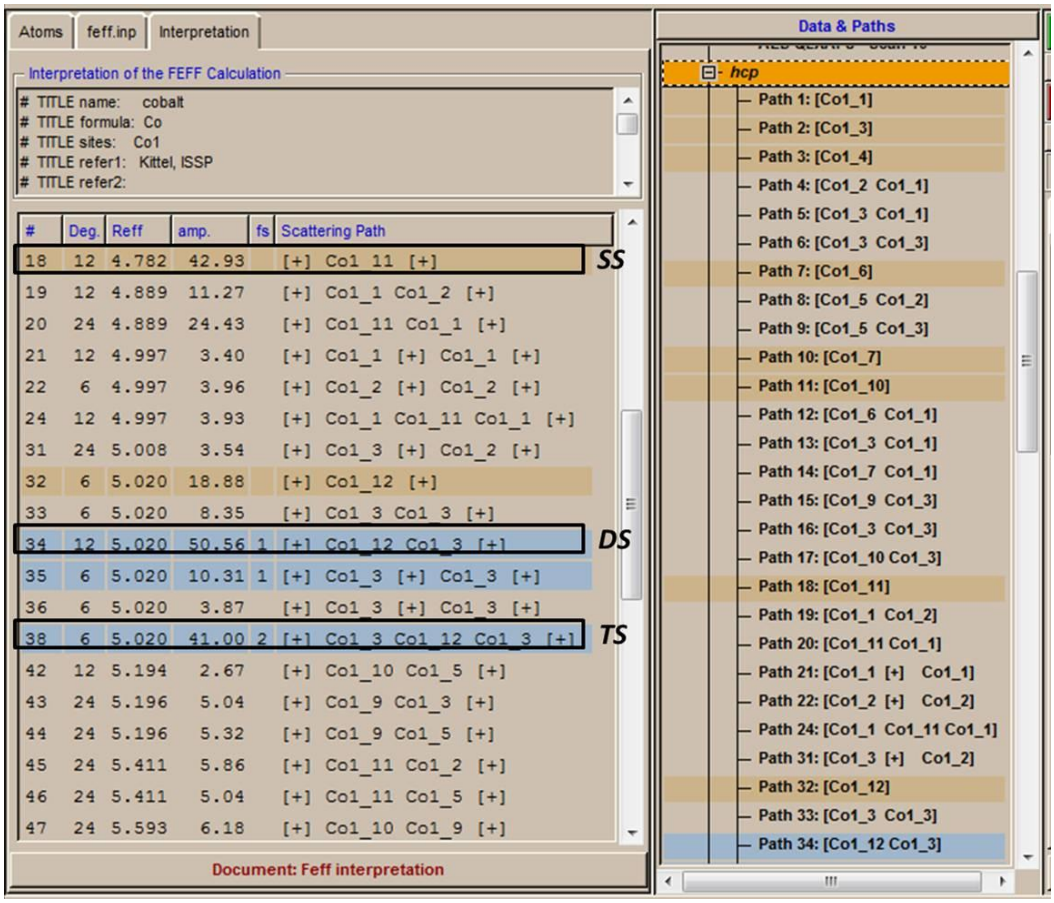

Figure 2-16. *Artemis multi-cluster modelling. Single- (SS), double- (DS) and triple-scattering (TS) paths are highlighted.*

2.5.5.2 PDF

The PDFgui program is capable of calculating the PDF of one or more structures, either independently or as a mixed phase system, and this makes it particularly desirable for PDF multi-cluster modelling. For a monatomic system, like that of metallic cobalt, multi-cluster models were constructed using the known coordinates and lattice constants for HCP ($P6_3/mmc$) and FCC ($Fm\bar{3}m$) Co allotropes. Multi-cluster modelling uses the same parameters as fitting of a single phase, as described earlier in the chapter. The introduction of *phase scale parameters* to the refinement, crucially, provides a quantitative description of the phase composition where the refined values for the HCP and FCC phases reflect the proportion of each phase contributing to the experimental PDF and hence the relative amounts of HCP and FCC within the sample. The program takes the phase scale factors and corrects for the average X-ray scattering power of each phase and the results are reported as

phase fractions in terms of atomic mass, number or unit cell (for a monoatomic system, such as Co, fractions by mass and number are the same). We report the results as per cent by mass (number) in this thesis work. These *phase scale parameters* are analogous to the amplitude mixing parameters in EXAFS multi-cluster modelling.

Within the phase configuration (Figure 2-17) the lattice parameters (*a*, *c*), phase scale factor, δ parameter and temperature factors (U_{11}, U_{22}, U_{33}) are refined for each phase during the fit. Structural parameters such as anisotropic ADPs (U_{ij}, i≠j) and occupancies are set to their respective default values, 0 and 1. The phase parameters relating to nanoparticles (as described earlier) are not refined and kept set to their default values. For fitting of the experimental Co PDFs in this study only $\delta 1$ was refined, since this resulted in the most stable refinements. The atomic displacement parameters (ADPs) for FCC phase are constrained in all directions to be the same and refined ($U_{11} = U_{22} = U_{33}$) during the fit due to the cubic nature of the cluster. This reduces the number of free parameters in the fit and avoids parameter correlations. For the HCP phase, analysis was executed in this manner as well since these constraints proved most successful in the parameterisation of the modelInitial values for the ADPs were between 0.003 and 0.01, though the refinement routine was insensitive to the choice of starting values.

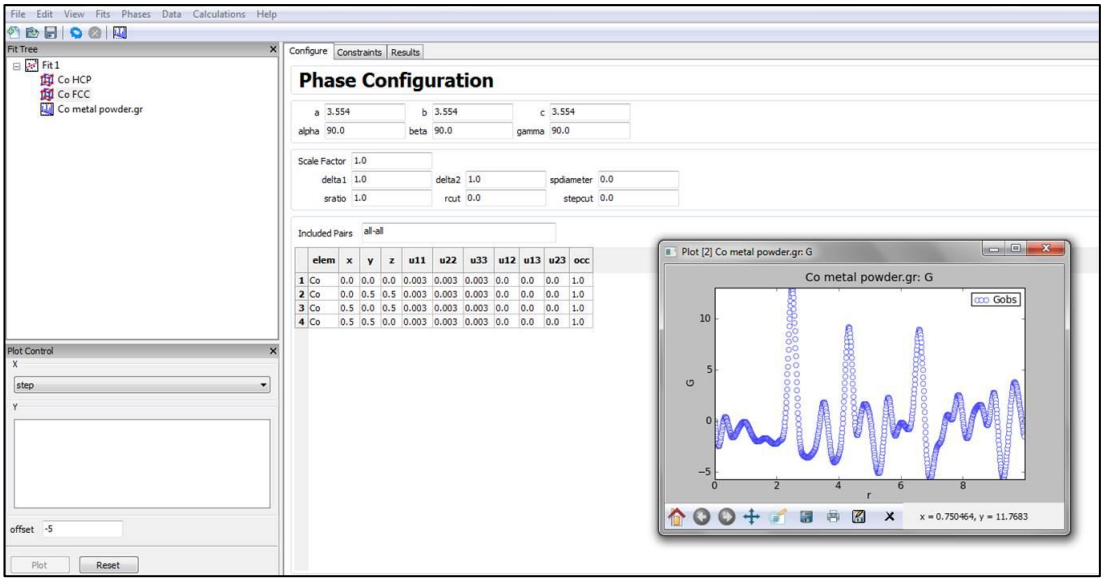

Figure 2-17. *PDFgui multi cluster modelling.*

2.6 References

[1] Brailsford, J. F., *British Journal of Radiology*, (1946) **19**, 453.

[2] Elder, F. R.; Gurewitsch, A. M.; Langmuir, R. V.; Pollock, H. C., *Physical Review*, (1947) **71**, 829.

[3] Koch, E. E., *Handbook on Synchrotron Radiation*, North Holland: (1983); Vol. 1b.

[4] Tomboulian, D. H.; Hartman, P. L., *Physical Review*, (1956) **102**, 1423.

[5] www.diamond.ac.uk

[6] Elleaume, P., Future storage ring synchrotron sources, In *Synchrotron Radiation Instrumentation*, Warwick, T.; Arthur, J.; Padmore, H. A.; Stohr, J. Eds.; (2004); Vol. 705, pp 149.

[7] Suortti, P.; Thomlinson, W., *Physics in Medicine and Biology*, (2003) **48**, R1.

[8] Lewis, R., *Physics in Medicine and Biology*, (1997) **42**, 1213.

[9] Koningsberger, D. C.; Mojet, B. L.; van Dorssen, G. E.; Ramaker, D. E., *Topics in Catalysis*, (2000) **10**, 143.

[10] Somorjai, G., Li, Y, *Introduction to Surface Chemistry and Catalysis*, Wiley: (2010).

[11] Thomas, J. M.; Sankar, G., *Accounts of Chemical Research*, (2001) **34**, 571.

[12] Bazin, D.; Mottet, C.; Tréglia, G., *Applied Catalysis A: General*, (2000) **200**, 47.

[13] Ice, G., *Metallurgical and Material Transactions A*, (2008) **39**, 3058.

[14] Miki, H.; Lin, S.; Sasaki, M.; Katoh, T.; Imai, S.; Nakayama, Y., *Diamond and Related Materials*, (2001) **10**, 937.

[15] Poulsen, H. F.; Garbe, S.; Lorentzen, T.; Juul Jensen, D.; Poulsen, F. W.; Andersen, N. H.; Frello, T.; Feidenhans'l, R.; Graafsma, H., *Journal of Synchrotron Radiation*, (1997) **4**, 147.

[16] Braslau, A.; Deutsch, M.; Pershan, P. S.; Weiss, A. H.; Als-Nielsen, J.; Bohr, J., *Physical Review Letters*, (1985) **54**, 114.

[17] Materlik, G.; Zegenhagen, J., *Physics Letters A*, (1984) **104**, 47.

[18] Miles, A. J.; Wallace, B. A., *Chemical Society Reviews*, (2006) **35**, 39.

[19] Hendrickson, W., *Science*, (1991) **254**, 51.

[20] Hendrickson, W. A.; Pähler, A.; Smith, J. L.; Satow, Y.; Merritt, E. A.; Phizackerley, R. P., *Proceedings of the National Academy of Sciences*, (1989) **86**, 2190.

[21] Weik, M.; Ravelli, R. B. G.; Kryger, G.; McSweeney, S.; Raves, M. L.; Harel, M.; Gros, P.; Silman, I.; Kroon, J.; Sussman, J. L., *Proceedings of the National Academy of Sciences*, (2000) **97**, 623.

[22] Brown, G. E.; Sturchio, N. C., *Reviews in Mineralogy and Geochemistry*, (2002) **49**, 1.

[23] White, R. N.; Smith, J. V.; Spears, D. A.; Rivers, M. L.; Sutton, S. R., *Fuel*, (1989) **68**, 1480.

[24] Henderson, C. M. B.; Cressey, G.; Redfern, S. A. T., *Radiation Physics and Chemistry*, (1995) **45**, 459.

[25] Einfeld, D.; Hasnain, S. S.; Sayers, Z.; Schopper, H.; Winick, H., *Radiation Physics and Chemistry*, (2004) **71**, 693.

[26] Kim, K. J., *Optical Engineering*, (1995) **34**, 342.

[27] http://pd.chem.ucl.ac.uk/pdnn/inst2/work.htm

[28] Kamitsubo, H., *Journal of Synchrotron Radiation*, (1998) **5**, 162.

[29] Dong C-L Guo J, C. Y.-Y., Ching-Lin C, *SPIE*, (2007),

[30] Shaw, G. B.; Grant, C. D.; Shirota, H.; Castner, E. W., Jr.; Meyer, G. J.; Chen, L. X., *Journal of the American Chemical Society*, (2007) **129**, 2147.

[31] Winick, H., *Synchrotron Radiation Sources: A Primer*, World Scientific: (1995).

[32] Mills, D., *Thirs Generation Hard X-ray Synchrotron Radiation Sources: Source Properties, Optics and Experimental Techniques*, Wiley New York, (2002).

[33] De Broglie, M., *C. R. Acad. Sci. Paris*, (1913) **157**, 924.

[34] Fricke, H., *Physical Review*, (1920) **16**, 202.

[35] Kronig, R. D. L., *Zeitschrift Fur Physik*, (1931) **70**, 317.

[36] Lytle, F. W., *Journal of Synchrotron Radiation*, (1999) **6**, 123.

[37] Sayers, D. E.; Stern, E. A.; Lytle, F. W., *Physical Review Letters*, (1971) **27**, 1204.

[38] M, N., Fundamentals of XAFS, In *Consortium for Advanced Radiation Sources*, Chicago, (2004).

[39] Bianconi, A., *Applied Surface Science*, (1980) **6**, 392.

[40] Fujikawa, T.; Matsuura, T.; Kuroda, H., *Journal of the Physical Society of Japan*, (1983) **52**, 905.

[41] Rehr, J. J.; Kas, J. J.; Vila, F. D.; Prange, M. P.; Jorissen, K., *Physical Chemistry Chemical Physics*, (2010) **12**, 5503.

[42] Foster, A. L.; Brown, G. E.; Tingle, T. N.; Parks, G. A., *American Mineralogist*, (1998) **83**, 553.

[43] Lobinski, R.; Moulin, C.; Ortega, R., *Biochimie*, (2006) **88**, 1591.

[44] Peterson, M. L.; Brown, G. E.; Parks, G. A.; Stein, C. L., *Geochimica Et Cosmochimica Acta*, (1997) **61**, 3399.

[45] Ressler, T.; Wong, J.; Roos, J.; Smith, I. L., *Environmental Science & Technology*, (2000) **34**, 950.

[46] Waldo, G. S.; Carlson, R. M. K.; Moldowan, J. M.; Peters, K. E.; Pennerhahn, J. E., *Geochimica Et Cosmochimica Acta*, (1991) **55**, 801.

[47] Rehr, J. J.; Albers, R. C., *Reviews of Modern Physics*, (2000) **72**, 621.

[48] Penner-Hahn, J. E., *eLS*,

[49] Bunker, G., *Introduction to XAFS. A Pratical Guide to X-ray Absorption Fine Structure Spectroscopy*, Cambridge: (2010).

[50] Stern, E. A., *Physical Review B*, (1993) **48**, 9825.

[51] http://www.csrri.iit.edu/mucal.html

[52] http://www-ssrl.slac.stanford.edu/mes/xafs

[53] Frazer, B. H.; Gilbert, B.; Sonderegger, B. R.; De Stasio, G., *Surface Science*, (2003) **537**, 161.

[54] Sham, T. K.; Carr, R. G., *Journal of Chemical Physics*, (1985) **83**, 5914.

[55] Eisenberger, P., *Hyperfine Interactions*, (1981) **10**, 915.

[56] Lee, P. A.; Citrin, P. H.; Eisenberger, P.; Kincaid, B. M., *Reviews of Modern Physics*, (1981) **53**, 769.

[57] Hufnagel, T. C., *Nature Materials*, (2004) **3**, 666.

[58] Egami, T. B., S., *Underneath the Bragg Peaks: Structural Analysis of Complex Materials*, Elsevier: (2012); Vol. 2.

[59] Poraikoshits, E. A., *Annual Review of Materials Science*, (1976) **6**, 389.

[60] Young, C. A.; Goodwin, A. L., *Journal of Materials Chemistry*, (2011) **21**, 6464.

[61] Petkov, V., *Materials Today*, (2008) **11**, 28.

[62] Proffen, T.; Billinge, S. J. L.; Egami, T.; Louca, D., *Zeitschrift Fur Kristallographie*, (2003) **218**, 132.

[63] Dove, M. T.; Tucker, M. G.; Keen, D. A., *European Journal of Mineralogy*, (2002) **14**, 331.

[64] Keating, J.; Sankar, G.; Hyde, T. I.; Kohara, S.; Ohara, K., *Physical Chemistry Chemical Physics*, (2013) **15**, 8555.

[65] Cliffe, M. J.; Dove, M. T.; Drabold, D. A.; Goodwin, A. L., *Physical Review Letters*, (2010) **104**,

[66] Tucker, M. G.; Keen, D. A.; Dove, M. T.; Goodwin, A. L.; Hui, Q., *Journal of Physics-Condensed Matter*, (2007) **19**,

[67] Goodwin, A. L.; Michel, F. M.; Phillips, B. L.; Keen, D. A.; Dove, M. T.; Reeder, R. J., *Chemistry of Materials*, (2010) **22**, 3197.

[68] Farrow, C. L.; Juhas, P.; Liu, J. W.; Bryndin, D.; Bozin, E. S.; Bloch, J.; Proffen, T.; Billinge, S. J. L., *Journal of Physics-Condensed Matter*, (2007) **19**,

[69] Marquardt, D. W., *Journal of the Society for Industrial and Applied Mathematics*, (1963) **11**, 431.

[70] Levenberg, K., *Quart. Appl. Math.*, (1944) **2**,

[71] Overview of the standard EXAFS data analysis procedure, http://gbxafs.iit.edu/

[72] Klementev, K. V., *Nuclear Instruments & Methods in Physics Research Section a-Accelerators Spectrometers Detectors and Associated Equipment*, (2000) **448**, 299.

[73] Ravel, B.; Newville, M., *Journal of Synchrotron Radiation*, (2005) **12**, 537.

[74] Newville, M., *Journal of Synchrotron Radiation*, (2001) **8**, 322.

[75] Cook, J. W.; Sayers, D. E., *Journal of Applied Physics*, (1981) **52**, 5024.

[76] Gunter, M. M.; Bems, B.; Schlogl, R.; Ressler, T., *Journal of Synchrotron Radiation*, (2001) **8**, 619.

[77] Badaut, V.; Schlegel, M. L.; Descostes, M.; Moutiers, G., *Environmental Science & Technology*, (2012) **46**, 10820.

[78] Ohyama, J.; Teramura, K.; Okuoka, S.-i.; Yamazoe, S.; Kato, K.; Shishido, T.; Tanaka, T., *Langmuir*, (2010) **26**, 13907.

[79] Lengke, M. F.; Ravel, B.; Fleet, M. E.; Wanger, G.; Gordon, R. A.; Southam, G., *Environmental Science & Technology*, (2006) **40**, 6304.

[80] Sobczak, J. W.; Sobczak, E.; Drelinkiewicz, A.; Hasik, M.; Wenda, E., *Journal of Alloys and Compounds*, (2004) **362**, 162.

[81] Binsted, N.; Hasnain, S. S., *Journal of Synchrotron Radiation*, (1996) **3**, 185.

[82] Binsted, N., EXCURV98, CCLRC Daresbury Laboratory program (1998).

[83] Zabinsky, S. I.; Rehr, J. J.; Ankudinov, A.; Albers, R. C.; Eller, M. J., *Physical Review B*, (1995) **52**, 2995.

[84] Rehr, J. J.; Albers, R. C., *Physical Review B*, (1990) **41**, 8139.

[85] Jaouen, M.; Hug, G.; Ravel, B.; Ankudinov, A. L.; Rehr, J. J., *Europhysics Letters*, (2000) **49**, 343.

[86] Isshiki, M.; Ohishi, Y.; Goto, S.; Takeshita, K.; Ishikawa, T., *Nuclear Instruments & Methods in Physics Research Section A-Accelerators Spectrometers Detectors and Associated Equipment*, (2001) **467**, 663.

[87] Yano, J.; Yachandra V., *Photosynthesis Research*, (2009) **102**, 241

Chapter 3 The dynamic structure of allotropic cobalt characterised using multi-cluster methodologies

3.1 Chapter Overview

Using *ex situ* and *in situ* PDF and XAS techniques an investigation has been performed to understand the mixed phase composition contained within a variety of cobalt metal powders. The cobalt metal system contains HCP and FCC structures which only differ in the medium-range ordering. By developing multi-cluster methodologies using crystallographic data, the structure of metallic cobalt, a model Fischer-Tropsch catalyst, has been examined in detail. The HCP and FCC phase composition over the course of the phase transformation was determined using EXAFS and PDF multi-cluster methodologies. These methodologies have demonstrated the effectiveness of both XAS and PDF techniques for characterising the mixed phase systems and have provided new insight into the medium-range ordering which has hitherto been poorly characterised.

3.2 Introduction

Metallic Co promoted catalysis, in particular the Fischer-Tropsch synthesis, is generally accepted to proceed *via* surface sites of reduced Co metal [1-3]. The active state and structure responsible for this type of Co based catalysis is, however, not fully understood principally because the active catalyst has been shown to exhibit mixed metallic and oxide species[1]. Structurally, bulk metallic Co is itself of interest owing to the presence of both hexagonal closed pack (HCP) and face centred cubic (FCC) allotropes. Whilst the structure of metallic Co is widely understood to be HCP, bulk metallic powders in fact constitute a mixed phase of FCC and HCP allotropes at room temperature[4]. The FCC and HCP structures share similarities in the way that the unit cells are packed together each atom being surrounded by 12 neighbouring atoms and achieving the highest atomic packing factor (APF) that is possible, 74 % [5]. Differences arise in the stacking sequence between planes in the HCP and FCC lattices. The HCP lattice is stacked together so that every other layer is the same (-A-B-A-B-A-B-) whereas in FCC lattice stacking every third layer is the same (-A-B-C-A-B-C-)[6]. The stacking sequences in HCP and FCC structures are depicted in Figure 3-1. Furthermore, at room temperature bulk Co metal powder does not exhibit a distinct pure biphasic composition but rather a faulted mixture of the two crystal phases where incongruities in the stacking sequences exist [7, 8].

Thermodynamically, Co allotropes are very close in energy separated by only *ca*. 1eV and HCP is the stable low temperature phase[9]. Upon heating however, to temperatures above *ca*. 420 °C, Co undergoes a Martensitic-type allotropic phase transformation where the HCP phase converts to a stable high temperature FCC phase [8, 10-12] however this is a slow process[13] and increasing FCC phase composition occurs with temperature until complete transformation of HCP to FCC is achieved above 500 ºC[14]. The mechanism of this diffusionless type transformation is understood to proceed via movement of atoms between adjacent planes of atoms by less than a full interatomic distance[15]. This process is reversible where the FCC to HCP transformation takes place upon cooling with considerable hysteresis. Studies have shown some (approximately 25-30 %) of the FCC phase is

retained and a higher proportion of the FCC phase is retained with air cooling for small cobalt particle sizes[16].

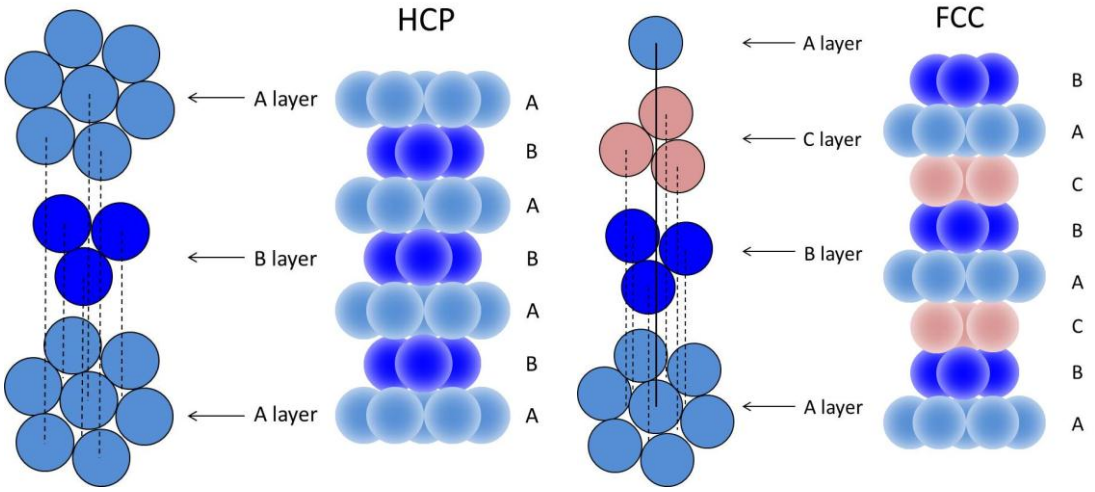

Figure 3-1. *Stacking sequences in cobalt HCP and FCC structures.*

It is of fundamental importance to be able to characterise the HCP/FCC mixtures to develop our physicochemical knowledge of the active state of the catalytic system therefore equipping us with information required to derive a structure-function relationship. Catalyst performance has been shown to be dependent upon phase composition where it has frequently been shown that the Co HCP phase is more active towards CO hydrogenation[17, 18]. Co catalysed FT syntheses proceeds at temperatures in the range 200 - 240 °C [19, 20] thus identifying the relative phase contributions at room temperature alone does not provide insight into the structural changes occurring during catalyst activation and reduction. Understanding the phase transformation processes and characterising the structural changes in the metallic particles are imperative to enhancing activity and selectivity of future Co FT catalysts. Carrying out these investigations on real catalytic systems is challenging due to the nature of the reacting environment where waxes in the catalyst are formed [21]. Advanced setups at synchrotron beamlines have, however, enabled *operando* and *in situ* experiments to be performed [22-25]. Some of the studies undertaken have

linked activity to catalyst structure yet still there lacks a sufficient structural knowledge at the fundamental level. It is, therefore, desirable to use model catalytic systems, such as metallic Co powders, to develop our understanding at the atomic level and then apply this knowledge to working industrial catalysts.

Literature at present lacks in detailed experimental evidence as to the transformations occurring at temperatures around the phase transformation. Early investigations in the 1960s on the HCP ↔ FCC transformation in metallic Co powders were unable to study the process since transformations at these temperatures took place in less time than required for each measurement (about ten minutes)[12]. It is known that localised disorder exists within the HCP and FCC allotropes over the transformation [26, 27] thus non-crystalline characterisation techniques are desirable for investigations on the Co system. More recently a study employing ^{59}Co NMR spectroscopy on Co metal powders demonstrated its effectiveness in probing the local ordering around Co sites during the phase transformation of small Co particles. This study highlighted the localised disorder around Co sites attributed to HCP/FCC deformation fault[16]. XRD contributed to this investigation by providing insight into the mixed phase composition of the Co system where metallic samples were heat treated to various temperatures. Discrepancies arose however between the results of NMR and XRD where inherent stacking faults in the defect structure and small particle sizes (crystallite sizes in the nanometer range) exist. More significantly, limitations arose from laboratory techniques that were performed *ex situ* at room temperature. Quantifying the phase composition accurately at temperatures above and below the HCP ↔ FCC phase transformation temperature remains to be carried out. Overlap of peaks pertaining to both Co HCP and FCC phases precludes any accurate determination of phase composition using XRD[28].

Discrimination of the structures at the atomic level, through EXAFS for example, is particularly challenging since both HCP and FCC allotropes have identical first and second nearest-neighbour coordination numbers, 12 and 6 respectively, and share equal interatomic distances (to within 0.01 Å) for the first and second coordination

shells [29]. Table 3-1 displays the short- and medium-range ordering of the metallic Co structure where differences between HCP and FCC structures are manifested in the medium-range ordering, above 4 Å. When a radial distance, i.e. 6 Å, is imposed, there are marginally more Co atoms in the HCP cluster (80) than in the FCC cluster (76), however a greater disparity arises between the number and distance of consecutive coordination shells. In EXAFS, where scattering phenomena are strongly dependent upon geometry, this makes the two structures distinguishable. In particular, through multiple-scattering where the effect is much greater in FCC due to the absence of alignment of first- and fourth-nearest neighbours in HCP[30]. Resolution of HCP and FCC structures is therefore, in principal, possible through analysis of the medium-range ordering. A few studies have employed EXAFS although these have been restricted to the first few coordination shells[31] or have not directly looked at HCP/FCC phase composition[11]. XANES spectroscopy has been shown to be useful in identifying Co HCP and FCC phases in mixtures however full quantitative information was not performed[28, 32]. Furthermore, in real samples or nanoparticles, often XANES is inadequate in resolving or reproducing spectral features calculated by theory[33].

In EXAFS formalism the exponential damping term, in addition to the $1/R^2$ dependence upon amplitude, restricts the radial distance to which the analysis can be reliably performed. With increasing distance, the number of variables required to model EXAFS data far outweighs the number of data points available which is given by the Nyquist criterion (Equation 2-9). Thus, the amount of reliable information that can be extracted through EXAFS analysis is limited and analysis, therefore, is frequently restricted to the first few coordination shells. The PDF technique is complementary to EXAFS and, crucially, it does not have the same above limitation imposed on it as EXAFS. The available data in *R*- and *Q*- space, in PDF, far exceeds that in EXAFS measurements enabling structural analysis to be performed to much greater length scales and making it a much preferred technique to investigate the medium-range ordering.

Table 3-1. *The short- and medium-range ordering of metallic Co detailing the radial distance and coordination number (in brackets) of each coordination shell, up to the 8th, in Co HCP and FCC allotropes (obtained using FEFF calculations of HCP and FCC crystal phases).*

Coordination Shell	R_{Co-Co} / Å (CN)	
	HCP	**FCC**
1	2.51 (12)	2.51 (12)
2	3.54 (6)	3.54 (6)
3	4.07 (2)	4.35 (24)
4	4.34 (18)	5.03 (12)
5	4.78 (12)	5.62 (24)
6	5.01 (6)	6.16 (8)
7	5.60 (12)	6.65 (48)
8	5.95 (12)	7.11 (6)

The investigation of a reduced catalyst, such as that employed in FT synthesis, by understanding cobalt HCP and FCC structures requires XAS and PDF techniques to bring detailed information over the medium-range ordering at temperatures below and above the phase transformation temperature.

3.3 Aims and objectives

Using a combination of *ex situ* and *in situ* XAS/XRD and PDF techniques our aim is to establish multi-cluster methodologies by obtaining detailed structural information on HCP and FCC Co structures, in particular through the medium-range ordering. We will then extend the multi-cluster methodology to determining the Co HCP/FCC

phase composition below and above the phase transformation temperature. The results from both these techniques will be evaluated and rationalised.

3.4 Experimental

3.4.1 Sample preparation

All cobalt samples used in this study were provided by Johnson Matthey Technology Centre, Sonning Common. The heat treated and ball milled Co metal powder samples used in this study were CC200, CC700, SC700 and BM. CC and BM samples were used in accordance with Speight *et al*'s 2009 diffraction and NMR studies [16, 34]. "CC200" denotes the sample was heat treated to 200 °C then "crash cooled" by quenching in liquid nitrogen. "BM" relates here to the "Aldrich BM" sample used in Speight *et al*'s 2009 NMR study which was subject to a 24 hr milling time. "SC700" denotes heat treatment to 700 °C with subsequent cooling in air, "slow cooled". The untreated as-received Co metal powder sample used in this study was obtained from Sigma-Aldrich (99.8 % purity).

3.4.2 X-ray total scattering

X-ray total scattering data were collected at BL04B2 (High Energy X-ray Diffraction) beamline [19] of the SPring-8 synchrotron, Japan. The storage ring operates with an energy of 8 GeV. For *ex situ* measurements, Co metal powder samples were prepared by grinding and loading into a stainless steel sample holder with the powdered samples sealed in place using Kapton tape. *In situ* measurements were made with Co metal powder samples that were prepared by loading into evacuated quartz capillary tubes (0.7 mm internal diameter). The beamline has a two-axis diffractometer installed and which was used in these experiments as shown in Figure 3-2(a). Data were recorded *ex situ* at room temperature for BM, CC200, CC700 and SC700 sample powders and *in situ* at room temperature, 350 °C and 550 °C, in transmission geometry. The two-axis diffractometer was equipped with a high temperature furnace which enabled *in situ* experiments to be carried out (Figure 3-2 (b)). Scattered X-rays from the sample were collected in step-scan mode using a Ge detector integrated with a multichannel analyser at a wavelength of λ = 0.2018 Å tuned by a Si (220) monochromator. This enabled a momentum transfer, Q_{max}, of

up to 25.0 $Å^{-1}$ to be achieved. Due to the intense Bragg peaks from the metallic samples and the need for accurate determination of background and diffuse intensities to high *Q* values, data collection was performed continuously and in four segments over a 2θ range of 0.3 to 48.2°, corresponding to a *Q* range of 0.16 to 25.43 $Å^{-1}$, where counting times and step sizes were varied accordingly. For both *in situ* and *ex situ* data collection samples were measured for approximately 3.5 hours.

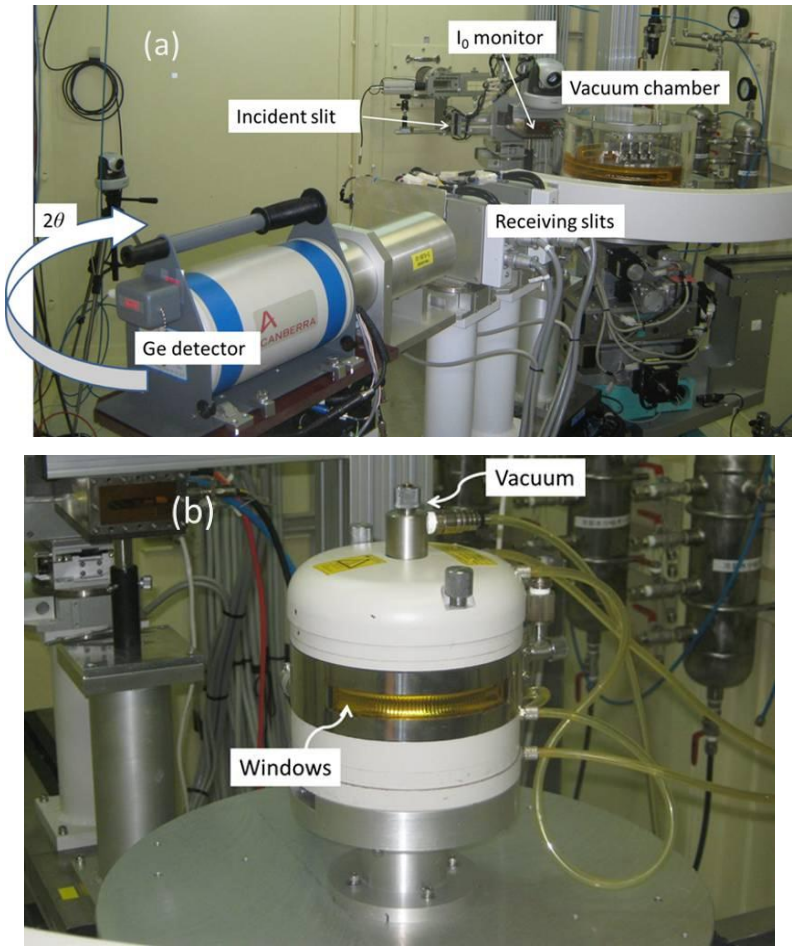

Figure 3-2. *(a) BL04B2 High energy X-ray diffraction beamline, SPring-8. (b) High temperature furnace on BL04B2 beamline used for in situ PDF measurements.*

.

3.4.3 X-ray absorption spectroscopy

Ex situ XAS measurements at the Co K-edge, for cobalt metal powder samples were performed at the Dutch - Belgian beamline, BM26A at the European Synchrotron Radiation Facility (ESRF). The storage ring operates at 6.0 GeV with a typical current of between 170 and 200 mA. The station is equipped with a Si(111) double crystal monochromator. Higher harmonic rejection was performed using vertically focussing mirrors installed after the monochromator. The energy resolution was 1eV at the Co K edge (7709 eV). Ionisation chambers filled with appropriate gas mixtures were used to detect the intensities of the incident beam (I_0), and the transmitted beam (I_1). EXAFS data were acquired in step scans over a *k*- range (*k* being the photoelectron wave vector) of 3 $Å^{-1}$ to 14.5 $Å^{-1}$. A typical scan time taken was *ca*. 20 minutes. Samples (50 mg of sample pelletized, 12.5 mm pellets) were suspended on a ceramic holder and loaded into the sample chamber.

3.4.4 Combined X-ray absorption spectroscopy/X-ray diffraction

Combined XRD/XAS measurements were performed on the as-received cobalt metal powder sample *in situ* at the BM29 beamline of the ESRF. The beamline is equipped with "Quick-EXAFS" (QEXAFS) continuous scanning mode and using Si (111) double crystal monochromator. XAS data were collected at the Co K-edge (7709 eV) in transmission mode. A full scan between 7600 and 8900 eV was taken every 240s taking with a data acquisition time of 1s per scan. Detectors use ionisation chambers I_0, I_1 and I_2. XRD was performed sequentially with enough time for the monochromator to reset to 7500 eV (1.653 Å) using a MAR345 area plate detector which recorded angle-dispersive XRD data between 0.01 and 56.7 ° 2θ. Approximately 7 mg of a cobalt metal powder sample was mixed with γ-Al_2O_3 as a diluent to make 50mg of self-supporting wafer and was loaded into a specially designed *in situ* spectroscopic cell provided by the beamline (Figure 3-3). The experiment was carried out under a 5% H_2/N_2 atmosphere with a temperature profile that began at room temperature and increased to 575 °C at 5°/min. After heat treatment samples were cooled down to room temperature whilst continuing to collect XAS and XRD data.

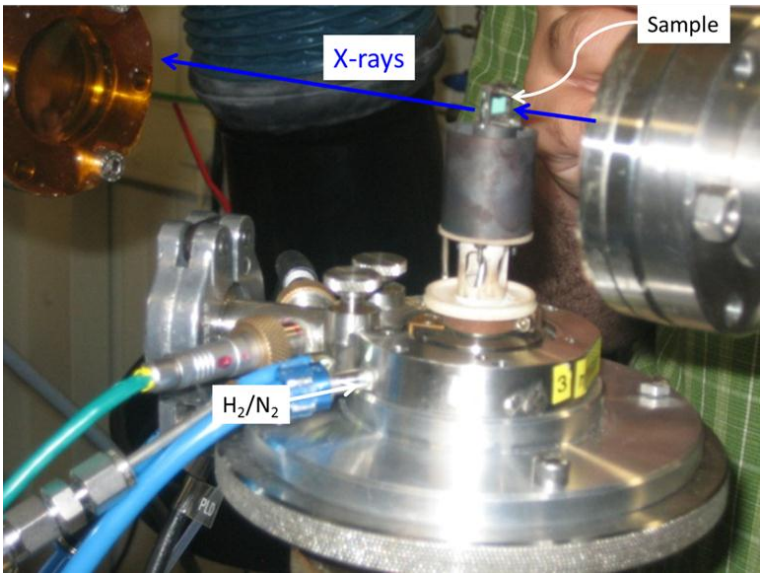

Figure 3-3. *In situ spectroscopic cell used for QuickXAS measurements at BM29 beamline.*

3.4.5 Data analysis

3.4.5.1 XRD analysis

Rietveld analysis was performed on CC200, CC700 and SC700 Co metal powder samples using diffraction data obtained from X-ray total scattering measurements recorded at BL04B2. Spring-8. TOPAS-Academic software was used for the analysis. $P6_3/mmc$ and $Fm\bar{3}m$ space groups were used for HCP and FCC phases, respectively, in the analysis. A wavelength of 0.2018 Å was used in analysis.

3.4.5.2 PDF analysis

The processing of raw X-ray total scattering data to obtain the $G(r)$ was executed using a beamline macro and the Igor program and is discussed in detail in chapter two. A Q_{max} of 25.0 $Å^{-1}$ was used in the data analysis.

3.4.5.3 PDF multi-cluster modelling

Modelling of the experimental PDF data was performed using PDFgui[35] and the details of the multi-cluster methodology are discussed in chapter two. *R*-space fits were performed over a 1 to 10 Å range for this study, since below the first Co─Co interatomic distance of *ca*. 2.50 Å there is no structural information. Data were Fourier transformed up to 10 Å. Differences in the PDF between HCP and FCC structures are observed above 4 Å thus a sufficient portion of the data in *r*-space (4 to 10 Å) is used for resolving HCP and FCC structures. The analysis was performed using a Q_{max} of 25.0 $Å^{-1}$. The Q_{damp} parameter was refined and Q_{broad} was set to the default value of zero, as this parameter had no effect on the fit due to the 10 Å upper fit range.

The multi-cluster model containing Co HCP and FCC phases was generated using CIFs which have the crystallographic space groups $P6_3/mmc$ and $Fm\bar{3}m$, respectively. The FCC (*a*), HCP (*a*,*c*) lattice parameters, *phase scale factors* and *atomic displacement parameters* (*U)* were refined for both phases. The *delta parameter,* δ_1, was refined and constrained to be the same for each phase. The introduction of the δ_2 to the fit had no effect and these parameters are highly correlated so in practise only one is varied. The ADPs (*U*) for the HCP and FCC phase were refined isotropically and constrained to be the same for each phase. $P6_3/mmc$ and $Fm\bar{3}m$ space groups contain atoms which lie on special positions and were therefore not refined for each phase. Structural parameters including the *anisotropic ADPs* and *occupancies* were set to default values, 0 and 1, respectively. The *spdiameter* parameter was not refined and set to the default value of 0. This analysis routine was kept consistent for all cobalt metal powder PDF data.

3.4.5.4 XAS analysis

The removal of background and normalisation of raw XAS data were performed using the Athena program[36]. Routine normalisation and background subtraction procedures were employed in this study using *ex situ* and *in situ* Co K-edge XAS

data. The value for E_0 selected in the data processing was chosen to be the maximum of the first peak in the derivative spectra.

3.4.5.5 EXAFS multi-cluster modelling

EXAFS analysis was performed using Artemis[36]. A general description of the multi-cluster methodology is given in chapter two. The refinement of EXAFS data was performed in *R*-space from 1 to 6 Å using a *k*-range of 3.2 to 12.0 $Å^{-1}$ in the analysis of *ex situ* data and 3.2 to 10.5 $Å^{-1}$ for *in situ* data. A smaller terminating k_{max} was selected for *in situ* data analysis due to the increased *S*/*N* ratio at higher temperatures which limits the available data in *k*-space. The extracted EXAFS was refined using a structural model with structural parameters including: the amplitude reduction factor (S_0^2), bond distances (*R*), Debye-Waller factors (σ^2), threshold energy (E_0) and HCP and FCC amplitude mixing parameters (*x* and *y*). The use of cobalt metal powder, as a standard, to extract the S_0^2 value is an appropriate routine in these analyses, however it is noteworthy that this method results in a lower S_0^2 value compared to using cobalt foil as a standard. The reported values and uncertainties of bond distances are little affected by the fitting of S_0^2 using the first coordination shell, however when constraining S_0^2 globally for full data fitting, additional uncertainty to the reported values of the amplitude mixing parameters should be taken into account. The overall phase composition results are not affected in this manner.

Multi-cluster models of mixed phase Co systems were developed using CIFs for Co HCP and FCC phases. FEFF calculations generated structures (clusters) up to 6 Å. Single, double and triple scattering paths are displayed for both clusters and added to the model in a stepwise fashion. Path degeneracies (coordination numbers), other than for the first two coordination shells, vary for HCP and FCC structures therefore the parameterisation of the structural model for each data set had to be varied, to some extent, accounting for the different phase compositions. All scattering paths, in total 69 for HCP and 34 for FCC, were included in the model in a systematic

fashion where paths were added and removed in order to determine their effect on the overall fit.

Various cluster models were employed in an attempt to reduce the number of independent variables (N_{var}). The correlated Debye model, for example, parameterises Debye Waller factors as a function of the Debye temperature of cobalt. This proved not to be a robust model for analysis of the mixed phase cobalt system as *in situ* data were collected above the Debye temperature [37]. For metallic systems an isotropic expansion model can be used; each coordination shell expands or contracts by the same amount and is described by an expansion coefficient, α, which increases or decreases all scattering path lengths in the cluster by this value. Attempts were made to validate such a model for the Co system system, however this was an over-parameterisation for fitting two phases and so not developed further.

The multi-cluster model used in the analyses in this investigation required bond distance parameters for each phase that were assigned to single, double and triple scattering paths which were close in distance, R, the half-path length. Only the parameters for the HCP cluster (ΔR_h) were allowed to vary and those for the FCC cluster (ΔR_f) were defined in terms of the HCP cluster parameters. This is a viable method to minimise the number of bond distance parameters being refined whereby ΔR_f values are updated during the fit. The Debye Waller factors, σ^2, were modelled in a similar fashion by grouping scattering paths together that are close in distance by assignment of the same σ^2 parameter. This enabled numerous multiple-scattering paths contributing to higher shells to be constrained to the same σ^2 value thereby minimising the number of variables, N_{var}, in the fit. The HCP/FCC phase compositions in all the cobalt samples were determined using the results of the refinement of the amplitude mixing parameters, x and y (for HCP and FCC phases, respectively).

3.5 Results and Discussion

The results of the PDF analysis of *ex situ* X-ray total scattering data from various cobalt metal powder samples using multi – cluster models to determine the phase composition are first described. Further development of the PDF methodology by implementing with *in situ* data is then reported with an aim to understanding the Co HCP to FCC phase transformation. Finally, results from complementary *ex situ* and *in situ* XAS studies are evaluated with the similar aim of determining the Co phase composition and transformation using EXAFS multi – cluster modelling.

3.5.1 *Ex situ* PDF analysis of Co metal powders

The normalised total scattering structure functions, $S(Q)$, obtained from *ex situ* data for Co metal powder samples CC200, CC700, SC700 and BM are shown in Figure 3-4. The most intense scattering is clearly seen in the SC700 sample which displays the sharpest reflections, which are visible up to 25 $Å^{-1}$, in comparison with other data where peaks in *S(Q)* are broader and less intense. This can be explained by the heating of the metal powder, followed by the slow air cooling process, which induces the formation of well-defined crystallites that gives rise to the sharp peaks in the *S(Q)*. In all the data the peaks are located at the same positions, however for the BM sample the reduction in intensities and broadening of the peaks make the *S(Q)* data more difficult to interpret with respect to the other three samples. The mechanical ball milling action can broaden the diffraction peaks due to the reduction in particle size. This effect is frequently observed in nanocrystallites[37, 38]

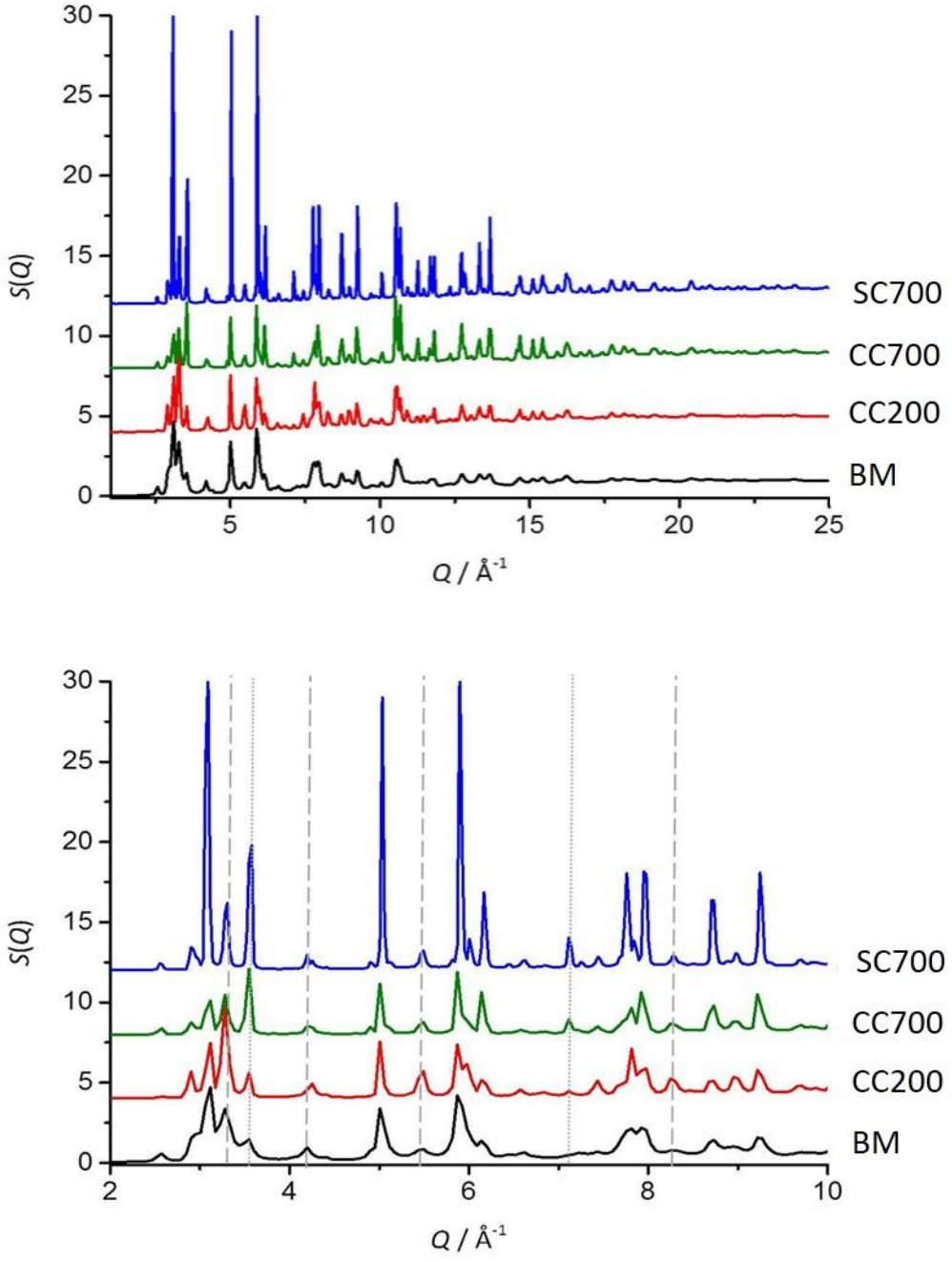

Figure 3-4. *Stacked plots of the normalised total scattering structure function, S(Q), obtained from ex situ PDF measurements on Co metal powders. The full region (above) and enlarged region (below) in Q-space are displayed. Peaks belonging to FCC (dotted line) and HCP (dashed line) phases are annotated in the enlarged Q-region. All other peaks are mixtures pertaining to HCP and FCC cobalt.*

Figure 3-5 displays the Co HCP and FCC unit cells with the first four nearest-neighbour distances annotated. The corresponding HCP and FCC distances are highlighted in Figure 3-6 which displays the PDF fits up to 10 Å for the BM sample using two different structural models; one using Co HCP and the using Co FCC. It is clear that neither model completely represents the data, in particular above ca. 4 Å, where there is considerable mismatch between the experimental and calculated PDF peak intensities. The first two peaks at *ca*. 2.49 and 3.52 Å corresponding to the first and second coordination shells in metallic Co are modelled adequately, which is not unexpected since both allotropes share similar first and second shell Co─Co distances and coordination numbers. Emphasised here is the inability to fully characterise the metallic cobalt sample, in particular based on the short-range ordering which comprises a mixed HCP/FCC phase, by modelling with a single crystallographic HCP or FCC phase. In order to fully resolve the structures present and to quantitatively determine the phase composition, multi – cluster models are required that include higher shell distances.

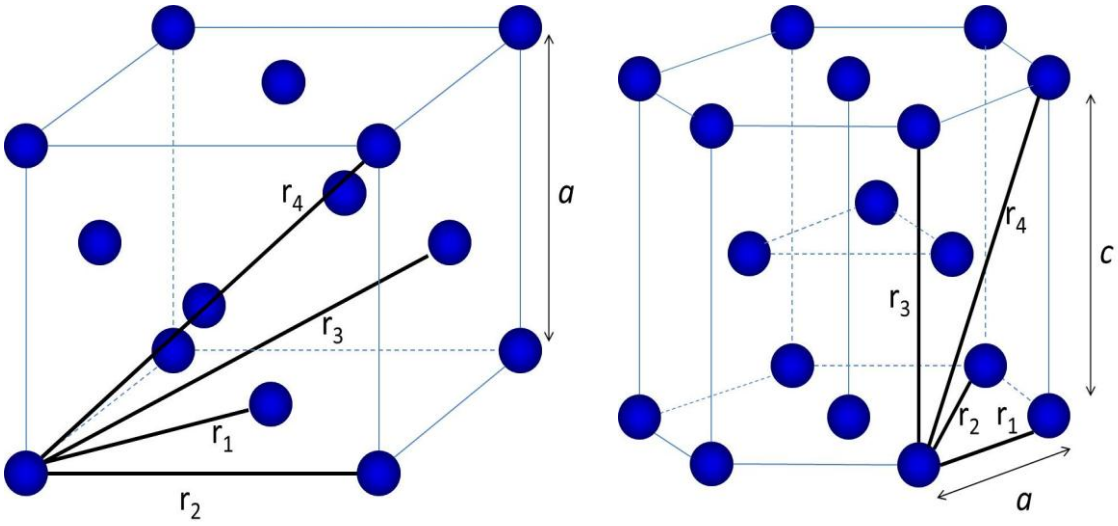

Figure 3-5. *Cobalt HCP (left) and FCC (right) unit cells. The first four nearest-neighbour distances and the lattice parameters 'a' and 'c' are highlighted.*

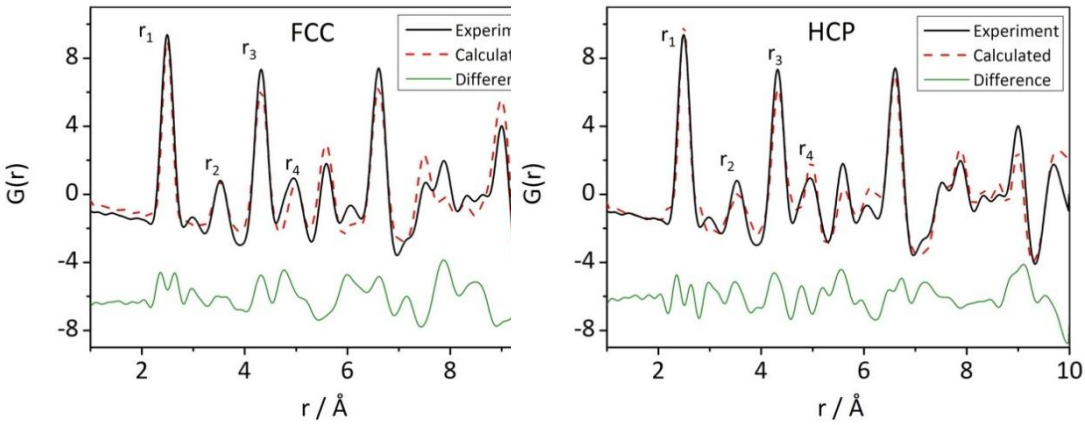

Figure 3-6. *Best fits of the experimental PDF data (black line) to the calculated PDF (red line) for the BM sample using structural models of Co HCP (R_w = 0.30) and Co FCC (R_w = 0.35). The residual spectrum (green line) is shown below. Peaks belonging to the first four nearest-neighbour distances are annotated.*

Figure 3-7 illustrates the best PDF fits of the experimental data belonging to the BM, CC200, SC700 and CC700 samples using multi-cluster modelling. The PDF fit for the BM sample is much improved over the single phase fits where the data show very good agreement with the model (R_w = 11 %) over the full fit range of 1 to 10 Å. The SC700 PDF data show an excellent agreement to the multi – cluster model (R_w = 7 %) where the residual spectrum is almost a flat line. The CC200 PDF data show a reasonably good agreement (R_w = 18 %) although some peak amplitudes and positions are not so accurately modelled. Nevertheless, the model generates an adequate fit to the data. There are clear differences in the PDF of the CC700 sample compared to the other Co powders, notably at *ca*. 1.90 and 3.05 Å where peaks are not well modelled. The 6 to 9 Å region of the PDF displays a greater residuum between experimental and calculated PDFs (R_w = 36 %). It is very likely that some oxidic component in the sample is responsible for the inadequate fitting model since the peak positions are consistent with Co─O distances found in higher valent Co^{3+}–O species. The addition of bulk cobalt oxide phases, CoO and Co_3O_4, to the model did not improve the fit. It is, therefore, quite likely that surface oxide species exist in this system. These phases may not exhibit sufficient long-range order to be studied

based on crystallographic data which is a requirement in PDFgui. From interpretation of *S(Q)* data (Figure 3-4) it is unclear as to whether the CC700 sample has undergone any oxidation since extraneous reflections originating from an oxidic species could not be assigned. Table 3-2 reports the refined values of the structural parameters obtained from PDF fitting. The FCC and HCP lattice parameters have refined values that are consistent with crystal structure data. The *c*/*a* ratio in the samples varies between 1.610 and 1.626, closely matching the value of 1.633 in an ideal HCP crystal structure.

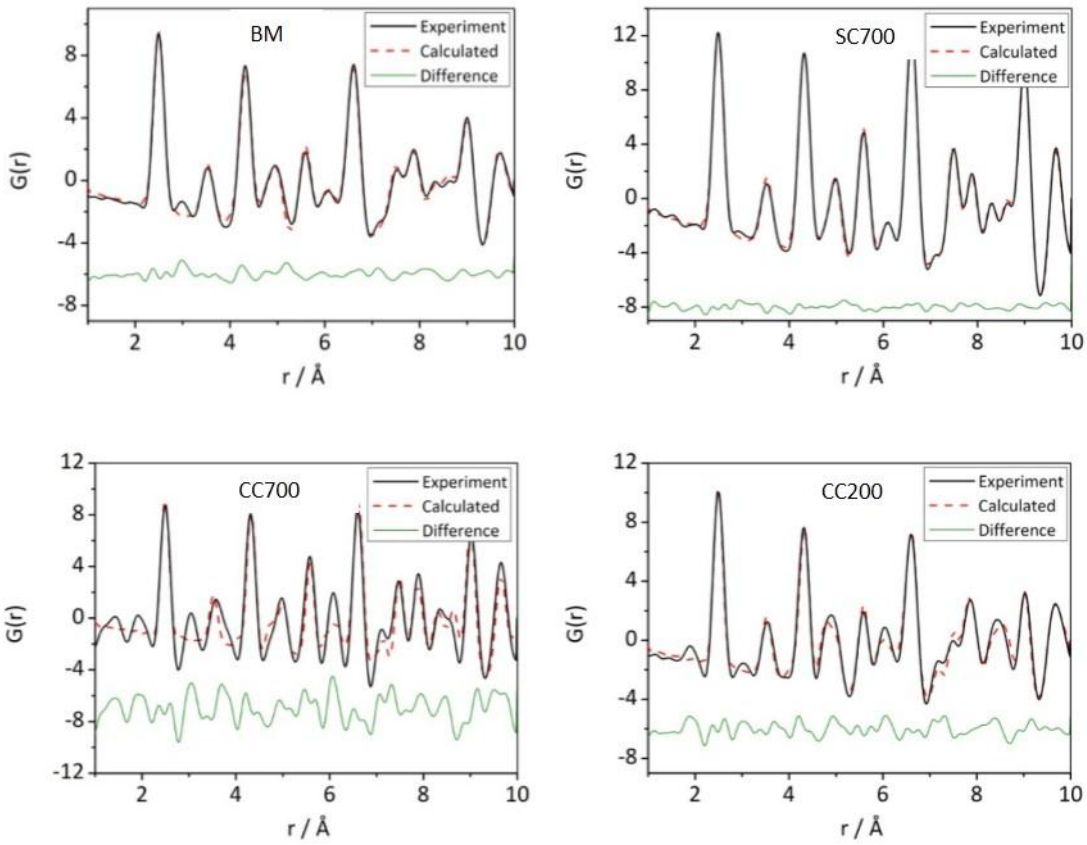

Figure 3-7. *Best fits of ex situ Co PDF data for the BM, SC700, CC700 and CC200 samples. Experimental PDFs (black line) are fit to calculated PDFs (red line) using multi-cluster models. Good agreement is obtained with the exception of the CC700 data where sample oxidation is responsible for the much larger fit residuum.*

Table 3-2. *Results of PDF fitting for various Co metal powder samples using multi – cluster models. Refined values of HCP and FCC lattice parameters(a and c), isotropic ADPs (U_{iso}), the vibrational correlation term (δ_1), HCP and FCC phase scale factors (SF) and the instrumental resolution damping parameter (Q_{damp}) are reported.*

	BM	**CC200**	**SC700**	**CC700**
a (HCP) / Å	2.510(4)	2.500(2)	2.506(5)	2.510(4)
c (HCP) / Å	4.077(12)	4.065(5)	4.056(13)	4.040(8)
a (FCC) / Å	3.528(4)	3.537(4)	3.528(1)	3.526(1)
U_{iso} / Å^2	0.0115(13)	0.0067(12)	0.0088(0)	0.0044(0)
δ_1	1.02(13)	0.75(17)	0.74(8)	0.39(22)
SF_{HCP}	0.36(2)	0.46(1)	0.22(1)	0.18(1)
SF_{FCC}	0.32(2)	0.17(1)	0.65(1)	0.30(1)
Q_{damp}	0.041	0.044	0*	0.002
R_w (%)	10	18	6	36

*Q_{damp} unstable and therefore fixed in the refinement

The HCP and FCC phase scale factors provide a quantitative measure of the Co phase composition and this is graphically represented in Figure 3-8 as the relative HCP and FCC phase abundance. PDF analysis indicates that all Co samples comprise a mixed HCP/FCC phase composition. The BM sample contains a slightly more dominant HCP phase (55 %) which is the thermodynamically stable phase induced *via* ball mill action. Previous studies have revealed that the milling time can be preferentially adjusted to obtain varying HCP and FCC phase compositions and our results are in agreement with this[39]. The SC700 sample contains a 24 % and 76 % phase composition for HCP and FCC phases, respectively, indicating that during the cooling process from above the phase transformation temperature the reverse FCC to HCP transformation takes place, to some extent, assuming that at 750 °C only the FCC phase is present. Fitting results of the CC200 PDF data also indicate a mixed phase composition where HCP is the dominant phase (74 %). CC700 data display a much poorer agreement with the model (R_w = 36 %) which yields a 62 %

FCC and 38 % HCP phase composition. The thermodynamics of the phase transformation would suggest that, at 750 ºC, the sample consists of a single FCC phase and quenching the sample in liquid nitrogen 'locks in' the sample composition. Clearly the model fails to account for some component of the PDF, in particular in the short-range ordering. It is possible that some surface oxide species may have contaminated the metallic phase which is more difficult to model in the PDF. The reliability of the analysis using CC700 PDF data is therefore questionable.

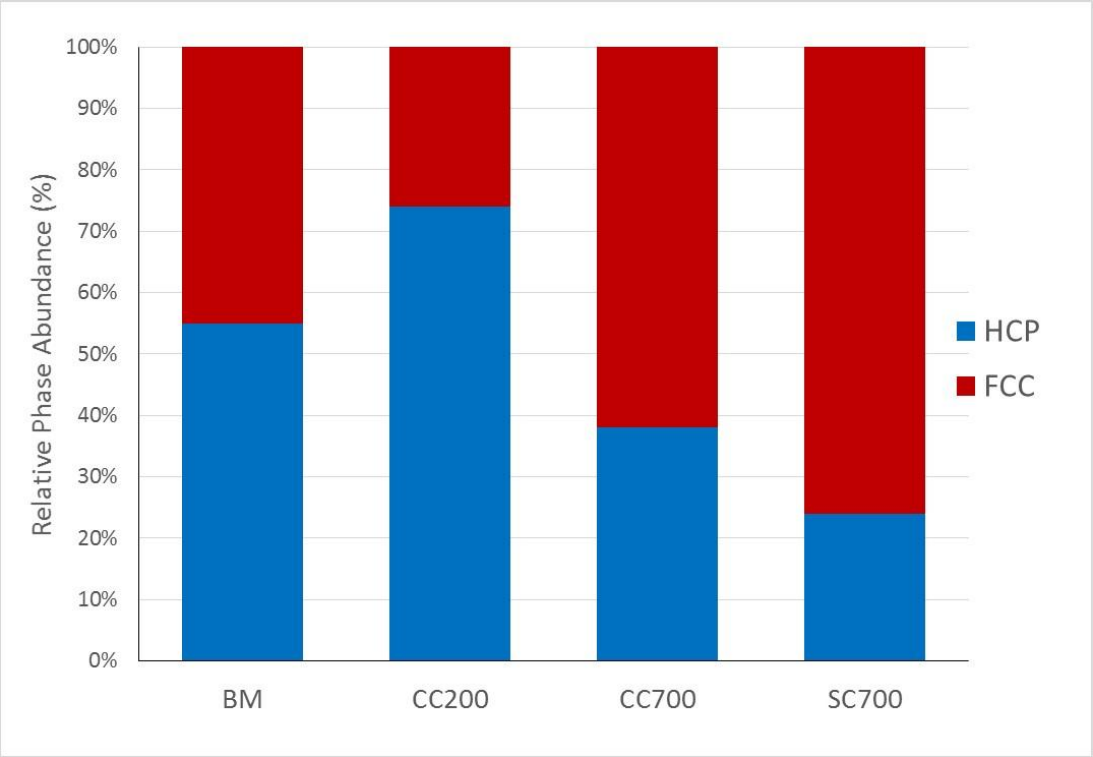

Figure 3-8. *HCP and FCC cobalt phase composition in various cobalt metal powder samples determined from PDF analysis using multi – cluster models. The errors from least squares fitting are as follows: BM ±3%, CC200 ±2%, CC700 ±1% and SC700 ±2%.*

3.5.2 *Ex situ* XRD analysis of Co metal powders

The results of Rietveld analysis on a variety of Co metal powders are listed in Table 3-3. The analysis was performed using data between 5 and 15° 2θ. The best fits of the experimental diffraction data (obtained from X-ray total scattering

measurements) to calculated structures based on HCP and FCC Co are displayed in Figure 3-9.

Table 3-3. *Results of Rietveld analysis for various Co metal powders*

Sample	**CC200**		**CC700**		**SC700**	
Phase	FCC	HCP	FCC	HCP	FCC	HCP
a (Å)	3.5466(8)	2.5052(25)	3.54678(24)	2.5074(8)	3.54301(30)	2.5050(17)
b (Å)	3.5466(8)	2.5052(25)	3.54678(24)	2.5074(8)	3.54301(30)	2.5050(17)
c (Å)	3.5466(8)	4.083(7)	3.54678(24)	4.0752(26)	3.54301(30)	4.075(6)
V (Å^3)	44.610(18)	22.19(5)	44.617(5)	22.188(17)	44.475(7)	22.15(4)
U_{iso} (Å^2)	0.0032(21)	0.0044(13)	0.0157(11)	0.0030(40)	0.0044(14)	0.0012(29)
Phase fraction	0.43(0.04)	0.57(0.01)	0.76(0.05)	0.24(0.01)	0.73(0.04)	0.27(0.01)
R_{wp}	0.2812		0.2852		0.3111	

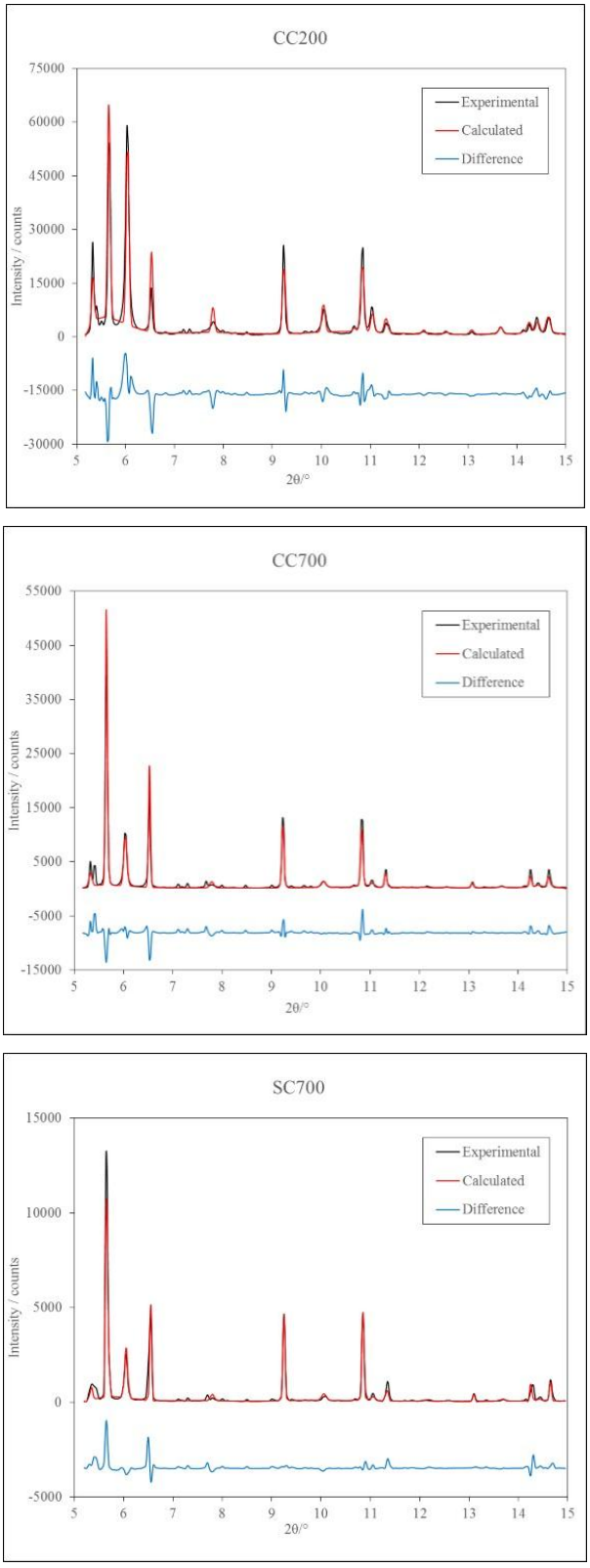

Figure 3-9. *Best fits of diffraction data obtained from X-ray total scattering measurements to calculated patterns based on HCP and FCC Co structures via Rietveld analysis.*

From the Rwp values listed in Table 3-3 it is evident that there is some mismatch between the experimental diffraction data and the calculated diffraction patterns. This is highlighted by the difference spectrum below each fit. Mismatch in the experimental and calculated peak intensities, particularly at low angle, is observed and may originate from fitting of the background function which is challenging since the data obtained from experiments was optimised for PDF analysis. The best fits were obtained using a Gaussian peak function for FCC Co phase and a Pseudo-Voigt peak function for the HCP Co phase. Figure 3-10 graphically depicts the HCP and FCC phase fractions obtained from Rietveld analysis represented as weight fractions and is compared to the phase composition analysis obtained using PDF data. The agreement between both techniques is, in general, good. Phase compositions from SC700 data are in very good agreement. CC200 and CC700 data show larger disparities between XRD and PDF analyses although the results are within 17 per cent or less. Additional peaks of low intensity that are not modelled by the calculated XRD patterns are likely evidence for partial oxidation of these samples which was also indicated from PDF analysis using the same data. This may potentially explain the difference in phase composition analysis for CC200 and CC700 data between the two techniques.

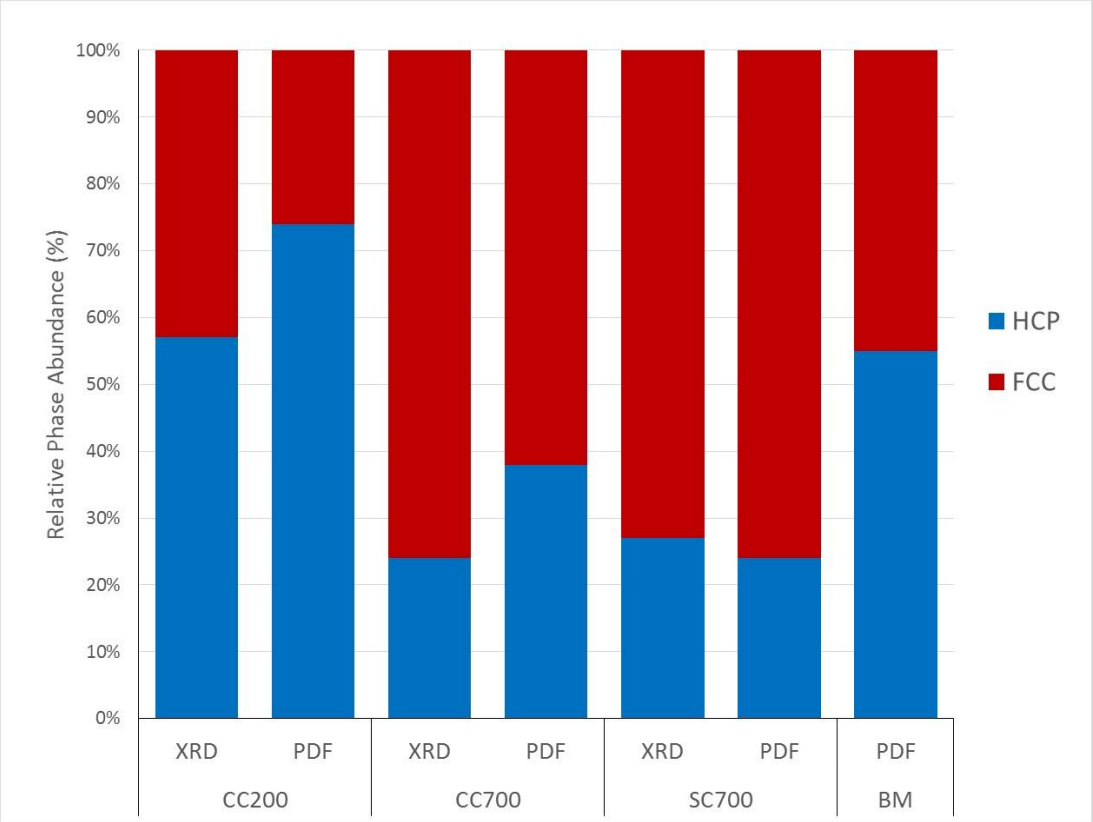

Figure 3-10. *Phase composition results from Rietveld analysis of diffraction data from various Co powders. For comparison, the results from PDF analysis are also shown. The errors from Rietveld analysis are within ±5%.*

3.5.3 *In situ* PDF analysis of Co metal powder

Figure 3-9 displays the *S(Q)* data of the as-received cobalt metal powder from the *in situ* heating. These temperatures were chosen to represent the structure of cobalt below and above the phase transformation temperature. The *S(Q)* data at room temperature and at 350 °C bear close resemblance albeit with a small reduction in the intensities of the peaks upon heating due to thermal effects. The allotropic HCP to FCC phase transformation is not expected to occur by 350 °C and therefore the data are consistent with this hypothesis. At 550 °C the differences in *S*(*Q*) are noticeable and is evidence to suggest that the sample has undergone some structural transformation at this higher temperature. Having validated the multi – cluster methodology for mixed Co HCP and FCC phase structures using *ex situ* PDF data, the methodology was then developed *via* implementation of the *in situ* Co PDF data in order to follow the HCP to FCC phase transformation at higher temperature.

Figure 3-10 illustrates the best fits of the experimental PDFs measured at room temperature, 350 and 550 °C to the calculated PDFs using multi – cluster modelling, over an *r*-range of 1 to 10 Å. Values for the structural parameters extracted from PDF analysis are summarised in Table 3-3.

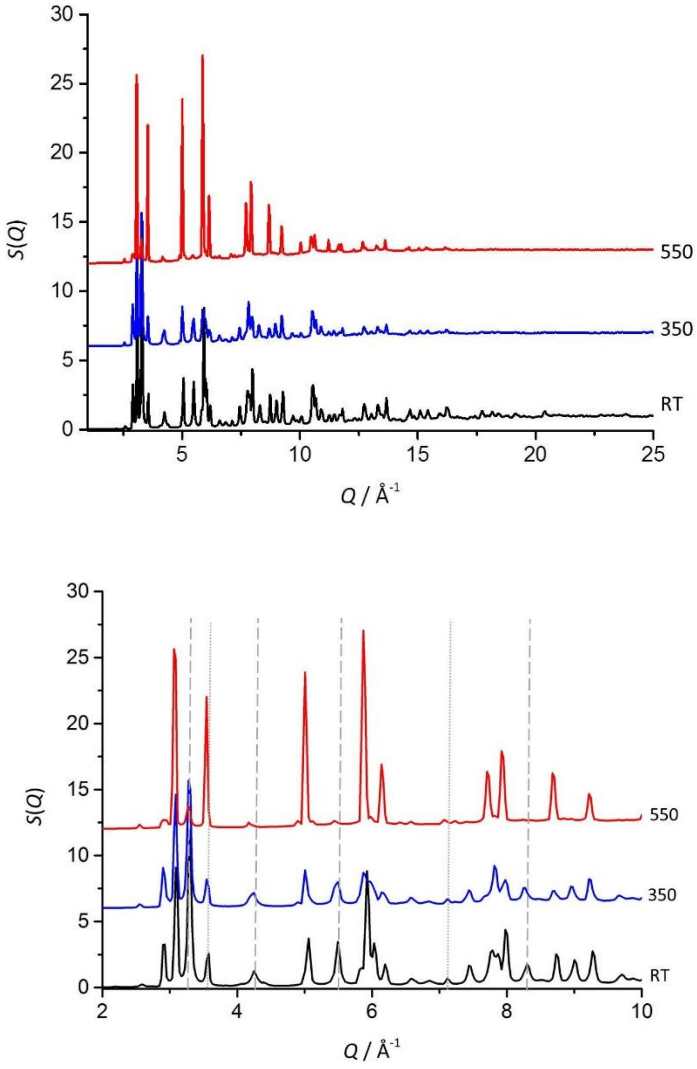

Figure 3-11. *The normalised total scattering structure function, S(Q), from in situ heating of cobalt metal powder measured at room temperature (black), 350 °C (blue) and 550 °C (red). The full region (above) and enlarged region (below) in Q-space are displayed. Peaks belonging to FCC (dotted line) and HCP (dashed line) phases are annotated in the enlarged Q-region. All other peaks are mixtures of HCP and FCC cobalt.*

Table 3-4. *Results of PDF analysis of cobalt metal powder measured in situ at various temperatures.*

	RT	**350 C**	**550 C**
a (HCP) / Å	2.495(2)	2.505(3)	2.485(7)
c (HCP) / Å	4.071(4)	4.067(6)	4.245(8)
a (FCC) / Å	3.529(2)	3.531(2)	3.543(1)
U_{iso} / Å^2	0.0084(5)	0.0014(5)	0.0184(4)
δ_1	0.45(11)	0.95(10)	1.08(8)
SF_{HCP}	0.70(2)	0.61(2)	0.09(2)
SF_{FCC}	0.25(1)	0.16(1)	0.97(2)
Q_{damp}	0.052(8)	0*	0*
R_w (%)	12	23	26

*Q_{damp} unstable and therefore fixed in the refinement

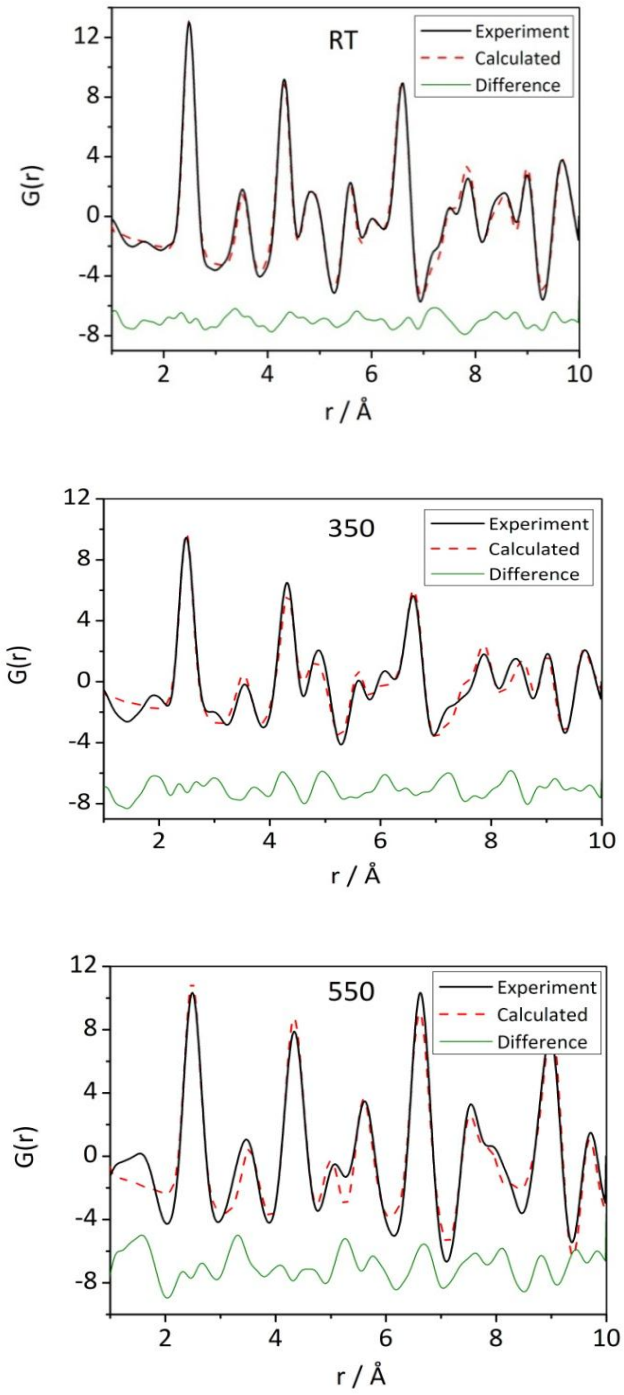

Figure 3-92. *PDF best fits obtained using multi-cluster modelling of in situ cobalt PDF data at room temperature, 350 °C and 550 °C. Experimental PDFs (black line) are fit to calculated PDFs (red line) using multi-cluster models.*

The PDF data obtained at room temperature show a very good agreement to the calculated PDF (R_w = 12 %). The refined HCP and FCC phase scale factors indicate a mixed phase with a dominant HCP component (although further corrections are applied to these parameters to obtain the real composition). The HCP (*a* and *c*) and FCC (*a*) lattice parameters are consistent with crystallographic data. At 350 °C there is a small component in the PDF that is not captured by the HCP/FCC model which is indicated by the larger residuum (R_w = 23 %). It is unclear as to the nature of this additional component although the residual spectrum (below in green) oscillates with a comparable amplitude at high- and low-*r*. It is important to note that this crystallographic based analysis has not taken into account the static disorder that exists at phase boundaries. The HCP *c*/*a* ratios are 1.632 and 1.624 for RT and 350 data respectively, in good agreement with the ideal *c*/*a* ratio in HCP of 1.633. The FCC lattice parameter increases by 0.0014 Å on heating to 350 °C due to the thermal expansion of the FCC lattice and the increase in thermal disorder is modelled through the increase in the isotropic ADPs. The delta (δ_1) parameter, which accounts for low-*r* peak sharpening due to correlated atomic motion, also increases which is correlated to temperature. The phase scale factors suggest a mixed phase system at 350 °C where HCP remains the dominant phase. At 550 °C the thermodynamics of the HCP to FCC phase transformation suggest that this process is complete. PDF analysis indicates that the sample contains some HCP phase at this temperature where the HCP phase scale factor takes a non-negative and non-negligible value, i.e. its presence is implied and is not modelling some of the noise in the PDF. The quality of the fit is similar to the data at 350 °C and there is a significant low-*r* portion to the data, below *ca*. 3.5 Å, that is not accurately modelled, in particular a peak at *ca*. 1.6 Å. The second peak in the PDF, representing the second nearest-neighbour distance, has moved to lower-*r*. It is possible that this peak is a convolution of Co─Co (metallic second shell) and Co─O (oxide first shell) peaks thus suggesting that partial oxidation of the metallic sample has taken place. The FCC lattice parameter increases by 0.012 Å due to thermal expansion of the lattice however the HCP *c*/*a* ratio is 1.709, considerably larger than that at room temperature and 350 °C.

Figure 3-11 depicts the HCP and FCC Co phase composition derived from PDF analysis in the cobalt metal powder sample at each temperature obtained from refinement of the phase scale factors. At room temperature the sample contains a phase composition of 76 % and 24 % for HCP and FCC structures, respectively. At 350 °C the Co sample contains the same phase composition as at room temperature, within the uncertainty limits. The 79 % HCP and 21 % FCC phase composition indicates that Co has not undergone the phase transformation, consistent with studies on the phase transformation that reveal the transformation takes place above *ca*. 420°C [12]. The differences are displayed in the structural parameters where the ADPs and the lattice parameters have increased due to increased thermal motion and expansion of the lattices. At 550 °C multi–cluster modelling of the PDF data supports the HCP to FCC phase transformation. The results suggest however that this is incomplete and a residual of *ca*. 10 % HCP phase exists. The larger fit residuum and larger HCP *c*/*a* ratio obtained modelling the high temperature data is evidence for some non–metallic component to the PDF. The HCP phase may be over fitting and trying to model this component, possibly a disordered phase, which is also present in the 350 °C due to the comparable fit residua.

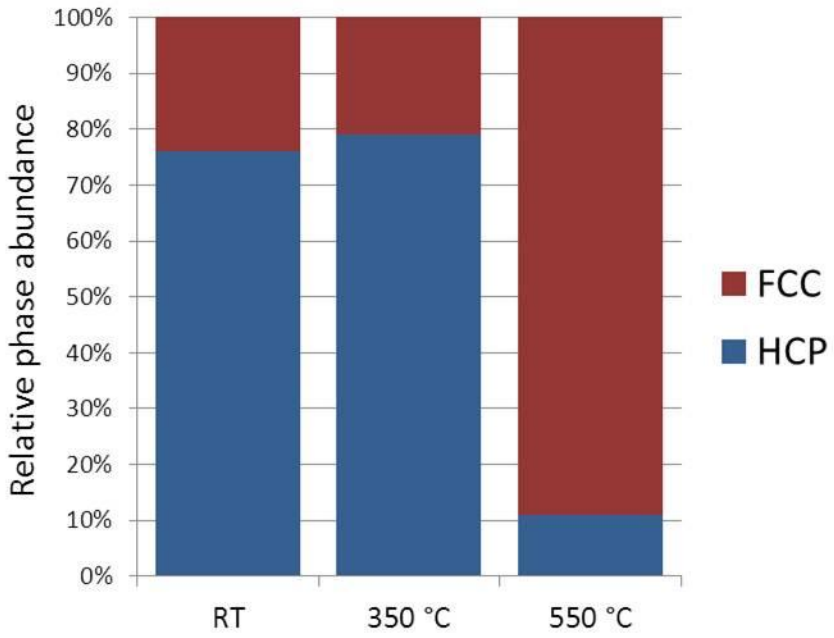

Figure 3-103. *Cobalt phase composition, below and above the phase transformation temperature, from multi-cluster PDF modelling of in situ data.*

3.5.4 *Ex situ* XAS of Co metal powders

3.5.4.1 XANES

The normalised μ(E) XANES spectra obtained from *ex situ* Co K-edge XAS measurements on Co metal powders are displayed in Figure 3-12. The threshold position of the absorption edges (E_0), taken as the maximum of the first peak in the derivative spectrum, are listed in Table 3-4 and the derivative spectra are also displayed in Figure 3-12. The increase in absorption probability arises due to the electric dipole-allowed $1s \rightarrow 4p$ transition where a core *s* electron is promoted into an unoccupied *p* state. All four samples display a shoulder on the rising edge at *ca.* 7710 eV. This characteristic feature of Co metal originates from the transition of an *s* state electron to a bound *s-p* hybridised state although this is frequently referred termed the $1s \rightarrow 4p$ transition involving shake-down processes [40].

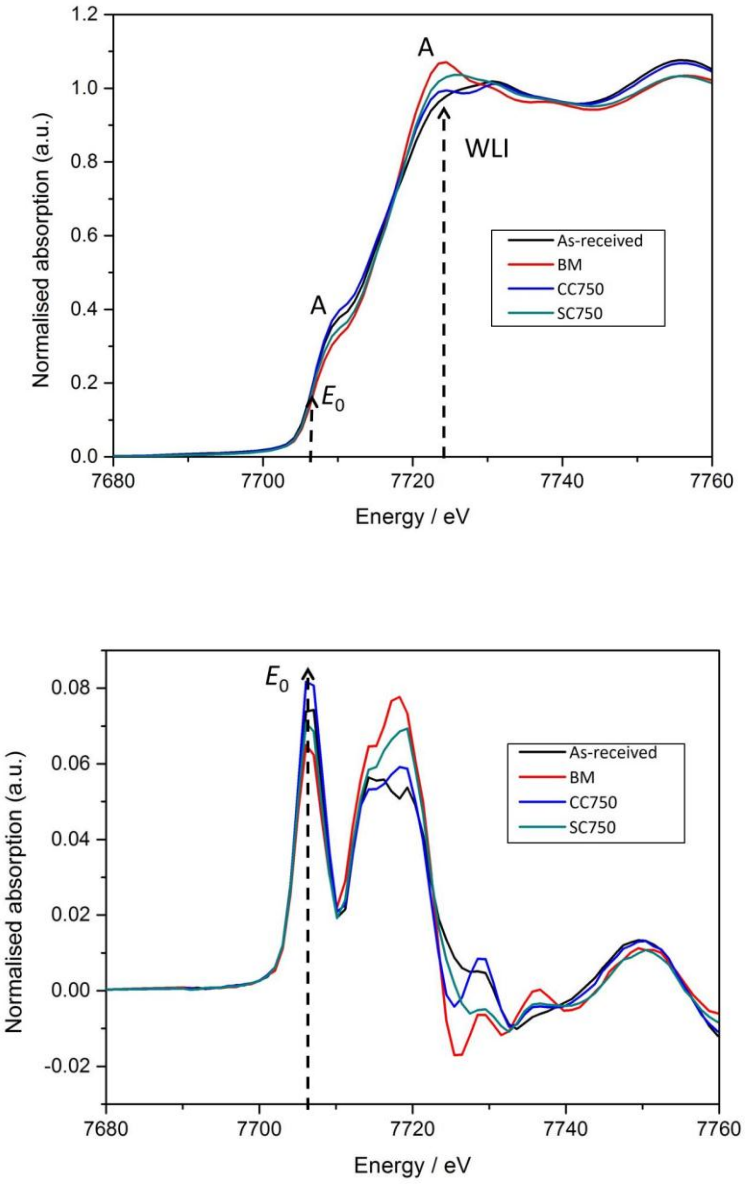

Figure 3-114. *(a) Normalised ex situ XANES μ(E) spectra for Co metal powder samples; as-received, BM, CC700 and SC700. E_0 is the threshold energy. 'WLI' denotes the white line intensity at the top of the main absorption edge. Features marked 'A' are assigned, in all samples, to the 1s → 4p transition. This prominence of the WLI in the metallic BM and SC700 XANES imply these samples have some oxidic component. Spectral features of the as-received and CC700 samples are purely metallic on the other hand. (b) Derivative XANES μ(E)spectra for Co metal powder samples. The position of E_0, taken as the maximum in the derivative, is displayed.*

Table 3-5. *Edge energies (E_0) and white line intensities (WLI) for various Co powder samples.*

Sample	E_0 (eV)	WLI (a.u.)
As-received	7706.6	1.01
BM	7706.5	1.07
CC700	7706.6	0.99
SC700	7706.5	1.04

The main differences in the XANES between metallic samples are observed in the lineshapes at the rising edge maxima; the white lines (WLI). Figure 3-12 indicates the positions of E_0 and the WLI. One such feature is a broad lineshape like that seen in the as-received sample (red). The other is a doublet in this region, a 'double–hump', similar to that seen in the CC700 sample (green). The nature of the singlet and doublet white lines is thought to originate from HCP and FCC structures where, with increasing energy, the photoelectron experiences longer range electronic effects that are manifested in the XANES region[41]. The XANES regions are strongly influenced by multiple-scattering phenomena which would explain the differences between FCC and HCP structures. These processes are not fully understood however and detailed XANES analysis to support this is beyond the scope of this investigation.

The BM and SC700 XANES spectra display increased white line intensities in comparison to the as-received and CC700 samples thus suggesting some non-metallic like character in the samples. In addition to electronic effects, XANES lineshapes are influenced by the local coordination geometry surrounding the absorbing atom, i.e. ligand effects [42-45]. The white line is most prominent in the BM sample and is intensified by the presence of coordinating ligands such as oxygen. This occurs when the oxygen *p* orbitals are brought closer to the metal *p* orbitals and this increases the probability of the dipole allowed $1s \rightarrow 4p$ transition. Based on these diagnostic spectral features it is very likely that the SC700 and BM samples

have undergone partial oxidation. The edge positions between the samples vary by 0.2 eV (within error limits) and thus oxidation cannot be quantified using the edge positions. This would, accordingly, suggest a very small oxidic component in BM and SC700 samples.

3.5.4.2 EXAFS

EXAFS parameters including bond distances and Debye-Waller factors and the phase composition were derived from curve fitting analysis using *ex situ* Co K-edge EXAFS data. The multi–cluster methodology was implemented with EXAFS data in order to determine the Co HCP/FCC phase composition in various cobalt metal powders and the results are evaluated herein.

The calculated k^3-weighted $\chi(k)$ spectra and the associated Fourier transforms (phase shift uncorrected) for Co HCP and FCC structures are shown in Figure 3-13. The differences between structures are apparent when inspecting the Fourier transforms (FT) of the EXAFS above *ca*. 3.5 Å. The different amplitudes of the peaks between the two structures arise from the difference in number, degeneracy and distance of the HCP and FCC scattering paths in this region.

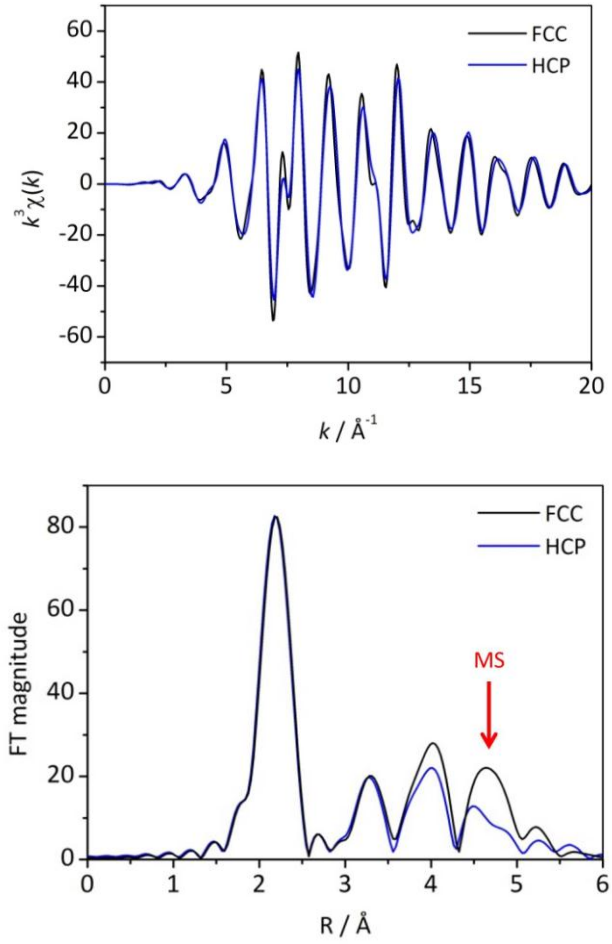

Figure 3-125. *Calculated EXAFS (above) and the associated Fourier transforms (below) for Co HCP and FCC structures (FT range 2-15 Å^{-1}). Multiple-scattering effects originate at higher coordination shells and are more intense in the FCC structure which accounts for the enhanced intensity of the fourth peak in the FT.*

Both Co structures exhibit multiple-scattering phenomena at higher coordination shells, i.e. beyond the second, which gives rise to higher than expected peak amplitudes. These multiple-scattering effects are particularly strong in FCC, where the fourth peak is more intense due to the collinear scattering geometry having a strong focusing effect[46]. Figure 3-14 graphically depicts the strong multiple-scattering effects in the FCC structure. This effect is more pronounced in the FCC cluster than the HCP cluster as indicated by a greater enhancement in intensity of the fourth peak corresponding to a distance of 5.026 Å. There are several explanations for this: (1) The fourth nearest-neighbour distance is exactly twice the first shell

distance in FCC of 2.513 Å. This is depicted in Figure 3-6 where $r_4 = 2r_1$. In HCP, the first shell coordination, $N = 12$, is split so that there are six nearest neighbours at $R = 2.498$ Å and six at $R = 2.510$ Å (obtained from FEFF calculations using HCP crystal structure) which gives an average of 2.504 Å, marginally smaller than the FCC distance. As a result this alignment exists in the HCP (0001) basal plane but is all but lost in other planes whereas in FCC this effect is isotropic [47]. (2) There exists a much larger number of multiple-scattering paths in the HCP structure and this can result in phase cancellation in the EXAFS and thus the reduction in amplitude of some peaks in the Fourier transform.

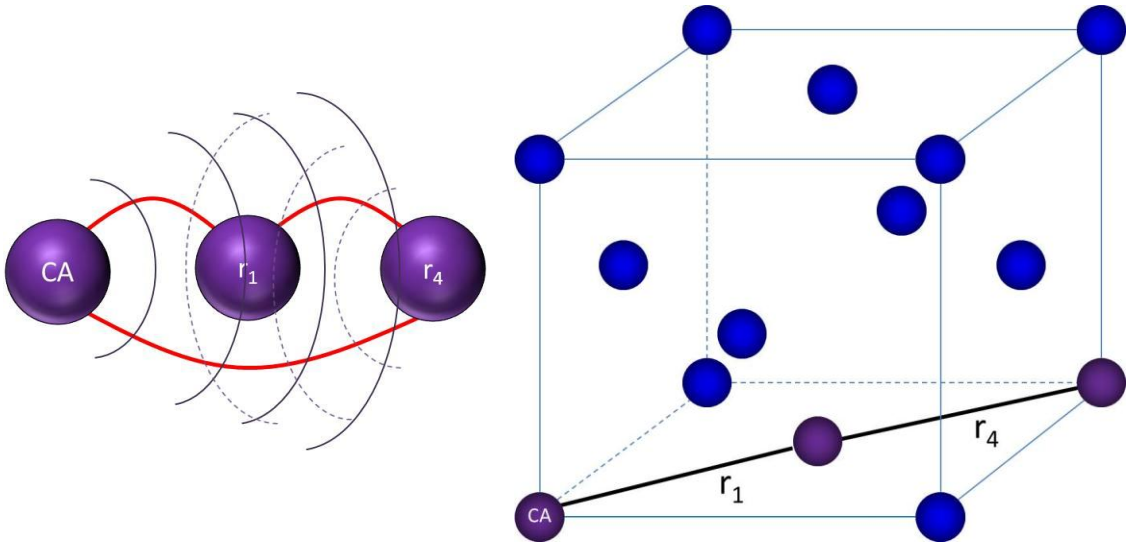

Figure 3-136. *The origin of multiple-scattering phenomena in the Co FCC structure. The collinear geometry of the first and fourth near-neighbour distances has a focusing effect (illustrated on left) which enhances the intensity of the fourth peak in the FT (see Figure 3-13).*

Figure 3-15 displays the best fit of the EXAFS and associated Fourier transforms from *ex situ* data of the as-received cobalt metal powder sample. These fits represent the attempt at modelling the data using Co HCP and FCC phases exclusively. The first peak corresponding to the Co─Co bond distance fits well to both models which are in accordance with equal first nearest-neighbour coordination number of 12 and

bond distance of *ca*. 2.50 Å in HCP and FCC structures (Table 3-1). In the 4 to 6 Å region, which encompasses the third and fifth coordination shell, single cluster models fail to adequately model the metallic system, in particular between 5 and 6 Å where there is largest mismatch between experiment and theory. These results are unsurprising since both HCP and FCC allotropes share identical local geometry, below 4 Å, and the structures are indistinguishable in this region. HCP and FCC structures can be resolved using EXAFS by analysing higher coordination shells. This is challenging, however, since coordination shells become progressively closer in distance and account for significant multiple-scattering effects.

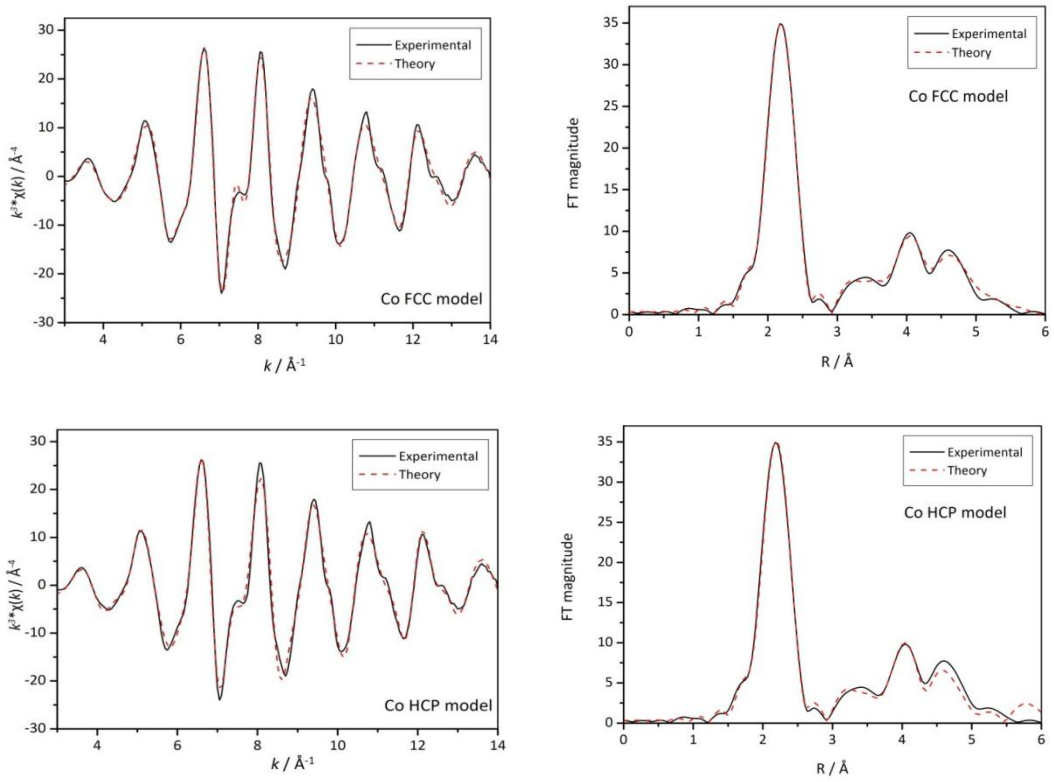

Figure 3-147. *Best fits of the EXAFS (left) and associated Fourier transforms (right) of as-received cobalt metal powder using single-cluster modelling of Co HCP and FCC phases. Fit R-factors of 0.0016 and 0.0009 are obtained using HCP and FCC models, respectively.*

Fitting the EXAFS data of the As-received, BM, SC700 and CC700 samples using multi–cluster models indicate an excellent agreement to the calculated structures.

The best fits of the EXAFS and FTs are displayed in Figure 3-16. Table 3-5 summarises the *R*-factors and reduced χ^2 values for the various models. The reduction in both reduced χ^2 and *R*-factor indicates, clearly, that the multi-cluster HCP/FCC model provides the best description of the data. All peaks in the FT are modelled well, even up to 6 Å, with just a slightly larger residual in the second peak, at *ca*. 3.4 Å, which displays a low intensity and broad amplitude in the Fourier transforms of all samples.

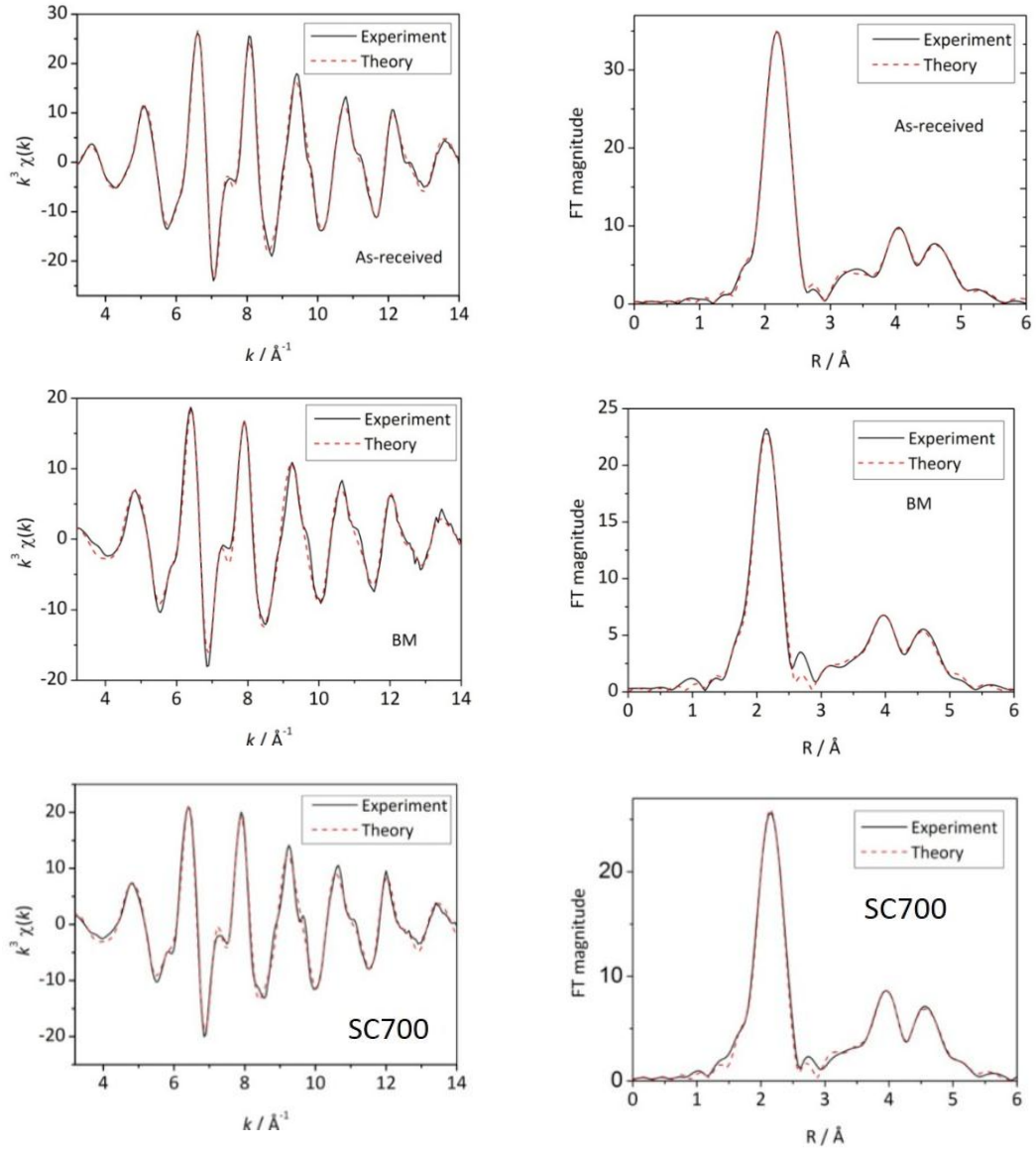

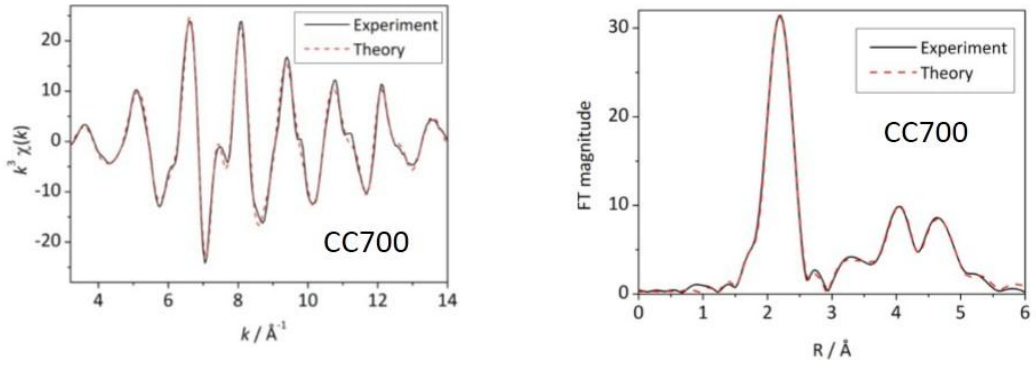

Figure 3-158. *Best fits of the EXAFS (left) and associated Fourier transforms (right) of ex situ Co K-edge EXAFS data of various cobalt metal powder samples using multi–cluster models. NB: FT data is uncorrected for phase shift. For all samples the HCP/FCC multi-cluster models yield a very good agreement with the data.*

Table 3-6. *Statistical summary of the models used for fitting of as-received cobalt metal powder.*

Model	**Reduced χ^2**	***R*-factor**
HCP	1223	0.0016
FCC	451	0.0009
HCP/FCC	165	0.0003

Results from the structural refinement of the *ex situ* EXAFS data are evaluated in Table 3-6. In general the parameterisation of the cluster models was kept the same for all samples with the exception of the BM sample in which the number of independent variables was adjusted from 17 to 15 to obtain the best fit. At higher-*R* where the distance between coordination shells becomes progressively smaller, the refined distances increase, as does the associated estimated uncertainties. EXAFS is a local structural probe and the exponentially damping amplitude terms from the inelastic losses and mean free path of the electron, in addition to the inverse *R* squared term, limit the R_{max} employed in the analysis. The accuracy with which EXAFS analysis can derive these distances at higher values of *R* is therefore

significantly reduced. The Debye–Waller factors increase on going from the first to the second shell then take relatively stable values ($\sigma^2 \approx 0.01$ Å^2) beyond the second shell. The parameterisation of the Debye-Waller factors was increased at higher distances to reflect the rigid structures in the cobalt systems. The uncertainties in the Debye-Waller factor do, however, increase due to the highly correlated amplitude terms and the limitations of the available data in *k*-space. The S_0^2 parameter for CC700 and SC700 samples was set to 0.67 and for the BM sample to 0.69. These values were obtained by fitting the EXAFS data prior to multi–cluster modelling, due to the absence of Co foil data, using the first shell only. This ensured the best fit was obtained when introducing amplitude mixing parameters into the refinement and fitting all *R*-space data with a cluster size of 6 Å.

A careful and detailed parameterisation of all the single and multiple-scattering paths in the multi–cluster models was essential in minimising the correlations between parameters and the resultant enlarged uncertainties. Varying the parameterisation can significantly affect the quality of the fit and the magnitude of *x* and *y* values. In the case of the SC700 and BM samples the best fit was obtained by parameterisation of the model that yield values of *x* and *y* that do not sum to one. This implies that there is some component of the EXAFS data that the model cannot account for and indeed, SC700 and BM samples show the greatest residua between the experimental and calculated data. Nevertheless fits of acceptable quality and physically meaningful values were obtained and the refined amplitude mixing parameters were normalised to obtain, quantitatively, the HCP and FCC phase composition. Fitting of the As-received and CC700 data result in *x* and *y* values that sum closely to one and have also been normalised with respect to each other to give the phase composition as a % by phase.

Table 3-7. *Refinement results from multi-cluster modelling of ex situ Co K-edge EXAFS data for various Co metal powder samples. The uncertainties on the first shell Debye-Waller factors are below 10%. Subsequent shell Debye-Waller factors range between 10 and 20 %.*

	As-received	**BM**	**CC700**	**SC700**
S_0^2 (set)	0.71	0.69	0.67	0.67
N_{ind}	34	34	34	34
N_{var}	17	15	17	17
ΔE_0 (eV)	7.12	-2.43	7.64	-2.79
k-range (Å^{-1})	3.2-12	3.2-12	3.2-12	3.2-12
HCP				
R_1	2.49±0.001	2.50±0.006	2.50±0.002	2.49±0.003
R_2	3.53±0.006	3.55±0.021	3.54±0.007	3.52±0.015
R_3	4.08±0.006	4.08±0.013	4.07±0.006	4.08±0.012
R_4	4.35±0.006	4.35±0.013	4.35±0.006	4.35±0.012
R_5	4.81±0.053	5.12±0.168	4.79±0.081	4.68±0.069
R_6	5.04±0.056	5.21±0.088	5.09±0.052	5.14±0.015
R_7	5.61±0.032	5.80±0.088	5.56±0.067	5.78±0.011
σ^2_1	0.006	0.007	0.006	0.006
σ^2_2	0.011	0.012	0.010	0.012
σ^2_3	0.009	0.011	0.009	0.010
σ^2_4	0.009	0.011	0.009	0.010
σ^2_5	0.009	0.011	0.009	0.008
σ^2_6	0.010	0.010	0.008	0.010
σ^2_7	0.010	0.010	0.008	0.010
FCC				
R_1	2.50±0.001	2.51±0.006	2.50±0.002	2.50±0.003
R_2	3.55±0.006	3.56±0.021	3.55±0.007	3.54±0.015
R_3	4.36±0.006	4.36±0.013	4.36±0.006	4.36±0.015
R_4	5.00±0.037	5.03±0.021	5.00±0.010	5.02±0.018
R_5	5.70±0.037	5.63±0.041	5.69±0.018	5.64±0.023
σ^2_1	0.006	0.007	0.006	0.006
σ^2_2	0.011	0.012	0.010	0.013

σ^2_3	0.009	0.011	0.009	0.010
σ^2_4	0.010	0.010	0.008	0.010
σ^2_5	0.010	0.010	0.008	0.010
x (HCP)	0.59±0.06	0.23±0.15	0.41±0.10	0.19±0.18
y (FCC)	0.44±0.06	0.59±0.15	0.56±0.10	0.69±0.18
R_{fit}	0.0003	0.0054	0.0007	0.0029

Figure 3-17 illustrates the Co HCP and FCC phase composition, reported as % phase fraction, for the various cobalt samples. The analysis indicates that the As-received sample comprises a reasonably equal mixed phase of 57 % HCP and 43 % FCC composition. The SC700 sample contains a more dominant FCC phase which suggests that after cooling in air, from above the transformation temperature, the reverse FCC to HCP transformation occurs, and *ca*. 20 % HCP is formed under these conditions. The CC700 sample shows a smaller component of the stable high temperature FCC phase, contrary to what is hypothesised since crash cooling should "lock in" the high temperature cubic phase, however less FCC is formed under these conditions than with the SC700 sample. This unexpected 20 % difference in FCC content between different cooling methods is potentially attributed to oxidation of the SC700 sample and the oxidic component is modelled by the cubic phase. This could explain why there is non-unity in summation of the amplitude mixing parameters and the larger fit residuum. The BM sample further exemplifies the potential oxide contamination of a metallic sample where the small peak at *ca*. 2.7 Å in the k^3-weighted FT is observed. A second shell distance belonging to Co^{2+}─Co^{2+} (oxide) could conceivably appear at *ca*. 2.7 Å as proposed in Figure 3-18. The prominent sidelobes at the right side of the main peak, however, impede the identification of low-*Z* scatteres, such as O, using different *k*-weighted FTs due to the behaviour of Co phase shift function and back-scattering amplitude. The diagnostic white line intensity in the XANES (Figure 3-12), however, is supportive evidence for oxygenated species. The phase composition of the BM sample obtained from EXAFS analysis is 72 % FCC and 28 % HCP. Due to the potential partial oxidation of the BM sample, the FCC phase component of *ca*. 70 % is likely to be an overestimation. The incorporation of bulk oxide phases into the multi–cluster models for both BM and SC700 EXAFS data analysis was attempted but was

unsuccessful in capturing oxygenated species and therefore it is our belief that some surface oxide species lacking long-range order are formed which exhibit a Co─O bond length that deviates from that in the bulk.

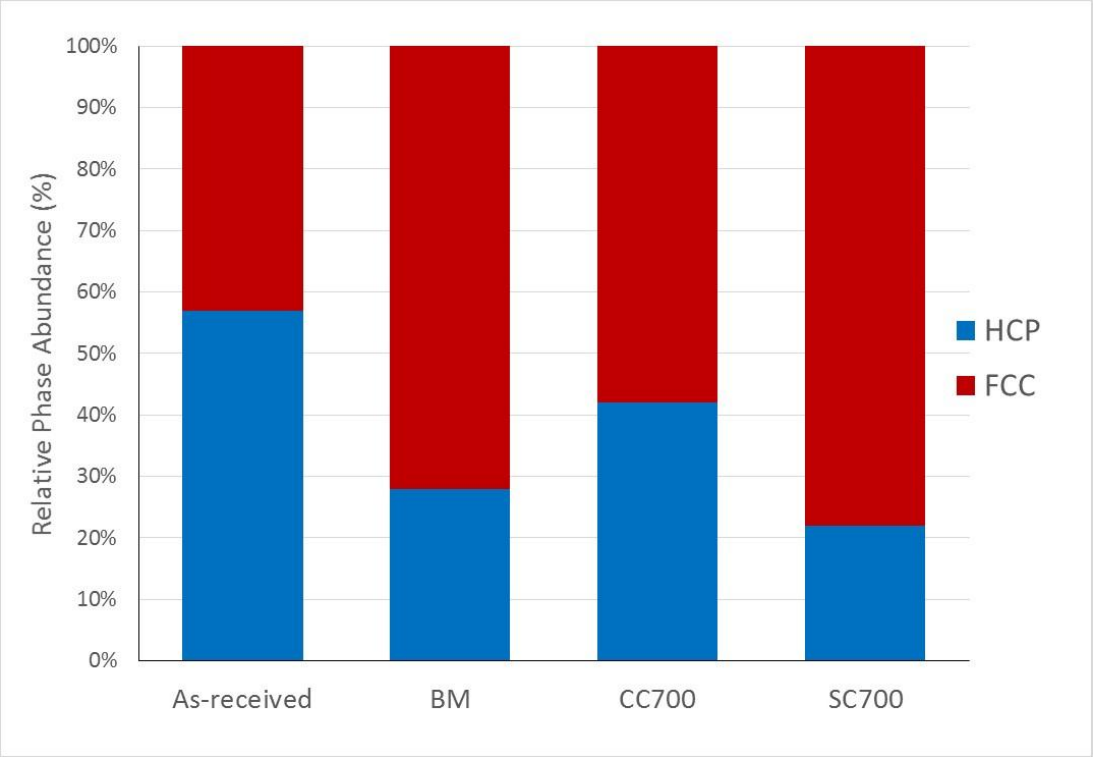

Figure 3-169. *Co phase composition in various Co samples as HCP/FCC fraction. Results were obtained from Co K-edge EXAFS analysis using multi – cluster models. The errors from least squares fitting are as follows: As-received ±6%, BM ±18%, CC700 ±10% and SC700 ±20%.*

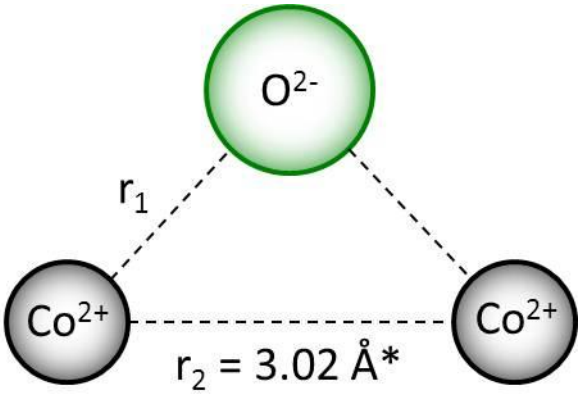

Figure 3-20. *Potential origin of the small peak at ca. 2.7 Å in the FT (phase shift uncorrected) of the BM sample attributed to oxide contamination. The oxidic species we propose lacks sufficient long-range order to be detected from EXAFS analysis where crystallographic data is required by the program. A surface oxide species is likely to exist in small amounts, which does not have bulk characteristics, and which is why the second shell distance, r_2, from Co scattering, is detected only.*2.7Å plus phase shift.*

3.5.5 *In situ* XRD/XAS of Co metal powder

3.5.5.1 X-ray Diffraction

The *in situ* X-ray diffraction patterns obtained from the heating of the As-received cobalt metal powder with sequential XRD/XAS measurements are shown in Figure 3-19. The broad peaks in the XRD pattern that do not belong to metallic Co HCP and FCC phases originate from γ-Al_2O_3 (diluent). The reflections belonging to both HCP and FCC phases, in the 2θ range 32 to 44°, are highlighted. The peak at *ca*. 35° 2θ is an overlap of the HCP (002) and FCC (111) reflections, which gains in intensity between 444 °C and 561 °C. The emergence of peak at ca. 41° 2θ, belonging to the FCC (022) reflection, and the decrease in intensity of diffraction peaks at *ca*. 33° and 37.5° 2θ, belonging to HCP (010) and HCP (011) reflections respectively, also occur over this temperature regime. *In situ* XRD indicates, therefore, that the HCP to FCC phase transformation is kinetically hindered, proceeding between 444 and 561 °C. Moreover XRD highlights the inability to fully

resolve the Co HCP and FCC structures due to the overlapping reflections from HCP, FCC and γ-Al_2O_3 phases and the need for further characterisations techniques to fully characterise this mixed phase system.

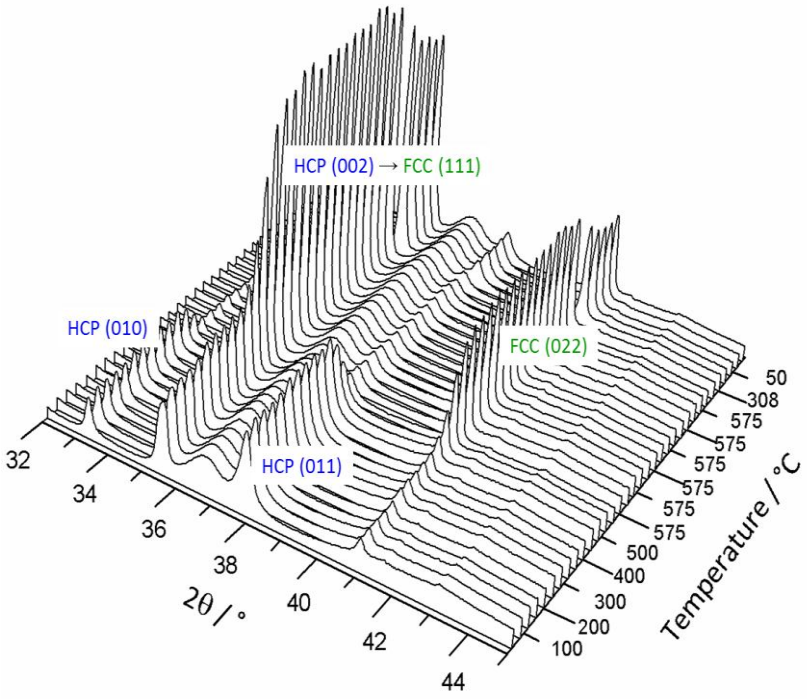

Figure 3-21. *In situ X-ray diffraction patterns obtained from heating and cooling of as-received Co metal powder. Reflections belonging to Co HCP and FCC phases are labelled. Additional broad peaks originate from γ-Al_2O_3.*

3.5.5.2 XANES analysis

The XANES spectra obtained from *in situ* Co K-edge measurements on cobalt metal powder as a function of temperature are plotted over the energy range 7680 to 7790 eV in Figure 3-20. From inspection of these plots it is evident that cobalt remains in the reduced state as indicated by the position in energy of the rising absorption edge, at 7713 eV, and the shoulder located at the mid-point of the edge which confirm the Co^0 state. These features remain static upon heating and cooling. As previously observed in our study on the *ex situ* Co K-edge XANES, the formation of a 'double-

hump' at the white line is apparent (Figure 3-20 inset). This spectral feature begins at around 522 °C and persists up to the final scan at room temperature, after cooling, and is a phenomenological effect of the HCP to FCC allotropic phase transformation, which occurs in this temperature regime. Temperature effects in the near-edge region of the absorption spectrum are rarely, if at all, a consideration in XANES fingerprinting.

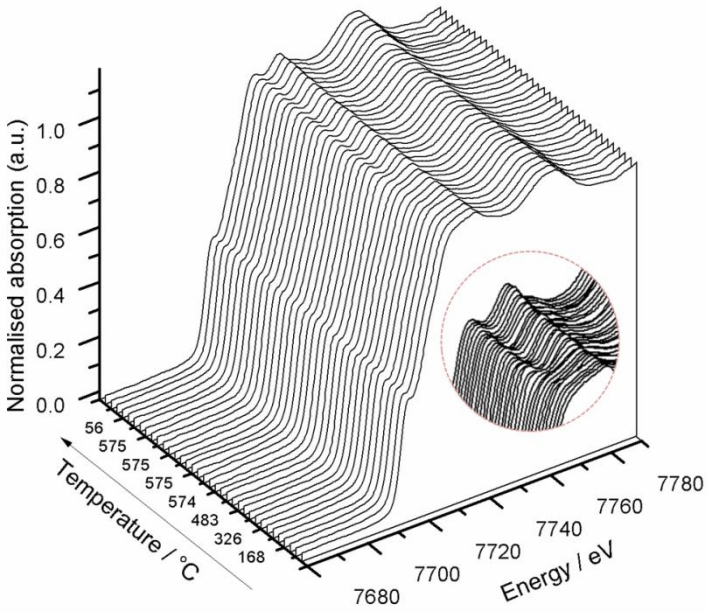

Figure 3-22. *In situ XANES plots from the heating to 575 °C and cooling to room temperature of as-received Co metal powder. Inset shows the formation of a double-hump at the top of the rising edge, with onset at ca. 522 °C.*

3.5.5.3 EXAFS analysis

The multi–cluster models developed and optimised using *ex situ* Co K-edge EXAFS data were implemented for the *in situ* Co K-edge QuickEXAFS data of cobalt metal powder to elucidate the cobalt phase composition and its phase transformation. Analysis was performed in order to extract detailed structural information including Debye–Waller factors and bond distances and in particular to see how the phase composition varies with temperature through refinement of the amplitude mixing parameters.

It is noteworthy that, at higher temperatures, the data contain a higher level of noise. The increase in thermal motion is modelled by the Debye–Waller factor however the lower signal-to-noise ratio at high temperatures is detrimental by shortening the useable data in *k*-space in the analysis. Indeed this is one of the major drawbacks of the EXAFS technique in that the information extracted from analysis is limited by the available data: a shortened *k*-range reduces N_{var}. The multi-cluster model has a high degree of parameterisation and for these reasons a terminating k_{max} of 10.5 $Å^{-1}$ was selected for the analyses. Some data sets measured at higher temperature (isothermally after 80, 92 and 96 minutes) contained considerable noise at high-*k* and resulted in instabilities in the refinement. For these reasons they have been excluded in the reported data analysis.

Figure 3-21 is the plot of the *in situ* k^2-weighted Fourier transform data (phase shift uncorrected) from heating of the as-received Co metal powder up to 575 ^{0}C and subsequent cooling to room temperature. The amplitude of the peaks in the Fourier transform are attenuated by the thermal disorder component the Debye–Waller factor, as can be seen by the decrease in amplitude of the first shell peak, with increasing temperature and its restoration upon cooling to room temperature. The position of the first peak, at *ca*. 2.15 Å, in the Fourier transform remains unchanged and corresponds to the first Co─Co coordination shell, i.e. the metallic Co—Co bond distance. The Co—Co coordination number is 12 for FCC and HCP structures, therefore any variation in the peak amplitudes is solely due to thermal effects.

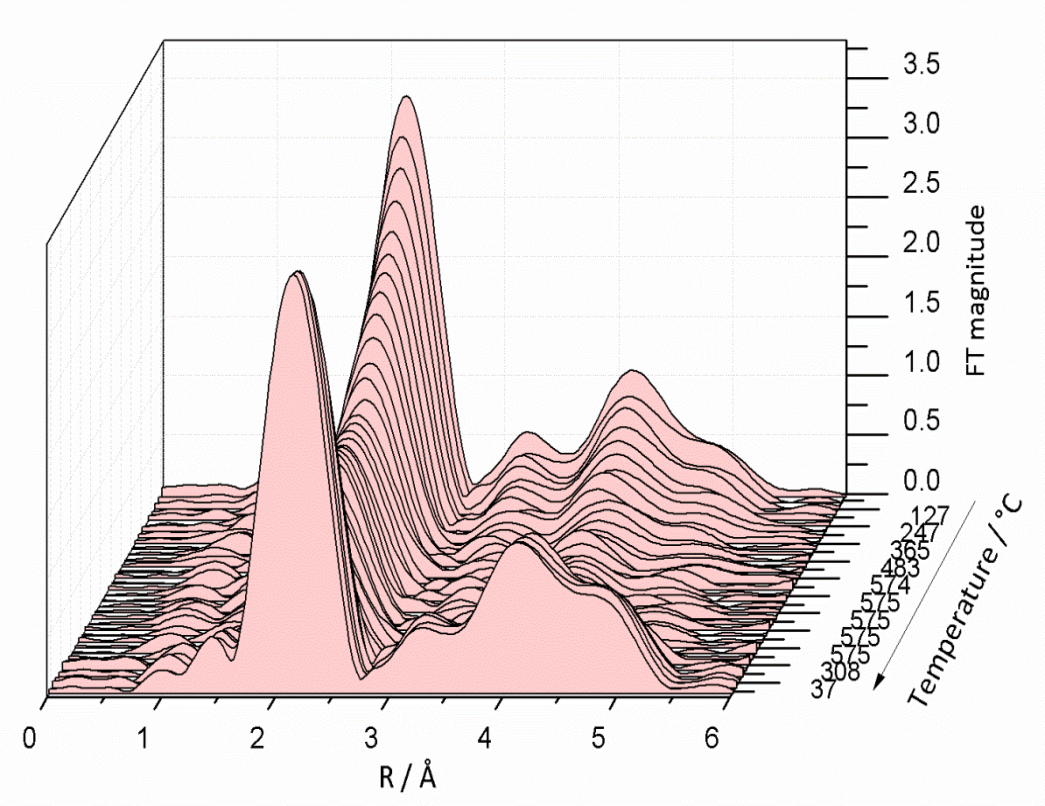

Figure 3-173. *In situ Co K-edge EXAFS Fourier transform spectra (k^2-weighted) from heating to 575 °C and cooling to room temperature of as-received cobalt metal powder.*

The results of the refinement of the HCP and FCC Co─Co bond distances, as a function of temperature, are represented in Figure 3-22. The values range between 2.475 and 2.510 Å, with the exception of an outlier at 84 min, and are consistent with crystallographic data. HCP and FCC lattice expansion with increasing temperature is expected to take place however there is no supporting evidence for this from the EXAFS derived bond distances. This is a common phenomenon in EXAFS at elevated temperatures where a Gaussian function for peak fitting is inappropriate due to the anharmonic behaviour arising from the vibrations of atom pairs exhibiting an asymmetric distribution of bond lengths[48]. The first shell Debye–Waller factors are plotted in Figure 3-22 and display a strong positive correlation with temperature. This is due to the increase in thermal vibrations of the atoms in the first coordination shell generating a greater mean square displacement of bond distances. There is some variation in the Debye-Waller factor between 60 and 116 min. and this is attributed to changes in static disorder in the cobalt system,

since the measurements are under isothermal conditions there should be little change in thermal contributions. The agreement (*R*) factors of each fit are plot in Figure 3-22 and are, in general, low. This clearly indicates a good agreement between the measured and calculated EXAFS data and thus the successful implementation of the multi–cluster models with QuickEXAFS data on the cobalt metal powder system. Representative best fits of *in situ* EXAFS data and the associated FTs are displayed in Figure 3-23.

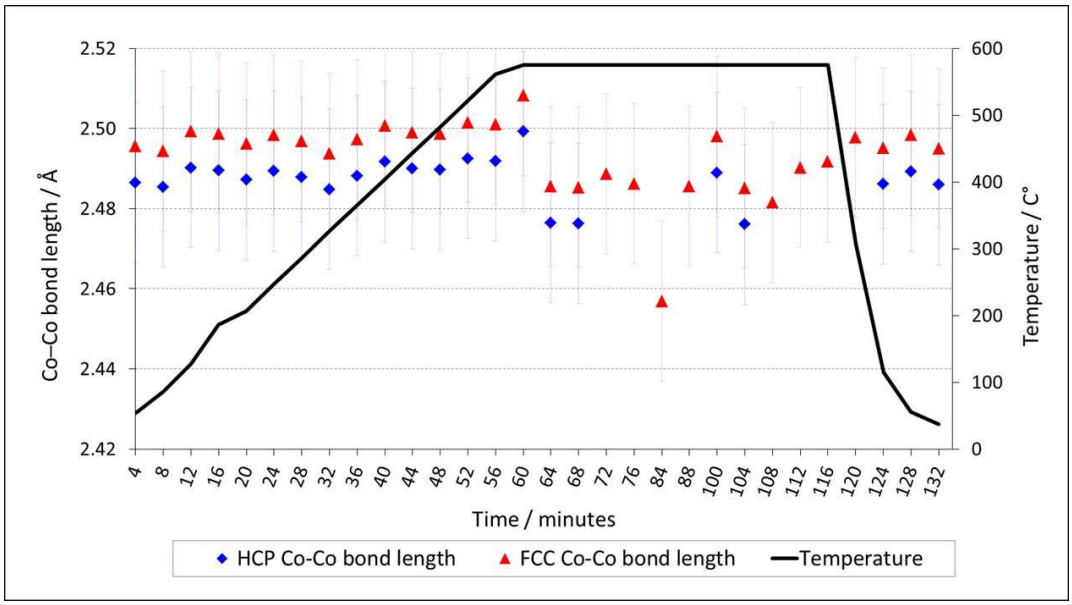

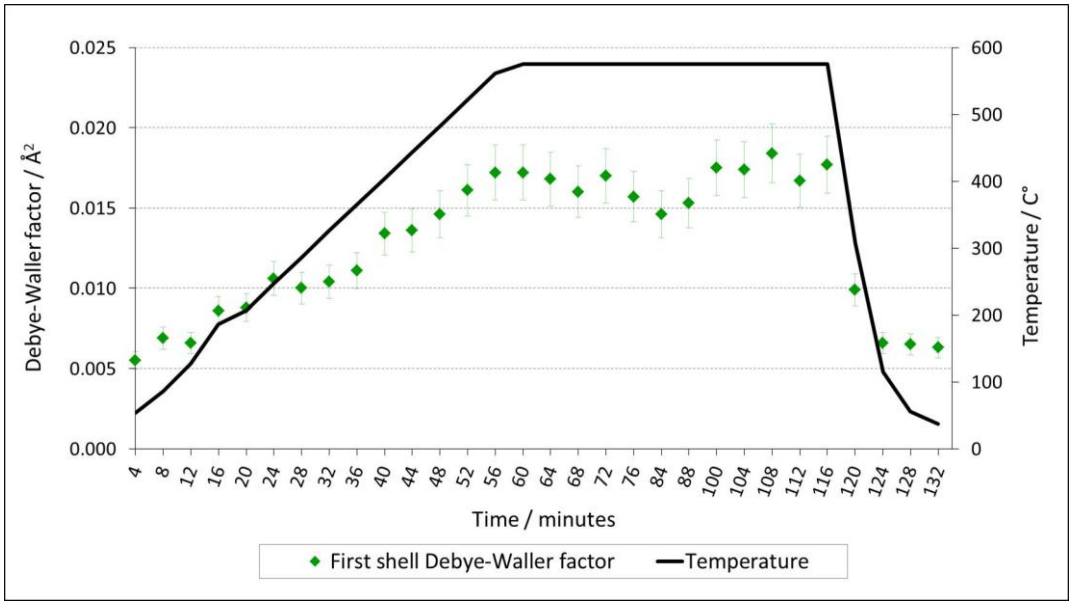

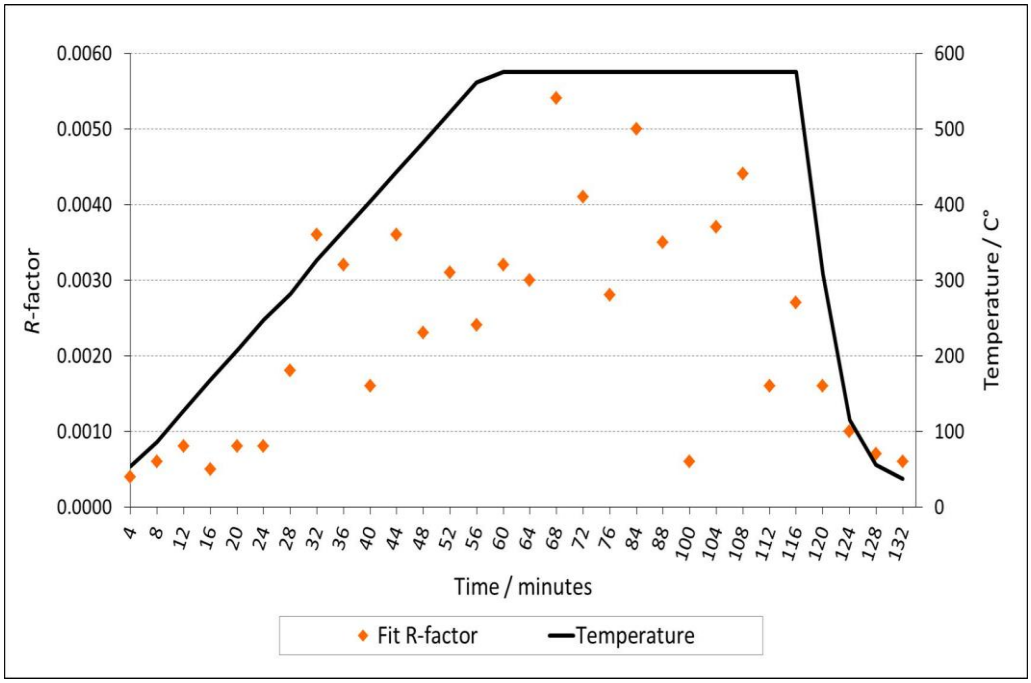

Figure 3-184. *The variation of Co—Co bond lengths (above), first shell Debye – Waller factors (middle) and fit R-factors (below) with temperature from EXAFS analysis of in situ Co K-edge EXAFS data using multi-cluster models.*

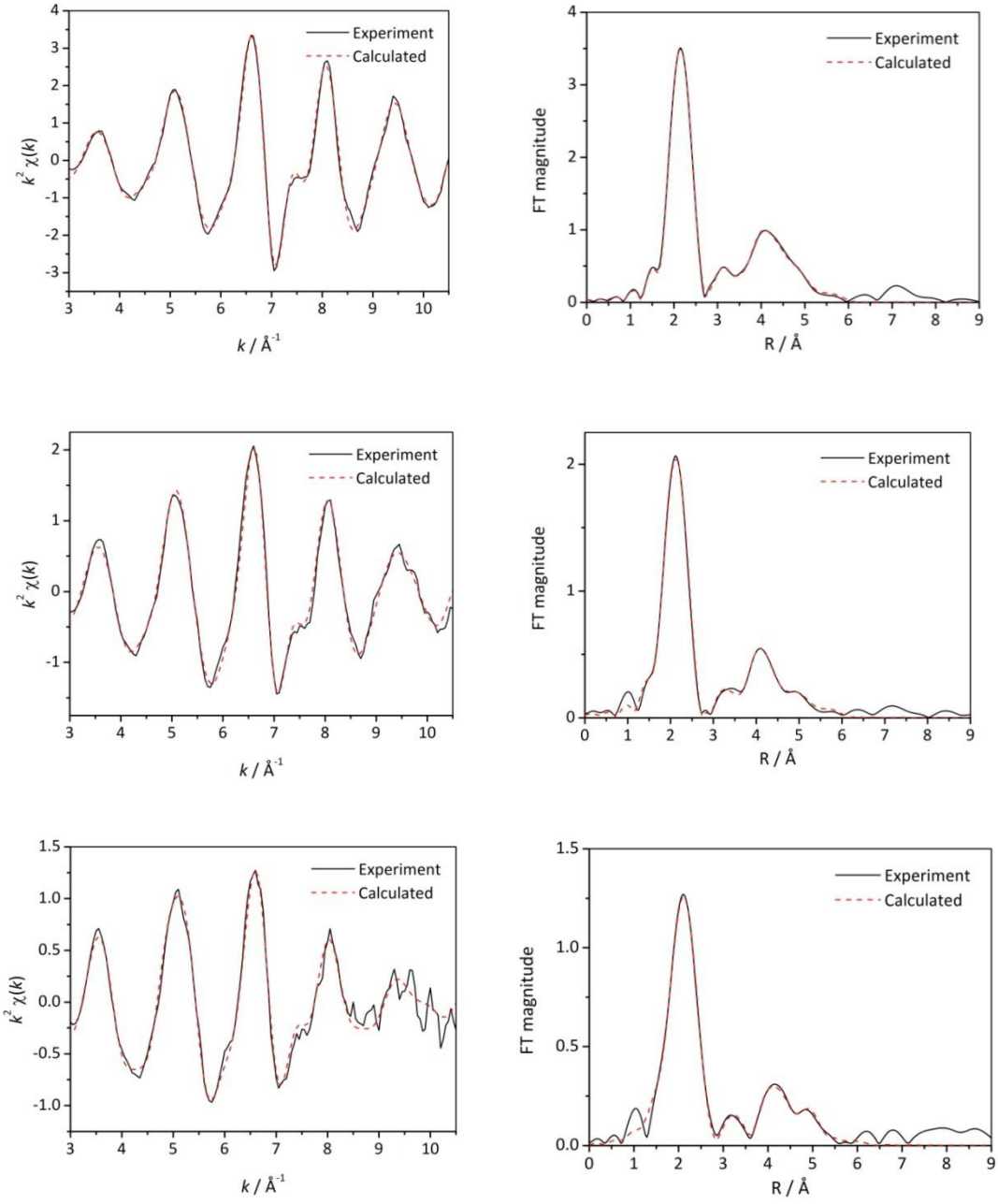

Figure 3-195. *Representative best fits obtained from multi-cluster modelling of k^2-weighted Co K-edge in situ EXAFS data (left) and associated FTs (right) measured at 54 °C (top), 326 °C (middle) and the final scan at 575 °C (bottom).*

The refinement of the amplitude mixing parameters for HCP and FCC clusters yield, quantitatively, the Co phase composition and this is represented for *in situ* Co data as a function of temperature in Figure 3-24. The analyses clearly indicate the metallic sample comprises a mixed HCP/FCC phase in the starting material and a mixed phase exists with heating up to 575 °C. The HCP phase is the more dominant phase, although the results do show that in modelling of some of the data between 54 and 575 °C FCC is more dominant. This is due to some instability of the refinements due to the data quality and not any structural effects. The HCP content falls dramatically in the third scan at 575 °C, corresponding to a time interval of 240 seconds between scans. An almost pure FCC phase is detected in the subsequent scan at 575 °C (some HCP is captured in the analysis however this falls within experimental uncertainty) thus elucidating the HCP to FCC transformation. This implies that the transformation is complete and takes place quickly with respect to the timescale of the measurements. Proceeding isothermal scans, with some exceptions due to refinement instabilities, display a single FCC phase. The data upon cooling suggest there is hysteresis in the FCC to HCP transformation *via* the reappearance of the HCP phase in the measured data at 115 °C. At room temperature, unlike prior to the ramping, the structural composition contains a more dominant FCC phase.

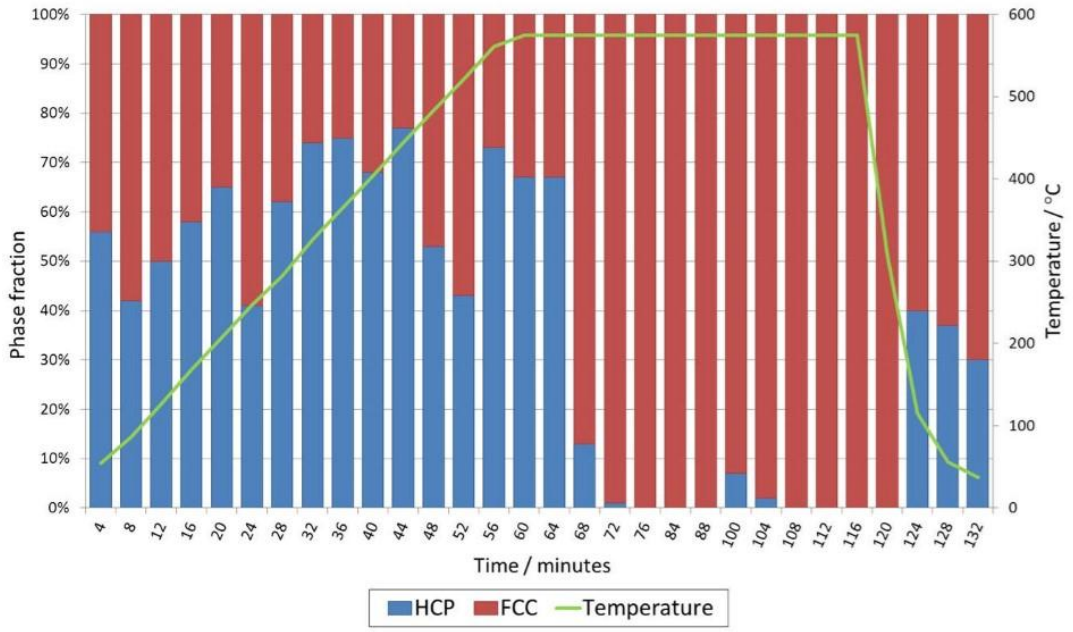

Figure 3-206. *Phase composition analysis. Results show the Co HCP/FCC phase fraction within the Co metal powder determined using multi–cluster modelling of in situ Co K-edge EXAFS data. EXAFS data measured after 80, 92 and 96 minutes (under isothermal conditions) have been excluded due to instabilities in the fitting routine.*

3.6 Conclusion

Previously, the phase composition of metallic Co powders had been investigated using techniques including NMR and XRD probing the short-range and average long-range structures, respectively[16]. These laboratory based techniques have encountered difficulties in characterising this type of system due to faulted regions such as phase boundaries, that can be XRD amorphous, and small particle sizes, that can be 'silent' to the NMR signal. Furthermore discrepancies between the results obtained from these techniques that were performed *ex situ,* highlighted the need for more in depth structural studies. This investigation has successfully addressed some of the issues surrounding the characterisation of a mixed phase model Co Fischer–Tropsch system through extending structural studies to the medium-range ordering using high resolution techniques at synchrotron sources. XAS and PDF techniques circumvent problematic issues encountered by conventional characterisation techniques including small particle sizes and disordered regions, as is crucial to their growing practical application. Although addressing the inherent localised disorder, arising from stacking faults and phase boundaries, has not been the focus of this study (this would warrant future work), detailed structural information on HCP and FCC structures in a variety of Co metal powders has been garnered, for the first time, through application of these techniques.

For pure metallic cobalt samples these proved to be robust models for modelling *ex situ* data, where the use of single clusters to model PDF and EXAFS data were inadequate. From PDF, excellent agreement was obtained in modelling some of the experimental data. In some cases sample oxidation hindered the characterisation of the metallic species and oxidic components could not be accounted for in the model, most likely through formation of non-bulk like surface species. Attempts were also made to include additional phases; at present this was unsuccessful and so the analysis was constrained to using biphasic models. When the PDF fits were of good quality, the uncertainties on the phase scale parameters, which measure phase composition, were low. Rietveld analysis of *ex situ* diffraction data also provided a quantitative measure of phase composition in some Co metal powders. In general, the results were in good agreement with those obtained from PDF multi-cluster

modelling. Thus, improving the reliability of results obtained from using PDF multi-cluster models. These results also suggested that some additional oxidic phases may be present. Interpretation of e*x situ* XANES spectra also highlighted oxide contamination in some of the Co samples, supporting the results from EXAFS multi–cluster modelling (*via* lower *R* factors). Good agreement with experimental data was obtained elsewhere using HCP/FCC multi-cluster models which required a high degree of parameterisation to reduce the number of variables in the fitting and correlations between them. The magnitude of the uncertainties in the coordination number, *N*, derived from EXAFS analysis, is comparable to those obtained in deriving the HCP/FCC phase composition.

The multi–cluster methodology was further developed by implementing with *in situ* EXAFS and PDF data with the aim of tracking the HCP to FCC phase transformation as a function of temperature. PDF, in this instance, is a more accurate tool for following the transformation because the number of refineable parameters in EXAFS analysis is limited by the available data in *k*- and *R*- space. Modelling the EXAFS with temperature resolved data showed encouraging results in the first study of its kind however the available *k*-space data was restricted at higher temperatures due to lower S/N ratios and where peak broadening in the Fourier transforms limits the information content of the data, thus affecting the interpretation of Co phase composition over the transformation. Minimising the number of parameters that are refined in multi-cluster models and the correlations between them has proved to be crucial to obtain reliable results. Amplitude mixing parameters in EXAFS modelling can vary significantly and are very sensitive to the parameterisation of the model. PDF gives potentially more reliable results due to the far greater available data in *r*-space and absence of multiple-scattering effects which seem to dominate the EXAFS when analysing cluster sizes extending up to 6 Å

Through the development of analytical methodologies in this work, as applied to a model catalytic system, the characterisation of multi-component phases, irrespective of local distortions or long range disorder, has been demonstrated successfully. Importantly, quantitative information on phase composition and transformation has

been garnered through development of multi–cluster modelling methodologies. This is particularly challenging for EXAFS data where analysis is routinely restricted to the first few coordination shells.

Future possibilities could see structural studies on Co powders by a combined PDF/XAS technique. This would be much preferable over employing each technique separately as any environmental, sample or beamline fluctuations that may arise performing spectroscopic and scattering studies individually may be eliminated. This combined setup is currently not available however advancements in synchrotron technology may soon enable this setup to be achieved. Furthermore, a combined PDF and EXAFS analysis approach is already available using RMC modelling although currently understanding phase transformation behaviour has not been implemented.

3.7 References

[1] Khodakov, A. Y.; Chu, W.; Fongarland, P., *Chemical Reviews*, (2007) **107**, 1692.

[2] Khodakov, A. Y., *Catalysis Today*, (2009) **144**, 251.

[3] Wang, Z. J.; Yan, Z.; Liu, C. J.; Goodman, D. W., *Chemcatchem*, (2011) **3**, 551.

[4] Barakat, N. A. M.; Kim, B.; Park, S. J.; Jo, Y.; Jung, M.-H.; Kim, H. Y., *Journal of Materials Chemistry*, (2009) **19**, 7371.

[5] Suryanarayana, C.; Norton, M. G., Lattices and Crystal Structures, In *X-Ray Diffraction*, Springer US: (1998); pp 21.

[6] Bidaux, J. E.; Schaller, R.; Benoit, W., *Acta Metallurgica*, (1989) **37**, 803.

[7] Ducreux, O.; Rebours, B.; Lynch, J.; Roy-Auberger, M.; Bazin, D., *Oil & Gas Science and Technology-Revue de l'IFP Energies Nouvelles*, (2009) **64**, 49.

[8] Edalati, K.; Toh, S.; Arita, M.; Watanabe, M.; Horita, Z., *Applied Physics Letters*, (2013) **102**,

[9] Pun, G. P. P.; Mishin, Y., *Physical Review B*, (2012) **86**,

[10] Guillermet, A. F., *International Journal of Thermophysics*, (1987) **8**, 481.

[11] Yoo, C. S.; Soderlind, P.; Cynn, H., *Journal of Physics-Condensed Matter*, (1998) **10**, L311.

[12] Houska, C. R.; Averbach, B. L.; Cohen, M., *Acta Metallurgica*, (1960) **8**, 81.

[13] Betteridge, W., *Progress in Materials Science*, (1979) **24**, 51.

[14] Zhang, Y. Q.; Jacobs, G.; Sparks, D. E.; Dry, M. E.; Davis, B. H., *Catalysis Today*, (2002) **71**, 411.

[15] Basinski, Z. S.; Christian, J. W., *Philosophical Magazine Series 7*, (1953) **44**, 791.

[16] Speight, R.; Wong, A.; Ellis, P.; Bishop, P. T.; Hyde, T. I.; Bastow, T. J.; Smith, M. E., *Physical Review B*, (2009) **79**,

[17] Sadeqzadeh, M.; Karaca, H.; Safonova, O. V.; Fongarland, P.; Chambrey, S.; Roussel, P.; Griboval-Constant, A.; Lacroix, M.; Curulla-Ferre, D.; Luck, F.; Khodakov, A. Y., *Catalysis Today*, (2011) **164**, 62.

[18] Enache, D. I.; Rebours, B.; Roy-Auberger, M.; Revel, R., *Journal of Catalysis*, (2002) **205**, 346.

[19] Dry, M. E., *Catalysis Today*, (2002) **71**, 227.

[20] Schulz, H., *Applied Catalysis A: General*, (1999) **186**, 3.

[21] Moodley, D. J.; van de Loosdrecht, J.; Saib, A. M.; Overett, M. J.; Datye, A. K.; Niemantsverdriet, J. W., *Applied Catalysis A-General*, (2009) **354**, 102.

[22] Rochet, A.; Moizan, V.; Diehl, F.; Pichon, C.; Briois, V., *Catalysis Today*, (2013) **205**, 94.

[23] Rochet, A.; Moizan, V.; Pichon, C.; Diehl, F.; Berliet, A.; Briois, V., *Catalysis Today*, (2011) **171**, 186.

[24] Karaca, H.; Safonova, O. V.; Chambrey, S.; Fongarland, P.; Roussel, P.; Griboval-Constant, A.; Lacroix, M.; Khodakov, A. Y., *Journal of Catalysis*, (2011) **277**, 14.

[25] Moodley, D. J.; Saib, A. M.; van de Loosdrecht, J.; Welker-Nieuwoudt, C. A.; Sigwebela, B. H.; Niemantsverdriet, J. W., *Catalysis Today*, (2011) **171**, 192.

[26] Toledano, P.; Krexner, G.; Prem, M.; Weber, H. P.; Dmitriev, V. P., *Physical Review B*, (2001) **64**,

[27] Frey, F.; Boysen, H., *Acta Crystallographica Section A*, (1981) **37**, 819.

[28] Song, Y.; Modrow, H.; Henry, L. L.; Saw, C. K.; Doomes, E. E.; Palshin, V.; Hormes, J.; Kumar, C. S. S. R., *Chemistry of Materials*, (2006) **18**, 2817.

[29] Cheng, G.; Carter, J. D.; Guo, T., *Chemical Physics Letters*, (2004) **400**, 122.

[30] Lefevre, P.; Chandesris, D.; Magnan, H.; Heckmann, O., *Journal De Physique IV*, (1994) **4**, 159.

[31] Rodriquez, A. F.; Sobal, N. S.; Wiedwald, U.; Spasova, M.; Hilgendorff, M.; Giersig, M.; Farle, M.; Arvanitis, D., *Journal of Magnetism and Magnetic Materials*, (2004) **272**, E1207.

[32] Kuehn, T.-J.; Caliebe, W.; Matoussevitch, N.; Boennemann, H.; Hormes, J., *Applied Organometallic Chemistry*, (2011) **25**, 577.

[33] Sprouster, D. J.; Giulian, R.; Schnohr, C. S.; Araujo, L. L.; Kluth, P.; Byrne, A. P.; Foran, G. J.; Johannessen, B.; Ridgway, M. C., *Physical Review B*, (2009) **80**,

[34] Speight, R.; Wong, A.; Ellis, P.; Hyde, T.; Bishop, P. T.; Smith, M. E., *Solid State Nuclear Magnetic Resonance*, (2009) **35**, 67.

[35] Farrow, C. L.; Juhas, P.; Liu, J. W.; Bryndin, D.; Bozin, E. S.; Bloch, J.; Proffen, T.; Billinge, S. J. L., *Journal of Physics-Condensed Matter*, (2007) **19**,

[36] Ravel, B.; Newville, M., *Journal of Synchrotron Radiation*, (2005) **12**, 537.

[37] Budrovic, Z.; Van Swygenhoven, H.; Derlet, P. M.; Van Petegem, S.; Schmitt, B., *Science*, (2004) **304**, 273.

[38] Jiang, H.; Ruhle, M.; Lavernia, E., *Journal of Materials. Research*, (1999) **14**, 549.

[39] Louidi, S.; Bentayeb, F. Z.; Tebib, W.; Sunol, J. J.; Escoda, L.; Mercier, A. M., *Materials Chemistry and Physics*, (2012) **132**, 761.

[40] Yoon, W. S.; Lee, K. K.; Kim, K. B., *Journal of the Electrochemical Society*, (2000) **147**, 2023.

[41] Bianconi, A., *Applied Surface Science*, (1980) **6**, 392.

[42] Colpas, G. J.; Maroney, M. J.; Bagyinka, C.; Kumar, M.; Willis, W. S.; Suib, S. L.; Mascharak, P. K.; Baidya, N., *Inorganic Chemistry*, (1991) **30**, 920.

[43] Koyama, Y.; Arai, H.; Ogumi, Z.; Tanaka, I.; Uchimoto, Y., *Physical Review B*, (2012) **85**, 075129.

[44] Antolini, E.; Salgado, J. R. C.; Giz, M. J.; Gonzalez, E. R., *International Journal of Hydrogen Energy*, (2005) **30**, 1213.

[45] de Groot, F. M. F., XANES spectra of transition metal compounds, In *14th International Conference on X-Ray Absorption Fine Structure*, DiCicco, A.; Filipponi, A. Eds.; (2009); Vol. 190.

[46] Chandesris, D.; Le Fevre, P.; Magnan, H.; Chaumin-Midoir, A.; Jaffres, H.; Scheurer, F.; Barbier, L., *Journal of Physics-Condensed Matter*, (2003) **15**, S657.

[47] Le Fevre, P.; Magnan, H.; Chandesris, D., *Surface Science*, (1996) **352–354**, 923.

[48] Fornasini, P.; Beccara, S. A.; Dalba, G.; Grisenti, R.; Sanson, A.; Vaccari, M.; Rocca, F., *Physical Review B*, (2004) **70**,

Chapter 4 A combined *in situ* XANES/EXAFS/XRD study of a model Fischer-Tropsch catalyst

4.1 Chapter Overview

In this chapter the results of an *in situ* investigation into the speciation of a model Fischer-Tropsch (FT) supported cobalt catalyst are discussed. A combination of X-ray absorption spectroscopy (XAS) and X-ray diffraction (XRD) was employed to understand the structure of the catalyst in its precursor state and time resolved studies were performed in order to deduce the structural changes occurring within the catalyst undergoing reduction. The 20 wt.% Co/Al_2O_3 catalyst was reduced at 500 °C under hydrogen which is realistic in terms of Fischer-Tropsch operating temperatures and relevant to real working catalysts. Results of XANES analysis, including linear combination fitting using a set of reference materials, supported those from EXAFS analysis. XRD supported both XANES and EXAFS analysis, highlighting that there is a significant unreduced component to the reduced catalyst. EXAFS proved to be indispensable in understanding the structure of the unreduced component within the catalyst which leads us to believe that Co^{2+} ions insert into the γ-alumina framework upon reduction generating hard-to-reduce, non-bulk like, species.

4.2 Introduction

In chapter two the structure of a model FT catalyst, Co metal powder, was investigated wherein the HCP/FCC phase composition in various Co metal powders and at temperatures below and above the phase transformation temperature was determined. This was a methodological development which expanded our fundamental understanding of the mixed phase system in the reduced catalyst. In an attempt to complete this investigation into the structure of the active and precursor state, it is our aim to study the speciation of a working catalyst undergoing reduction.

There are numerous issues surrounding supported cobalt catalysts used in FT synthesis relating to their activation, deactivation [1-6], reduction [7, 8] [9], metal-support interactions [10, 11], crystallite size [2, 12], reducibility, promoters [13-16] and water effects [17, 18] [19]. These factors often exhibit interdependencies and the scope and number of investigations into cobalt FT catalysts is extensive. With respect to catalyst structure, there still exist discrepancies in the experimental evidence in the literature primarily due to the varying conditions under which these studies were performed. As a result, research in this field continues to expand.

As described previously, it is widely understood that the catalyst in its active state contains reduced cobalt metal particles supported on high surface area carriers such as alumina [20-22]. The structure–function relationship is incomplete however due to the existence of additional cobalt phases, as cobalt oxides in the catalyst (Co_3O_4, CoO, $CoAl_2O_4$) although they do not possess catalytic activity [21]. Catalyst calcination generates a supported Co_3O_4 phase *via* the thermal/reductive decomposition of cobalt nitrate [14]. Although metal-support interactions play an important role in FT catalysis by essentially anchoring the metal particles onto the support, the stabilising interaction of Co with alumina can significantly affect the reducibility of the oxide leading to a detrimental effect on catalytic activity[8, 23]. The strong metal-support interactions generate hard–to–reduce oxide-support compounds that do not produce active sites for FT synthesis [23, 24]. Silica–supported Co catalysts have been shown to form irreducible Co species upon calcination through migration

of Co^{2+} into the support matrix[25]. This effect is much stronger in γ-alumina supported catalysts due to the stronger metal-support interaction [23, 26] as illustrated in Figure 4-1. To a lesser extent this is also a significant effect in α-supported catalysts[27]. Studies have shown that with increased cobalt loading, larger Co clusters are formed and the reducibility is improved through a decrease of interactions with the support [26, 28].

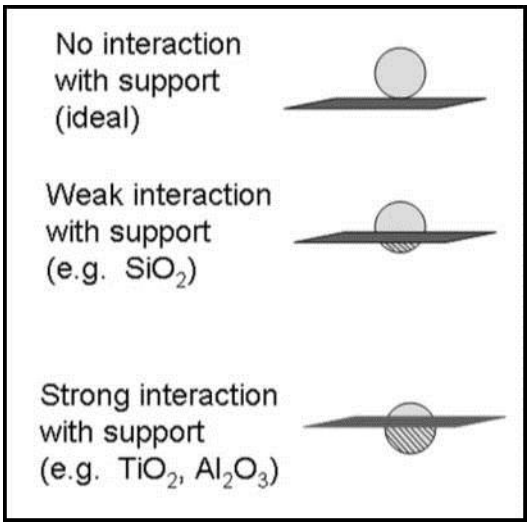

Figure 4-1. *Variations in strength of metal-support interactions based on different supports. These interactions have a profound effect on catalyst reducibility and crystallite size [29].*

The formation of hard–to–reduce species upon calcination arises due to similarities in the structures of Co_3O_4 and Al_2O_3 and their respective ionic radii where the defect spinel structure of γ-alumina facilitates the migration of Co^{2+} ions (from Co_3O_4) into the support framework [27, 30]. Diffusion of Al^{3+} into the Co_3O_4 spinel framework can also occur through isovalent substitution particularly at high calcination temperatures. Contrarily, some authors report that irreducible Co phases are not formed during calcination but during reduction of the Co catalyst [31] or indeed both [32-34]. Irrespective of whether calcination or reduction is responsible, the formation of cobalt-alumina phases impacts strongly on the generation of FT active Co^0 particles [14]. Temperature programmed reduction (TPR) is a useful tool to understand the catalyst reduction however there is controversy in the literature as to

the nature of the reduction species where cobalt loading, calcination temperature and promoter effect can cloud interpretation [26, 35]. Highly dispersed, amorphous species appear at higher reduction temperatures in the TPR between *ca*. 500 and 800 °C [31].

The structural similarities of the calcination product – Co_3O_4 and the γ-alumina support phase – severely impedes characterisation using XRD. Moreover, when metal-support phases are generated they are not necessarily bulk like structures; Co^{2+} has been shown to migrate into cation vacancies of the first few layers of the alumina framework [27], thus are characterised as surface type species lacking long-range order. Some authors have reported the formation of an irreducible cobalt aluminate, $CoAl_2O_4$, phase [29, 36] and some have linked its formation to Co particle size [28] and calcination temperature [37]. Some of the investigations highlighted in this introduction emphasise that a complex interplay of particle size, dispersion and reducibility exists. Furthermore, these types of studies demonstrate that before correlations can be made to catalytic performance, a full structural knowledge of the system is essential. Various parameters seem to control catalyst structure; literature, however, is lacking in agreement as to the nature of the reduced species contained within the catalyst. XAS has been widely applied to the study of these supported Co catalysts since it provides excellent information on the local structure and can be performed *in situ* under realistic conditions. In addition to *ex situ* XAS structural studies [14, 38], Khodakov and co-workers have carried out a series of time resolved XANES and EXAFS investigations [39-42] to investigate the activation, speciation and reducibility of alumina and silica supported catalysts under realistic FT conditions. *Ex situ* and *in situ* XAS has also been employed extensively by Davis and co-workers to investigate calcination [43], reduction[35, 44] and promoter effects [36, 45]. XAS has been shown to be a powerful tool in detecting cobalt aluminate phases where both XANES and EXAFS have been employed to probe the local atomic structure around cobalt sites [46-48]. Notwithstanding new structural information garnered using these techniques on the nature of the unreduced species, there is no clear agreement as to whether or not cobalt aluminate is formed.

In summary, there is abundant literature surrounding Co FT catalysts. XAS seems to be an ideal technique for investigations of the structure of the precursor and active state of supported cobalt catalysts due to the non-crystalline nature of cobalt-alumina phases having properties that deviate from that of the bulk.

4.3 Aims and objectives

Our aim is to understand the reduction behaviour of a realistic unpromoted Co/Al_2O_3 FT catalyst using combined *in situ* XANES/EXAFS/XRD techniques. More specifically, we will use time resolved X-ray absorption spectroscopy for speciation within the catalyst undergoing reduction. XRD and laboratory TPR data will be used to support our findings. Due to the vast amount of literature that surrounds the formation of surface and bulk like oxidic Co species upon catalyst activation and reduction, we shall put our results into context with reference to the existing literature.

4.4 Experimental

4.4.1 Sample preparation

This study used a model 20 wt.% Co/Al_2O_3 catalyst which was prepared by Johnson Matthey. The catalyst was prepared by dissolving 19.76 g of cobalt nitrate hexahydrate (Alfa Aesar) in 9 ml of demineralised water by warming 16 g of gamma alumina (HP14-150, Sasol, 150 m^2 g^{-1}) was added to the solution. The resulting pink solid was dried at 105°C for 3 hrs and calcined in static air at 400°C for 1 h using a 2°C/min ramp rate. Reference materials used in this study were Co_3O_4, CoO and Co metal powder. These were all obtained from Alfa Aesar.

4.4.2 Laboratory temperature programmed reduction (TPR)

For TPR measurements the following samples were used: 1) 2.72 g of Co_3O_4 mixed with 8 g of γ-Al_2O_3. 2) 2.54 g of CoO mixed with 8 g of γ-Al_2O_3. 3) A 20 wt.% Co/Al_2O_3 catalyst (as described above). A 10 % H_2/Ar gas mix was used using a flow rate of 30 ml/min and a ramp rate of 10°C/min with a 10 min hold at the maximum TPR temperature.

4.4.3 Combined *in situ* X-ray absorption spectroscopy/X-ray diffraction

The combined XAS/XRD measurements were performed at the BM29 beamline of the ESRF as described in chapter two. For this investigation, an identical setup and scan parameters as the investigation on cobalt metal powders in chapter two were used. Samples were ground using a pestle and mortar and mixed with γ-alumina, as diluent, to produce a homogeneous powder sample. For the reference materials, the following masses of each powder were used: 13 mg of CoO and 13 mg of Co_3O_4. 40 mg of the Co/Al_2O_3 catalyst were used. The varying weight of samples used reflect the varying wt.% of Co within each sample and the relative concentrations of Co once physically mixed with γ-alumina. The sample weights were calculated *a priori* to ensure the absorption at the edge jump in the X-ray absorption spectrum was

optimised. For *in situ* TPR experiments using Co_3O_4 and CoO, the maximum TPR temperature reached was 550 °C. For the Co/Al_2O_3 catalyst the TPR reached 500 °C. A 5 °C/min ramp rate was used in all experiments. After heat treatment samples were cooled down to room temperature whilst continuing to collect XAS and XRD data.

4.4.4 Data analysis

4.4.4.1 XAS analysis

For background subtraction and normalisation, Athena [49] was used where routine data reduction procedures were employed. For XANES analysis, E_0 was selected to be the energy of the maximum in the first derivative. EXAFS analysis was performed using the EXCURVE98 program [50]. Co_3O_4, CoO and Co metal powder were used as reference materials in XANES linear combination fitting and EXAFS analysis. The amplitude reduction factor, S_0^2(obtained from cobalt metal powder), was set at 0.71 for analysis. For EXAFS analysis of Co_3O_4 and Co/Al_2O_3, samples the first two coordination shells were fit. In data where more than one species exist only the first coordination shell of each species were fit to ensure that over-fitting of the data was not an issue.

4.4.4.2 XRD analysis

In order to extract the two dimensional X-ray diffraction patterns raw XRD data was converted using the *Fit2D* program [51]. Subsequent background removal and peak fitting was performed using the *Fityk* program [52]. Analysis was restricted to measuring the peak areas of the reflections that showed clear, well defined peaks. Due to the poorly crystalline nature of the dominant γ-alumina support phase, extraneous reflections originating from the in situ cell and the quality of the diffraction data obtained from *in situ* measurements, Pawley fitting or Rietveld analysis were not performed. Phase identification was achieved by fingerprinting the diffraction patterns using the positions of the reflections with literature values. The

assignment of the peaks in the Co/Al_2O_3 data could thus be made using the reference materials. Clear changes could be observed in peak areas and thus was sufficient in determining the emergence and disappearance of cobalt containing phases over the course of the reduction.

4.5 Results and Discussion

The results of the temperature programmed reduction of the Co/Al_2O_3 catalyst and cobalt oxide reference materials are first discussed. *In situ* XANES and EXAFS analyses are subsequently evaluated with respect to the Co/Al_2O_3 catalyst and cobalt oxide reference materials. Combined *in situ* X-ray diffraction shall also be reported with respect to the Co/Al_2O_3 catalyst only. Finally, a proposed structure is hypothesised by rationalising the results from these techniques.

4.5.1 Temperature programmed reduction (TPR)

Qualitative information regarding cobalt reducibility is generated through TPR experiments and can be cross correlated with results from XANES, EXAFS and XRD analyses. A single hydrogen consumption peak is observed in the TPR curves for CoO and Co_3O_4 (Figure 4-2) at around 360 and 370 °C (10 °C/min), respectively, and corresponds to the direct and uninhibited reductions to metallic cobalt. In CoO this represents the Co^{2+} to Co^0 reduction and in Co_3O_4 this is attributed to Co^{3+} to Co^0 reduction. The two reduction steps, $Co^{3+} \rightarrow Co^{2+}$ and $Co^{2+} \rightarrow Co^0$, in Co_3O_4 only display a single peak in the TPR and this is arises because both steps have lower activation energies compared to the alumina supported catalyst due to the absence of support interactions [53].

The TPR profile of the 20 wt. % Co/Al_2O_3 sample, calcined at 400 °C, in Figure 4-2 contains several hydrogen consumption peaks. A small peak (A) is observed at 260°C, likely attributed to the reductive decomposition of residual cobalt nitrate or the reduction of CoO(OH) species [54, 55]. A more intense peak at around 325 °C (B) can be assigned to the reduction of Co^{3+} to Co^{2+} species (1) corresponding to reduction of Co_3O_4 to CoO crystallites which is an easy reduction step indicated by the relatively narrow temperature range of the peak. The intensity of the peak is related to the proportion of reducible Co ions; Co_3O_4 has a normal spinel structure where one third of Co^{2+} ions in tetrahedral (T_d) positions and two thirds of Co^{3+} ions in octahedral (O_h) positions [56]. It is, therefore, the most intense peak in the TPR. It

is well known that catalyst calcination results in the decomposition of cobalt nitrate complexes to preferentially form Co_3O_4 crystallites [57]. In our study a calcination temperature of 400 °C would not favour formation of a $CoAl_2O_4$ phase upon calcination and indeed no reduction peak is observed a higher temperature indicating almost complete reduction. The TPR profile exhibits a much broader higher temperature peak (C), beginning at around 400 °C and extending up to around 750 °C, and is assigned to $Co^{2+} \rightarrow Co^0$ reduction of CoO to metallic Co (2). The very broad nature of this peak originates from the much harder to reduce Co^{2+} species. The TPR profiles demonstrate that the reduction behaviour of the Co/Al_2O_3 catalyst is distinctly different from that of bulk Co_3O_4 despite being isostructural prior to reduction.

$$Co_3O_4 + H_2 \rightarrow 3CoO + H_2O \quad (1)$$

$$CoO + H_2 \rightarrow Co + H_2O \quad (2)$$

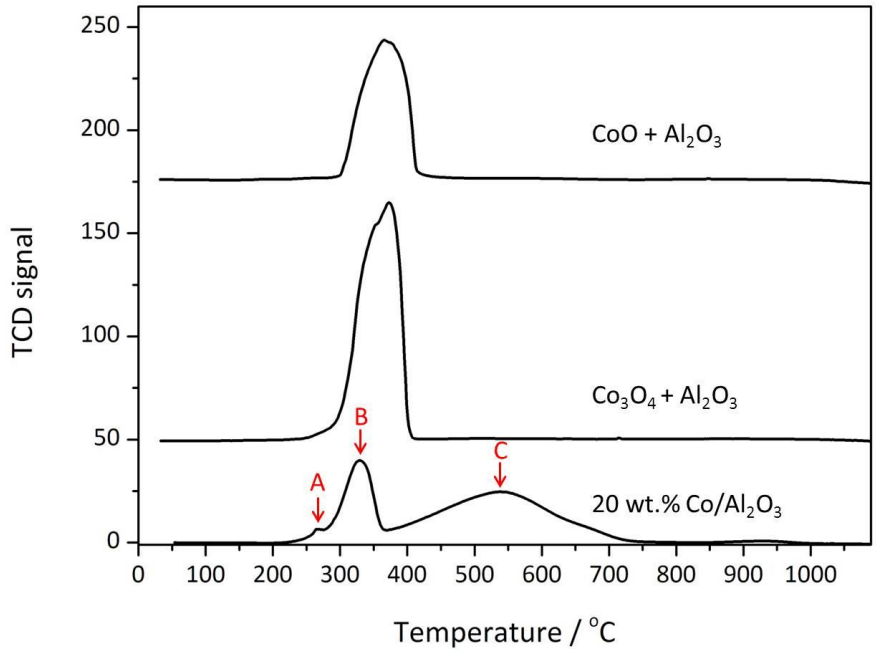

Figure 4-2. *TPR profiles of 20 wt.% Co/Al_2O_3 catalyst (calcined at 400 °C) and Co_3O_4 and CoO mixed with γ-alumina (10% H_2/Ar mixture, 30 ml/min flow, ramping rate 10°C/min).*

4.5.2 XANES

For speciation of the Co/Al_2O_3 catalyst using XANES, spectral features in the reference materials can be used to fingerprint the catalyst XANES spectrum. We shall briefly discuss the origins of the features we see in the XANES belonging to Co metal and its oxides. The XANES data obtained at room temperature for Co_3O_4, CoO and metallic Co are displayed in Figure 4-3. The position of E_0 shifts to higher energy with increasing Co oxidation state in the sequence $Co^0 \rightarrow CoO \rightarrow Co_3O_4$. In Co_3O_4 the higher valent ions, in addition to the local geometry of the Co atoms, give rise to the different lineshape of the XANES in comparison to the CoO reference material, which contains only Co^{2+} species. The small pre-edge feature, at *ca*. 7712 eV, in the spinel arises from the 1*s* → 3*d* dipole forbidden transition and gains intensity due to the overlap of oxygen *p* orbitals with cobalt *d* orbitals; termed '*dp* mixing' [58]. The intensity of the pre-edge feature below the absorption edge is strongly dependent on the coordination geometry of the metal ion and is a diagnostic spectral feature used in XANES analysis to discriminate structures based on their

local coordination geometries. In Co_3O_4 the pre-edge feature is more prominent than in CoO. This arises due to the non-centrosymmetric nature of Co^{2+} ions (T_d) in Co_3O_4 compared to O_h Co^{2+} ions in CoO. With increasing photoelectron energy the XANES lineshapes have further distinguishing features between the metallic and oxidic species. The white line intensity of CoO is more intense, and at lower energy, than that of Co_3O_4. This is due to the very directional bonding exhibited in CoO where the Co─O bonding in the octahedra have strong overlap and thus the white line intensity is enhanced [59, 60].

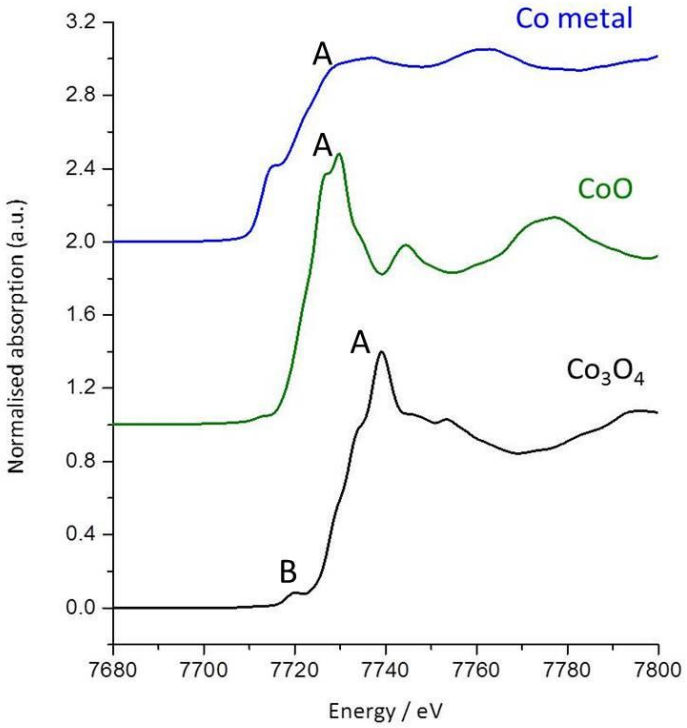

Figure 4-3. *Stacked XANES spectra of metallic Co, CoO and Co_3O_4 reference materials. The feature marked 'A' corresponds to the 1s → 4p transition observed in all spectra. The pre-edge feature marked 'B' in Co_3O_4 arises due to Co^{2+} ions with T_d symmetry. This feature is absent in CoO due to centrosymmetric O_h symmetry of the Co^{2+} ions.*

4.5.3 *In situ* XANES analysis

In situ XANES data were collected for cobalt oxide reference materials and the Co/Al_2O_3 catalyst. These plots highlight the dynamic spectral features associated with the reference materials and catalyst over the course of the reduction and can be used to fingerprint the *in situ* catalyst spectra. Semi-quantitative information can be readily obtained by analysing the position in energy of the absorption edge and the intensity of the white line which evolve in the *in situ* XANES spectra. Identifying the evolution of these diagnostic features is particularly useful for determining the nature of the species present over the course of the reduction. Using the XANES spectra of reference materials, linear combination fitting (LCF) of the Co/Al_2O_3 XANES was performed to obtain a quantitative measure of the Co species composed within the catalyst over the course of the reduction and thus an overall extent of reduction in the catalyst. *R*-factors were consistently low indicating the appropriate standards were used in the spectral fitting. With respect to the reduction of the two reference oxides described first, the catalyst XANES analysis is described here.

4.5.3.1 Co_3O_4

In situ XANES spectra from the reduction of the Co_3O_4 reference material are displayed in Figure 4-4 highlighting the fast changes occurring over the course of the reduction. The variation in the edge position and white line intensity, plot in Figure 4-5, reflects this. The white line and pre-edge feature, signatures of oxide and spinel structures respectively, are maintained up to 352 °C at which point there is a rapid change in the XANES. The fast reduction in white line intensity is mirrored by the decrease in energy of the edge position. The decrease in intensity and shift to lower energy of the white line with simultaneous decrease in edge energy indicates the point of reduction of Co^{3+} to Co^{2+} which occurs fast between 333 and 392 °C (69 and 80 min). At 372 °C, the spectrum closely resembles that of CoO where the pre-edge peak is half way between that of Co_3O_4 and the metallic shoulder peak at the mid-point of the edge. The XANES features after heating to 550 °C are consistent with those of metallic cobalt; disappearance of the white line intensity and emergence of the shoulder at the mid-point of the edge (see Figure 4-3). The normalised white line intensity falls below 1 at the end of the reduction confirming the pure metallic nature

of the reduced species. The rapidly changing XANES features between 352 °C and 392 °C suggest the fast and complete reduction of Co_3O_4 to CoO to Co metal where CoO exists as a short-lived intermediate species.

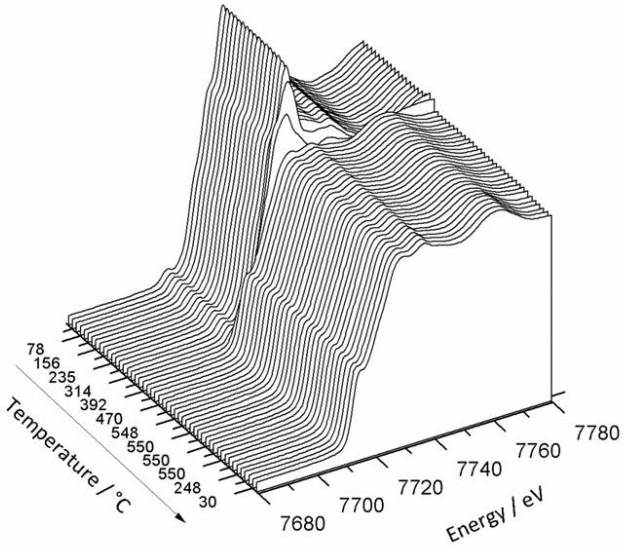

Figure 4-4. *Co_3O_4 reference material in situ XANES spectra obtained with heating under hydrogen.*

Figure 4-5. *Absorption edge (E_0) and white line analysis for the Co_3O_4 reference material.*

The fitting standards used for LCF of the Co_3O_4 XANES consisted of i) the initial room temperature XANES of the Co_3O_4 reference material as a Co_3O_4 standard, ii) the initial room temperature XANES of the CoO reference material as a CoO standard and iii) the final room temperature XANES after the reduction of the Co_3O_4 reference material as a reduced metallic Co standard. The use of the reduced Co_3O_4 XANES as metallic Co standard was preferred over using that of the Co metal powder XANES data since improved fits were obtained *via* this method. The results of the Co_3O_4 XANES LCF are illustrated in Figure 4-6 which displays the relative concentrations of each cobalt species over the reduction. The results indicate that the reduction to CoO begins from 333 °C; up to this point Co_3O_4 has the spinel structure. Although a slight decrease in the Co_3O_4 internal standard is observed prior to this, this is likely attributed to the uncertainty in the fitting procedure. At 372 °C the maximum CoO content is reached, *ca*. 50 %, where the coexistence of metallic and spinel phases is also observed at 42 and 9 % respectively. The reduction to Co^0 is complete by 412 °C where only fully reduced species are detected in the LCF (CoO is detected at very low concentrations < 5% and considered to be absent). LCF

confirms, quantitatively, here that CoO exists only as a short lived intermediate species and Co_3O_4 fully reduces to metallic cobalt.

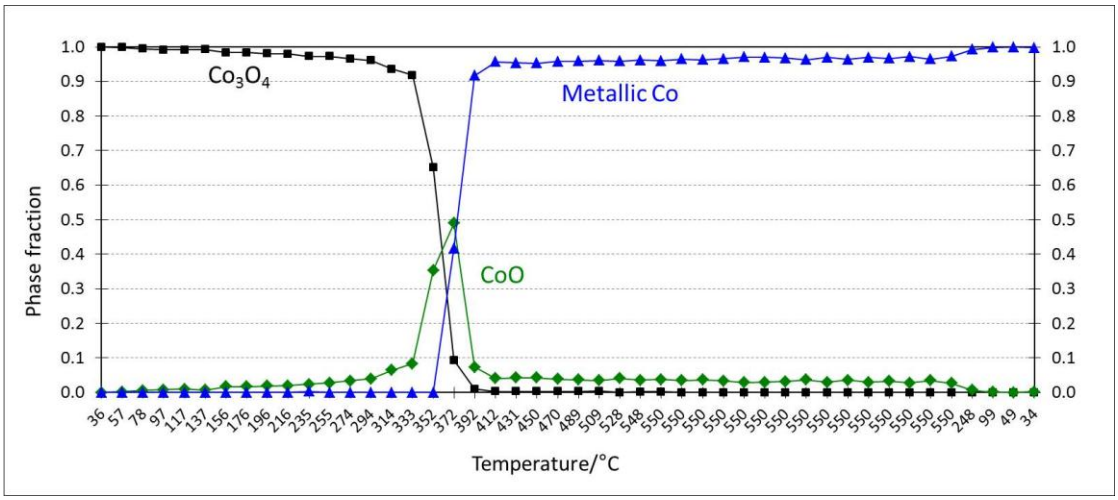

Figure 4-6. *The relative concentration profiles in Co_3O_4 obtained from XANES LCF. Estimated uncertainties are within the size of the symbols.*

4.5.3.2 CoO

The *in situ* XANES profiles belonging to the CoO reference material are displayed in Figure 4-7. There are clear changes in the XANES lineshapes beginning at 356 °C, characterised by the fall-off in intensity of the white line concomitant with the disappearance of the pre-edge and emergence of the shoulder at the mid-point of the rising absorption edge. From analysis of the absorption edge and white line intensity, represented in Figure 4-8, these features show a strong positive correlation. The simultaneous sudden decrease in white line intensity and edge position between 60 and 72 minutes (337 and 395 °C) highlights the fast, one step, $Co^{2+} \rightarrow Co^0$, reduction of CoO. At the end of the reduction the white line intensity falls to below 1 confirming fully reduced Co species are present. An overall shift of 6.7 eV in the edge position between the pre- and post-reduced material is observed. This observation highlights that there is discordancy between edge analyses of Co_3O_4 and CoO XANES data. It is expected that, due to the higher valent Co ions in the spinel structure, the energy shift is larger than that seen in CoO, however this is clearly not the case. The edge position at which point the Co_3O_4 undergoes the first reduction

pathway to CoO is consistent with the value for the pre-reduced CoO material, *ca*. 7721 eV, however the subsequent shift of the edge position to lower energy is *ca*. 1.5 eV compared to ca. 6.5 eV in the single reduction of CoO to Co^0. The origin of this anomaly in edge positions, likely pertaining to the CoO reference material rather than Co_3O_4, remains unclear. LCF analysis for CoO was not performed owing to the direct $Co^{2+} \rightarrow Co^0$ reduction pathway that the material undergoes.

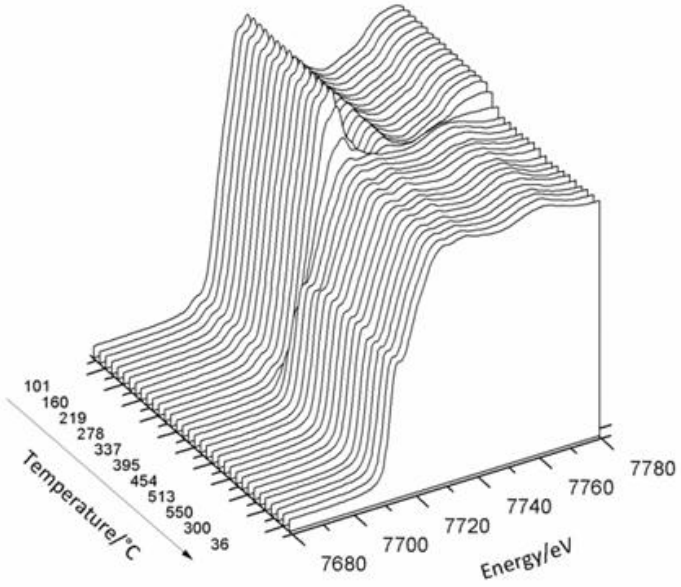

Figure 4-7. *CoO reference material in situ XANES spectra obtained with heating under hydrogen.*

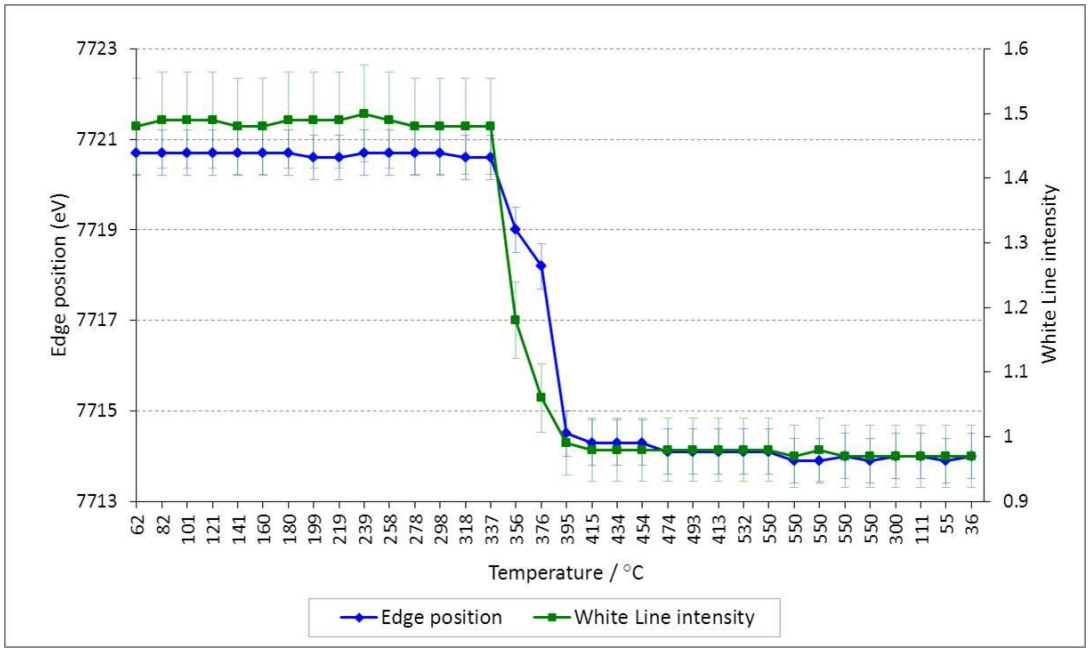

Figure 4-8. *Absorption edge (E_0) and white line analysis for the CoO reference material.*

4.5.3.3 Co/Al_2O_3 catalyst

The *in situ* XANES data of the Co/Al_2O_3 catalyst are displayed in Figure 4-9. It is evident that the starting material has the spinel structure as evidenced by the first XANES spectrum which closely resembles that of bulk Co_3O_4. The position of the main absorption edge and the pre-edge, at 7722.5 and 7713.6 eV, respectively, is equal to that found in the spinel structure. The Co_3O_4 structure is maintained within the catalyst during the reduction up to the data recorded at 295 °C. At 315 °C a change in the XANES indicates the first reduction pathway, $Co^{3+} \rightarrow Co^{2+}$, begins where the reduction in white line intensity coinciding with the reduction in pre-edge intensity suggests the formation of a CoO phase. From the edge and white line analysis, Figure 4-10, it is evident that the trend in the edge position and white line intensity is not as discernible as in the reference materials. Interestingly, the XANES reduction profile of the catalyst does not match that of the bulk Co_3O_4 reference material, where there are marked differences in the XANES profiles attributed to the Co^{3+} to Co^{2+} reduction. Whereas bulk Co_3O_4 reveals a rapid conversion to a fully reduced Co species *via* a short lived CoO intermediate, a decrease in white line intensity at 315 °C with a subsequent increase in white line

intensity up to 354 °C observed in the Co/Al_2O_3 XANES suggests an alternative reduction pathway takes place. This observation on the white line intensity during the first reduction step has been previously observed [35]. The disappearance of the pre-edge peak with a simultaneous enhancement of the white line intensity indicates that maximum CoO content is reached within the catalyst at 354 °C. The following reduction step in the catalyst does not appear to proceed *via* a fast and single step to metallic cobalt, as observed in bulk Co_3O_4. On the contrary, a slow reduction in white line intensity from 374 °C, concomitant with gradual movement in the shoulder on the rising edge to higher energy, reveals a slow incomplete reduction to metallic Co. The final scan at the end of the reduction displays a XANES profile that does not match that of metallic Co; there is a white line visible. The edge position reveals a more gradual shift to lower energy than in Co_3O_4, which is 2.3 eV relative to the 3.6 eV shift seen in bulk Co_3O_4 suggesting that the sample has undergone a partial reduction to metallic cobalt. This is confirmed by a normalised white line intensity of *ca*. 1.2 which is observed at the end of reduction indicating some oxidic component remains. These factors strongly suggest there is a distinct two step reduction process taking place that does not proceed *via* the same pathway as in bulk Co_3O_4; the first, Co_3O_4 to CoO, relatively fast starting from 295 °C and the subsequent partial, CoO to Co^0, reduction more facile and beginning at 354 °C. This evidence reveals the final state of the Co/Al_2O_3 is a partially reduced species. These findings can be supported by interpretation of the laboratory TPR studies.

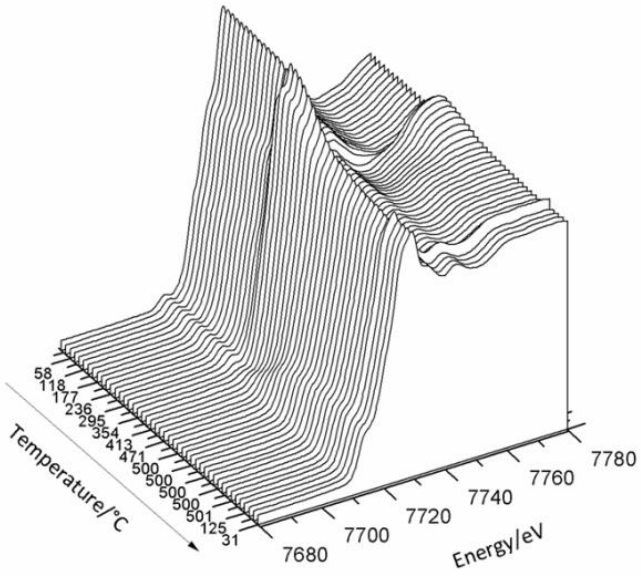

Figure 4-9. *Co/Al_2O_3 catalyst material in situ XANES spectra obtained with heating under hydrogen.*

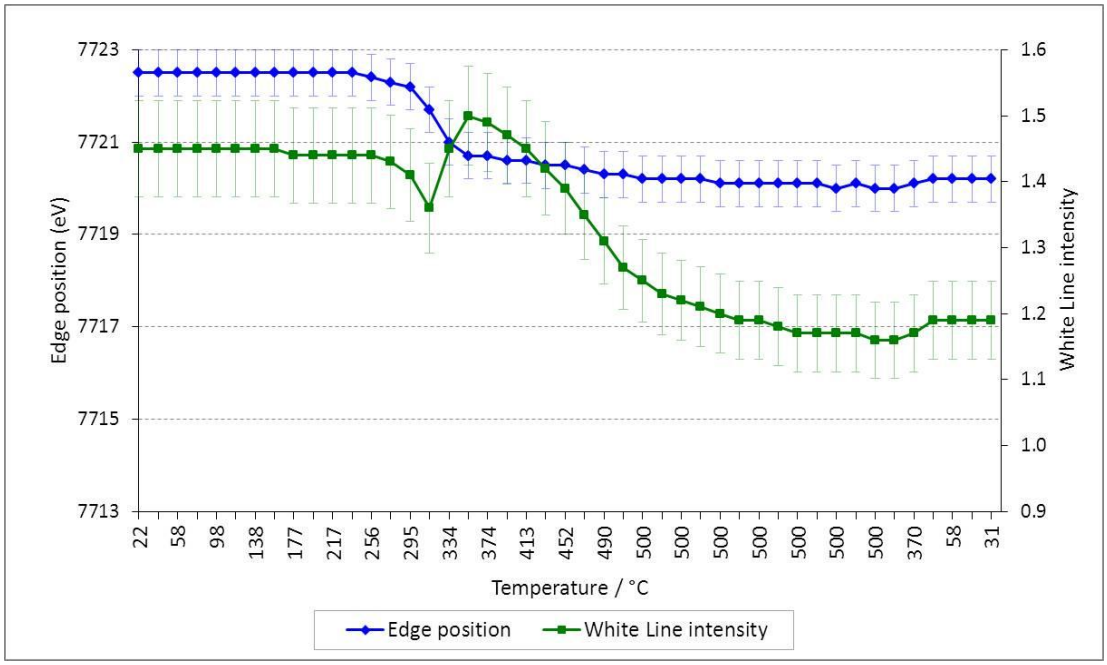

Figure 4-10. *Absorption edge (E_0) and white line analysis for the Co/Al_2O_3 catalyst.*

Results of the XANES LCF of the Co/Al_2O_3 catalyst are represented in Figure 4-11. For this analysis it was necessary to change the standards used in the fitting. Standard spectra used to represent the Co^{3+}/Co^{2+}, Co^{2+} and Co^0 species in the catalyst were that of (i) pre-reduced Co_3O_4 as a Co_3O_4 standard, (ii) Co/Al_2O_3 measured at 354 °C as a CoO (internal) standard (iii) Co_3O_4 measured at room temperature after reduction as a metallic Co standard. Since the white line intensity appears to reach a maximum in the catalyst XANES spectrum at 354 °C this was taken to be the CoO standard. Excellent linear combination fits were obtained using the fit range of −30 to +70 eV around the absorption edge. Figure 4-12 displays representative fits from LCF analysis. The results confirm that the pre-reduced catalyst contains a bulk-like spinel structure. At 315 °C the CoO phase emerges and continues to increase concomitant with the disappearance of Co_3O_4 up to 354 °C, at which point a single Co^{2+} species is detected and the reduction to CoO is complete. Unlike in bulk Co_3O_4, where a fully reduced metallic species is formed at 412 °C, the catalyst undergoes a slow, partial reduction to metallic Co along the trajectory of the reduction, under isothermal conditions. The extent of reduction is *ca*. 60 %. Upon cooling the proportion of metallic Co decreases slightly. The difference between the LCF concentration profiles of the Co_3O_4 reference material and the Co/Al_2O_3 catalyst verifies the observations made by absorption edge and white line intensity analyses.

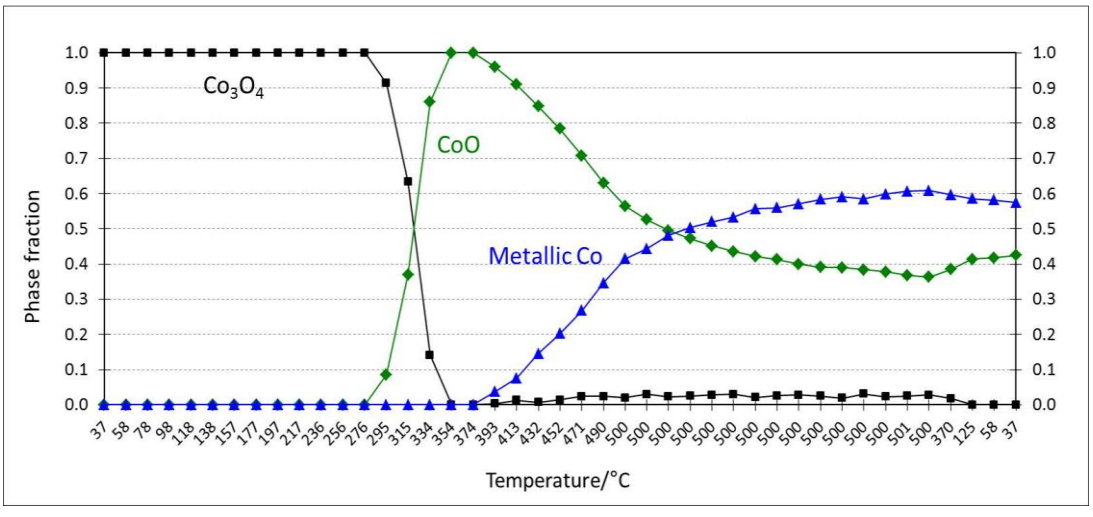

Figure 4-11. *The relative concentration profiles in the Co/Al_2O_3 catalyst obtained from XANES LCF. Estimated uncertainties are within the size of the symbols.*

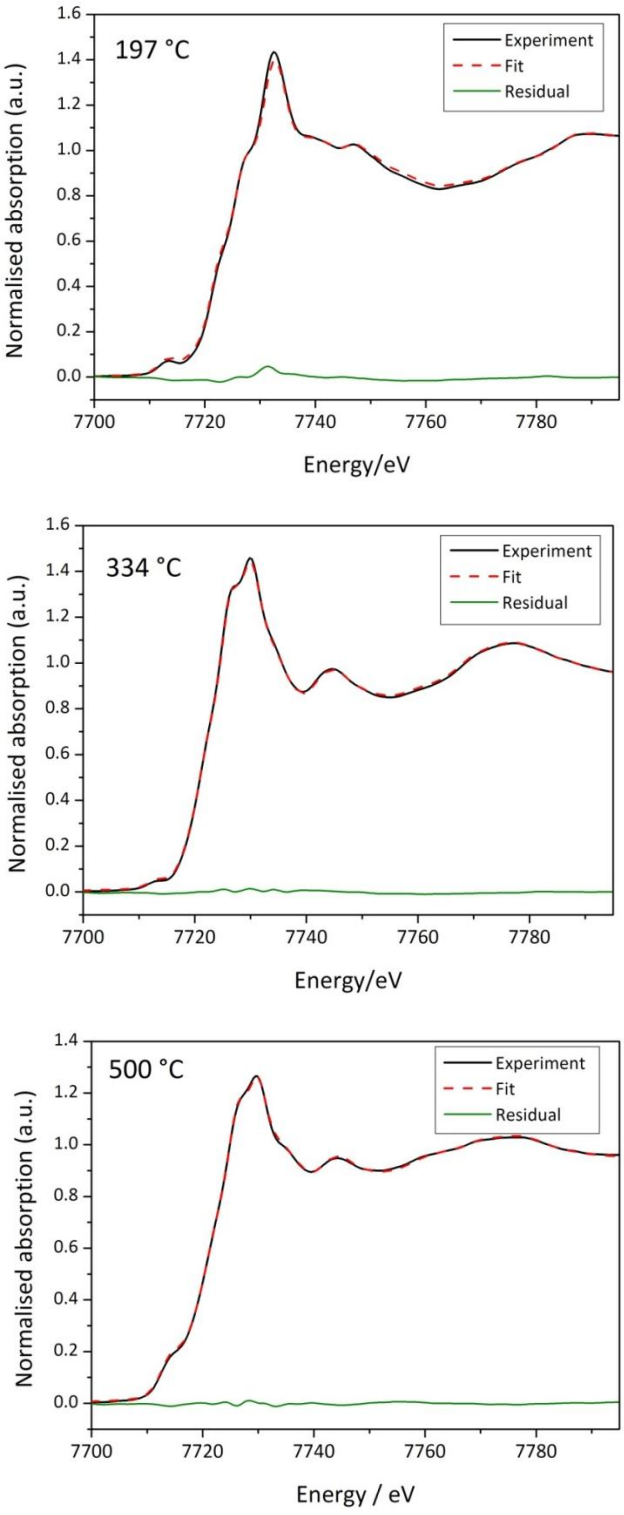

Figure 4-12. *Representative linear combination fits of the catalyst XANES measured at 197 °C, 334 °C and 500 °C. Experimental (black line), best fit (red dashed line) and difference (green line) spectra are displayed.*

4.5.4 *In situ* EXAFS

The Fourier transforms (FT) of the background subtracted and normalised *in situ* Co K-edge EXAFS data of the Co_3O_4 reference material and the Co/Al_2O_3 catalyst sample are depicted in Figure 4-13. The differences in the evolutionary features in the FT plots of the two materials correspond to structural transformations and emphasise the alternative reduction pathways in the two materials. The EXAFS FT plots are uncorrected for phase shifts (a feature of the program) thus the positions of the peaks in the FT plot are not true interatomic distances but are offset by *ca*. 0.4 – 0.5 Å. Evidently, changes are occurring in bulk Co_3O_4 from 352 °C where the first two peaks at *ca*. 1.4 and 2.6 Å, belonging to the Co─O (oxide) and Co─Co (oxide) coordination shells, rapidly transform to a single peak at *ca*. 2.1 Å. This distance represents the first shell Co─Co metallic cobalt scattering contribution. Assumptions based on *in situ* FT plots are in agreement with observations from XANES data. The reduction in amplitude of the peaks, not attributed to chemical reduction, is due to the attenuation of the thermal disorder component of the Debye-Waller factor thus no structural changes are occurring. For clarity, the EXAFS data measured upon cooling have been omitted.

The FT plots belonging to the Co/Al_2O_3 catalyst closely resemble those of bulk Co_3O_4 as the sample is heated to 315 °C. At this temperature a slow reduction process is evident as the Co─O (oxide) and Co─Co (oxide) shells at *ca*. 1.4 and 2.6 Å gradually transform to a single peak in the FT at *ca*. 2.1 Å at the end of the reduction. The Co/Al_2O_3 sample does not clearly display evidence for a fully reduced species in contrast to bulk Co_3O_4. The peaks evolve in a more convoluted manner and certainly further analysis is required to elucidate the underlying structural transformations occurring. Whilst the peak amplitudes are, as aforementioned, modulated by the Debye-Waller factor, the reduction in the amplitude of the peak at the end of the reduction may be related to some under-coordination and therefore incomplete reduction. Furthermore, the first, most intense, peak in the FT, at the end of the reduction is characterised by its asymmetry and position, being slightly lower (*ca*. 0.03 Å) than this peak seen in Co_3O_4. These observations can be explained by the first two Co—O coordination shells, belonging

to CoO, overlapping with the metallic Co—Co coordination shell. EXAFS curve fitting procedures are required to corroborate this.

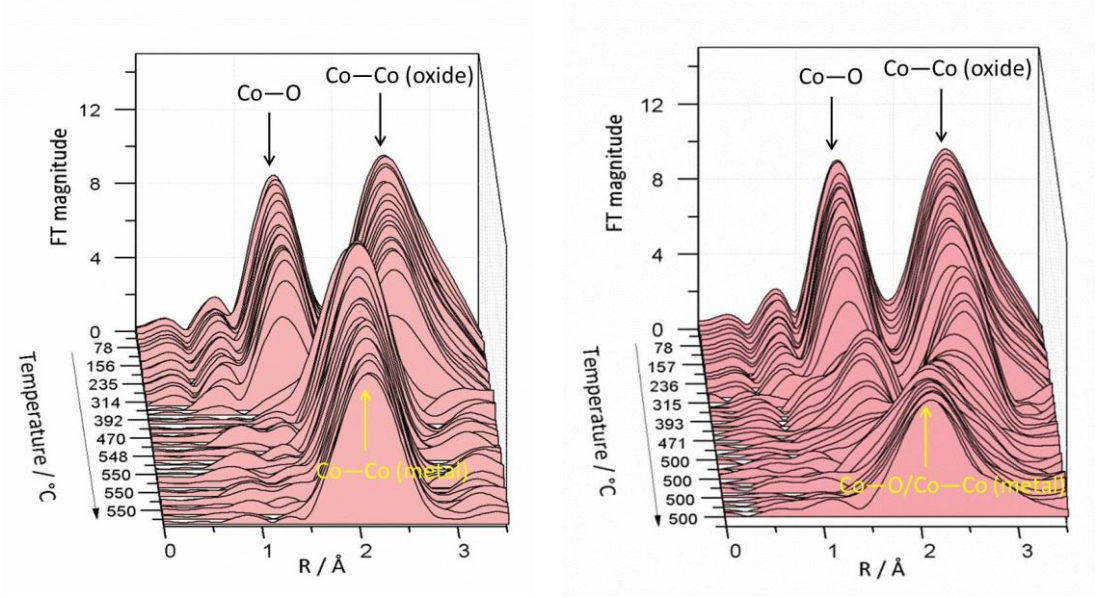

Figure 4-13. *k^3-weighted in situ Co K-edge EXAFS Fourier transform plots (phase shift uncorrected) for the Co_3O_4 reference material (left) and the Co/Al_2O_3 catalyst (right) using a k-range of 3.0 – 10.0 $Å^{-1}$. Final scans taken on cooling have been omitted to aid comparison between samples.*

4.5.4.1 Co_3O_4 EXAFS analysis

Figure 4-14 represents the results of EXAFS analysis for bulk Co_3O_4 displaying the variations in the Co—O (Co oxide) and Co—Co (Co metal) coordination numbers, bond lengths and Debye-Waller factors. At room temperature a Co—O bond distance of 1.90 Å is observed reflecting the averages of the oxygen bonded Co^{3+} and Co^{2+} environments in the spinel structure. A Co—O bond distance of 1.91±0.1 Å is maintained up to 352 °C with a slight decrease in coordination to 4.6. This is explained by the correlations between the coordination number and Debye Waller factor and is unlikely to be any structural effect. The first shell Debye-Waller factor increases from 0.006 $Å^2$ in the room temperature EXAFS data to 0.016 $Å^2$ at 352 °C which is double the value at the previous temperature measurement (0.007 $Å^2$). The Debye-Waller factor is temperature dependent however the magnitude of this sudden

increase suggests that increased static disorder is introduced into the system. The EXAFS data at 372 °C fit with the inclusion of an additional Co—O scattering to the model, yielding a Co—O bond distance of 2.00 Å. At this point the Co—O coordination number of 2.1 is significantly reduced from that of bulk CoO where N = 6[61] . The best fit of the EXAFS is achieved with the introduction of metallic Co—Co ($R_{Co\text{-}Co}$=2.48 Å) scattering which yields a Co—Co coordination number of 5.5. At 392 °C the Co—O bond distance is found to be 2.08 Å and the Co—Co (metallic) coordination number increases further to 10.1. At 392 °C the Co—O coordination drops to 0.6. The maximum Co—O coordination of 2.1 at 372 °C is direct evidence for the incomplete reduction of Co_3O_4 to CoO. The coexistence of metallic and oxidic species at 392 °C provides evidence for CoO as an intermediate phase during the reduction to metallic Co, unlike the transient CoO phase in Co_3O_4 reduction which is more difficult to detect. From 412 °C, until the end of the reduction, the EXAFS data is modelled with only Co—Co scattering ($R_{Co\text{-}Co}$ is fixed to 2.48 Å); the absence of Co—O scattering in the first coordination shell indicates a complete reduction takes place. The Debye-Waller factor takes a fairly consistent value of 0.029±0.004 $Å^2$ up to the final scan on heating then decreases back to room temperature. The first shell Co—Co coordination number is under-coordinated from that of bulk metal (N = 12[61]) and this is attributed to dispersion effects. EXAFS analysis of bulk Co_3O_4 corroborates the findings from XANES analysis, that Co_3O_4 undergoes a fast and complete reduction, $Co_3O_4 \rightarrow CoO \rightarrow Co$.

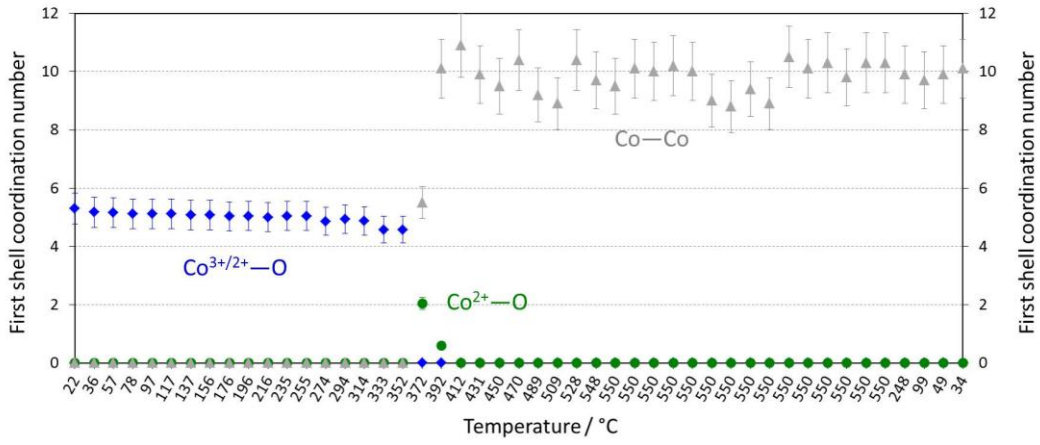

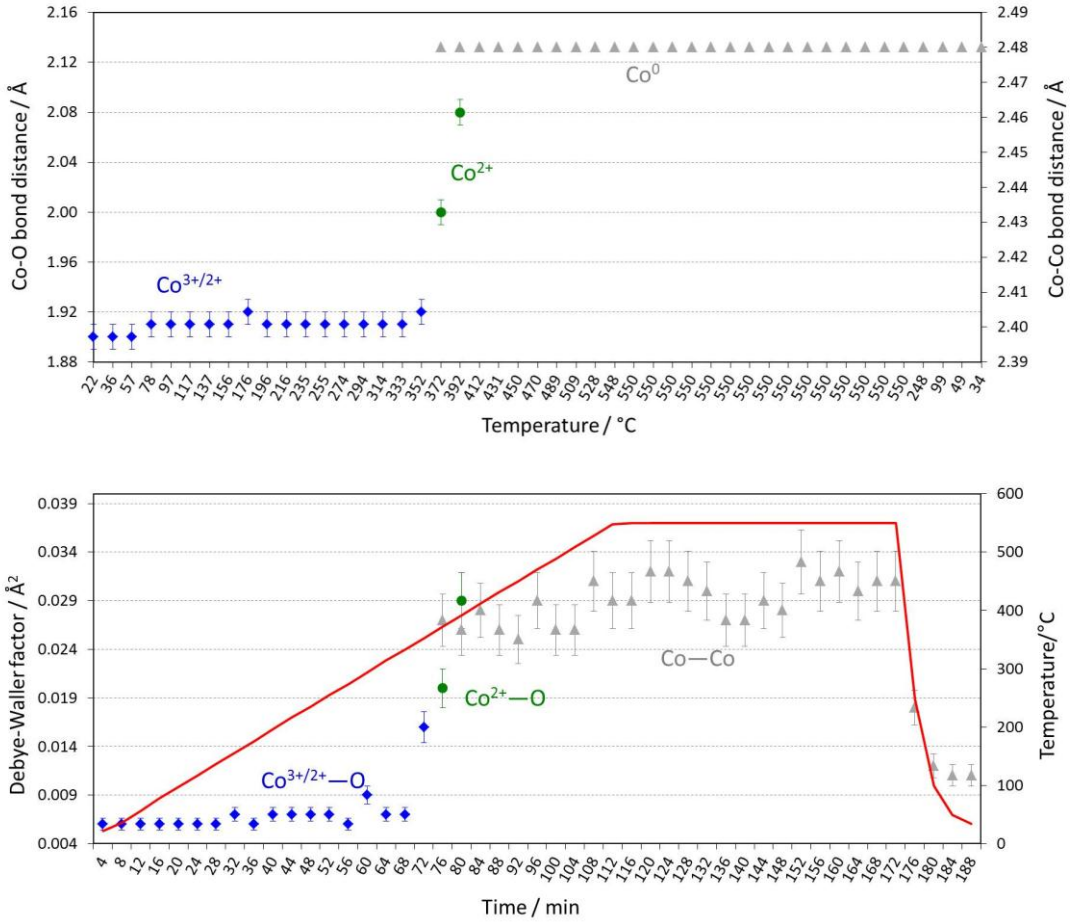

Figure 4-14. *Results from in situ EXAFS analysis of the Co_3O_4 reference material. The charts display the evolution of the Co─O and Co─Co coordination numbers (top), bond distances (middle) and Debye-Waller factors (bottom) over the course of the reduction. Note, the Co—Co bond distance is fixed at 2.48 Å in the analysis.*

4.5.4.2 Co/Al_2O_3 catalyst

Results of the *in situ* EXAFS analysis for the Co/Al_2O_3 catalyst are depicted in Figure 4-15. Representative best fits of the EXAFS data and corresponding FTs are illustrated in Figure 4-16. The Co—O bond length within the starting material of the catalyst was found to be 1.91 Å which is consistent, ±0.01 Å, with that found within the Co_3O_4 reference material. The refined coordination number of 5.3 also confirms the spinel structure of the catalyst after activation (prior to reduction). Upon heating to 315 °C the Co—O bond length increase slightly to 1.95 Å, the Debye-Waller factor increases to 0.014 $Å^2$ and the first shell coordination number drops to 4.1. EXAFS data in the following scan, measured at 334 °C, fits with the inclusion of an

additional Co—O scattering contribution based on a CoO octahedron. This second shell has a reduced coordination number of 2.7 and elongated bond length of 2.15 Å. This reflects the emergence of CoO which coexists with Co_3O_4 in the catalyst. In next two measurements, up to 374 °C, EXAFS data are modelled as a mixed phase of Co_3O_4 and CoO where the spinel coordination drops to 0.9 and the CoO first shell coordination reaches a maximum of 6.0; the uncertainty the coordination number carries explains the bulk like coordination number for CoO. Over this temperature regime, 334 to 374 °C the $Co^{2+/3+}$—O bond length (Co_3O_4) increases to 2.0 Å and the Co^{2+}—O bond length (CoO) of the second coordination shell reaches 2.12 Å, consistent with that found in the literature data [61]. At the point where Co_3O_4 and CoO simultaneously exist, the first shell Debye-Waller factors for both Co_3O_4 and CoO both drop considerably and this is thought to be an artefact of correlations between Debye-Waller factors and coordination numbers. By 393 °C, EXAFS data fits to a single shell of Co^{2+}—O at 2.09 Å with a coordination number of 6.1, reflecting the full reduction of Co^{3+} to Co^{2+}. Briefly, CoO exists as a single phase, until 432 °C a metallic Co phase emerges, indicating the beginning of the reduction of Co^{2+} to Co^0. The Co—Co bond length was set to be 2.48 Å for the inclusion of metallic Co—Co scattering to the model as this resulted in the most stable refinements and best fits of all subsequent *in situ* EXAFS data. The Co—Co (metallic) coordination number continues to increase, up to a maximum of *ca*. 7 at the end of the dwell at 500 °C. Correspondingly, the Co—O coordination drops over this period, to 2.6. The data, up to the end of the reduction is modelled with the inclusion of both Co—O and metallic Co—Co scattering contributions indicating that the catalyst sample undergoes an incomplete reduction to metallic Co, where in the final room temperature scan, after cooling, the relative phase proportion of oxidic and metallic species is of the order 45 and 55 %, respectively. Whilst we use the term "oxidic" for the unreduced component in the data, the Co—O bond length in this structure was found to be 2.08 Å which indicates that the cobalt oxide species is unlike that of bulk CoO, which contains a bond length of 2.13 Å.

As will be discussed later in the chapter there are various hypotheses surrounding the nature of the oxidic species and proposals as to its formation and is primarily associated with cobalt-alumina interactions. These results from this *in situ* EXAFS

analysis strongly support literature studies implying that Co^{2+} reduction is incomplete below 600 °C and whose origin is the strong cobalt-support interactions on alumina supported catalysts[62-64]. The slow and incomplete reduction of CoO to metallic Co, elucidated here through EXAFS, supports the results of XANES LCF both qualitatively and quantitatively where the extent of reduction is determined to be between *ca*. 55 and 60% from both techniques.

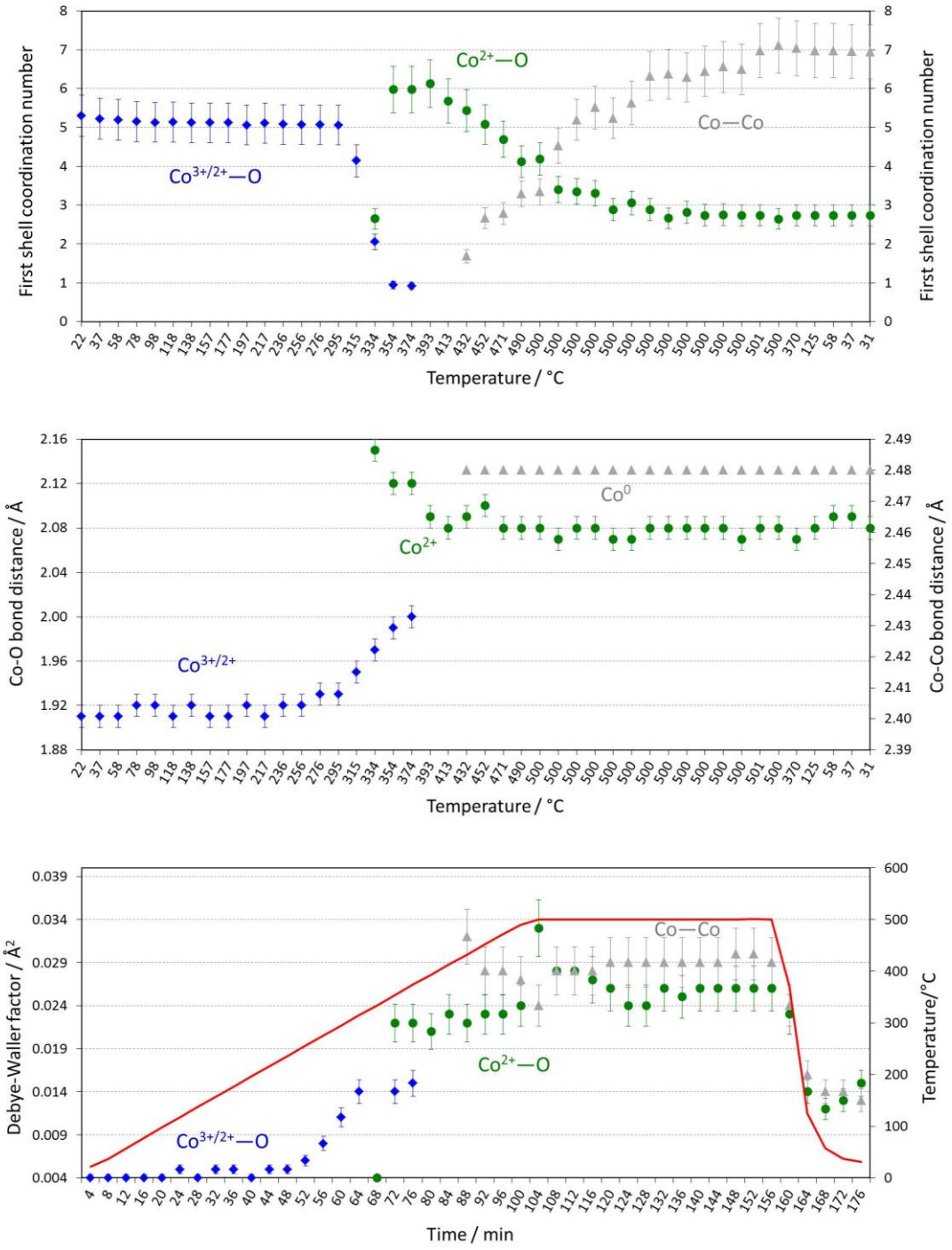

Figure 4-15. *Results from in situ EXAFS analysis of the Co/Al_2O_3 catalyst plotting the evolution of the Co─O and Co─Co coordination numbers (top), bond distances (middle) and Debye-Waller factors (bottom) over the course of the reduction. Note, the Co—Co bond distance is fixed at 2.48 Å in the analysis.*

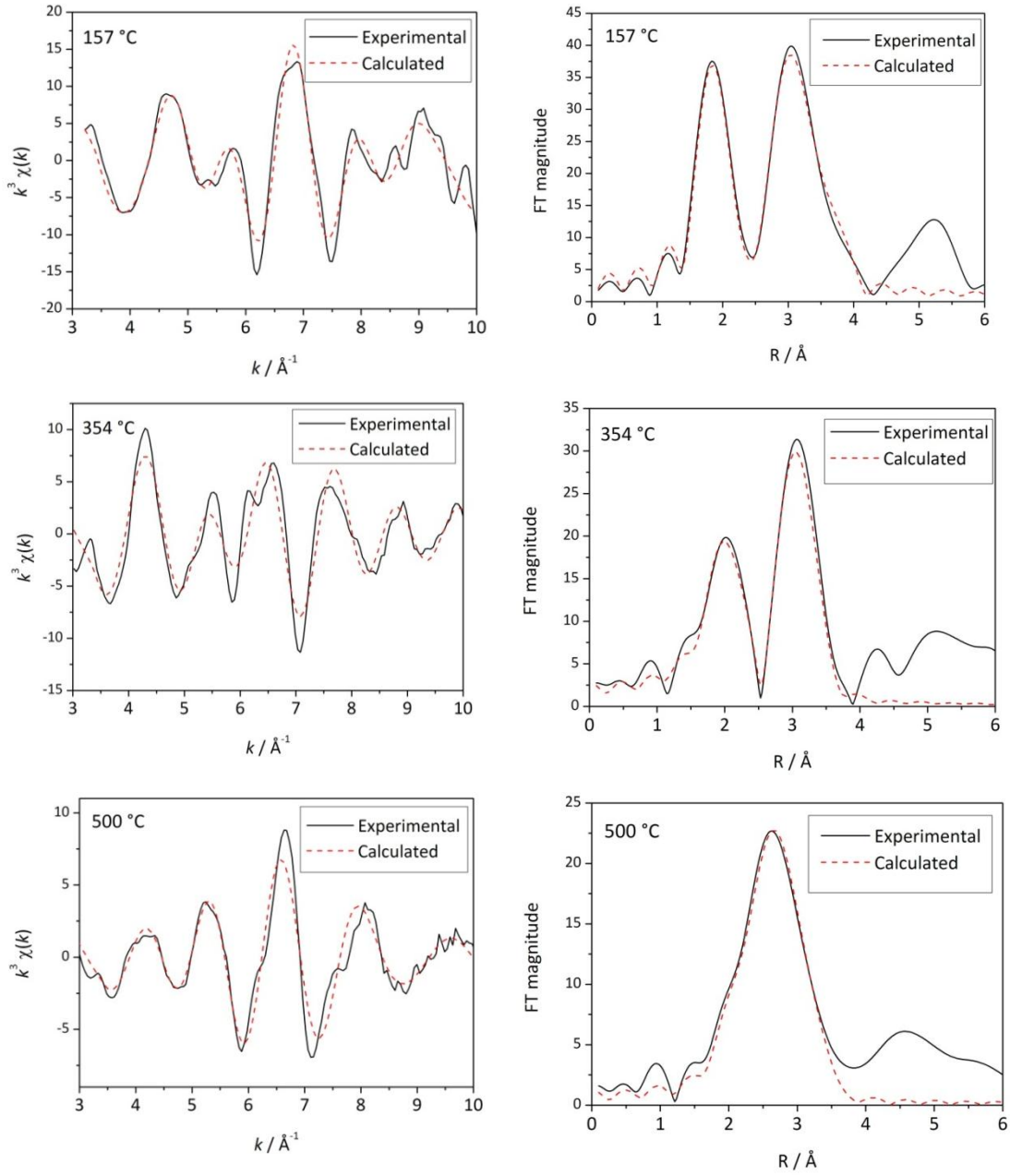

Figure 4-16. *Representative best fits of Co K-edge in situ EXAFS data (left) and associated Fourier transforms (right) of the Co/Al_2O_3 catalyst measured at 157 °C, 354 °C and 500 °C.*

4.5.5 XRD analysis

Figure 4-17 displays the *in situ* XRD patterns for the catalyst undergoing reduction. Broad peaks in the patterns originate from the poorly crystalline nature of the γ-alumina support phase. Accordingly, the presence of γ-alumina makes XRD analysis problematic. Additionally, the scattering of X-rays due to the *in situ* cell environment gives extraneous peaks in the patters that are not indexed to the Co or Al containing structures. Attempting to fit an accurate background without removing data belonging to cobalt metal and oxide reflections is challenging. With these issues in mind, an analysis of the integrated peaks areas for the Co/Al_2O_3 *in situ* XRD data was performed.

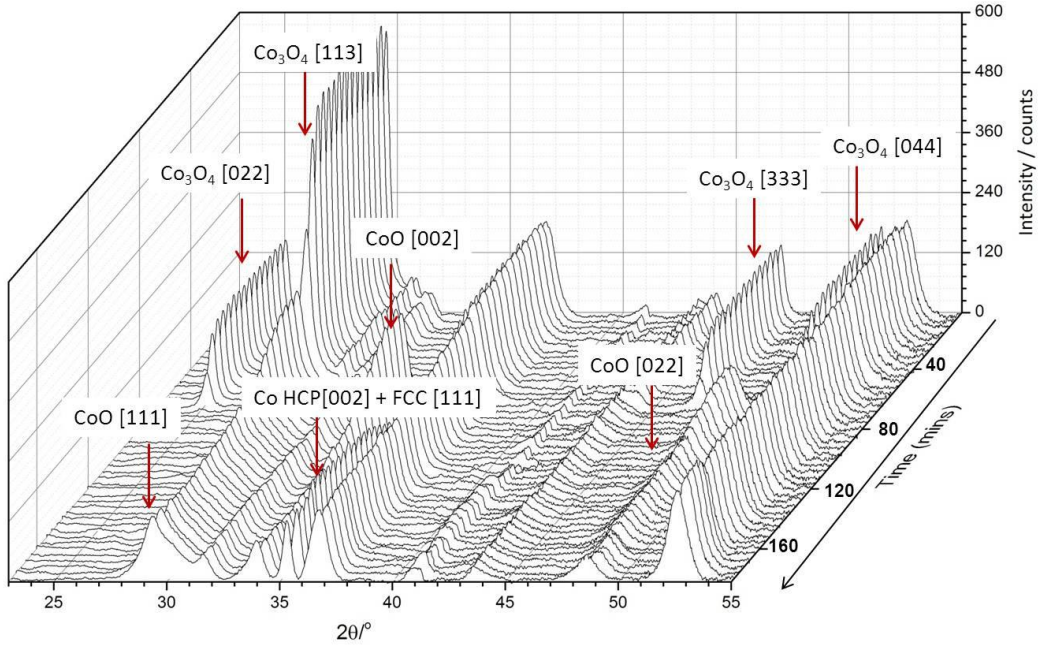

Figure 4-17. *Co/Al_2O_3 catalyst in situ X-ray diffraction patterns for obtained with heating under hydrogen. Reflections belonging to Co_3O_4, CoO and metallic Co are indicated. All other reflections, that are persistent throughout, originate from the γ-alumina support phase.*

The evolution of the integrated peak areas for the Co_3O_4 [044], CoO [022] and the Co metal mixed HCP [002] and FCC [111] reflections are plot in Figure 4-18. These reflections were selected as they displayed the largest peak areas for each phase and some of the peaks in the data are mixtures of reflections belonging to different species and thus hinder this type of analysis.

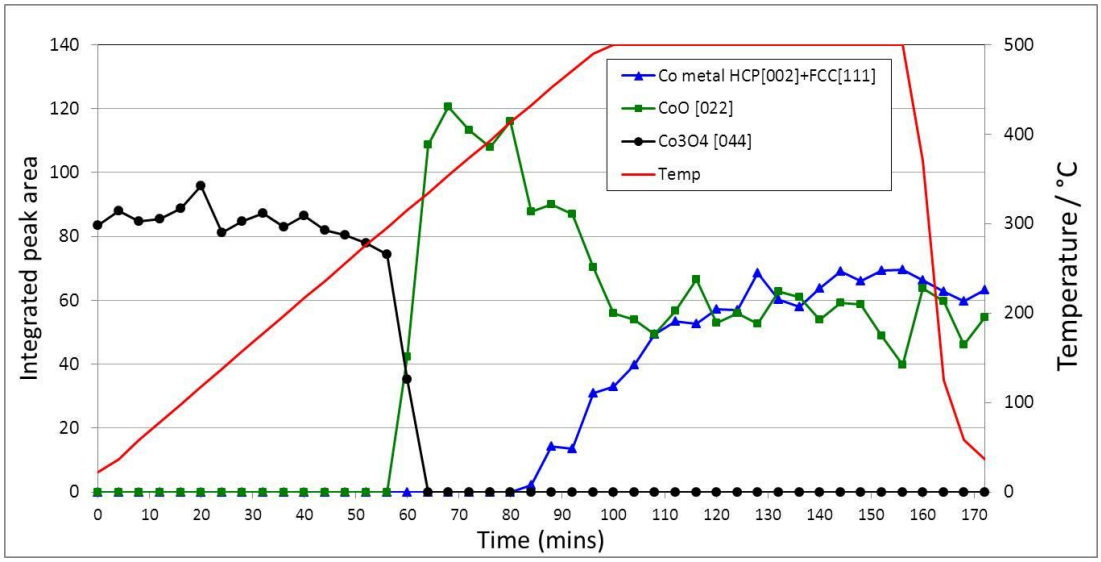

Figure 4-18. *Peak area analysis for the Co/Al_2O_3 catalyst using in situ XRD data.*

The integrated peak area for the Co_3O_4 [044] reflection falls rapidly after 56 min (295 °C) at which point the emergence of the CoO [022] reflection is observed. After 68 min (354 °C) the integrated peak area reaches a maximum and the catalyst contains a single CoO phase thus evidencing a full Co^{3+} to Co^{2+} reduction. The integrated peak area of the CoO [022] reflection then appears to drop as the heating under hydrogen proceeds. The appearance of the metallic Co phase is evident after 84 min (432 °C) due to the emergence of the peak at ca. 35 °, corresponding to the HCP [002] and FCC [111] reflections, and signifies the onset of reduction of CoO to metallic cobalt. This is a slow process which appears to only increase very slightly under isothermal conditions, once the reduction temperature of 500 °C is reached. At the end of the reduction, after cooling back to room temperature, there still exists some CoO indicating that the catalyst has undergone an incomplete reduction to the metallic species. Although a quantitative measure of the degree of reduction has not

been obtained these results support those from XANES and EXAFS in that (i) The first reduction step is relatively quick and complete to CoO, (ii) The second reduction step is slow and incomplete to metallic cobalt.

The incomplete reduction of the Co/Al_2O_3 catalyst elucidated through XRD, XANES and EXAFS analyses leads us to inquire as to the nature of the unreduced cobalt species contained within the catalyst. The results of these *in situ* X-ray techniques along with laboratory TPR are discussed below.

4.5.6 Discussion

XANES can be used, at a qualitative level, to identify whether or not $CoAl_2O_4$ is formed under reducing conditions. $CoAl_2O_4$ exhibits a normal spinel structure where 100 % of Co^{2+} ions are located in tetrahedral sites [65]. Hypothetically the XANES should, therefore, display a prominent pre-edge peak arising from the $1s \rightarrow 3d$ transition due to T_d symmetry of the ions [66, 67]. The XANES of the reduced catalyst does not exhibit this pre-edge feature and thus we can assume that there exists no Co^{2+} species of T_d symmetry. This is consistent with the EXAFS Co—O bond length of 2.08 Å which is likely to be too large for T_d Co^{2+} species. Due to the absence of XANES data for bulk $CoAl_2O_4$ no standard could be used to identify this species in the catalyst independently by LCF. XANES alone, however, is unable to unequivocally confirm the absence or presence of $CoAl_2O_4$, especially as the normalised and derivative XANES is very similar to that of Co_3O_4 [36]. Furthermore, the shoulder at the mid-point on the rising absorption edge for metallic Co, as displayed in Figure 4-3, can shift to lower energy when mixtures are present and this may obscure any pre-edge peak that may exist. EXAFS, on the other hand, does not necessitate the measurement of such a standard and is therefore much more conclusive.

We have used EXAFS to probe the catalyst local structure and it has the revealed the absence of any irreducible bulk-like cobalt species. There are, however, some hard-

to-reduce Co^{2+} particles formed at 500 °C which have structural characteristics dissimilar to those of $CoAl_2O_4$. EXAFS analysis of the Co/Al_2O_3 catalyst, after reduction, derives a Co—O bond length of 2.08 Å which is quite different to the Co—O bond length found in bulk CoO which was found to be 2.13 Å (inadequate *in situ* data quality of CoO prevented the full EXAFS analysis of this reference material and thus the results are not reported. The data acquired under ambient conditions, however, enabled us to determine the Co—O bond length in the bulk structure). This result suggests that there is a non-bulk like CoO phase in the reduced catalyst and, at 500 °C, contains hard to reduce Co^{2+} species. No Co^{3+} species can account for such a large inter-atomic distance either and would be thermodynamically unfavourable regardless. Moreover, the Co—O bond length of 2.08 Å is unambiguous evidence which precludes the formation of a bulk $CoAl_2O_4$ phase, wherein a Co—O bond length of 1.95 Å would be elucidated through EXAFS [68]. These results strongly suggest the interaction of Co^{2+} ions with the alumina support generating a non-bulk like and hard-to-reduce species.

The results of XRD analysis support the analysis of XAS data in that (1) the pre-reduced catalyst contains the spinel structure; (2) Full Co_3O_4 to CoO reduction takes place at ca. 350 °C; (3) the reduction from CoO to metallic Co is a slow process and incomplete. The mixed metallic/oxide phase within the catalyst, in addition to the overlapping reflections belonging to HCP and FCC phase, prevents a full determination of the metallic structure.

TPR profile of the Co/Al_2O_3 catalyst (Figure 4-2) reveals that, at 500 °C, not all cobalt oxide crystallites are reduced to metallic Co. The TPR of bulk CoO mixed with alumina (Figure 4-2) on the other hand shows that the reduction temperature of CoO to metallic Co crystallites are around the region 300 to 400 °C and therefore it could be assumed that all CoO, as Co^{2+}, is reduced by 500 °C. Evidently this is not the case and a significant fraction (*ca*. 45 %) of Co^{2+} ions remain. Whereas in bulk CoO the crystallites are "free" and therefore more easily reduced, in the Co/Al_2O_3 catalyst the oxidic Co species may be highly dispersed and/or have a strong interaction with the support hindering the reduction and thus elevating the reduction

temperature. The broad peak ranging from around 400 to 750 °C signifies a pseudo particle size distribution of easily reducible crystallites to the left and harder to reduce Co crystallites to the right. At 500 °C, the area under the TPR curve, to the left of this temperature, is equivalent to the fraction of Co^{2+} particles that have been reduced to Co^0. In the Co/Al_2O_3 catalyst there is clearly some interaction of Co^{2+} ions with the Al_2O_3 support which brings about the very broad reduction peak. Overall, at 500 °C, the catalyst contains a large proportion of the unreduced species which, from XANES and EXAFS analyses, is of the order *ca*. 45 %. It is clear that cobalt-alumina interactions play a significant role in generating these species and to understand the origin of the irreducible Co component within the catalyst it is important to look at the defect structure of γ-alumina itself.

γ-Al_2O_3 ($Fd\bar{3}m$) has a structure with intrinsic defects that are manifested *via* the formation of tetrahedral and octahedral interstices. These interstitial spaces, or "holes", are generated by the HCP array of oxygen, O^{2-}, within the structure. As a result Al^{3+} ions occupy two thirds of the octahedral holes in the lattice [69, 70]. This allows metal cations, usually of II and III valency, to migrate into these vacant sites. The distance between the O^{2-} ions within the γ-Al_2O_3 lattice determines the type of cation that can fill these holes; for cations whose ionic radius (r^+) is between 0.22 and 0.41 of the O^{2-} ionic radius (r^-) of 1.26 Å, they can occupy the tetrahedral holes in Al_2O_3. If the ratio falls between 0.41 and 0.73 then cations are located within the octahedral sites [71].

Based on our findings we propose several EXAFS models to account for the origins of the unreduced component within the Co/Al_2O_3 catalyst after reduction:

1. Isolated Co^{2+} ions located in the octahedral holes of the Al_2O_3 lattice: The migration of Co^{2+} ions (that are generated from Co^{3+} to Co^{2+} reduction and not from within the spinel structure) into the Al_2O_3 lattice would yield stabilised Co particles that are not easily reduced. Co^{2+} (low spin) has an ionic radius of 0.79 Å [72] and thus an r^+/r^- ratio of 0.63. It is quite feasible,

therefore, that Co^{2+} ions migrate into the alumina framework, filling an octahedral hole. This postulation is based on the EXAFS derived Co—O bond length of 2.08 Å which is too large for Co^{2+} to be located in a tetrahedral site and consistent with earlier similar EXAFS study on γ-alumina supported bimetallic Co-Mo catalysts [73]. A pictorial representation of this structure is depicted in Figure 4-19. NEED TO MENTION CHARGE BALANCE BY OH- AND REMOVAL OF Al3+.

2. Co^{2+} species are anchored onto the surface of the alumina support and so remain in close contact with it: Strong interactions with the support create substoichiometric cobalt surface phases which are difficult to detect *via* XAS and XRD and which are not easily reduced.

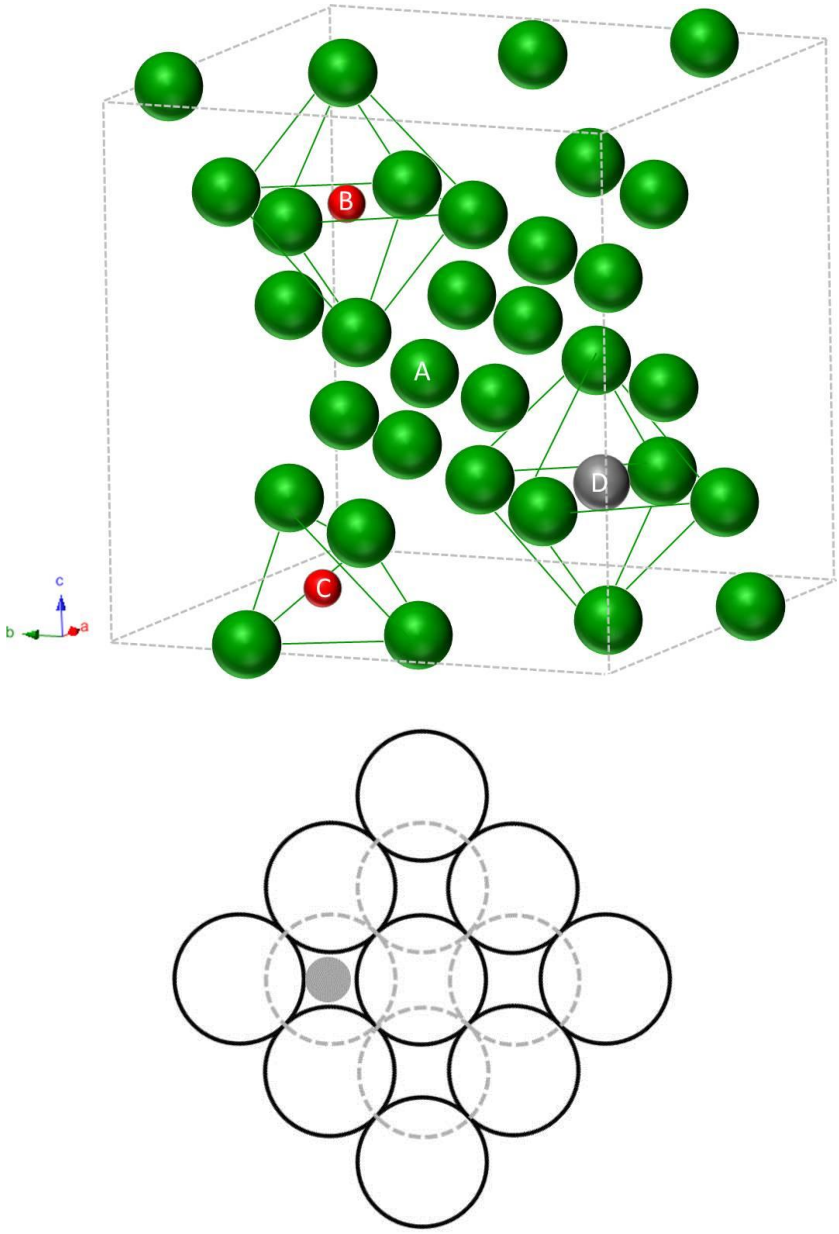

Figure 4-19. *Top: Pictorial view of Co^{2+} ion (D) located in an octahedral hole within the γ-Al_2O_3 lattice where the majority of Al^{3+} ions have been omitted. The γ-Al_2O_3 structure contains cation vacancies where Al^{3+} ions are randomly distributed over tetrahedral (C) and octahedral (B) sites. O^{2-} ions (A) occupy FCC lattice positions. Atomic representation is not to scale or stoichiometry. Below: View down the 100 surface of γ-Al_2O_3 with Co^{2+} in an octahedral hole [adapted from Sankar et al[74]].*

4.6 Conclusion

The reduction behaviour of a model FT catalyst has been investigated using *in situ* XAS/XRD techniques under conditions that are comparable to the reduction of an industrial catalyst and therefore these results are significant in their application to working catalytic systems. By employing the *in situ* XAS technique we have been able to track the structural changes of a γ-alumina supported Co catalyst over the course of its reduction by extracting detailed information surrounding the local atomic structure. Combined with XRD, to probe the long range order, this has enabled us to glean insight into the reduction behaviour of the catalyst. XANES has provided information regarding the electronic and geometric state of Co and using EXAFS the local atomic structure surrounding the Co has been determined. The combination of these techniques is critical in elucidating the catalyst structure over the course of the reduction. Supporting data from laboratory TPR has allowed us to put these results in context.

Using a set of Co containing reference materials, the speciation of the Co/Al_2O_3 catalyst over the course of the *in situ* experiment has been elucidated using XANES LCF. These results reveal that the reduction behaviour of the Co catalyst is quite different to that of the bulk Co_3O_4 reference material. Both the alumina supported catalyst and the bulk cobalt oxide contain the spinel structure prior to reduction and this is maintained in the initial stages of heating under hydrogen. Whilst the reduction of bulk Co_3O_4 to metallic Co occurs relative quickly, *via* CoO as a short lived intermediate, the Co/Al_2O_3 catalyst follows a different trajectory as evidenced by XANES LCF. These results indicate that the pre-reduced catalyst undergoes a complete reduction to CoO which is followed by a slow and partial reduction to the metallic species. The extent of reduction has been shown to be of the order ca. 60 % using this technique. The semi-quantitative evaluation using XANES LCF is concordant with the observations of the *in situ* XANES spectra which, by using the white line intensity and absorption edge position, provides evidence for the incomplete reduction from CoO to metallic Co.

Results of EXAFS analysis from *in situ* data have generated detailed information on the local catalyst structure as it undergoes structural transformations during reduction. The results from EXAFS analysis strongly suggest that the Co/Al_2O_3 catalyst evolves differently under reduction conditions to that of Co_3O_4. The reduction behaviour of the Co/Al_2O_3 catalyst is characterised here by the variation in Co—O and Co—Co bond lengths and first shell coordination numbers. Co_3O_4 undergoes a relatively quick reduction to metallic Co, where the coexistence of $Co^{3+/2+}$—O (spinel) and Co^{2+}—O (CoO) occurs very briefly indicating that CoO exists as a transient phase in the reduction. The complete reduction to metallic Co takes place by 412 °C. Contrastingly, the reduction in the Co/Al_2O_3 catalyst proceeds via an intermediate CoO phase in which the reduction is slower but complete to the Co^{2+} species. The following reduction step, $Co^{2+} \rightarrow Co^0$, is kinetically hindered and after a dwell time of *ca*. 60 minutes the catalyst has undergone an incomplete reduction to metallic Co. The extent of reduction, deduced through EXAFS, is of the order *ca*. 55% which is in good agreement with results of XANES analysis. XRD analysis supports the results from spectroscopic techniques by confirming the catalyst (i) contains Co_3O_4 prior to reduction; (ii) fully reduces to CoO; (iii) undergoes a slow and incomplete reduction to a metallic species. The overlapping reflections belonging to CoO, Co HCP and Co FCC phases impede the full characterisation of the reduced structure *via* XRD.

The absence of any pre-edge peak in the XANES of the Co/Al_2O_3 catalyst after reduction reveals the absence of Co ions of T_d symmetry, or any significant fraction thereof. This implies that the unreduced component of the catalyst contains only Co^{2+} ions of O_h symmetry. Indeed, results of the LCF confirm CoO is present from a XANES point of view. The structure of the unreduced Co^{2+}, however, is not readily assigned to bulk like "free" CoO whereby the results of EXAFS analysis of the reduced Co/Al_2O_3 reveal a Co^{2+}—O bond length of 2.08 Å, much lower than 2.13 Å, the distance found in the bulk. This is a significant result as similar investigations in the literature have proposed that $CoAl_2O_4$ is formed during reduction [44]. The Co^{2+}—O distance found in $CoAl_2O_4$ is 1.95 Å [68] which cannot be extracted through EXAFS analysis thus precludes the formation of $CoAl_2O_4$ based on these results. Furthermore, the literature proposes that Co^{2+} may be located in a tetrahedral hole in

the γ-alumina framework. We do not see any evidence for tetrahedral coordination of Co^{2+} ions from XANES analysis. Based on these EXAFS results we propose that Co^{2+} migrates into the γ-alumina framework upon reduction and occupies octahedral holes. This fraction of cobalt incorporated into the alumina support is not reduced by hydrogen at 500 °C. It should be noted that our evidence is based on our experimental conditions and thus cobalt aluminate formation above 500 °C cannot be excluded. The EXAFS observed distance of 2.08 Å is justifiable based on ionic radii of a low spin Co^{2+} in this site and this distance is too large to fill a tetrahedral site. It is also feasible that Co^{2+} species interact with the surface of the alumina support *via* the creation of substoichiometric surface phases. In both hypotheses these Co^{2+} species lack long-range order, i.e. are non-bulk like. The alumina support anchors these cobalt particles, thereby stabilising them, a phenomenon that is frequently encountered in supported metal catalysts which plays a cooperative role in catalytic activity. In the case of FT catalysis however, this interaction clearly has a detrimental effect by prohibiting the formation of reduced Co particles which are active in FT synthesis.

Further work in this area would include computational modelling studies on the Co^{2+} state within the γ-alumina framework. This would provide further in depth information surrounding the nature of the Co species that exists after reduction. This would develop a clearer picture of the coordination environment around the Co^{2+} ion.

4.7 References

[1] Tavasoli, A.; Abbaslou, R. M. M.; Dalai, A. K., *Applied Catalysis A-General*, (2008) **346**, 58.

[2] Saib, A. M.; Borgna, A.; de Loosdrecht, J. v.; van Berge, P. J.; Niemantsverdriet, J. W., *Applied Catalysis A-General*, (2006) **312**, 12.

[3] van de Loosdrecht, J.; Bazhinimaev, B.; Dalmon, J. A.; Niemantsverdriet, J. W.; Tsybulya, S. V.; Saib, A. M.; van Berge, P. J.; Visagie, J. L., *Catalysis Today*, (2007) **123**, 293.

[4] Moodley, D. J.; van de Loosdrecht, J.; Saib, A. M.; Overett, M. J.; Datye, A. K.; Niemantsverdriet, J. W., *Applied Catalysis A-General*, (2009) **354**, 102.

[5] Saib, A. M.; Moodley, D. J.; Ciobica, I. M.; Hauman, M. M.; Sigwebela, B. H.; Weststrate, C. J.; Niemantsverdriet, J. W.; van de Loosdrecht, J., *Catalysis Today*, (2010) **154**, 271.

[6] Schanke, D.; Hilmen, A. M.; Bergene, E.; Kinnari, K.; Rytter, E.; Adnanes, E.; Holmen, A., *Catalysis Letters*, (1995) **34**, 269.

[7] Enache, D. I.; Rebours, B.; Roy-Auberger, M.; Revel, R., *Journal of Catalysis*, (2002) **205**, 346.

[8] Jacobs, G.; Das, T. K.; Zhang, Y. Q.; Li, J. L.; Racoillet, G.; Davis, B. H., *Applied Catalysis A-General*, (2002) **233**, 263.

[9] Borg, O.; Erib, S.; Blekkan, E. A.; Storsaeter, S.; Wigum, H.; Rytter, E.; Holmen, A., *Journal of Catalysis*, (2007) **248**, 89.

[10] Sirijaruphan, A.; Horvath, A.; Goodwin, J. G.; Oukaci, R., *Catalysis Letters*, (2003) **91**, 89.

[11] Schanke, D.; Vada, S.; Blekkan, E. A.; Hilmen, A. M.; Hoff, A.; Holmen, A., *Journal of Catalysis*, (1995) **156**, 85.

[12] Fischer, N.; van Steen, E.; Claeys, M., *Journal of Catalysis*, (2013) **299**, 67.

[13] Schanke, D.; Vada, S.; Blekkan, E. A.; Hilmen, A. M.; Hoff, A.; Holmen, A., *Journal of Catalysis*, (1995) **156**, 85.

[14] Chu, W.; Chernavskii, P. A.; Gengembre, L.; Pankina, G. A.; Fongarland, P.; Khodakov, A. Y., *Journal of Catalysis*, (2007) **252**, 215.

[15] Jager, B.; Espinoza, R., *Catalysis Today*, (1995) **23**, 17.

[16] Ma, W.; Jacobs, G.; Keogh, R. A.; Bukur, D. B.; Davis, B. H., *Applied Catalysis A-General*, (2012) **437**, 1.

[17] Zhang, Y. L.; Wei, D. G.; Hammache, S.; Goodwin, J. G., *Journal of Catalysis*, (1999) **188**, 281.

[18] Schanke, D.; Hilmen, A. M.; Bergene, E.; Kinnari, K.; Rytter, E.; Adnanes, E.; Holmen, A., *Catalysis Letters*, (1995) **34**, 269.

[19] Dalai, A. K.; Davis, B. H., *Applied Catalysis A-General*, (2008) **348**, 1.

[20] Khodakov, A. Y., *Catalysis Today*, (2009) **144**, 251.

[21] Khodakov, A. Y.; Chu, W.; Fongarland, P., *Chemical Reviews*, (2007) **107**, 1692.

[22] Wang, Z.-j.; Yan, Z.; Liu, C.-j.; Goodman, D. W., *Chemcatchem*, (2011) **3**, 551.

[23] Jacobs, G.; Ma, W.; Davis, B. H.; Cronauer, D. C.; Kropf, A. J.; Marshall, C. L., *Catalysis Letters*, (2010) **140**, 106.

[24] Khodakov, A. Y., *Catalysis Today*, (2009) **144**, 251.

[25] Coulter, K. E.; Sault, A. G., *Journal of Catalysis*, (1995) **154**, 56.

[26] Jacobs, G.; Das, T. K.; Zhang, Y. Q.; Li, J. L.; Racoillet, G.; Davis, B. H., *Applied Catalysis A-General*, (2002) **233**, 263.

[27] Bolt, P. H.; Habraken, F.; Geus, J. W., *Journal of Solid State Chemistry*, (1998) **135**, 59.

[28] Wang, W. J.; Chen, Y. W., *Applied Catalysis*, (1991) **77**, 223.

[29] Jacobs, G.; Chaney, J. A.; Patterson, P. M.; Das, T. K.; Maillot, J. C.; Davis, B. H., *Journal of Synchrotron Radiation*, (2004) **11**, 414.

[30] Chin, R. L.; Hercules, D. M., *Journal of Physical Chemistry*, (1982) **86**, 360.

[31] Hilmen, A. M.; Schanke, D.; Holmen, A., *Catalysis Letters*, (1996) **38**, 143.

[32] Coulter, K. E.; Sault, A. G., *Journal of Catalysis*, (1995) **154**, 56.

[33] Bolt, P. H.; Habraken, F.; Geus, J. W., *Journal of Solid State Chemistry*, (1998) **135**, 59.

[34] Chu, W.; Chernavskii, P. A.; Gengembre, L.; Pankina, G. A.; Fongarland, P.; Khodakov, A. Y., *Journal of Catalysis*, (2007) **252**, 215.

[35] Jacobs, G.; Ji, Y.; Davis, B. H.; Cronauer, D.; Kropf, A. J.; Marshall, C. L., *Applied Catalysis A-General*, (2007) **333**, 177.

[36] Jacobs, G.; Patterson, P. M.; Zhang, Y. Q.; Das, T.; Li, J. L.; Davis, B. H., *Applied Catalysis A-General*, (2002) **233**, 215.

[37] van de Loosdrecht, J.; Bazhinimaev, B.; Dalmon, J. A.; Niemantsverdriet, J. W.; Tsybulya, S. V.; Saib, A. M.; van Berge, P. J.; Visagie, J. L., *Catalysis Today*, (2007) **123**, 293.

[38] Fechete, I.; Wang, Y.; Vedrine, J. C., *Catalysis Today*, (2012) **189**, 2.

[39] Hong, J.; Marceau, E.; Khodakov, A. Y.; Griboval-Constant, A.; La Fontaine, C.; Briois, V., *Chemistry-A European Journal*, (2012) **18**, 2802.

[40] Sadeqzadeh, M.; Karaca, H.; Safonova, O. V.; Fongarland, P.; Chambrey, S.; Roussel, P.; Griboval-Constant, A.; Lacroix, M.; Curulla-Ferre, D.; Luck, F.; Khodakov, A. Y., *Catalysis Today*, (2011) **164**, 62.

[41] Girardon, J. S.; Quinet, E.; Griboval-Constant, A.; Chernavskii, P. A.; Gengembre, L.; Khodakov, A. Y., *Journal of Catalysis*, (2007) **248**, 143.

[42] Khodakov, A. Y.; Lynch, J.; Bazin, D.; Rebours, B.; Zanier, N.; Moisson, B.; Chaumette, P., *Journal of Catalysis*, (1997) **168**, 16.

[43] Jacobs, G.; Ma, W.; Davis, B. H.; Cronauer, D. C.; Kropf, A. J.; Marshall, C. L., *Catalysis Letters*, (2010) **140**, 106.

[44] Jacobs, G.; Chaney, J. A.; Patterson, P. M.; Das, T. K.; Davis, B. H., *Applied Catalysis A-General*, (2004) **264**, 203.

[45] Das, T. K.; Jacobs, G.; Patterson, P. M.; Conner, W. A.; Li, J. L.; Davis, B. H., *Fuel*, (2003) **82**, 805.

[46] Jacobs, G.; Patterson, P. M.; Zhang, Y. Q.; Das, T.; Li, J. L.; Davis, B. H., *Applied Catalysis A-General*, (2002) **233**, 215.

[47] Moodley, D. J.; Saib, A. M.; van de Loosdrecht, J.; Welker-Nieuwoudt, C. A.; Sigwebela, B. H.; Niemantsverdriet, J. W., *Catalysis Today*, (2011) **171**, 192.

[48] Tsakoumis, N. E.; Voronov, A.; Ronning, M.; van Beek, W.; Borg, O.; Rytter, E.; Holmen, A., *Journal of Catalysis*, (2012) **291**, 138.

[49] Ravel, B.; Newville, M., *Journal of Synchrotron Radiation*, (2005) **12**, 537.

[50] Binsted, N., EXCURV98, CCLRC Daresbury Laboratory program (1998).

[51] Hammersley, A., ESRF Internal Report ESRF97HA02T (1997).

[52] Wojdyr, M., *Journal of Applied Crystallography*, (2010) **43**, 1126.

[53] Duan, H. M.; Xu, D. Y.; Li, W. Z.; Xu, H. Y., *Catalysis Letters*, (2008) **124**, 318.

[54] van de Loosdrecht, J.; Barradas, S.; Caricato, E. A.; Ngwenya, N. G.; Nkwanyana, P. S.; Rawat, M. A. S.; Sigwebela, B. H.; van Berge, P. J.; Visagie, J. L., *Topics in Catalysis*, (2003) **26**, 121.

[55] Borg, O.; Blekkan, E. A.; Eri, S.; Akporiaye, D.; Vigerust, B.; Rytter, E.; Holmen, A., *Topics in Catalysis*, (2007) **45**, 39.

[56] Smith, W. L.; Hobson, A. D., *Acta Crystallographica Section B-Structural Science*, (1973) **B 29**, 362.

[57] Becker, H.; Turek, T.; Güttel, R., *Catalysis Today*, (2013) **215**, 8.

[58] Yamamoto, T., *X-Ray Spectrometry*, (2008) **37**, 572.

[59] Sankar, G.; Thomas, J. M.; Rey, F.; Greaves, G. N., *Journal of the Chemical Society-Chemical Communications*, (1995), 2549.

[60] Grandjean, D.; Beale, A. M.; Petukhov, A. V.; Weckhuysen, B. M., *Journal of the American Chemical Society*, (2005) **127**, 14454.

[61] Huffman, G. P.; Shah, N.; Zhao, J. M.; Huggins, F. E.; Hoost, T. E.; Halvorsen, S.; Goodwin, J. G., *Journal of Catalysis*, (1995) **151**, 17.

[62] Storsæter, S.; Tøtdal, B.; Walmsley, J. C.; Tanem, B. S.; Holmen, A., *Journal of Catalysis*, (2005) **236**, 139.

[63] Jacobs, G.; Das, T. K.; Zhang, Y. Q.; Li, J. L.; Racoillet, G.; Davis, B. H., *Applied Catalysis A-General*, (2002) **233**, 263.

[64] Jacobs, G.; Chaney, J. A.; Patterson, P. M.; Das, T. K.; Maillot, J. C.; Davis, B. H., *Journal of Synchrotron Radiation*, (2004) **11**, 414.

[65] Greenwood N, E. A., *Chemistry of the Elements*, Pergamon Press: New York, (1984); p 1294.

[66] Barrett, P. A.; Sankar, G.; Catlow, C. R. A.; Thomas, J. M., *Journal of Physical Chemistry*, (1996) **100**, 8977.

[67] Moen, A.; Nicholson, D. G.; Ronning, M.; Emerich, H., *Journal of Materials Chemistry*, (1998) **8**, 2533.

[68] Pettiti, I.; Colonna, S.; De Rossi, S.; Faticanti, M.; Minelli, G.; Porta, P., *Physical Chemistry Chemical Physics*, (2004) **6**, 1350.

[69] Lodziana, Z.; Topsoe, N.-Y.; Norskov, J. K., *Nat Mater*, (2004) **3**, 289.

[70] Paglia, G.; Buckley, C. E.; Udovic, T. J.; Rohl, A. L.; Jones, F.; Maitland, C. F.; Connolly, J., *Chemistry of Materials*, (2004) **16**, 1914.

[71] Huang P, H. P. M., Li Y, Sumner M, *Handbook of soil Sciences: Properties and Processes*, CRC Press: (2012).

[72] Degen, O.; Eitinger, T., *Journal of Bacteriology*, (2002) **184**, 3569.

[73] Sankar, G.; Vasudevan, S.; Rao, C. N. R., *Journal of Physical Chemistry*, (1987) **91**, 2011.

[74] Sankar, G.; Vasudevan, S.; Rao, C. N. R., *Journal of Physical Chemistry*, (1986) **90**, 5325.

Chapter 5 Elucidation of structure and the nature of PdO-Pd transformation using *in situ* PDF and XAS techniques

5.1 Chapter Overview

The PdO-Pd phase transformation in a 4 wt.% Pd/Al_2O_3 catalyst has been investigated using *in situ* X-ray absorption spectroscopy (XAS) and *in situ* X-ray total scattering (also known as high-energy X-ray diffraction) techniques. Both the partial and total pair distribution functions (PDF) from these respective techniques have been analysed in depth. New information from PDF analysis of total scattering data has been garnered using the differential PDF (d-PDF) approach where only correlations orginating from PdO and metallic Pd are extracted. This method circumvents problems encountered in characerising the catalytically active components due to the diffuse scattering from the disordered γ-Al_2O_3 support phase. Quantitative analysis of the palladium components within the catalyst, allowed for the phase composition to be established at various temperatures. The transformation from PdO to Pd takes place and, although rapid above 850 °C, appears to be incomplete at 900 °C. Complementary *in situ* XANES and EXAFS were performed and the results of the analyses support the observations, that residual PdO is detected at elevated temperatures. Hysteresis in the transformation upon cooling is confirmed from XAS studies where reoxidation occurs below 680 °C.

5.2 Introduction

Supported palladium catalysts have found several applications in the field of catalysis, in particular, methane combustion, hydrogenation and for diesel oxidation (in combination with other metals)[1-5]. Owing to successful applications in these fields, several studies have focussed on the oxidation and reduction properties of palladium supported catalysts and more importantly the transformation of PdO to Pd metal in air at elevated temperatures, where it has been shown, for example, that the conversion of PdO to Pd during the high temperature methane oxidation reaction has a profound effect on catalyst reactivity[1, 6, 7]. This transformation is found to be reversible but with a hysteresis in the reaction; the first PdO to Pd transformation occurs above 850 ˚C and the reverse (oxidation of Pd metal) takes place below 700˚C[6]. It is also observed that the transformation from PdO to Pd generally leads to a decrease in catalytic activity[8]. Some studies have, however, demonstrated that metallic Pd exhibits higher activity than PdO for the methane oxidation reaction particularly at higher temperatures[5, 9]. Studies by Lyobovsky *et al*, performed on α-alumina plates, have consistently shown that catalyst activity increases as the PdO is transformed to Pd metal[10].

Understanding the phase transformation is of considerable importance for high temperature combustion catalysis where predictable catalyst activity is necessary for stable operation. Several techniques have been employed in the literature to investigate this phase transformation, which include thermogravimetric analysis[11] , electron microscopy[6], X-ray photoelectron spectroscopy[6, 12], X-ray diffraction[6] and X-ray absorption spectroscopy at the Pd K-edge[13] to understand the kinetics of transformation, morphological effects and in general reactivity of the oxide and metal. In addition to this, studies have also been conducted to investigate the nature of the support such as on promoted alumina and ceria[14]. The key issue which remains unclear is whether the transformation is complete when the conversion of PdO to Pd metal occurs at elevated temperatures. Moreover, detailed structural information relating to the PdO ↔ Pd transformation in air derived from *in situ* studies are scarce[15] and other studies employed in this area have been performed *ex situ*[6]. For these purposes it is necessary to use X-ray absorption spectroscopy, as

this technique is sensitive to only local structure and does not depend on long-range order[16, 17]and is ideal for *in situ* investigations of this nature. Furthermore, if a highly dispersed phase is present in small quantities (of the order of *ca.* 10%) X-ray diffraction will not provide adequate information.

While XAS is considered as the most suitable technique for such investigations, the recent advances in the X-ray total scattering technique make it well suited to study the structure of materials with limited structural coherence. In particular, using the pair distribution function (PDF) method, it is possible to extract the structure of amorphous materials[18-20] which is indeed how this technique was first developed. More recently the PDF method has been successfully applied to characterise materials of technological importance that display ordered and disordered components at varying length scales such as defect structures and locally disordered materials as well as nano-crystalline materials[21-23] Furthermore, this technique can provide structural information over much larger distances compared to XAS since this method does not suffer from $1/r^2$ dependence of amplitude as well as effects from multiple-scattering which prevents a clear determination of the structure of disordered solids using the XAS technique. We have demonstrated the efficacy of this technique in chapter three by determining the phase composition in metallic cobalt powders using *in situ* PDF data.

In order to employ this technique for supported catalytic systems, in particular to extract information on the metal oxide/metal particles which are present in low concentrations, it is necessary to employ differential PDF method in which the major support oxide component is removed by subtraction; this method of analysis has been successfully applied to supported metal clusters[24] and some earlier work on amorphous systems[25]. More recently *in situ* studies on nanoporous materials, zeolites, TiO_2 and Al_2O_3-supported nanoparticles have been investigated using the differential PDF approach[23, 26-28].

5.3 Aims and Objectives

The aim of this study is to understand the PdO ↔ Pd phase transformation in a supported palladium catalyst using *in situ* PDF and XAS techniques. By employing the differential PDF approach we aim to obtain a quantitative measure of the metallic/oxide phase composition at ambient and elevated temperatures. The results from *in situ* PDF will be cross-correlated with those from *in situ* XANES and EXAFS analyses.

5.4 Experimental

5.4.1 Sample preparation

A model 4 wt.% Pd/Al_2O_3 catalyst was prepared by a conventional procedure using a $Pd(NO_3)_2$ precursor salt via incipient wetness impregnation onto a SASOL γ-Al_2O_3 support with subsequent drying and calcination at 500 °C for 2 hrs. A sample from the batch of γ-Al_2O_3 (SASOL) was used as received for *in situ* PDF and XAS studies.

5.4.2 X-ray total scattering measurements

In situ PDF data were collected at BL04B2 (High-Energy X-ray Diffraction) beam line at the SPring-8 synchrotron, Japan. Details of the beam line are described in chapter two and in the literature [18]. For this work γ-Al_2O_3 and 4 wt.% Pd/Al_2O_3 samples were prepared by grinding and loading into quartz capillaries (1.0 mm internal diameter). Data were recorded for γ-Al_2O_3–supported Pd and the bare γ-Al_2O_3 support samples in air at room temperature, 700 °C (below the transformation as described in the literature) and at 900 °C (above the transformation temperature as described earlier). Scattered X-rays from the sample were collected in step-scan mode using a Ge detector integrated with a multichannel analyser at a wavelength of λ = 0.2018 Å over a 2θ range of 0.3 to 48.2°, corresponding to a Q range of 0.16 to 25.43 $Å^{-1}$, where counting times and step sizes were varied accordingly. Although recent advances in detector technology have facilitated very fast data acquisition, thus enabling the characterisation of dynamic systems using 2D image plate (detectors such as flat plate Si detectors)[28-30], it was not necessary to use such techniques in this particular case since the transformation is temperature dependent. For kinetic dependent studies it is appropriate to employ such time-resolved studies. Indeed it is somewhat more industrially relevant to understand these transformations averaged over longer timescales. Furthermore, the long measurements (ca. 3.5h) employed in this study allowed for high quality data to be acquired with a low background and the minimisation of incoherent scattering at high-Q.

5.4.3 X-ray absorption spectroscopy measurements

XAS data were measured *in situ* at the Pd K-edge (24,350 eV) at specific temperatures at BM26A, at the European Synchrotron Radiation Facility (ESRF). This beam line is equipped with a Si(111) monochromator and ionization chambers for measuring incident and transmitted beam intensities. A custom made high-temperature *in situ* cell was used for this study. EXAFS data were acquired in step scans over a *k* range (*k* being the photoelectron wave vector) from 3 $Å^{-1}$ to 12 $Å^{-1}$. In a typical experiment 100 mg of the Pd/Al_2O_3 catalyst was pelletised and loaded into a custom made *in situ* cell. XAS data collection was carried out while heating the sample at 5°C/min, in air, from room temperature to 900 °C and the data collection continued during cooling back to room temperature. A typical scan time taken was *ca*. 15 minutes.

5.3.4 Data analysis

5.4.4.1 PDF analysis

In order to extract the $G(r)$ data, raw X-ray total scattering data were processed using Igor (WaveMetrics, Inc., Lake Oswego, OR, USA) software and a macro developed by BL04B2 beam line to correct for instrument background, polarisation, self-absorption, and Compton scattering. X-ray total scattering data of an empty quartz capillary was used as a background, measured using similar experimental parameters. A terminating Q_{max} of 25.0 $Å^{-1}$ was used in the analysis and the Fourier transformation of the reduced $Q[S(Q)-1]$ resulted in a pair distribution function, $G(r)$, with a resolution Δr ($=2\pi/Q_{max}$) of 0.25 Å. To characterise the metal particles of interest and track the structural changes in the Pd/Al_2O_3 sample it was necessary to remove the diffuse scattering component originating from the γ-Al_2O_3 support phase which dominates the PDF. By subtracting the PDF of the Al_2O_3 support phase from that of the Pd/Al_2O_3, the differential PDF (d-PDF) is generated and the Pd-X (X = Pd, O) correlations within the sample can be isolated.

$$[G(r)\ Pd/Al_2O_3\ \text{catalyst/support}] - [G(r)\ Al_2O_3\ \text{support}] = G(r)\ \text{Pd catalyst}$$

Oxygen scattering is not removed *via* this subtraction, however the amplitude of O-O X-ray scattering is small and therefore is not a heavily weighted component of the PDF. This subtraction can be performed on the structure factor, $S(Q)$, or the total pair distribution function, $G(r)$. Generating the differential PDF (d-PDF) using $G(r)$ is preferred because systematic errors in the analysis cancel and moreover, the data can be normalised with respect to the first peak in the PDF which corresponds to the Al-O correlation. The Al-O peak at 1.84 Å is well below the first Pd-O or Pd-Pd in PdO and metallic Pd structures so should not affect the interpretation and analysis of the metal particles. It is important to note, and in fact crucial to the reliability of the methodology, that upon heating the first Al-O correlation in γ-Al_2O_3 moves to lower distance and thus the d-PDF would be unreliable in the low-*r* region. To circumvent these issues the d-PDFs were obtained using the γ-Al_2O_3 support phase as a background in $G(r)$ data modelling, measured at the same temperature as the Pd/Al_2O_3 sample. With these considerations in place the metal particle d-PDF is readily obtained.

The reduced d-PDF contains structural information that can be obtained directly without further correction or curve fitting analysis. The peak positions in the d-PDF provide a direct measurement of the interatomic distances from Pd species within the sample and, unlike in EXAFS analysis which must take into account atomic potentials and phase shifts, this can be obtained without any theoretical description of the system *a priori*. To obtain more detailed quantitative structural information, fitting the experimental PDF to a structural model is required. Structural refinement using a model was performed using PDFgui software[31]. PDF analysis is a real-space structural refinement yielding structural parameters analogous to the Rietveld method and is a desirable program for modelling systems with crystallographic components since a structure file containing atomic coordinates, such as a crystallographic information file, can be used, complementary to the periodic boundary conditions that the program uses. Analysis was performed using a Q_{max} of 25 $Å^{-1}$ and *r*-space fits were obtained over a 1 to 10 Å range (higher distance fits were performed although the quality of fits obtained were of the same order as a smaller fit range and the results from varying fit ranges were in agreement). Instrumental peak dampening and broadening parameters, Q_{damp} and Q_{broad}, were

unstable and thus not refined. These parameters have little or no effect on the PDF up to 10 Å. The d-PDFs generated were analysed by taking PdO and Pd metal clusters simultaneously, as multi-cluster models. For each phase the lattice parameters (PdO *a*,*c* and Pd *a*), phase scale factors (X), the linear atomic correlation factor (δ_1) and atomic displacement parameters (*U)* were refined. Fits were optimised by refining the atomic displacement parameters isotropically and constraining the values to be the same for each phase. The atomic coordinates of $Fm\bar{3}m$ and $P4_2/mmc$ metallic Pd and PdO structures, respectively, are all located on special positions and thus fixed in the refinement. The anisotropic atomic displacement parameters and occupancies were set to default values, 0 and 1, respectively. The *spdiameter* parameter, which is used to determine the nanoparticle size, can be highly correlated to other parameters determining peak shape and height and did not yield acceptable values in the refinement and was therefore set to zero and not refined. Useful particle size information from XRD did not improve the stability of this parameter in refinements. The two delta parameters, δ_1 and δ_2, account for low-*r* peak sharpening in the PDF due to correlated atomic motion. For analysis of the Pd systems only δ_1 had an effect on the fit and was therefore refined.

The parameterisation of variables in this manner is a consistent approach to a mixed Pd phase system which reduces the number of free parameters in the fit and correlations between them. The phase scale factors for each cluster were refined and provide a quantitative description of the phase composition where the respective values of the PdO and Pd metallic phases reflect the contribution of each phase to the experimental PDF, hence the relative amounts of PdO and Pd metal within the sample. The goodness of fit, $R_{w,}$ values were found to be larger than which is traditionally obtained in PDF analysis, attributed to artefacts and statistical error introduced by the subtraction method. In all instances a refinement generating physically meaningful values of structural parameters was a criterion for a successful model.

5.4.4.2 XANES linear combination fitting

Linear combination fitting (LCF) of normalised catalyst XANES $\mu(E)$ spectra was performed with the Athena program[32] using XANES spectra of bulk PdO and Pd foil reference materials representing Pd^{2+} and Pd^{0} species, respectively. Fits were performed on data at each temperature over the range −30 eV to +60 eV around the absorption edge. Spectra were calibrated in energy with respect to Pd foil data (24,355 eV) and standards were constrained to use the same E_0. The weightings for each standard were constrained to be between 0 and 1 and to sum to 1 and best linear combinations fits were obtained using this routine. The fit quality was examined using *R*-factors and were consistently low (R = 0.00020±0.00009) and for this reason are not individually reported in the results section.

5.4.4.3 EXAFS analysis

Raw XAS data were background subtracted and normalised using Athena software[32]. The extracted $\chi(k)$ data was subject to curve fitting analysis using the EXCURVE98 program. Phase shifts and backscattering factors were calculated *ab-initio* using Hedin-Lundqvist potentials. EXAFS data were analysed using a single scattering curved wave approximation [33] and the refinement performed with a k^3 weighting using a *k*-range of 3.0 to 10.0 $Å^{-1}$. Data were processed without using any Fourier filtering techniques. The non-structural parameter AFAC (S_0^2) was obtained from first shell analysis of Pd foil EXAFS data. The refinement of the AFAC, with the Pd-Pd coordination number set to the crystallographic value (FCC structure, N=12), yielded a value of 0.83 and this was fixed for analysis of Pd/ Al_2O_3 EXAFS data. Analysis was limited to the first two shells in the Fourier transformed data (of Pd-O and Pd-Pd) and multiple scattering calculations were not required for this approach.

5.5 Results and discussion

The results obtained from *in situ* PDF measurements shall first be dsicussed which includes differential PDF multi-cluster modelling. Following this, the results from *in situ* XANES and EXAFS analysis shall be evaluated and compared to those from differential PDF modelling.

5.5.1 Particle size characterisation

Our recently published article in PCCP provides details on particle size characterisation [34]. In summary, *in situ* XRD was employed on the 4 wt. % Pd/Al_2O_3 system and identified only PdO particles, of *ca*. 4.6 nm, in the starting material. Data recorded at 900 °C revealed only metallic Pd particles of *ca*. 23 nm. The increase in particle size was likely attributed to sintering at high temperature. TEM provided supporting particle size information which was in good agreement with XRD indicating the presence of small Pd containing particles, *ca*. 3-5 nm, in the starting material. Using TEM it was not possible to distinguish between PdO and Pd particles.

5.5.2 *In situ* PDF

Figure 5-1 displays the total scattering structure functions, $S(Q)$, for 4 wt.% Pd/Al_2O_3 and γ-Al_2O_3 samples measured at room temperature, 700 °C and 900 °C. The $S(Q)$ data for Pd-RT and Pd-700 are very similar suggesting the structure is maintained upon heating up to 700 °C. The Bragg peaks pertaining to the reflections of PdO are highlighted in the data. At 900 °C additional peaks in the $S(Q)$, originating from metallic Pd, are observed. The $S(Q)$ data for the γ-Al_2O_3 bare support phase shows very little difference over the heating and cooling cycle, thus confirming that only γ-Al_2O_3 is present and that no other transitional aluminas are formed during the heating and cooling process.

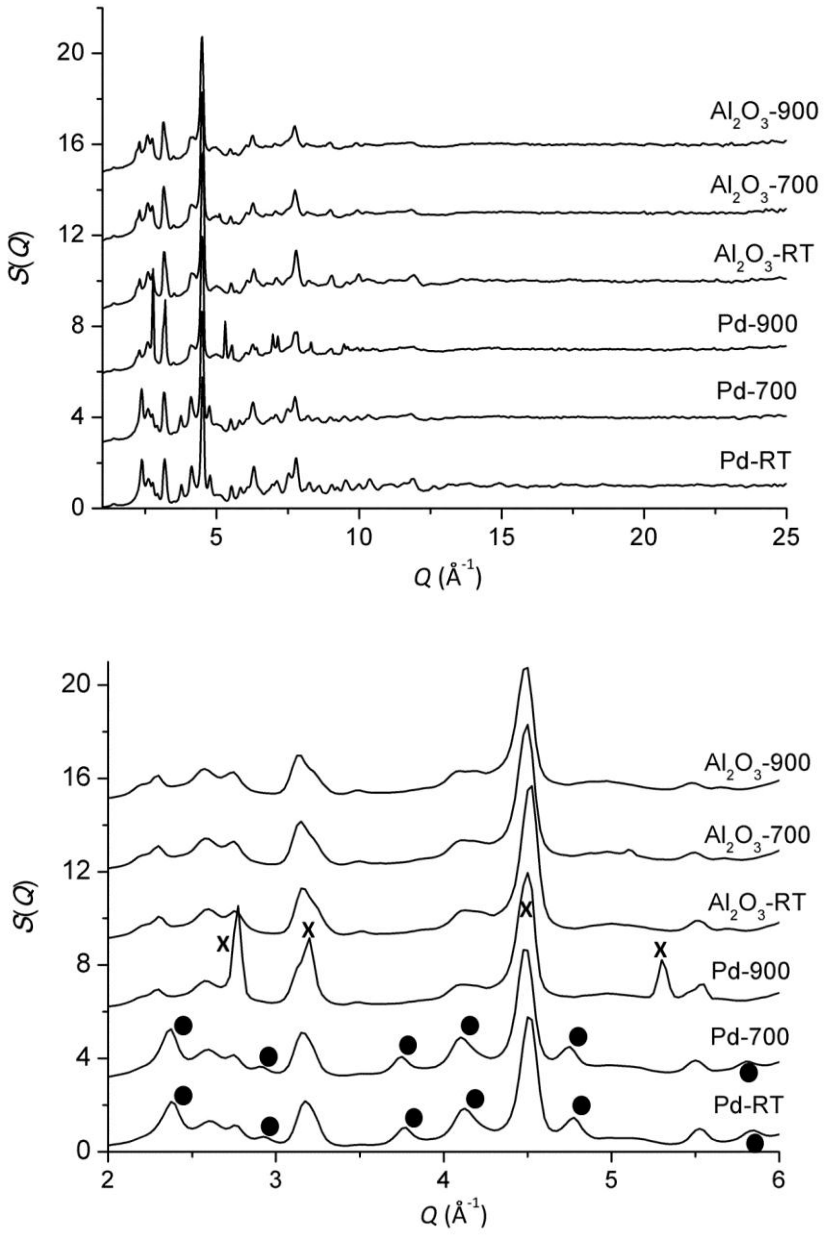

Figure 5-1. *Total scattering structure functions, S(Q), for 4 wt.% Pd/Al_2O_3 and γ-Al_2O_3 samples obtained in situ during heating. S(Q) (below) is expanded in the region 2 to 6 $Å^{-1}$ highlighting the reflections belonging to PdO (circles) and Pd metal (crosses). All other peaks originate from γ-Al_2O_3.*

The PDFs, in the *r*-range 1 to 10 Å, are displayed in Figure 5-2. Only the room temperature PDF of the γ-Al_2O_3 support is shown since the support PDF over several temperatures used in this study is largely similar (only the first peak originating from

the Al-O correlation shifts to lower distance). The experimentally observed PDF gives the sum of all partial PDFs thus giving all interatomic correlations within the sample. Atom pairs that are close in distance, however, may hinder the interpretation; Pd-Pd distance in the metal, for example, is close to 2.74 Å and the O-O distance from the support is *ca*. 2.65 Å therefore these peaks can have overlap, although the amplitudes of O-O scattering may be significantly smaller compared to those of Pd-Pd. Moreover, the poorly crystalline nature of the γ-Al_2O_3 support phase significantly hinders interpretation of the PDF and the metallic particles (at 4 wt.%). The first peak observed in each of the PDFs at 1.86 Å is identified as the first Al-O correlation from the γ-Al_2O_3 support. There is a shift in peak position to lower-*r* upon heating (1.86 → 1.84 Å) and this is the Al-O bond length decreasing due to dehydration of the γ-Al_2O_3 matrix which suggests some of the Al^{3+} ions may have tetrahedral coordination; it is difficult to rule of the presence of some 5 coordinated Al^{3+} ions. Underlying differences between the PDFs can nevertheless be observed indicating that the metal particles are undergoing structural changes and this is apparent when looking at the short-range order through the emergence of the peak between 2.75 and 2.80 Å.

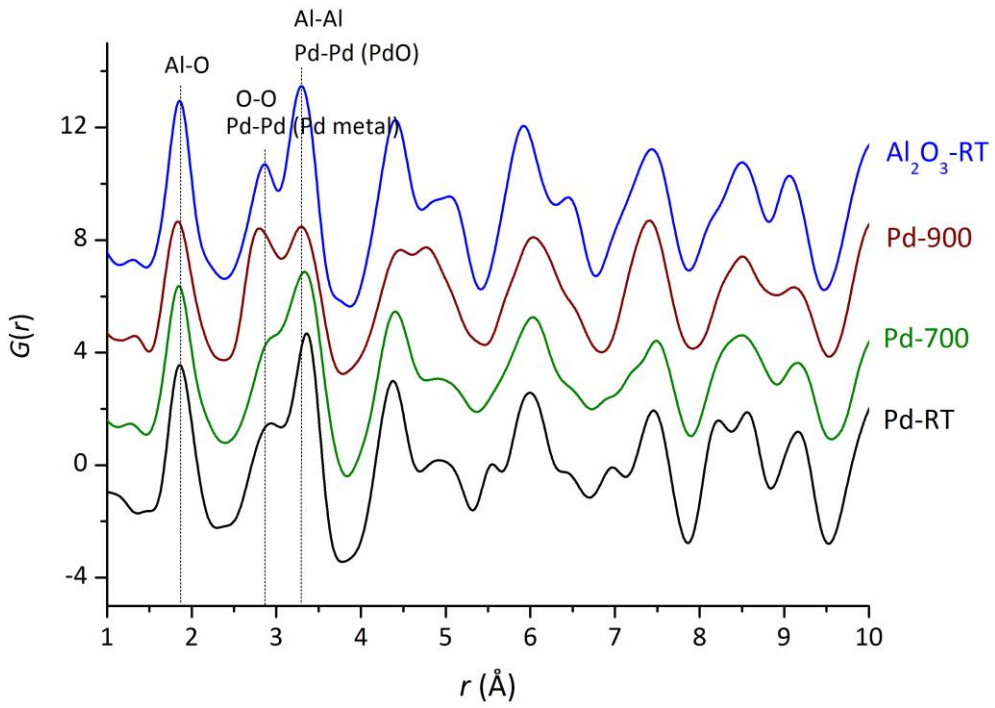

Figure 5-2. *In situ PDFs of the 4% Pd/Al_2O_3 sample at room temperature, 700 ˚C and 900 ˚C along with the PDF of the γ-Al_2O_3 support at room temperature. Short-range correlations belonging to γ-Al_2O_3, PdO and Pd metallic phases are annotated highlighting the overlapping peaks from the multi-phase system.*

The refined structural parameters obtained from fitting of *in situ* d-PDF data using multi-cluster modelling are listed in Table 5-1. The respective models, consisting of PdO and metallic Pd phases, show moderately good agreement with the experimental d-PDF data, where fits were performed up to 10 Å. Since the γ-Al_2O_3 matrix contribution has been removed from the total PDF, only Pd-Pd, Pd-O and O-O (contribution is small) correlations are present in the d-PDF. The best fits of the d-PDFs using multi-cluster modelling are illustrated in Figure 5-3.

Table 5-1. *Results of in situ d-PDF (1 to 10 Å range) analysis of Pd/Al_2O_3 using multi-cluster models. Relative phase fractions (X), calculated by PDFgui, for PdO and Pd phases are reported.*

	Pd-RT	**Pd-700**	**Pd-900**
a (PdO) / Å	3.029(5)	3.042(13)	3.298(45)
c (PdO) / Å	5.358(16)	5.393(37)	5.036(130)
a (Pd) / Å	3.952(35)	3.919(97)	3.936(6)
PdO cell volume / $Å^3$	49.145	49.913	54.781
U_{iso} Pd / $Å^2$	0.0058(16)	0.0116(45)	0.0245(29)
U_{iso} O / $Å^2$	0.0058(16)	0.0116(45)	0.0245(29)
X_{PdO}	0.97	0.98	0.34
X_{Pd}	0.03	0.02	0.66
R_w (%)	34	32	27

The Pd-RT d-PDF fit shows a relatively large residual (R_w = 34%) which is mainly due to some low amplitude peaks in the PDF in the low-*r* region. This is likely due to the *G*(*r*) subtraction which introduces artefacts into the d-PDF. This is rationalised by the presence of non-structural oscillations in the d-PDF which are found most prominently in the low-*r* region due to the Fourier transformation of *S*(*Q*) which has a large scattering contrast between oxygen and palladium.

Table 5-2 displays the inter-atomic distances obtained from best d-PDF fits using multi-cluster models. The first peak in the PDF (Figure 5-3) corresponds to the Pd-O bond length of *ca.* 2.02 Å. The refinement of the PdO and Pd phase scale factors indicate the sample consists predominantly of PdO. The Pd–Pd correlations originating from metallic Pd are not clearly observed and the value for the Pd phase scale factor is negligible. The PdO lattice parameters are consistent with crystallographic data for tetragonal PdO with space group symmetry $P4_2/mmc$[35]. The isotropic atomic displacement parameters, U_{iso}, increase, as expected, with temperature due to increased thermal motion.

Table 5-2. *Inter-atomic distances (in Ångströms) obtained from best d-PDF fits*.

Pd-RT	**Pd-700**	**Pd-900**
2.02 (Pd-O)	2.03(Pd-O)	2.08 (Pd-O)
2.68 (O-O)	2.70 (O-O)	2.52 (O-O)
3.03 (Pd-Pd, O-O)	3.04 (Pd-Pd, O-O)	2.78 (Pd-Pd)*
3.43 (Pd-Pd)	3.45 (Pd-Pd)	3.29 (Pd-Pd)
3.64 (Pd-Pd)	3.66 (Pd-Pd)	3.43 (Pd-Pd)
4.04 (O-O)	4.06 (O-O)	3.90 (Pd-O)
4.28 (Pd-Pd, O-O)	4.30 (Pd-Pd, O-O)	3.94 (Pd-Pd)*
4.29 (Pd-O)	4.32 (Pd-O)	4.12 (Pd-O)
4.74 (Pd-O)	4.76 (Pd-O)	4.15 (O-O)
		4.67 (Pd-Pd, O-O)
		4.82 (Pd-Pd)*

*Pd-Pd correlations from metallic palladium.

Modelling the d-PDF data at 700 °C shows an increase in the PdO lattice parameters which is likely to be due to thermal expansion of the lattice where the Pd-O bond distance increases to 2.03 Å and which is consistent with reported values[36]. The peaks in the d-PDF have broadened due to the increase in thermal disorder as indicated through the enlargement in the *U* parameter. Again, the low-*r* region displays the greatest difference between the model and experimental data, in particular the first peak (Pd-O) cannot be modelled accurately since the procedure we employ (PDFgui) requires a crystal structure model. Without much information from conventional diffraction, it is difficult to identify which type of crystal structure that may represent a distorted Pd-O distance or a PdO suboxide[37] therefore it may be necessary to employ other techniques, such as the Reverse Monte Carlo (RMC) method, to resolve this. This methodology has demonstrated its effectiveness in elucidating the structure of amorphous and poorly crystalline materials using total scattering PDF data[38, 39]. The Pd metal phase factor (X_{Pd}) is very low indicating, within experimental uncertainty, the likely absence of any Pd metallic phase. The

PdO structure and relative concentration is maintained at 700 °C where the fit (R_w = 32 %) is similar to that for Pd-RT data. Qualitatively, from phase composition, these results are consistent with the reduction behaviour of PdO where various studies have shown that the PdO to Pd^0 reduction does not take place until ~ 850 °C and this is also evident in supported Pd catalysts[4].

Multi–cluster analysis, by taking both PdO and Pd metal phases in the starting model, of Pd-900 data gives an improved fit with a fit residuum of 27 %. Low amplitude peaks, particularly between 3 and 6 Å are not well modelled, most likely resulting from generation of the d-PDF and lack of information about the phase associated with palladium oxide. The reduction in X_{PdO} and large increase in X_{Pd} indicates that the Pd/Al_2O_3 sample has undergone incomplete reduction since significant amounts of residual PdO are detected in the analysis. The emergence of the peak at *ca.* 2.80 Å corresponding to the Pd-Pd metallic bond distance is clearly observed; Pd-Pd distance obtained from this study (*ca*. 2.74Å) is likely to be due to the lattice expansion of Pd metal phase. PdO lattice parameters have changed significantly; the *a* parameter has increased by *ca.* 0.25 Å and the *c* parameter decreased by *ca*. 0.35 Å. It is important to note that this analysis was performed assuming PdO crystal structure is retained (search for a known phase containing Pd-Al-O in the CDS database did not yield any result). Perhaps there are some rearrangements at high temperature and PdO is present not as a bulk like structure but as some irreducible surface species. In the d-PDF features at *ca.* 5.5 Å do not fit well to the model in addition to the features around 2 Å where one would expect Pd-O correlations. Inspection of the diffraction data (Figure 5-1), $S(Q)$, does not reveal any reflections that may originate from a known palladium suboxide, PdO_x, hence it is difficult to model the PDF data associated with Pd-O correlations. Furthermore, highly dispersed particles of PdO may go undetected in the X-ray diffraction data. Quantitative phase composition obtained from the PDF analysis is given in Table 5-1. The results show at 900 ˚C *ca*. 70 % (by number) of metallic Pd is formed indicating the incomplete reduction of PdO to Pd^0. This is in contrast to the results obtained *via* laboratory XRD studies carried out by us and by other authors[40] which does not detect any unreduced PdO and the reduction is considered to be complete.

Selected interatomic distances obtained from the d-PDF analysis are listed in Table 5-2.

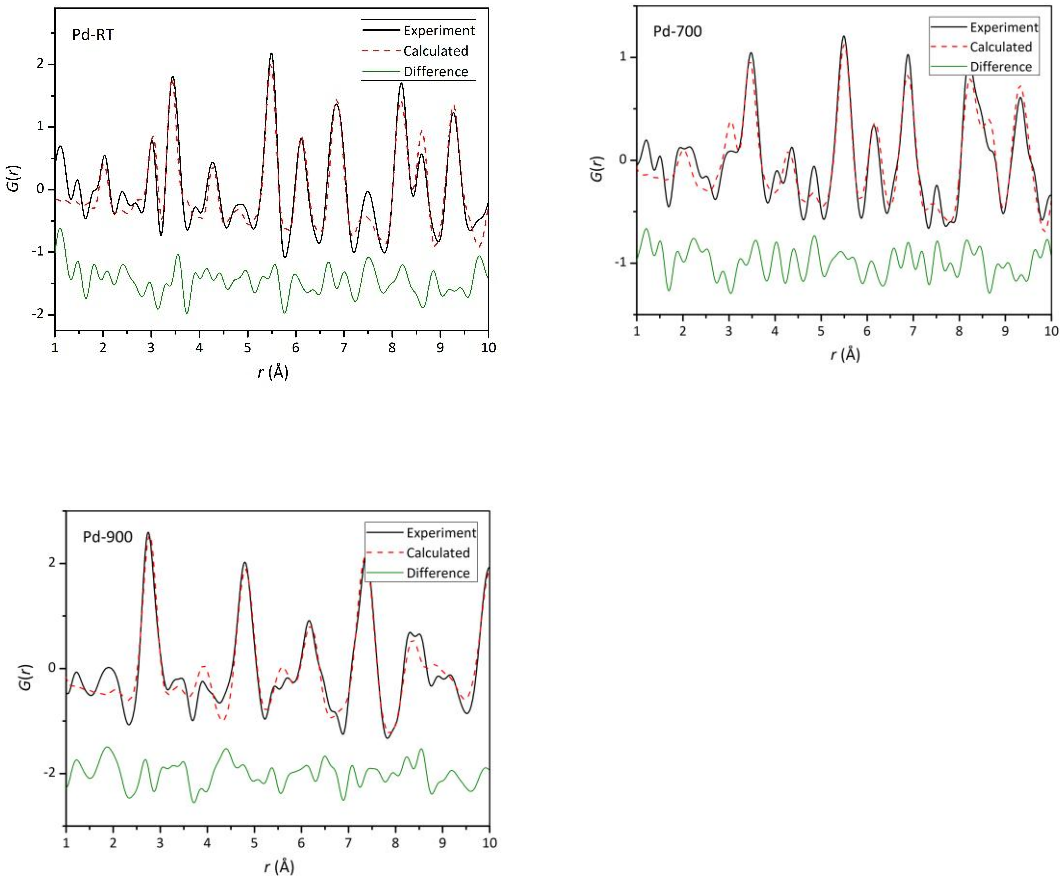

Figure 5-3. *Best fits of the experimental in situ d-PDFs (black line) measured at room temperature (top), 700 °C (middle) and 900 °C (bottom) to calculated PDFs (red line) using multi-cluster models (1-10 Å) with the residual spectrum below (green line).*

5.5.3 *In situ* XANES

The *in situ* Pd K-edge XANES spectra obtained from the heating and cooling of the Pd/Al_2O_3 model catalyst sample are displayed in Figure 5-4. XANES spectra of bulk PdO and Pd foil standard samples (Figure 5-4 inset) were used in fingerprinting the model catalyst XANES by the assignment of diagnostic spectral features originating from the XANES of the reference materials. These plots reveal three distinct regions from the *in situ* heating and cooling. The first region, marked (1), recorded between room temperature and *ca.* 830 °C closely resembles the XANES profile of the PdO reference material. The second region, marked (2), displays clear changes in the near-edge structure, evidenced by the decrease in white line intensity and shift of the absorption edge to lower energy by *ca*. 1.7 eV. In comparison a 2.1 eV shift is observed based on the model compounds which suggests that an incomplete reduction to Pd metal has taken place. These observations are consistent with d-PDF analysis. The presence of an isosbestic point at *ca*. 24,385 eV confirms that the sample is composed of the PdO and metallic Pd with no intermediate species being formed. The XANES profiles in region (3), data recorded during cooling cycle, between 580 °C and room temperature, match that of PdO confirming the reoxidation of the metallic phase to PdO.

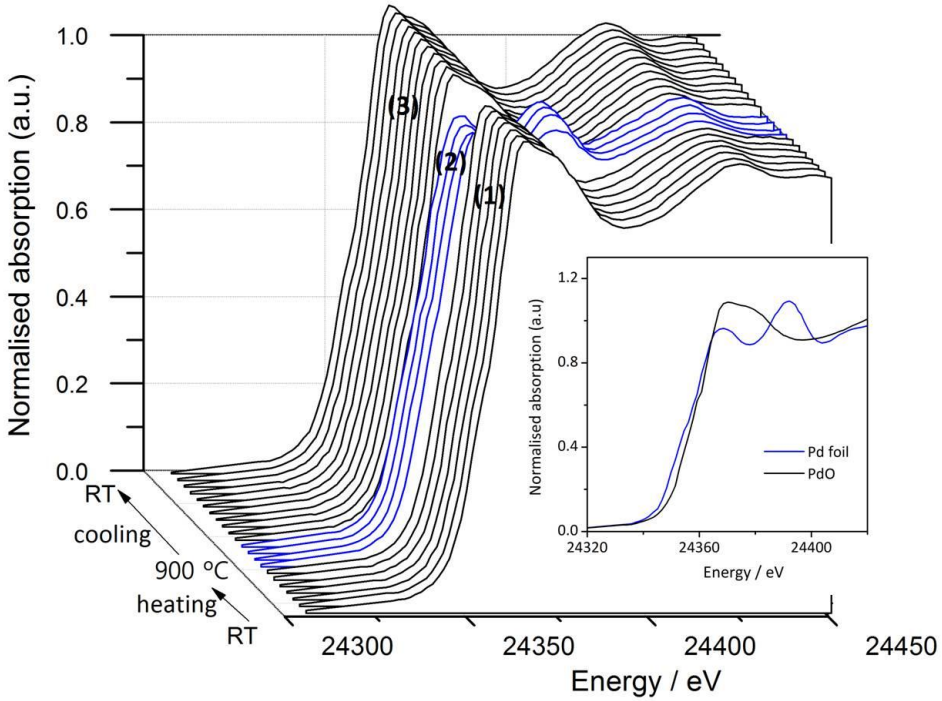

Figure 5-4. *In situ XANES plots from the heating and cooling of Pd/Al_2O_3 model catalyst. Insert shows the XANES of PdO and Pd foil reference materials. Three regions over the heating and cooling are observed. (1) The catalyst has PdO structure with heating to 830 °C. (2) The incomplete reduction to metallic Pd takes place at 900 °C and metallic Pd is detected on cooling to 680 °C. (3) The reoxidation to PdO has taken place at 580 °C.*

In order to extract quantitative information on the phase factions, linear combination fitting (LCF) of the normalised Pd K-edge XANES spectra was performed, taking PdO and Pd metal foil as reference compounds. Excellent quality fits were obtained using a fit range of −40 to +60 eV around the absorption edge, E_0, with typical agreement factors of R = 0.00020. Representative best fits from LCF using data measured at room temperature, *ca*. 900 °C and room temperature after cooling are illustrated in Figure 5-5. Phase composition analysis, yielding the fraction of PdO and Pd within the sample over the various temperatures, is displayed in Figure 5-6.

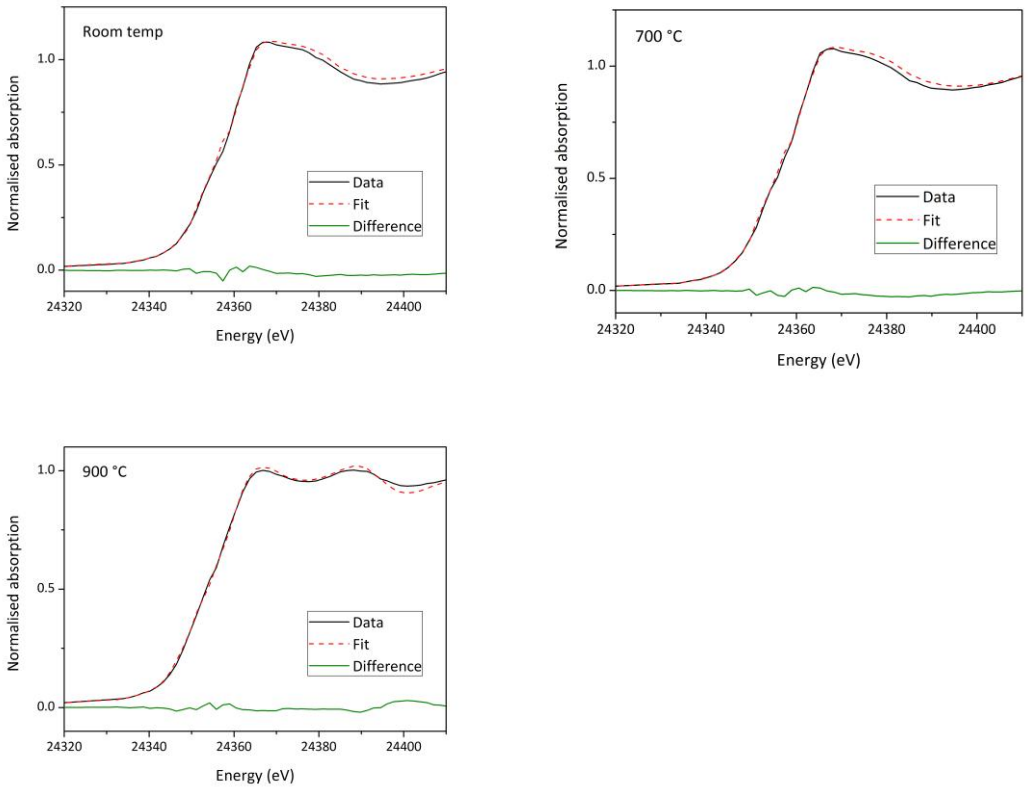

Figure 5-5. *Representative LCF best fits (red line) of the Pd/Al_2O_3 XANES (black line) measured at room temperature (top), 700 °C (middle) and 900 °C (bottom) along with the residual spectrum plot below in each. The estimated experimental uncertainty of the LCF analysis results is within 2 %.*

Results from the XANES LCF indicate that up to *ca.* 830 °C the sample has a single component PdO phase. Between 830 and 900 °C the incomplete reduction of PdO → Pd^0 takes place where the resultant phase composition from LCF is *ca.* 40 % and 60 % for PdO and Pd metal phases, respectively. On cooling the sample the onset of reoxidation occurs at *ca.* 680 °C and appears to have undergone almost a complete reoxidation by *ca.* 580 °C.

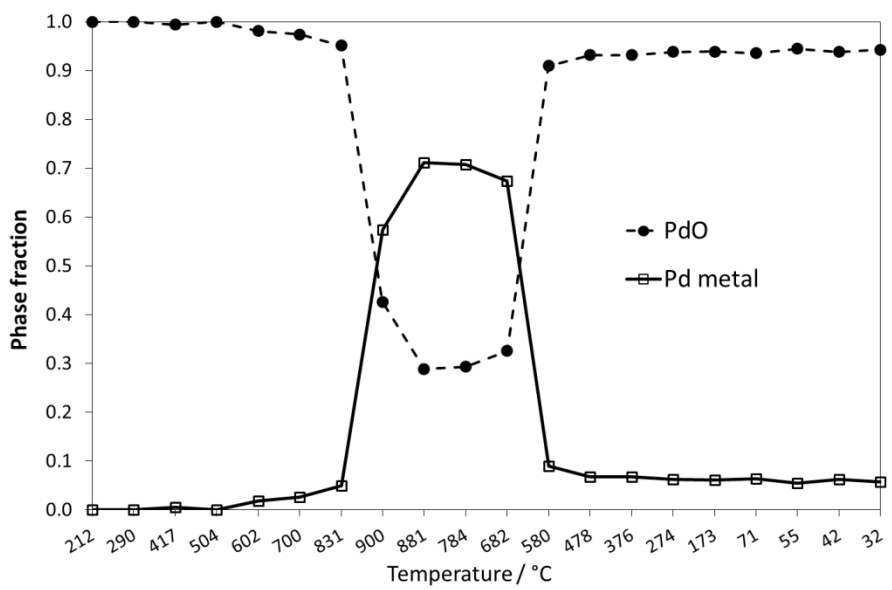

Figure 5-6. *Results of XANES LCF of 4 wt.% Pd/Al_2O_3 sample. The profile plots the relative concentration of Pd foil and PdO species within the sample against temperature. Errors on the calculated phase fractions are within the size of the symbols.*

5.5.4 *In situ* EXAFS

The Fourier transforms of EXAFS (phase shift uncorrected) for Pd/Al_2O_3 sample measured during heating and cooling cycle are shown in Figure 5-7. The first two peaks in the FT are assigned to the first two coordination shells of PdO at *ca*. 1.5 (Pd-O) and *ca*. 2.8 Å (Pd-Pd), respectively. These peak positions remain largely unchanged up to 800 °C. Above *ca*. 830 °C a single peak at *ca*. 2.4 Å emerges, consistent with a metallic first shell Pd-Pd distance, with a simultaneous decrease in the magnitude of the peaks at 1.5 and 2.8 Å is observed indicating the reduction of PdO to Pd^0. After 900 °C the metallic Pd-Pd peak amplitude gains intensity in the following cooling scans to 580 °C where the disappearance of metallic Pd-Pd coordination is observed with concomitant reappearance of Pd-O and Pd-Pd coordination shells belonging to PdO. The extent of reduction, determined from the coexistence of Pd species, cannot be estimated via inspection of FT magnitudes since the amplitude of the peaks in the FT are attenuated by thermal disorder component of the Debye-Waller factor. The refinement of the EXAFS data using a structural model was therefore performed to derived detailed structural information including

the respective phase fractions of PdO and metallic Pd. Figure 5-9 displays representative best fits of the EXAFS and associated Fourier transforms for data collected at 504 °C, 900 °C and at room temperature after cooling.

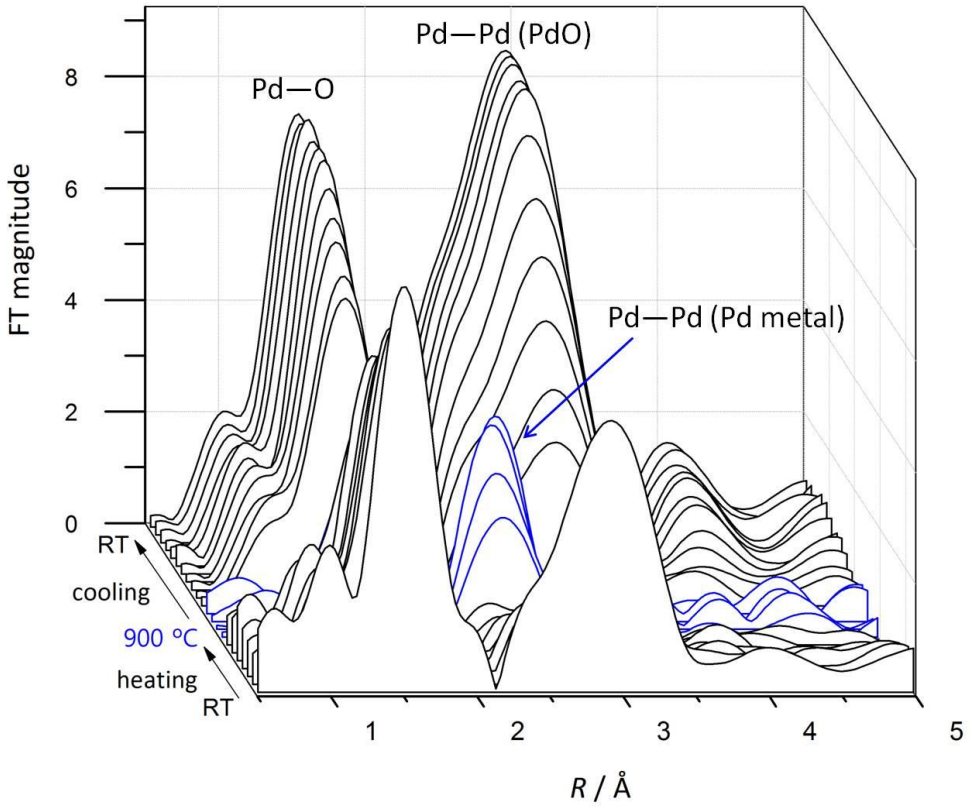

Figure 5-7. *In situ Fourier transformed Pd K-edge EXAFS data (phase shift uncorrected) for Pd/Al_2O_3 sample with heating to 900 °C and subsequent cooling. The PdO → Pd^0 reduction pathway is evident where the metallic Pd-Pd peak emerges at ~ 2.4 Å.*

The results of refined parameter values extracted through EXAFS analysis of *in situ* Pd K-edge EXAFS data are reported in Table 5-3. First shell analysis reveals the starting material has a structure very closely resembling that of bulk PdO where the Pd–O coordination in the Pd/Al_2O_3 sample is *ca.* 4 indicating the phase fraction of PdO is close to 100% which supports results from XANES LCF. The Pd-O bond distance of 2.01 Å is consistent with that of the bulk material and indicative of Pd^{2+}-O bonding. Second shell, Pd–Pd, correlations have also been included in the model with a refined distance of 3.02 Å which is similar to the distance seen in bulk PdO.

The first nearest neighbour Pd-O coordination gradually decreases upon heating to *ca*. 830 °C. This small decrease in coordination number can be explained by the increase in the first shell Debye-Waller factor since the two structural parameters are highly correlated. The Pd-O bond distance, 2.02 Å, does not change within experimental uncertainty, ± 0.01 Å. The EXAFS data at 900 C are modelled with the inclusion of metallic Pd-Pd coordination at 2.75 Å and a coordination number of 7 yielding a good agreement factor with this model. This under-coordination from that of the bulk metal (N = 12) is explained by the coexistence of oxide and metallic Pd species, where the Pd–O coordination number falls to 1.2. Whilst the error on the measured coordination number in EXAFS is routinely *ca*. 10% or higher, by using the under-coordination in first shell nearest neighbour (beyond the first shell the reliability of N reduces dramatically) from the bulk value in PdO and metallic Pd one can determine to some extent the relative amounts of each phase present and hence an estimation to the overall extent of reduction.

Table 5-3. *Structural parameters obtained from in situ EXAFS analysis of Pd/Al_2O_3 sample. Refined values for the threshold energy (ΔE), coordination number (N), interatomic distance (R) and Debye-Waller factors ($2\sigma^2$) are tabulated. Fitting results of Pd foil and PdO reference materials are shown for comparison. The estimated errors for the N, R and σ^2 were ca ±0.5, ±0.02 and ±0.001.*

(Ref material) Temp (˚C)	**1st shell PdO**			**2nd shell PdO**			**1st shell Pd metal**			R_{fit} **(%)**
	N	R_{Pd-O} (Å)	$2\sigma^2$ (Å^2)	*N*	R_{Pd-Pd} (Å)	$2\sigma^2$ (Å^2)	*N*	R_{Pd-Pd} (Å)	$2\sigma^2$ (Å^2)	
(PdO)	4.0	2.02	0.007	1.8	3.03	0.010				12.19
(Pd foil)							12	2.74	0.011	29.28
212	4.0	2.02	0.007	2.7	3.03	0.011				19.71
290	4.1	2.02	0.008	2.7	3.04	0.016				17.09
417	4.0	2.02	0.009	2.2	3.04	0.015				15.47
504	4.1	2.02	0.011	1.8	3.03	0.015				16.89
602	3.9	2.02	0.011	1.4	3.03	0.014				17.58
700	3.8	2.02	0.011	1.0	3.04	0.014				18.39
831	3.5	2.03	0.014	0.9	3.03	0.013				19.22
900	1.2	2.01	0.015	2.0	2.99	0.036	7	2.75	0.023	30.49
881	0.9	2.01	0.024	3.2	2.91	0.037	8.4	2.71	0.036	39.43
784	0.9	2.00	0.017	3.1	2.99	0.026	8.8	2.75	0.026	33.56
682	1.2	2.01	0.006	3.0	3.00	0.022	8.2	2.76	0.022	35.50
580	3.2	2.02	0.006	1.7	3.03	0.012				20.62
478	3.2	2.02	0.005	1.7	3.03	0.008				19.16
376	3.4	2.02	0.005	1.7	3.03	0.005				18.79
274	3.4	2.02	0.004	1.7	3.03	0.004				20.96
173	3.5	2.02	0.004	2.1	3.04	0.003				19.92
71	3.5	2.02	0.003	2.5	3.04	0.003				20.46
55	3.4	2.02	0.003	2.5	3.05	0.003				20.30
42	3.4	2.02	0.002	2.6	3.04	0.002				21.17
32	3.5	2.02	0.002	2.6	3.04	0.003				20.87

Figure 5-8 illustrates the phase fractions obtained from respective coordination numbers for PdO and metallic Pd phases over the full temperature resolved experiment. From fitting the EXAFS data at 900 °C, a 30 and 70 % phase composition for PdO and metallic Pd species, respectively, is obtained. In comparison XANES LCF fitting suggest a 40 % and 60 % composition for PdO and Pd, respectively, at 900 °C. $Pd^0 \rightarrow PdO$ reoxidation takes place between 680 and 580°C, at which point the reoxidation of Pd/Al_2O_3 is considered to be complete. At 580 °C data cannot be modelled with the inclusion of Pd-Pd scattering, the results yielding negative Debye-Waller factors or coordination numbers. The Debye-Waller factor gradually decreases on cooling back to room temperature and the Pd-O coordination gradually increases to a value close to that of bulk coordination. Over the course of the reduction and reoxidation, phase composition results from EXAFS and XANES analyses yield a consistently good agreement. Scans taken on cooling to room temperature reveal Pd/Al_2O_3 EXAFS data which are consistent with bulk PdO data.

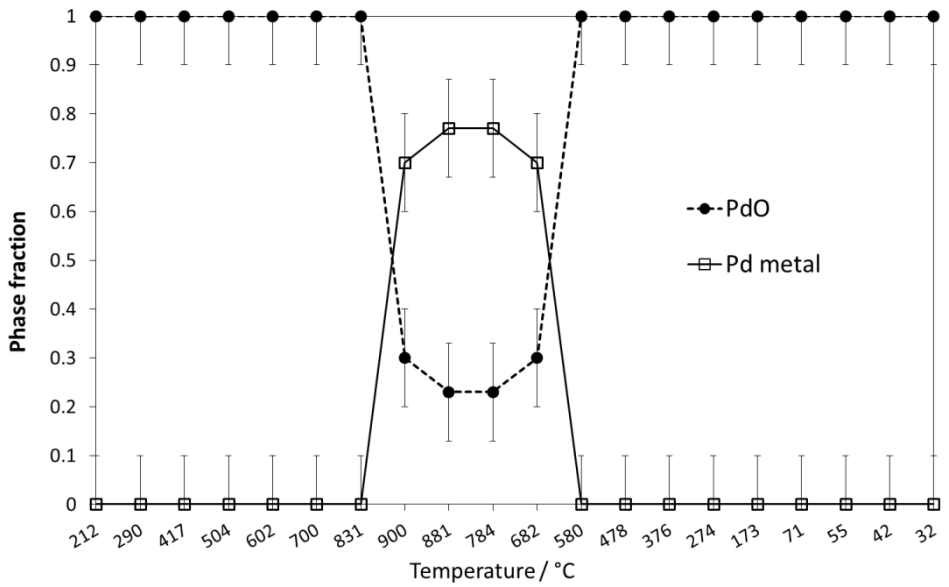

Figure 5-8. *Plot detailing the relative amounts of metallic Pd and PdO species present over heating and cooling cycle obtained using the first shell coordination number, N, from EXAFS analysis.*

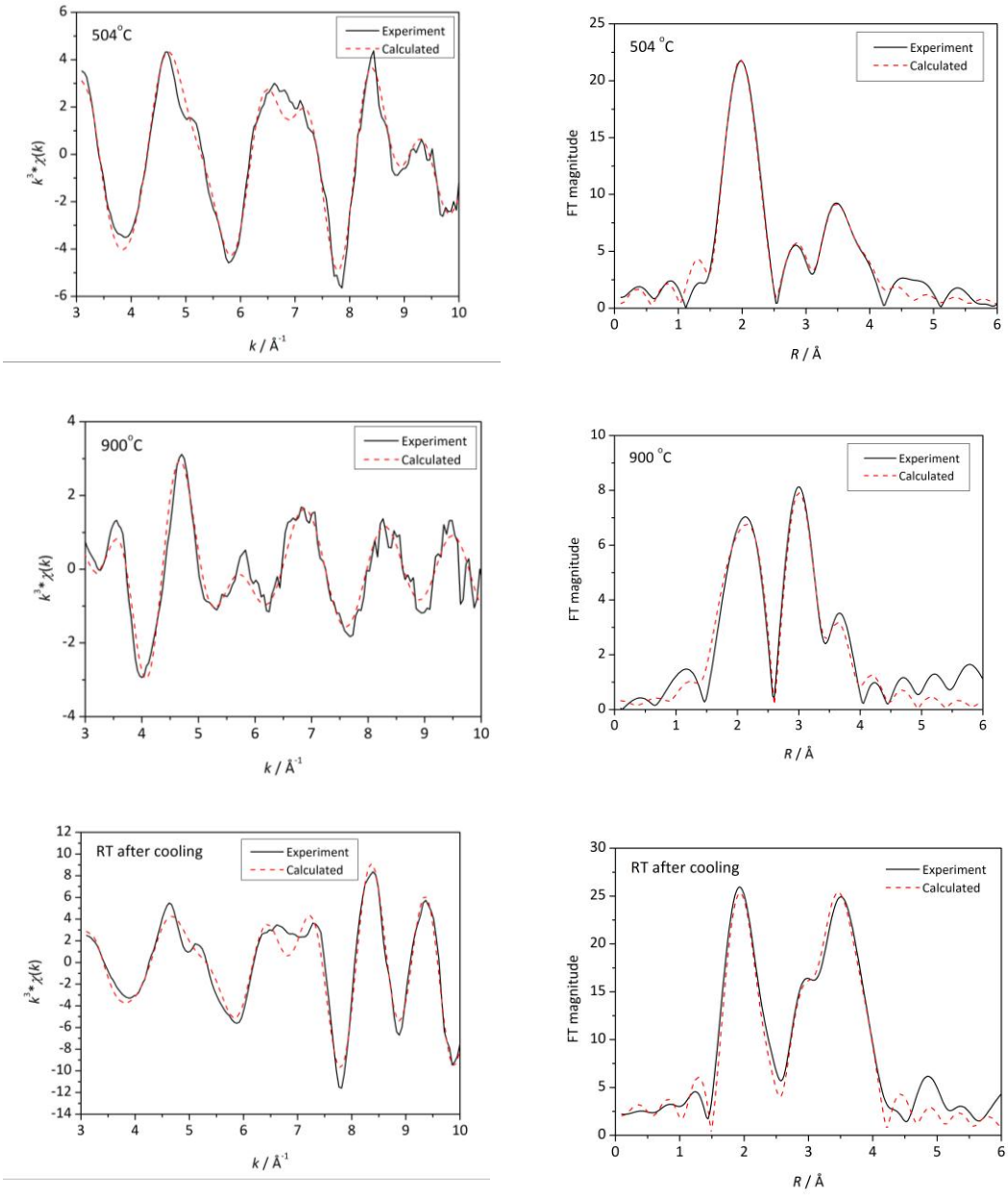

Figure 5-9. *Representative best fits of the Pd K-edge EXAFS and associated Fourier transforms from Pd/Al_2O_3 in situ data measured at 504 °C, 900 °C and room temperature after cooling.*

5.6 Conclusion

The structural transformations during the reduction and reoxidation of a model 4 wt.% Pd/Al_2O_3 catalyst have been examined in detail using *in situ* PDF, XANES and EXAFS techniques. New information on this system has been garnered using the differential PDF approach, yielding quantitative information on the phase composition at elevated temperatures, which would otherwise be lost due to the major γ-Al_2O_3 support component to the PDF. Although the use of the PDF method allowed us to determine structural information over a large length scale, which is not possible using EXAFS, this technique is unable to provide electronic state information. Therefore XANES and EXAFS were used to determine the phase composition and local structure of the reacting supported Pd catalyst.

Complementary *in situ* Pd K-edge XAS data were measured for the Pd/Al_2O_3 sample to provide additional structural information at comparable temperatures and to cross correlate the results of XANES, EXAFS and PDF analyses. From all techniques employed the Pd/Al_2O_3 sample is shown to undergo an incomplete PdO to Pd^0 reduction between 830 and 900 °C. Whereas conventional diffraction suggests that this process is full and complete at 900 °C, a multi–cluster analysis of the d-PDF obtained at 900 °C indicates that there is a significant (*ca*. 30 %) residual PdO component which may be due to (i) highly dispersed PdO like particles interacting with the support or (ii) the formation of PdO suboxides. PDF analysis results are in agreement with both XANES and EXAFS analyses, both observing incomplete reduction to the metal at 900 °C, of the order 40 and 30 % of residual PdO detected by XANES and EXAFS, respectively. *In situ* data obtained *via* all techniques also show evidence for the reoxidation of Pd^0 to PdO upon cooling to room temperature where the results of XANES and EXAFS analyses agree very well indicating that complete reoxidation of the Pd/Al_2O_3 sample takes place between 680 and 580 °C.

Thus by combining the strengths of the two techniques and by implementing the differential PDF analysis method, we have demonstrated the complementarities of

PDF and XAS techniques and their power in developing our understanding of complex supported catalytic systems containing low metal loadings.

5.7 References

[1] Anderson, R. B.; Stein, K. C.; Feenan, J. J.; Hofer, L. J. E., *Industrial and Engineering Chemistry*, (1961) **53**, 809.

[2] Ciuparu, D.; Lyubovsky, M. R.; Altman, E.; Pfefferle, L. D.; Datye, A., *Catalysis Reviews-Science and Engineering*, (2002) **44**, 593.

[3] Cordi, E. M.; Falconer, J. L., *Jouranl of Catalysis*, (1996) **162**, 104.

[4] Farrauto, R. J.; Hobson, M. C.; Kennelly, T.; Waterman, E. M., *Applied Catalysis A-General*, (1992) **81**, 227.

[5] Lyubovsky, M.; Pfefferle, L., *Catalysis Today*, (1999) **47**, 29.

[6] Datye, A. K.; Bravo, J.; Nelson, T. R.; Atanasova, P.; Lyubovsky, M.; Pfefferle, L., *Applied Catalysis A-General*, (2000) **198**, 179.

[7] Yang, S. W.; Maroto-Valiente, A.; Benito-Gonzalez, M.; Rodriguez-Ramos, I.; Guerrero-Ruiz, A., *Applied Catalysis B-Environmental*, (2000) **28**, 223.

[8] McCarty, J. G., *Catalysis Today*, (1995) **26**, 283.

[9] Hicks, R. F.; Qi, H. H.; Young, M. L.; Lee, R. G., *Journal of Catalysis*, (1990) **122**, 295.

[10] Lyubovsky, M.; Pfefferle, L., *Catalysis Today*, (1999) **47**, 29.

[11] Wolf, M. M.; Zhu, H.; Green, W. H.; Jackson, G. S., *Applied Catalysis A: General*, (2003) **244**, 323.

[12] Hoflund, G. B.; Hagelin, H. A. E.; Weaver, J. F.; Salaita, G. N., *Applied Surface Science*, (2003) **205**, 102.

[13] Keresszegi, C.; Grunwaldt, J. D.; Mallat, T.; Baiker, A., *Journal of Catalysis*, (2004) **222**, 268.

[14] Fern ndez-Garcia, M.; Iglesias-Juez, A.; Martinez-Arias, A.; Hungria, A. B.; Anderson, J. A.; Conesa, J. C.; Soria, J., *Journal of Catalysis.*, (2004) **221**, 594.

[15] Cho, S. J.; Kang, S. K., *Journal of Physical Chemistry B*, (2000) **104**, 8124.

[16] Gleeson, D.; Sankar, G.; Catlow, C. R. A.; Thomas, J. M.; Spano, G.; Bordiga, S.; Zecchina, A.; Lamberti, C., *Physical Chemistry Chemical Physics*, (2000) **2**, 4812.

[17] McCaulley, J. A., *Journal of Physical Chemistry.*, (1993) **97**, 10372.

[18] Kohara, S.; Itou, M.; Suzuya, K.; Inamura, Y.; Sakurai, Y.; Ohishi, Y.; Takata, M., *Journal of Physics-Condensed Matter*, (2007) **19**,

[19] Wakihara, T.; Yamakawa, T.; Tatami, J.; Komeya, K.; Meguro, T.; Kohara, S., *Journal of the American Ceramic Society*, (2007) **90**, 1562.

[20] Wakihara, T.; Kohara, S.; Sankar, G.; Saito, S.; Sanchez-Sanchez, M.; Overweg, A. R.; Fan, W.; Ogura, M.; Okubo, T., *Physical Chemistry Chemical Physics*, (2006) **8**, 224.

[21] Michel, F. M.; Ehm, L.; Antao, S. M.; Lee, P. L.; Chupas, P. J.; Liu, G.; Strongin, D. R.; Schoonen, M. A. A.; Phillips, B. L.; Parise, J. B., *Science*, (2007) **316**, 1726.

[22] Page, K.; Proffen, T.; Niederberger, M.; Seshadri, R., *Chemistry of Materials*, (2010) **22**, 4386.

[23] Newton, M. A.; Chapman, K. W.; Thompsett, D.; Chupas, P. J., *Journal of the American Chemical Society*, (2012) **134**, 5036.

[24] Liang, K. S.; Laderman, S. S.; Sinfelt, J. H., *Journal of Chemical Physics*, (1987) **86**, 2352.

[25] Fuoss, P. H.; Eisenberger, P.; Warburton, W. K.; Bienenstock, A., *Physical Review Letters*, (1981) **46**, 1537.

[26] Chupas, P. J.; Chapman, K. W.; Jennings, G.; Lee, P. L.; Grey, C. P., *Journal of the American Chemical Society*, (2007) **129**, 13822.

[27] Chapman, K. W.; Chupas, P. J.; Kepert, C. J., *Journal of the American Chemical Society*, (2005) **127**, 11232.

[28] Zhao, H.; Nenoff, T. M.; Jennings, G.; Chupas, P. J.; Chapman, K. W., *Journal of Physical Chemistry Letters*, (2011) **2**, 2742.

[29] Zhao, H.; Chupas, P. J.; Chapman, K. W., *Zeitschrift Fur Kristallographie*, (2012) **227**, 268.

[30] Chupas, P. J.; Qiu, X. Y.; Hanson, J. C.; Lee, P. L.; Grey, C. P.; Billinge, S. J. L., *Journal of Applied Crystallography*, (2003) **36**, 1342.

[31] Farrow, C. L.; Juhas, P.; Liu, J. W.; Bryndin, D.; Bozin, E. S.; Bloch, J.; Proffen, T.; Billinge, S. J. L., *Journal of Physics-Condensed Matter*, (2007) **19**,

[32] Ravel, B.; Newville, M., *Journal of Synchrotron Radiation*, (2005) **12**, 537.

[33] Gurman, S. J.; Binsted, N.; Ross, I., *Journal of Physics C-Solid State Physics*, (1984) **17**, 143.

[34] Keating, J.; Sankar, G.; Hyde, T. I.; Kohara, S.; Ohara, K., *Physical Chemistry Chemical Physics*, (2013) **15**, 8555.

[35] Waser, J.; Levy, H. A.; Peterson, S. W., *Acta Crystallographica*, (1953) **6**, 661.

[36] Bayer, G.; Wiedemann, H. G., *Thermochimica Acta*, (1975) **11**, 79.

[37] Zorn, K.; Giorgio, S.; Halwax, E.; Henry, C. R.; Grönbeck, H.; Rupprechter, G. n., *The Journal of Physical Chemistry C*, (2010) **115**, 1103.

[38] Goodwin, A. L.; Michel, F. M.; Phillips, B. L.; Keen, D. A.; Dove, M. T.; Reeder, R. J., *Chemistry of Materials*, (2010) **22**, 3197.

[39] Young, C. A.; Dixon, E.; Tucker, M. G.; Keen, D. A.; Hayward, M. A.; Goodwin, A. L., *Zeitschrift Fur Kristallographie*, (2012) **227**, 280.

[40] Baylet, A.; Marecot, P.; Duprez, D.; Castellazzi, P.; Groppi, G.; Forzatti, P., *Physical Chemistry Chemical Physics*, (2011) **13**, 4607.

Chapter 6 Speciation of VEC catalysts using chlorine K-edge XAS

6.1 Chapter overview

An investigation into the speciation of chlorine–containing platinum compounds in North American based automotive-exhaust catalysts using chlorine K-edge XAS was undertaken. We used the localised XANES regions of the X-ray absorption spectra to characterise the structure of unused (fresh) and used (road-aged) vehicle emission control (VEC) catalysts. Both gasoline Three-way Catalysts (TWC) and Diesel Oxidation Catalysts (DOC) VEC catalysts were utilised in this study from geographically varied locations. Our results reveal that no chloroplatinate species could be detected, even at the high sensitivity of Cl K-edge XAS to chlorine within the samples (< 30 ppm); the only chlorine that could be accounted for is that originating from the γ-alumina component of the catalysts. These results highlight the advantage of performing Cl K-edge measurements for VEC catalyst speciation at low concentration levels and, consequently, have important implications for environmental protection.

6.2 Introduction

Anthropogenic emission of various gases such as nitrogen oxides (NOx), carbon monoxide (CO), sulphur oxides (SOx) and unburned hydrocarbons (HC) to the atmosphere come from use of fossil fuels. During the 1960s it was identified that these "greenhouse" or toxic gases emitted from vehicle engine exhausts into the atmosphere posed a risk to health and the environment. Growing environmental concern lead to introduction of US environmental legislation in the 1970s to enforce that measures be taken to control and abate the emission of harmful secondary pollutants from vehicle engines [1]. Accordingly, this necessitated a concerted effort to be placed on developing efficient new catalysts for improving air quality and adhering to stringent controls. Conversion of these environmentally unacceptable gases to more acceptable ones, in particular to N_2, CO_2 and H_2O using catalysts has been a challenging task which has been overcome through the use of heterogeneous catalysts.

With the inclusion of diesel engines in today's growing vehicle industry, two types of automotive exhaust catalysts are widely used: (a) Two-way catalytic converters used in diesel engines to reduce hydrocarbon and carbon monoxide emissions and (b) Three-way converters widely used in gasoline engines. Three-way catalytic converters (TWC) have simultaneous tasks, in (i) oxidation of CO to CO_2 and (ii) oxidation of unburned hydrocarbons to CO_2 and H_2O and (iii) reduction of nitrogen oxides to nitrogen and oxygen [1]. Platinum group metal (PGM) based catalysts, which includes platinum, palladium and rhodium, have shown superior performance for vehicle emission control (VEC) [2]. These metals are dispersed on high surface area carriers, in particular alumina or ceria based supports. The catalyst monoliths in vehicles are treated with both PGMs and high surface area γ-alumina to achieve the desired catalytic performance [1]. Platinum, in particular is highly active for both diesel and gasoline applications. Local environmental legislation and the variable costs of raw materials and precious metals means these formulations vary from region to region but which typically contain 0.1 – 1 wt% of PGM [3].

A number of techniques [4, 5] have been employed in the literature to determine the structure and speciation of model and industrially relevant catalysts. Among these, X-ray absorption spectroscopy (XAS) has been preferentially used since it is

element-specific and is not constrained by long-range order, that which limits X-Ray Diffraction (XRD) [6]. X-ray photoelectron spectroscopy is also widely used, however, it is limited to the study of surface species; it is nevertheless a useful tool for catalytic studies [7]. Similarly, microscopy has been used extensively to determine particle morphology and element mapping [8, 9]. There is a growing concern on the reactivity of platinum nanoparticles in the catalyst with chlorine in the environment producing chloroplatinate species; chloroplatinate compounds are known to be hazardous to health. With concerns of toxicity in mind, a number of recent studies have focussed on the distribution and chemical form of PGMs in the environment [10-12]. Hence, there is a need to better investigate the speciation of platinum in authentic vehicle exhaust catalysts operated in real world conditions. A recent Pt L_3-edge XAS study by Hyde *et al* [13] showed that, in European samples, no detectable chloroplatinate species could be found.

Whilst many XAS studies focus on the metal edge, very few are performed at the chlorine K-edge. These low energy XAS studies are challenging and usually restricted to the measurement of XANES regions only. In spite of this, much information can be gleaned from analysis of the XANES wherein the local structure and chemical state of the chlorine is probed. Cl K-edge XAS has more recently been utilised to understand the nature of bonding interactions between chlorine and metals in transition metal complexes providing complementary structural information to that obtained from the metal K- and L-edges [14]. Experiments at the Cl K-edge have been undertaken to solve a range of problems in inorganic and bioinorganic chemistry as highlighted by Solomon *et al* [15]. From these XAS experiments ligand-metal covalent bonding interactions can be measured and ligand-metal orbital mixing quantified, hence Cl K-edge XAS is an ideal technique for probing metal chloride species. Moreover, due to the highly selective nature of XAS only the interactions associated with chlorine are observed. This is much more favourable over metal edge studies where, in addition to chlorine, every other component of the catalyst is detected (if in sufficient concentration). Cl K-edge XANES is well equipped for speciation studies providing clarification and resolution as to the nature of the chlorine present in real catalytic systems which may be present in low concentrations.

6.3 Aims and objectives

This investigation aims to employ low energy Cl K-edge XAS for the speciation of chloroplatinates within fresh and road aged Vehicle Emission Control (VEC) catalysts. Speciation using Pt L-edge XANES and EXAFS has been previously performed [13] in addition to SEM and XPS studies on these catalysts. However, this is not the focus of this investigation. Our aim is to show evidence for the existence or absence of platinum chloride or chloroplatinate species in VECs using Cl K-edge XANES data. This will allow for the detection of only chlorine-containing species and avoid the numerous contributions from other species that exist in these catalysts.

6.4 Experimental

6.4.1 Samples

Two sets of model compounds were used in this study: (1) NaCl, NH_4Cl and KCl, representing ionic systems and (2) Pt-Cl containing compounds: $PtCl_2$, $PtCl_4$, K_2PtCl_4, K_2PtCl_6, $(NH_4)_2PtCl_6$. These model compounds were selectively chosen to reflect their respective ionic and covalent metal-chloride bonding interactions and the variety of metal (Pt) oxidation states and geometries they exhibit. All model compounds used in this study were obtained from Alfa Aesar.

The VEC catalysts used in this study were North American three-way catalysts (TWCs) and diesel oxidation catalysts (DOCs) from selected geographic regions. Catalyst samples were supplied by the Manufactures of Emission Control Association (MECA) Arlington, VA. Catalyst samples were sourced from road aged vehicles from selected geographic regions both coastal and non-coastal environments. Two types of DOCs were studied; High Duty Diesel (HDD) and Light Duty Diesel (LDD). Replacement original equipment manufacturer (OEM) parts were sourced for the respective vehicles and utilised as control samples for this characterisation study and are referred to as 'Fresh'. Table 6-1 details the variety of VEC catalysts employed in this study and their respective origins. DOC samples were scrapings from fresh vehicle catalysts and road aged vehicle catalysts. TWC samples were from ground monoliths and likely to be contain platinum group metal (PGM) species in much lower concentrations than DOC samples.

Table 6-1. *Fresh and Aged catalyst samples and nomenclature utilised in this study*.

Catalyst Name	Ageing, Region
TWC	
TWC Fresh	
TWC AC	Road Aged, Coastal
TWC ANC	Road Aged, Non-coastal
DOC	
LDD Fresh	
LDD AC	Road Aged, Coastal
HDD Fresh	
HDD ANC	Road Aged, Non-coastal

6.4.2 Fluorescence and Total Electron-Yield XAS

Cl K-edge XAS measurements were carried out at the Canadian Double Crystal Monochromator beamline of the synchrotron radiation source (SRS), Madison, WI, USA. The beamline is shown in Figure 6-1. The ring energy operates at 800 MeV and also at 1 GeV; higher energy measurements were required for this XAS study. The beamline is located on a bending magnet and has an operating range of 1500 to 4000 eV. The Cl K-edge lies within this range at 2822 eV. Each spectrum was acquired over the energy range 2800 to 2900 eV. Cl K-edge XAS measurements were performed in fluorescence mode and using the total electron yield (TEY) technique. The differences between both methods are described in chapter two. The experimental setup of electron yield technique involves measuring the drain current of the cathode of a helium filled ion chamber. Sample powders were ground up and spread thinly and uniformly across a piece of conducting carbon tape which was mounted onto an aluminium plate and placed in front of the beam under ultra-high vacuum (Figure 6-1). The beam size covers approx. 12 μg of material. Electron yield is a surface sensitive technique due to its limited penetration depth (at most 50 Å, [16]). Electrons ejected from the surface of the sample ionise the helium and the

number of emitted electrons (upon excited state relaxation) is proportional to the absorption coefficient. An 11–channel detector was used for fluorescence measurements with the detector fixed in position at 90 ^{0} to the incoming X-ray beam.

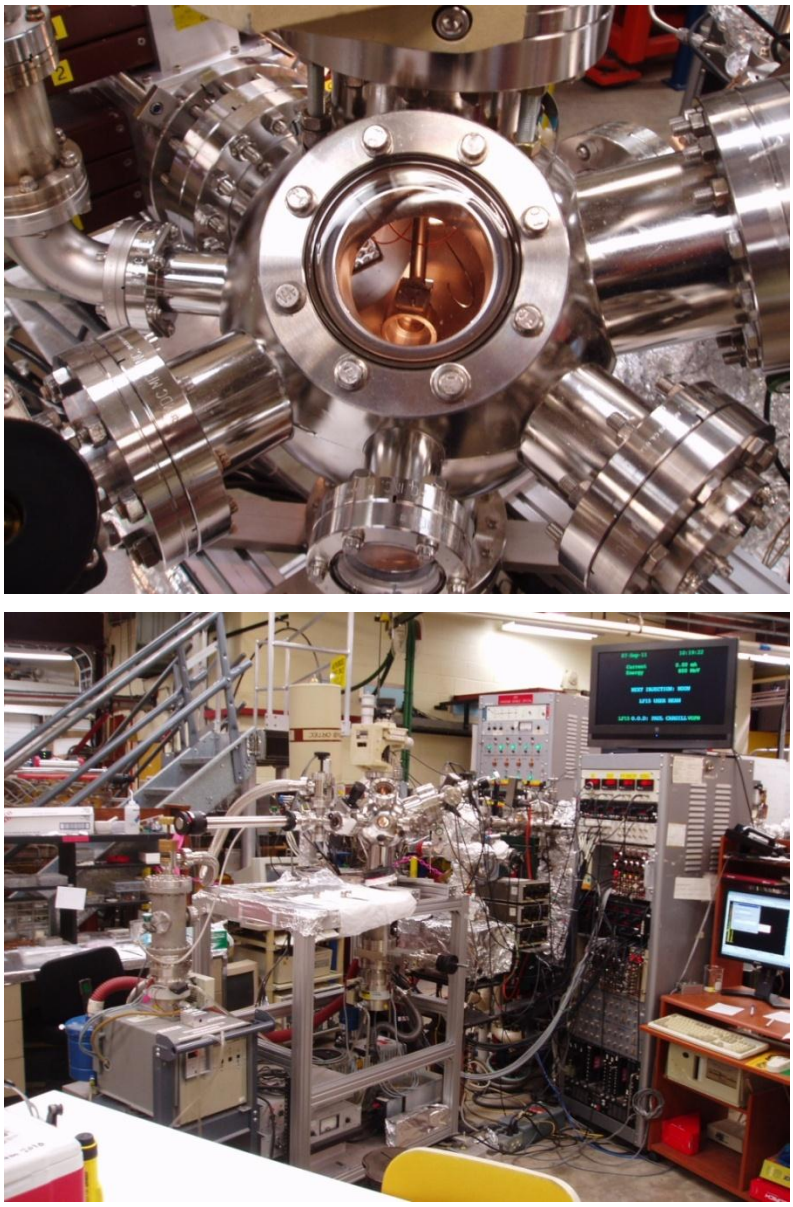

Figure 6-1. *Canadian Double Crystal Monochromator beamline at Aladdin storage ring, SRC. Sample chamber (top) for electron yield and fluorescence XAS measurements and beamline (bottom) under ultra-high vacuum.*

Chlorine–containing model compounds and catalyst sample powders were measured in both fluorescence and electron yield modes. In more concentrated samples, such

as the model compounds used in this study, self-absorption processes are an issue. This leads to distortion of the amplitudes in the XANES spectra and makes the normalisation problematic and unreliable. Detector saturation is also a common issue for fluorescence measurements where the experimental geometry is fixed in place. Consequently, the XANES spectra of all the model compounds in this study are from electron yield measurements where self-absorption is not an issue. Conversely, the XANES spectra of the catalyst samples are from fluorescence measurements since they fall within the thick dilute limit (refer to chapter two for explanation) and electron yield data is largely unusable. The amount of chlorine in the catalyst samples was significantly less than in the model compounds, therefore the measurements were made at 1 GeV to give a better signal-to-noise (S/N) ratio. The monochromator scanned an energy range of 2800 to 2900 eV which includes the XANES region of the X-ray absorption spectrum. Attempts were made to measure the EXAFS region (50 eV above the absorption edge and beyond) however the data were dominated by noise, restricting the useable data in *k*-space, and thus no meaningful information could be obtained from measuring the EXAFS. Notwithstanding the lack of extended fine structure information, XANES is highly sensitive to the immediate coordination around the absorbing atom and thus structural information pertaining to the chemical environment, specifically the bonding interactions, can be obtained and is the focus of this study.

6.4.3 Total chloride analysis

Combustion - Ion Chromatography (CIC) total chloride assay was carried out at Johnson Matthey, Sonning common and performed using a Mitsubishi AQF-2100H anion analyser connected to a Metrohm modular ion chromatograph with a Metrohm A Supp 5 250 anion column. A solid sample was introduced via an autosampler with WO_3 as the combustion improver and combusted at 1100°C under O_2. The resulting halide rich gas stream was bubbled and absorbed into UHP water; this was in turn injected into the ion chromatograph.

6.4.4 Data analysis

Raw XAS data were background subtracted and normalised using the Athena program. Due to the low concentrations of chlorine within the materials, in particular the catalyst samples, repeat scans were measured and merged to improve statistics and the S/N ratio. Merging of data using Athena is essentially an averaging technique and performed using raw $\mu(E)$ data. For interpretation of data with a low S/N ratio "smoothing" can be performed in the program in order to pronounce real spectral features that may be diluted by background noise. The data analysis in our study was not, however, subject to any smoothing to ensure subtle features are not removed by this process.

6.5 Results and discussion

The first part of this study focuses on Cl K-edge XAS measurements of chlorine–containing model compounds. Ionic and covalent bonding interactions involving chlorine can be differentiated by diagnostic spectral features in the XANES and shall be discussed with reference to the platinum containing model compounds. The next part of this study will evaluate data from Cl K-edge XAS measurements of real VEC catalyst samples, from fresh and vehicle road aged catalysts (DOCs and TWCs). To interpret the catalyst data, comparison and references will be made to the model compounds.

6.5.1 Chlorine containing model compounds

6.5.1.1 Ionic

Figure 6-2 displays the Cl K-edge XANES spectra for the ionic model compounds NH_4Cl, NaCl and KCl. This data were obtained from electron yield measurements. The sharp increase in absorption at the absorption edge, between 2822 to 2823 eV, in these samples gains intensity from the electric dipole allowed Cl $1s \rightarrow 4p$ transition. The XANES spectra of these ionic materials display significantly different lineshapes, in particular the white line intensity in all three materials shows considerable differences. For NaCl an intense white line is observed which subsequently falls to zero, this is due to problematic normalisation of these electron yield data. The position of the absorption edge between samples is close however, to within 1 eV. The positions of the main absorption edges are tabulated in Table 6-2 and these values represent the maxima in the respective derivative spectra.

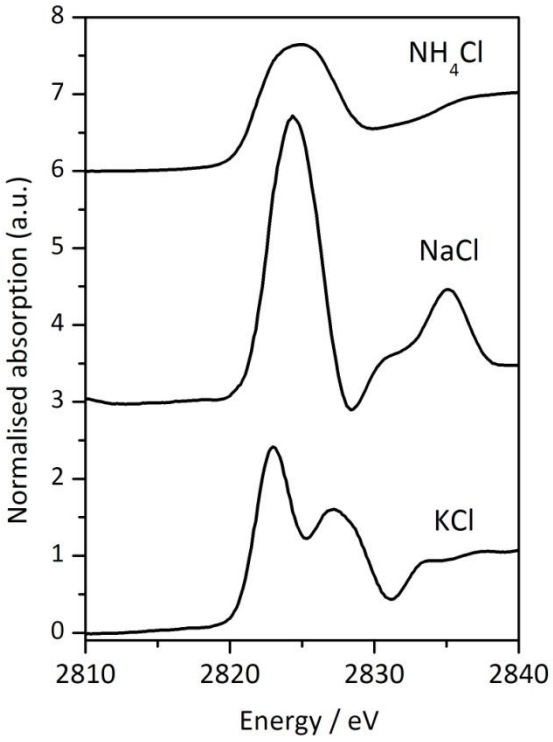

Figure 6-2. *Normalised Cl K-edge XANES spectra of a set of ionic model compounds: NH_4Cl (top), NaCl (middle) and KCl (bottom).*

Table 6-2. *Edge positions of ionic chlorine containing model compounds.*

Reference material	Edge position / eV
KCl	2822.0
NaCl	2822.7
NH_4Cl	2821.9

6.5.1.2 Covalent Pt-Cl

Cl K-edge XAS measurements of various platinum chloride and chloroplatinate samples were obtained and the electron yield XANES data are displayed in Figure 6-3. These platinum containing model compounds represent various coordination geometries and ligands covalently bonded to platinum in the Pt(II) and Pt(IV) oxidation states. The XANES spectra exhibit two distinct features present in all of all the model compounds; a pre-edge peak region marked 'A' (*ca*. 2816 – 2819 eV) and a main edge region marked 'B' (*ca*. 2820 – 2824 eV). Tabulated energy values of the positions of the pre-edge and main-edge peaks are listed in Table 6-3.

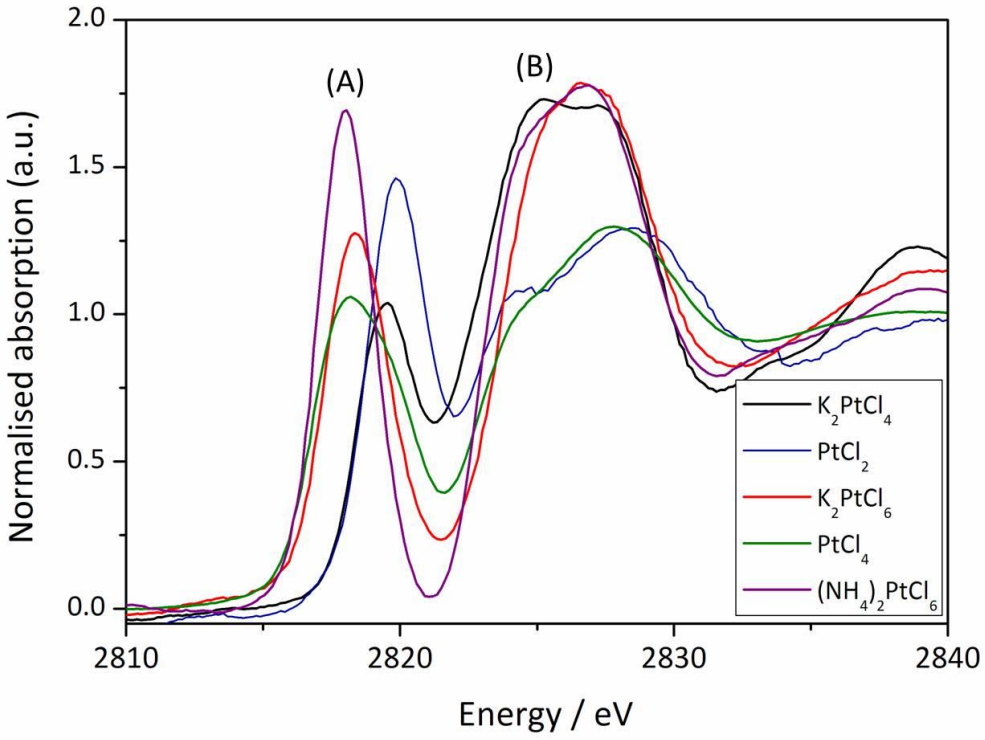

Figure 6-3. *Normalised Cl K-edge XANES spectra of Pt–containing model compounds. Intense pre-edge feature is observed (A) in all model compounds although the position and intensity varies. The shape of the absorption edge (B) in all model compounds display similarities related to coordination geometry.*

Table 6-3. *Pre-edge and main-edge positions of the platinum containing model compounds.*

Model compound	Pre-edge energy[A] / eV	Main-edge energy[B] / eV
K_2PtCl_4	2818.4	2823.4
$PtCl_2$	2818.7	2822.9
K_2PtCl_6	2817.3	2823.6
$PtCl_4$	2816.8	2822.7
$(NH_4)_2PtCl_6$	2816.9	2822.7

[A,B] Correspond to the pre-edge and main-edge peaks illustrated in Figure 6-2 and are taken as the maxima in the derivative spectra.

The main-edge peak, B, in all samples represents the increase in absorption intensity due to the electric dipole allowed Cl 1*s* → 4*p* transition. Unlike in metal edge XAS, where the binding energy can be directly related to the oxidation state of the absorbing atom, the position of the main-edge in Cl XAS is influenced by the effective nuclear charge on the chlorine. Thus the Pt oxidation state partly effects the edge position however this explains the apparent lack of correlation between edge position and Pt oxidation state where other effects are present. The intensity of the Cl 1*s* → 4*p* transition is related directly to the amount of Cl present. For K_2PtCl_6 and $(NH_3)_2PtCl_6$, which have the most Pt bound Cl, the most intense transitions are observed; $PtCl_4$ and $PtCl_2$ show comparatively weak main-edge intensities.

The pre-edge peak, A, at lower energy is also prominent in all the model compounds and is well resolved and separated from the main-edge peak, occurring at *ca*. 4 to 6 eV below the main-edge peak. This pre-edge intensity is attributed to the Cl 1*s* → 3*p* transition. The chlorine 3*p* orbitals are directly involved in bonding with the platinum 5*d* orbitals and so the pre-edge gains intensity if there is significant 3*p* character on the platinum 5*d* orbitals, from covalency. This electron excitation can alternatively be represented as a 1*s* → 5*d** dipole forbidden transition, gaining intensity due to the *p* character of the d orbital. Here, * represents the dominant character of the π antibonding metal orbital. The prominent pre-edge features in

Figure 6-3 vary in both intensity and position. The energy of the pre-edge transition is modulated by shifts in the core Cl 1*s* energy which is correlated to the relative charge of the chloride. More charge donation to the Pt creates a shift to a deeper binding energy. The energy of the pre-edge is, furthermore, affected by the HOMO energy which is determined by i) the geometry which has its origin in the splitting the *d*-orbital energies; ii) the coordination number and effective charge of the metal, shifting the overall energy of the *d* manifold [17]. The pre-edge feature is therefore a direct probe into the Pt—Cl molecular orbital and the covalent interactions [18]. In contrast, no pre-edge feature is observed in the XANES belonging to the ionic chlorides (Figure 6-2) since there are no partially filled *d* orbitals that overlap with Cl 3*p* orbitals and hence no covalent interactions.

6.5.2 VEC catalysts

6.5.2.1 Total chloride analysis

A Combustion – Ion Chromatography (CIC) total chloride assay was carried out on all catalysts and the results are listed in Table 6-4. The results of the assay indicate very low levels of chloride are present in all the catalyst samples. The total chloride content of the γ-alumina reference material is slightly greater than those of the catalysts suggesting that the chloride contained within the VECs is likely to originate from residual chloride in the alumina support.

Table 6-4. *Total chloride analysis of VECs and reference γ-alumina material as determined by combustion ion chromatography.*

VEC	Total chloride (ppm)
TWC Fresh	24
TWC AC	10
TWC ANC	13
LDD Fresh	17
LDD AC	19
HDD Fresh	<10
HDD ANC	22
γ-alumina reference	35

6.5.2.2 Cl K-edge XANES

Figure 6-4 displays the normalised Cl K-edge XANES spectra of the fresh and aged TWCs and DOCs (LDD and HDD) along with a plot of the γ-alumina reference XANES. Firstly, extraction of the fluorescence data after summing several spectra indicates an increase in absorption intensity between *ca*. 2820 and 2822 eV implicating the presence of chlorine and is designated to the Cl $1s \rightarrow 4p$ transition; Table 6-5 summarises the main-edge positions in XANES data of all the VECs. The fluorescence counts for respective TWCs and DOCs were found to be fairly low, however, suggesting chlorine is present in very low concentrations. Secondly, no evidence for a characteristic pre-edge feature, as is observed in all platinum containing model compounds, at < 2819 eV (Table 6-3), is detected in any of the catalysts. The higher energy XANES region, beyond *ca*. 2825 eV, also shows discordance with the model Pt compounds. There is a slight shift in the main-edge position of the VECs (*ca*. 1 – 2 eV) relative to the Pt containing model compounds which further suggests that the chlorine is in a different chemical environment compared to that of the model compounds. Although these spectra do suffer from a higher level of noise than the electron yield measurements on the Pt model

compounds it is quite evident that the XANES lineshapes in all the catalysts are very similar to that of the parent γ-alumina which does not contain platinum or any other metal. It is well known that alumina can contain residual chlorine in low levels from preparation methods and the results of CIC assay and XANES confirm this. The results of XANES analyses strongly suggest that the low levels of chlorine present in these catalyst systems are not associated, through direct bonding interactions, with platinum or any other PGM and that the chlorine signal originates from the residual chlorine within the γ-alumina support.

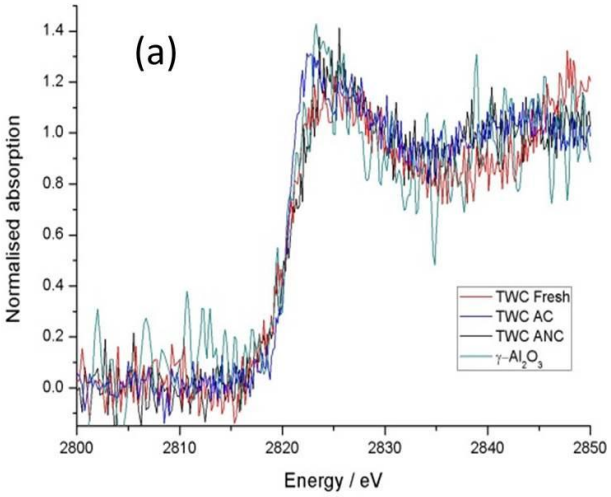

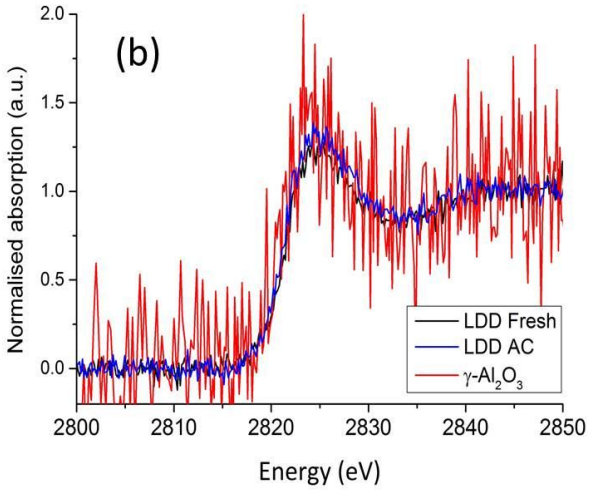

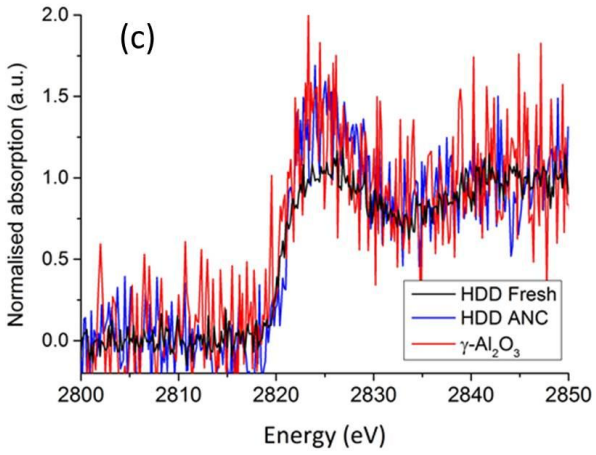

Figure 6-4. *Normalised Cl K-edge XANES spectra of: (a) fresh and aged Three-way catalysts from coastal (AC) and non-coastal areas (ANC); (b) fresh and aged LDD catalysts; (c) fresh and aged HDD catalysts. The Catalysts' XANES are compared with that of the γ-alumina reference material.*

Table 6-5. *Edge positions for TWCs and DOCs.*

Model compound	**Main-edge energy / eV**
TWC Fresh	2820.5
TWC AC	2819.7
TWC ANC	2820.6
LDD Fresh	2820.6
LDD AC	2820.5
HDD Fresh	2822.0
HDD ANC	2821.0
γ-alumina reference	2820.4

6.6 Conclusion

Chlorine K-edge X-ray absorption spectroscopic measurements have been performed on a variety of chlorine containing model compounds and on fresh and road aged VEC catalysts from a variety of sources. Few studies have been performed at the chlorine K-edge and so this investigation has brought new information surrounding potentially harmful chloroplatinate species in road aged VEC catalysts. We have demonstrated the power of element specificity in XAS where we have been able to record XANES data at the very low (ppm) levels within real vehicle road aged catalyst samples.

Using a set of platinum containing model compounds we have shown that the existence of characteristic pre-edge peaks in the XANES spectra are a direct measure of platinum – chloride covalent bonding interactions. By performing these speciation studies we have shown that fresh and vehicle road aged TWCs and DOCs do not contain chlorine associated with platinum through any direct interactions owing to the complete absence of any pre-edge features in the XANES of these catalysts. Very low levels of chlorine are detected using XANES data which is in strong agreement with total chloride assay that indicates levels of chlorine are less than 30 ppm. The observed chlorine signal is attributed to the residual chlorine in the parent γ-alumina with which the XANES of the VECs show greatest similarity.

Cl K-edge is complementary to metal edge measurements, which have been performed [13], and the findings are of great importance not just from an environmental protection point of view but also from a speciation point of view where performing low energy experiments at the Cl K-edge is a much more direct probe of metal – chloride interactions. Thus Cl K-edge measurements play an essential role in determining the existence of platinum – chloride species.

6.7 References

[1] Twigg, M. V., *Catalysis Today*, (2011) **163**, 33.

[2] Gandhi, H. S.; Graham, G. W.; McCabe, R. W., *Journal of Catalysis*, (2003) **216**, 433.

[3] Burch, R.; Breen, J. P.; Meunier, F. C., *Applied Catalysis B-Environmental*, (2002) **39**, 283.

[4] Kaspar, J.; Fornasiero, P., *Journal of Solid State Chemistry*, (2003) **171**, 19.

[5] Koningsberger, D., *X-Ray Absorption: Principles, Applications, Techniques of EXAFS, SEXAFS and XANES*, John Wiley & Sons Inc.: (1988).

[6] Russell, A. E.; Rose, A., *Chemical Reviews*, (2004) **104**, 4613.

[7] Ruhle, T.; Schneider, H.; Find, J.; Herein, D.; Pfander, N.; Wild, U.; Schlogl, R.; Nachtigall, D.; Artelt, S.; Heinrich, U., *Applied Catalysis B-Environmental*, (1997) **14**, 69.

[8] Ezekoye, O. K.; Drews, A. R.; Jen, H. W.; Kudla, R. J.; McCabe, R. W.; Sharma, M.; Howe, J. Y.; Allard, L. F.; Graham, G. W.; Pan, X. Q., *Journal of Catalysis*, (2011) **280**, 125.

[9] Ward, M. R.; Hyde, T.; Boyes, E. D.; Gai, P. L., *Chemcatchem*, (2012) **4**, 1622.

[10] Hutchinson, E. J.; Pearson, P. J. G., *Environmental Health Perspectives*, (2004) **112**, 132.

[11] Rauch, S.; Hemond, H. F.; Barbante, C.; Owari, M.; Morrison, G. M.; Peucker-Ehrenbrink, B.; Wass, U., *Environmental Science & Technology*, (2005) **39**, 8156.

[12] Rauch, S.; Hemond, H. F.; Peucker-Ehrenbrink, B.; Ek, K. H.; Morrison, G. M., *Environmental Science & Technology*, (2005) **39**, 9464.

[13] Hyde, T. I.; Ash, P. W.; Boyd, D. A.; Randlshofer, G.; Rothenbacher, K.; Sankar, G., *Platinum Metals Review*, (2011) **55**, 233.

[14] Boysen, R. B.; Szilagyi, R. K., *Inorganica Chimica Acta*, (2008) **361**, 1047.

[15] Solomon, E. I.; Hedman, B.; Hodgson, K. O.; Dey, A.; Szilagyi, R. K., *Coordination Chemistry Reviews*, (2005) **249**, 97.

[16] Stohr, J., *Prinicples, techniques and instrumentation of NEXAFS in NEXAFS spectroscopy*, Springer-Verlag: Berlin, (1992).

[17] Shadle, S. E.; Hedman, B.; Hodgson, K. O.; Solomon, E. I., *Inorganic Chemistry*, (1994) **33**, 4235.

[18] Kozimor, S. A.; Yang, P.; Batista, E. R.; Boland, K. S.; Burns, C. J.; Clark, D. L.; Conradson, S. D.; Martin, R. L.; Wilkerson, M. P.; Wolfsberg, L. E., *Journal of the American Chemical Society*, (2009) **131**, 12125.

Chapter 7 Summary and outlook

The advances in synchrotron radiation sources have propelled materials characterisation into a new era with ever more sophisticated methods being developed to tackle the structural elucidation of complex materials. Some of the problems, materials and techniques are not novel however advances in technology allow the measurement to be carried out at much faster time-scales so that challenging reacting systems can be tackled.

We employed *in situ* XAS and PDF to determine the short- and medium-range structure of allotropic cobalt using multi-cluster methodologies to garner detailed information on HCP and FCC structures within cobalt metal powders. Whilst limitations in the EXAFS technique prevent it from being used as a medium-range structural probe with accuracy, the implementation of multi-cluster models with *ex situ* and *in situ* data proved to be a reliable method of resolving HCP and FCC structured within the mixed phase cobalt system. Although the EXAFS methodology we have developed is based upon crystallographic structural models, good agreement between experiment and theory was obtained in the modelling and this approach was successful in capturing the HCP and FCC components over the course of the HCP → FCC phase transformation. On the other hand, the uncertainties in the derived phase composition analysis are high. Partly due to the effects of noise on *k*-space data at higher temperatures and moreover, the inherent correlations between the Debye-Waller factor and coordination number (or phase fraction) in EXAFS. Complementary *ex situ* and *in situ* PDF studies were performed to resolve the phase composition in HCP and FCC structures by analysing the short-, medium- and long-range order simultaneously. Unfortunately time resolved measurements were not possible at SPring-8, which is becoming fast available in other synchrotron radiation sources. The HCP and FCC multi-cluster methodology is ideally suited to PDF analysis which does not suffer from the same limitations as EXAFS; the medium-range ordering is modelled without the restrictions of *R*-space data. Furthermore, this is advantageous over conventional X-ray diffraction in that PDF analysis is executed in real-space and does not rely on long-range order.

Although this is true of the PDF technique, the multi-cluster methodology – analogous to that used in EXAFS – for use in this thesis work was limited to modelling the crystallographic components of the data. This restriction, however, did not prevent the extraction of in-depth structural information on this model FT catalyst system. Results from PDF and EXAFS, in general, were in good agreement however the *R*-dependence of EXAFS analysis proved PDF to be more accurate. To our knowledge, this is the first study of its kind, employing both PDF and EXAFS techniques to understand the fundamental atomic architecture of a model FT catalyst. Further potential work in this area will be to use Reverse Monte-Carlo modelling in such a way that both EXAFS and PDF data can be analysed simultaneously to a yield a more unique model.

Understanding the HCP and FCC composition in the cobalt system is not sufficient to complete our structural knowledge of supported cobalt catalysts, such as those used in FT synthesis. Although the active form of the catalyst is well known to be in the reduced state, of highly dispersed Co^0 particles, there are many issues which remain unclear in the literature pertaining to the reduced form of the catalyst. It is understood that the reductive treatment of a working alumina supported cobalt catalyst generates hard-to-reduce species which impact upon catalytic activity. There is no strong agreement, however, as to the nature of these species. Some authors propose that cobalt aluminate is formed, which is not easily reduced below 800 °C, whilst others suggest that "pseudo" aluminate like species are formed on the surface of the support. There is general consensus, however, that these hard-to-reduce species lack sufficient long-range order to be characterised by XRD. This has led to XAS being routinely employed in this area to understand the nature of the species within the catalyst in its precursor, active and deactivated state. The development of the QuickEXAFS technique has enabled us to carry out time-resolved speciation studies on a model FT catalyst to address some of the issues that have been highlighted in the literature using *in situ* combined XAS/XRD. Semi-quantitative information using XANES linear combination fitting provided evidence for a mixed metallic and cobalt oxide phase at the end of reduction; the extent of reduction was of the order *ca*. 60 %. This was consistent with literature findings. X-ray diffraction highlighted in this study that the poorly crystalline alumina support, in addition to the overlapping and extraneous reflections, impedes accurate

characterisation *via* this technique however the transient species in the reduction did corroborate the findings from XANES and EXAFS. EXAFS proved to be the most effective for gleaning insight into the nature of the species within the catalyst undergoing reduction. These findings supported those from XANES in that a mixed Co^{2+} and reduced Co^{0} coexist after reduction with a respective composition of 45 and 55 %. Crucially, EXAFS results indicated that the non-metallic component was an oxidic Co^{2+} species which could not be assigned to cobalt aluminate, at least as a bulk phase. This provided direct confirmation for the absence of cobalt aluminate formation within the catalyst. EXAFS yields bond lengths with high accuracy and the resulting Co—O bond length of 2.08 Å led us to propose a structure for the unreduced component of the reduced catalyst. This was that the reduced cobalt metal was the dominant species in the reduced catalyst and the minor component was a cobalt species which interacts strongly with the support which is hard to reduce in hydrogen at 500 °C. The EXAFS derived distance of 2.08 Å, contained within the unreduced phase, can be rationalised by cobalt ions diffusing into the alumina framework and locating themselves in octahedral holes within the alumina lattice. In this work the use of EXAFS has enhanced our understanding of the reduced species within the catalyst. To support our findings further work is necessary to complete this picture; the broad peak displayed in the TPR, representing Co^{2+} to Co^{0} reduction, can feasibly contain several oxidic Co species of varying reducibilities. Additional evidence for this type of species may be obtained through in depth modelling studies.

In another example of using the PDF technique, we gained new insight into the complex structure of a supported palladium catalyst. This work extended the multi-cluster methodology by using the differential PDF technique. One of the main drawbacks of using PDF, in particular to study complex multi-component systems, is that all atom—atom correlations are produced in the PDF. If the active component of interest is an element in low concentrations, as is frequently the case with supported noble metal catalysts, the PDF will be dominated by the unwanted constituents. In the case of supported palladium catalysts this is manifested in diffuse scattering from the γ-alumina support phase. By taking *in situ* PDF measurements of both Pd/Al_2O_3 catalyst and the γ-alumina support phase the alumina scattering could be removed, isolating just the palladium metal particles of

interest. XRD has been widely employed for characterising supported palladium catalyst however highly dispersed small metal particles hinders effective characterisation using XRD. Still it remains unclear as to whether the transformation of PdO to Pd is complete at elevated temperatures. With this in mind, we employed both differential PDF and EXAFS multi-cluster methodologies to study the phase transformation *in situ* thereby obtaining quantitative determination of phase composition at various temperatures. The results from both methodologies were in excellent agreement suggesting that the transformation is incomplete at 900 °C with a significant component of residual PdO being detected, of the order *ca*. 30 % from both techniques. Our findings have important implications for cross-correlating multi-cluster methodologies *via* implementation of crystallographic (differential PDF) and non-crystallographic (EXAFS) methodologies.

We exemplified the utilisation of low energy XAS for environmental speciation studies by taking real VEC catalysts with the aim of identifying the presence of absence of chloroplatinate species. Commonly, investigations of this nature are performed at metal edges which are easily accessed by the majority of XAS beamlines. With a potentially vast range of constituents contained within VEC catalysts the results can be complicated or inconclusive if performed from the metal edge alone, even with the element specificity of XAS. If a chlorinated platinum species is targeted then by performing chlorine K-edge studies the advantages are clear. Using a combination of both fluorescence and electron yield measurements we were able to assign characteristic XANES features to a set of model compounds containing platinum-chlorine species. This different perspective on platinum speciation proved to be a very powerful too where the characteristic XANES features exhibited by model compounds could not be identified in the VEC catalysts. Only chlorine associated with the parent alumina could be identified. The sensitivity of this technique showed very promising results for speciation studies to be performed at the chlorine edge. Furthermore, these results have significant implications from an environmental protection point of view. Investigations of this nature have also highlighted that real industrial materials can be challenging to measure by XAS where only XANES data could be recorded. Ideally, however, EXAFS data would be required for unambiguous confirmation. Optimising both experimental and

sample parameters is essential to obtain sufficient quality EXAFS data that can provide unambiguous confirmation of XANES analysis.

In summary, the multi-cluster methodologies that have been developed in this thesis, using EXAFS and PDF data, have brought new structural information, *via* the short- and medium-range ordering, on a variety of commercially relevant systems. The complementarities of the PDF and EXAFS technique are well understood and have been demonstrated in this work through advancing analytical methodologies that are critical in extracting new information on complex systems. The deployment of these techniques is becoming more commonplace in materials science and this thesis work has provided valuable insight to their application to industrial materials. We have shown using several examples of multi-phase systems the efficacy of EXAFS and PDF multi-cluster modelling. These fundamental studies provide the groundwork for more challenging systems to be studied.